DESIGN OPTIMIZATION OF COMPOSITE DEPLOYABLE BRIDGE SYSTEMS USING HYBRID META-HEURISTIC METHODS FOR RAPID POST-DISASTER MOBILITY

ASHRAF MOHAMED AHMED OSMAN

A Thesis

In the Department

of

Building, Civil and Environmental Engineering

Presented in Partial Fulfillment of the Requirements

For the Degree of

Doctor of Philosophy (Civil Engineering) at

Concordia University

Montréal, Québec, Canada

August 2016

Concordia University

School of Graduate Studies

This is to certify that the thesis prepared

By: **Mr. Ashraf Mohamed Ahmed Osman**

Entitled: **Design Optimization of Composite Deployable Bridge Systems Using Hybrid Meta-Heuristic Methods for Rapid Post-disaster Mobility**

and submitted in partial fulfillment of the requirements for the degree of

Doctor of Philosophy (Building, Civil and Environmental Engineering)

Complies with the regulations of this University and meets the accepted standards with respect to originality and quality.

Signed by the final examining committee:

_____ Chair
Dr. A. Awasthi

_____ External Examiner
Dr. Ex Maged A. Youssef

_____ Examiner, External to Program
Dr. R. Sedaghati

_____ Examiner
Dr. A. Bagchi

_____ Examiner
Dr. A. Bhowmick

_____ Supervisor
Dr. K. Galal

Approved by: _____
                Fariborz Haghighat, Ph.D., P.Eng, Graduate Program Director
                Department of Building, Civil and Environmental Engineering

August 22, 2016

                          _____
                          Dr. Amir Asif, Ph.D., PEng, Dean
                          Faculty of Engineering and Computer Science

ABSTRACT

Design optimization of composite deployable bridge systems using hybrid meta-heuristic methods for rapid post-disaster mobility

Ashraf Mohamed Ahmed Osman, Ph.D.

Concordia University, 2016

Recent decades have witnessed an increase in the transportation infrastructure damage caused by natural disasters such as earthquakes, high winds, floods, as well as man-made disasters. Such damages result in a disruption to the transportation infrastructure network; hence, limit the post-disaster relief operations. This led to the exigency of developing and using effective deployable bridge systems for rapid post-disaster mobility while minimizing the weight to capacity ratio. Recent researches for assessments of mobile bridging requirements concluded that current deployable metallic bridge systems are prone to their service life, unable to meet the increase in vehicle design loads, and any trials for the structures' strengthening will sacrifice the ease of mobility. Therefore, this research focuses on developing a lightweight deployable bridge system using composite laminates for lightweight bridging in the aftermath of natural disaster. The research investigates the structural design optimization for composite laminate deployable bridge systems, as well as the design, development and testing of composite sandwich core sections that act as the compression bearing element in a deployable bridge treadway structure.

The thesis is organized into two parts. The first part includes a new improved particle swarm meta-heuristic approach capable of effectively optimizing deployable bridge systems. The developed approach is extended to modify the technique for discrete design of composite laminates and maximum strength design of composite sandwich core sections. The second part focuses on developing, experimentally testing and numerically investigating the performance of different sandwich core configurations that will be used as the compression bearing element in a deployable fibre-reinforced polymer (FRP) bridge girder.

The first part investigated different optimization algorithms used for structural optimization. The uncertainty in the effectiveness of the available methods to handle complex structural models emphasized the need to develop an enhanced version of Particle Swarm Optimizer (PSO) without performing multiple operations using different techniques. The new technique implements a better emulation for the attraction and repulsion behavior of the swarm. The new algorithm is called Controlled Diversity Particle Swarm Optimizer (CD-PSO). The algorithm improved the performance of the classical PSO in terms of solution stability, quality, convergence rate and computational time. The CD-PSO is then hybridized with the Response Surface Methodology (RSM) to redirect the swarm search for probing feasible solutions in hyperspace using only the design parameters of strong influence on the objective function. This is triggered when the algorithm fails to obtain good solutions using CD-PSO. The performance of CD-PSO is tested on benchmark structures and compared to others in the literature. Consequently, both techniques, CD-, and hybrid CD-PSO are examined for the minimum weight design of large-scale deployable bridge structure. Furthermore, a discrete version of the algorithm is created to handle the discrete nature of the composite laminate sandwich core design.

The second part focuses on achieving an effective composite deployable bridge system, this is realized through maximizing shear strength, compression strength, and stiffness designs of light-weight composite sandwich cores of the treadway bridge's compression deck. Different composite sandwich cores are investigated and their progressive failure is numerically evaluated. The performance of the sandwich cores is experimentally tested in terms of flatwise compressive strength, edgewise compressive strength and shear strength capacities. Further, the cores' compression strength and shear strength capacities are numerically simulated and the results are validated with the experimental work. Based on the numerical and experimental tests findings, the sandwich cores plate properties are quantified for future implementation in optimized scaled deployable bridge treadway.

KEYWORDS: Meta-heuristic algorithm, Swarm intelligence, Particle swarm optimizer, Controlled diversity, composite sandwich cores, deployable bridges, CFRP beams.

To my beloved parents

ACKNOWLEDGEMENT

TABLE OF CONTENTS

LIST OF FIGURES

xvii

LIST OF TABLES

LIST OF EQUATIONS

LIST OF ABBREVIATIONS

ABC	Artificial Bee Colony
ABLE	Automotive Bridge Launching Equipment
ACO	Ant Colony Optimization
ANOVA	Analysis Of Variance
APDL	ANSYS Parametric Design Language
ARPSO	Attraction and Repulsion Particle Swarm Optimization
ATLSB	Axially Tensioned Long Span Bridge
ATRE-PSO	Attraction Repulsion of Particle Swarm Optimization
AVLB	Armored Vehicle Launched Bridge
AZO	Advanced Zero-Order
BAE	British Aerospace Marconi Electronic Systems
BB-BC	Big-Bang Big-Crunch optimizer
CAB	Composite Assault Bridge
CD-PSO	Controlled Diversity Particle Swarm Optimizer
CFI	Canada Foundation for Innovation
GFRP	Glass Fiber Reinforced Polymers
CFRP	Carbon Fiber Reinforced Polymers
CJAB	Composite Joint Assault Bridge
CLT	Classical Lamination Theory
CSB	Close Support Bridge
CSP	Chaotic Swarming of Particles

DGPSO	Diversity Guided Particle Swarm Optimization
DIC	Delamination In Compression
DIT	Delamination In Tension
DOE	Design Of Experiments
DSB	Dry Support Bridge
EA	Evolutionary Algorithms
ECBO	Enhanced Colliding Body Optimization
EP	Evolutionary Programming
FCF	Fiber Compressive Failure
FE	Finite Element
FEM	Finite Element Modelling
FMSF	Fiber-Matrix Shear-out Failure
FO	First-Order
FRIM	Film Resin Infusion Molding
FRP	Fiber Reinforced Polymers
FRQ-NT	Fonds de Recherche du Québec - Nature et Technologies
F.S.	Factor of Safety
FTF	Fibre Tensile Failure
GA	Genetic Algorithms
GLRM	General Linear Regression Model
GSB	General Support Bridge
HAB	Heavy Assault Bridge
HCD-PSO	Heuristic Controlled Diversity Particle Swarm Optimization

HFRP	Hybrid Fibre Reinforced Polymer
HPSACO	Heuristic Particle Swarm Ant Colony Optimizer
HPSO	Heuristic Particle Swarm Optimization
HS	Harmony Search optimizer
IBB	Inflammable Ball Bridge
LFPSO	Levy Flight Particle Swarm Optimization
LOC	Line Of Communication
LRM	Linear Regression Models
LSB	Long Span Bridge
LSD	Limit State Design
MCF	Matrix Compressive Failure
MERG	Military Engineering Group
MESI	Ministère de l'Économie, de la Science et de l'Innovation du Québec
MGB	Medium Girder Bridge
MLC	Military Loading Class
M.S.	Margin of Safety
MTF	Matrix Tensile Failure
OOA	Out Of Autoclave
PBO	Population-Based Optimization
PC-PSO	Passive Congregation Particle Swarm Optimization
PSO	Particle Swarm Optimization

PSO-A	Particle Swarm Optimization implementing all design variables
PSO-S	Particle Swarm Optimization implementing significant design variables
RO	Ray Optimization
RSA	Response Surface Analysis
RSM	Response Surface Methodology
RTM	Resin Transfer Molding
SCRIMP	Seemann Composite Resin Infusion Molding Process
SIB	Stay In Place
SSE	Sum of Squares of Errors
SSR	Sum of Squares of Residuals
SSTO	Total Sum of Squares of Residuals SSR and Errors SSE
SUMT	Sequential Unconstrained Minimization Technique
TATB	Tied Assault Truss Bridge
TDTC	Trilateral Design and Testing Code
UCSD	University of California, San Diego
UD	Unidirectional
VARTM	Vacuum Assist Resin Transfer Molding

<div align="right">

CHAPTER 1

Introduction

</div>

1.1 PROBLEM STATEMENT

The development of the transportation infrastructure network is one of the key factors contributing to the accelerated growth and stability of nations. Bridges are the principal elements within the infrastructure transportation network and are often considered as the lifelines for connecting communities and territories. The natural and human-caused disasters such as tsunamis, hurricanes, earthquakes, floods and unsatisfactory designs have been a major threat to the bridge infrastructures' safety in the recent decades. Moreover, several statistical studies expect an increase in the number of severe natural disasters by a factor of 5 over the next 50 years (Thomas and Kopczak, 2005). Figures 1.1, 1.2 and 1.3 show the level of damages happened to the bridge transportation infrastructures by different disaster events. Earlier research programs were focused on the prediction of and preparation for natural disasters, and not the immediate response or reconstruction phase following the disaster strike.

Figure 1.1 Bohol, Philippines Earthquake, Oct 2013, (Web-1)

Figure 1.2 New Jersey, N.Y., USA, Hurricane Sandy, Oct 2013, (Web-2)

Figure 1.3 Ibo River (Japan) flood by Typhoon, Aug 2009, (Web-3)

Research studies that address the logistical problems associated with disaster rescue operations are scarce (Kovács and Spens, 2007; Russell and Thrall, 2012). This necessitates the development and utilization of mobile and rapidly deployable bridge systems in order to restore the lifelines in the affected communities through successful gap-crossing operations. In addition, it is important

to mention that the rehabilitation of the damaged bridge infrastructure consumes a long period of time before being able to restore its serviceability to the transportation network.

1.2   RESEARCH SIGNIFICANCE AND MOTIVATION

The significance of the damage caused by natural disasters to the bridges infrastructure and post rescue efforts are presented herein through particularly highlighting three disaster events in the past two decades. The Indian Ocean tsunami (2004) had destroyed hundreds of bridges and roads for a large distance of kilometers near Banda Aceh, Indonesia. A considerable number of these bridges were vital links to population mass centers and industrial areas. The disruption caused to the transportation industry severely constrained the rescue efforts (Cluff, 2007; Saatcioglu *et al.*, 2006). The Hurricane Katrina (2005) hit three different states in the USA causing a damage to 44 bridges, five out of which were completely damaged, the rest of the bridges had different levels of damages, where 20 bridges were severely damaged, 10 bridges were moderately damaged, and 9 bridges were affected with a low level of damage. Hurricane Mitch (1998) was more destructive, the hurricane affected three countries in Central America (i.e. Honduras, Costa Rica, and Nicaragua). In Honduras, 70-80% of the transportation infrastructure was washed out including 98 bridges, as a result, the air rescue had been used. In Costa Rica, 192 bridges and 800 miles of roads were damaged and wiped out. In Nicaragua 92 bridges were washed out and 70% of roads' network could not be accessed (NOAA, 1998).

A NATO report (Bischmann, 1985) stated that in absence of bridges, 80% of water gaps cannot be crossed and considered as an obstacle for a disaster's supply lines. In North America and specifically Canadian territories, about 35% of the access routes are obstructed by natural gaps and are crossed by means of bridges, see Figure 1.4. Many deployable bridge solutions are developed by the military for disaster relief efforts and military operations (Russell and Thrall, 2012). Figure 1.5 shows an example of US Navy troops in a rescue mission after restoring a damaged bridge by a deployable one in Indonesia 2009 tsunami. The majority of these bridge systems are: capable of covering short natural gaps (less than 12 m), manufactured of steel or aluminum alloy metals, and support maximum loads up to 60 tons, whereas, few are of 70 tons capacity, Table A-1, and A-2 show a summary for worldwide metallic deployable bridges of capacity up to 60 tons and deployed as a single component or assembled using multiple components, respectively. Despite the fact that

a considerable percentage of the natural gaps are less than 12 m span (Kosmatka et al., 2000) (e.g. over 92% in central Europe and over 51% in Southeast Asia), see Figure 1.4., Comprehensive studies by Below (2003), Bischmann (1985), Repetski (2003), and Siegel (2000) on the deployable bridge systems' requirements illustrate the need of a bridge solution that is capable of covering at least 20m spans. Satisfying this requirement, supply lifelines to the vital areas will be accessible in the aftermath of natural disasters at Northeast, Northwest and Central Asia. Furthermore, the majority of the existing metallic bridge systems are approaching the end of their service life (Kosmatka, 2011). Any plans to increase the loading capacity of the existing deployable bridges to meet the recent increase in vehicle loads (i.e. 100 tons) would sacrifice the ease of its mobility, when considering the fact that deployable bridges are transported by means of tracked, truck vehicles, and helicopter carriers, see Figures 1.6.a, 1.6.b, and 1.6.c. Therefore, a system with versatile span coverage, light weight, and high loading capacity is much efficient and more recommended.
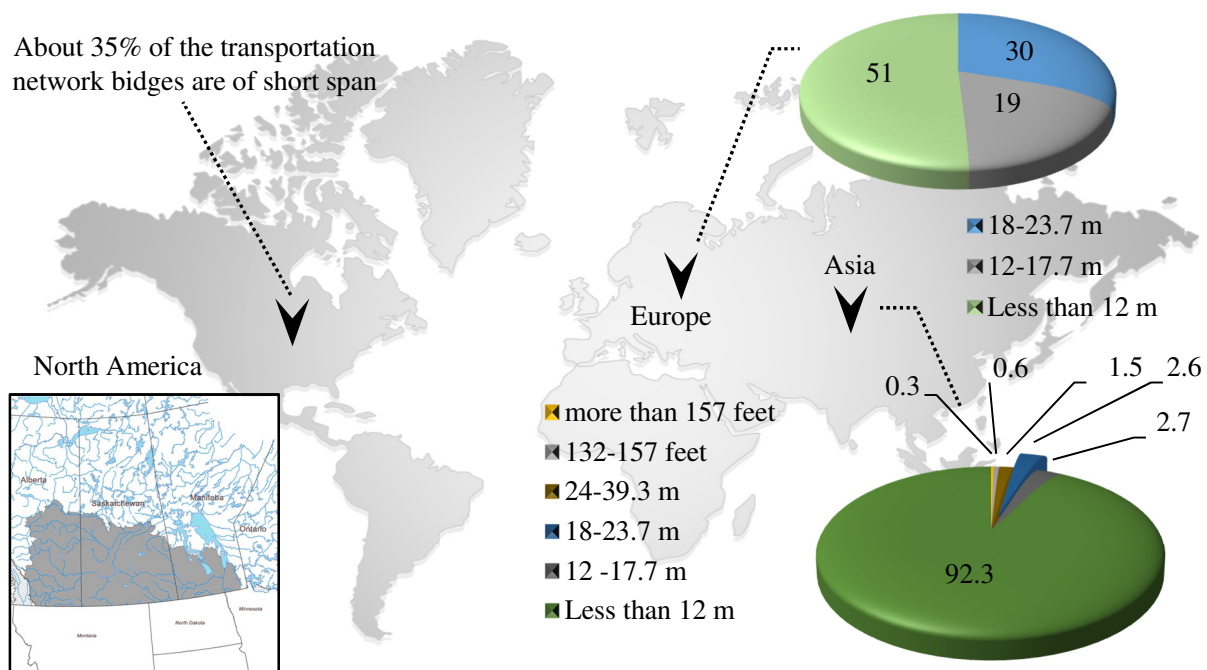
Figure 1.4 Crossing spans percentage of natural gaps' in different territories

All the aforementioned setbacks (i.e. limited deployable bridges span coverage, end of bridge systems service life, and achieve an acceptable loading capacity while obtaining a light weight bridge for rapid mobility) cast doubts on the effectiveness of deployable bridge solutions and increase the difficulty of such structure's design. Therefore, in order to achieve an effective

deployable bridge system which facilitates saving human beings' lives during post-disaster rescue efforts, three significant factors have to be considered. These factors are: light weight and high strength material for the bridge shall be used (i.e. fiber composite laminates), The use of a bridge modular unit that is commonly utilized to form a family of bridges for covering different spans, and finally the design process of such bridges must be optimized to reach an optimally minimized weight to loading capacity ratio.

Figure 1.5 Bridge destroyed in a tsunami near Banda Aceh, Jan 2005,.Sumatra, Indonesia (U.S. Navy, 2005)

(a) Resuce aids by tracked vehicle carriers, (Coker, 2009)

(b) Resuce aids by truck carriers (Coker, 2009)

(c) Resuce aids by Heliocopter carriers, (Coker, 2009)

Figure 1.6 Methods of deployable bridges mobility

Different structural shapes of bridge deployment systems have been used in the past decades. For instance, bridges that have used the truss shaped design such as:

a) The Medium Girder Bridge (MGB) that was manufactured of a modular trussed shape system. The bridge can be erected in several stories to cover versatile spans, from 9.9m to 45.8 m span, however, its main setback is the high number of manpower needed for the deployment operation and a relatively increased deployment time, about 90 min.(Coker, 2009),

4

b) The Tied Assault Truss Bridge (TATB) which is composed of tied arch structural folded units made of aluminum alloy. The system provides a fast deployment in minimal time. On the other hand, it is constrained to a fixed span coverage of 12m (Thomas and Sia, 2013).

Another type of deployable bridge systems used the arched structural design such as: a) the Churchill, A22 bridge layer, and b) the Composite Assault Bridge (CAB) (Kosmatka et al., 2000). The arched system provides an efficient load distribution over the bridge deck with no stress concentration points. However, its deficiency is the fixed span coverage. A third type of bridges have used the tapered shape design such as: a) the Heavy Assault Bridge (HAB) system (kerr, 1990), and b) the scissors deployment system of the Armored Vehicle Launched Bridge (AVLB) (Russell and Thrall, 2012). Although these systems are characterized by ease of deployment but again they have a limited span coverage. Finally, the bridge systems composed of beam modular units are characterized by low bridge profile, ease of assembly to cover multiple spans and can be functional in conjunction with different systems to cross wet or dry gaps like the Light-weight Causeway bridge System (LMCS) (Russell and Thrall, 2012) and the Dry Support Bridge (DSB), (Coker, 2009), respectively, in particular, the LMCS consists of aluminum Treadway beams supported over pneumatic floats. The bridge beam modular units are typically manufactured from metals, aluminum alloy or steel, which have relatively heavy weight and less strength when compared to fiber composite laminates. Therefore, the focus of this research is to investigate the reliability of using composites for the deployable bridge beam design, and to develop an innovative deck core configuration for the light weight mobility of these bridges. The design and analysis of deployable bridge structural components in this study complies with the Trilateral Design and Test Code for Military Bridging and Gap Crossing Equipment (TDTC, 2005). This code is different from the commonly used design codes for the civilian bridges, such as ASHTOO and CHBDC …etc. The TDTC does not impose a serviceability limit for the sake of more structural weight reduction as opposed to the other design codes. The design loads in the TDTC are very high and the axle loads spacing are very small. For instance, most of the existing deployable bridge have a carrying capacity of 600 kN or higher, a hypothetical vehicle of Military Loading Class of 600 kN (MLC60) has axle loads distributed over 10.97 m for a wheeled truck or 4.27 m for a tracked vehicle, whereas, in CHBDC the hypothetical wheeled vehicle CL-625 is used for the maximum case of loading in the bridge design which has a weight of 625 kN and the axle loads are spaced over 18 m vehicle length. In TDTC, the bridge structure and connections design has to sustain

different severe loading conditions during launching and retrieval as well as the stresses induced due to the passing vehicle loads, which is a not a similar case in the design of civilian bridges where mostly the bridge is constructed in the site over the crossed gap. Deployable bridges designed using the TDTC code provisions are only simply supported over the home and far banks; no fixation or anchorage mostly to the bank soil is considered. Moreover, the design has to take into account the slope, and height difference between bank conditions, in civilian bridges the banks has to be well leveled with adequate bearing capacity to carry the bridge support reactions.

Composite laminate structural elements are characterized by a large number of design parameters that can be implemented in the design of bridge beams to reach an optimal weight design and acceptable capacity, (i.e. ply orientation, stacking sequence, elements surface dimensionality and elements thicknesses…etc.). Moreover, optimizing the design parameters of the bridge beam geometry would lead to an optimal composite laminate stress distribution, hence, minimizing the bridge weight. Therefore, the design optimization of such bridge systems may seem to be advantageous for achieving an effective deployable bridge system and saving peoples' lives in the post-disaster rescue efforts.

The use of any optimization technique for an effective structural design optimization is not generic. In other words, no optimization algorithm can possibly be effective or even successful for all cases of interest. The physical problem's nature and field of application have a significant influence on the suitability and efficiency of different optimization algorithms (Das & Suganthan, 2011; Aimin Zhou et al., 2011). Therefore, this research study is motivated to develop a proper and competitive algorithm for design optimization of large scale structures and composite mobile bridge systems.

(c) Ramp module   (b) bridge beam

(a) Deck section
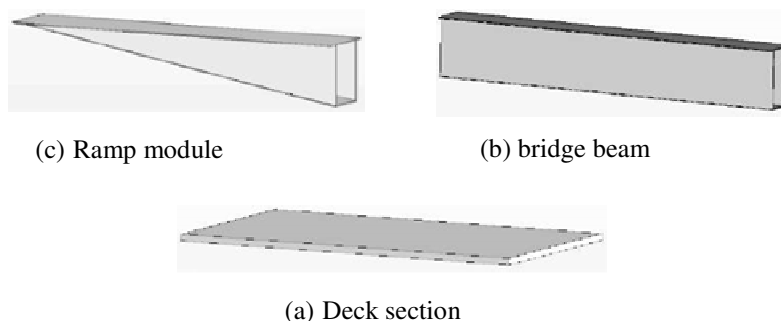
Figure 1.7 Elements for a typical deployable and mobile tread-way bridge beams system (Robinson, 2008)

6

1.3   OBJECTIVES AND SCOPE OF WORK

In order to meet the needs of light weight bridging in the aftermath of natural disasters, This research study aims to: develop a novel light weight sandwich core configurations to act as the compression bearing element of a bridge beam like structure, and use an effective structural design optimization metaheuristic approach to enhance the designed cores performance. In order to achieve these objectives the following goals are set:

- Design and develop light weight sandwich cores for the composite deployable bridge decks.
- Propose an effective optimization algorithm for design optimization of complex and large-scale structures.
- Increase the composite deployable bridge capacity/weight ratio by maximizing the compression and shear strength of the developed light-weight sandwich cores.

The scope of work can be divided into two parts. The first part can be summarized as follows:

- Evaluate different well-known swarm intelligence algorithms presented in the literature for the application of complex structure optimization.
- Based on this evaluation, propose a new method to enhance the candidate algorithm performance, i.e. Particle Swarm Optimization (PSO), and minimize to a considerable level it`s deficiency to structural optimization.
- Further, hybridize the modified swarm intelligence optimizer with Response Surface Methodology (RSM) as a tool to distinguish the influence level of design parameters in complex structural models.
- Create a discrete version of the developed algorithm and merge a studied technique for redirecting the design points to feasible regions.
- Re-formulate the discrete version of the algorithm to suite the discrete design nature of composite laminate structural optimization problems.

Whereas, the scope of the second part can be summarized as follows:

- Design and develop an innovative light weight sandwich composite cores for the bridge beam deck with high compressive and shear capacity,
- Conduct experimental testing to quantify the compression, and shear capacity of the developed sandwich cores.

- Numerically investigate the progressive compression, and shear failure of the designed cores.

- Validate the numerical models' results of the sandwich composite cores with the experimental results.

- Use the discrete version of the developed optimization algorithm to enhance the sandwich cores compression and shear capacity and compare it to the base design.

The aforementioned scope of work can be summarized using this schematic flow chart:

Experimental & Numerical Testing Procedure   Design Optimization Procedure

Material Characterization	Assessment of Optimization Techniques
Characterize different carbon/epoxy laminates through conducting coupons tests	*Assessing different gradient-based and population-based algorithms for the design optimization of deployable bridges*

Sandwich Cores Mathematical Analysis	Performance Enhancement of PSO
Mathematically analyze three composite sandwich cores for deployable bridges application based on the characterized materials properties	*Improving the performance of the chosen algorithm, (PSO), using a new diversity control technique for continuous optimization, CD-PSO is developed*

Experimental Testing	PSO: A hybrid Approach
Experimentally test the designed cores for: flatwise compression strength, edgewise compression strength and core shear strength	*Hybridize the modified CD-PSO algorithm with response surface analysis to enhance the algorithm performance when solving complex structures*

Numerical Validation	Discrete CD-PSO
Numerically validate the experimental results using progressive compression and shear failure analysis	*Create a discrete version of the modified algorithm and merge a technique to redirect the solutions that violated the constraints to feasible regions*
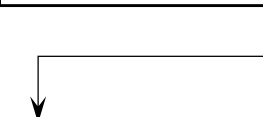
Enhancement of Sandwich Cores performance
- *Maximizing the strength and stiffness of the sandwich cores webs by changing the ply orientation.*

1.4   THESIS LAYOUT

This thesis contributes to the state of the art of deployable bridges used for rapid post-disaster mobility and proposes a methodology for achieving an effective deployable bridge system that is competitive with the recently developed in mobile bridges industry. The thesis is composed of seven chapters. The Introduction chapter is followed by Chapter 2 that includes literature survey of the existing deployable bridge systems used for disaster relief operations, followed by a representation that focuses on the mobile bridges fabricated of composites laminates and the recent research studies on enhancing the weight to capacity ratio of these bridges. Description of the effectiveness of structural design optimization for deployable bridges will be presented in Chapter 3. The chapter is dedicated to the assessment of different optimization algorithms to select the most effective one for bridge design optimization and concluded to a candidate optimization algorithm, i.e. PSO. Chapter 4 describes the newly developed optimization algorithm mechanism and discusses the evaluation of the algorithm's performance through the application over benchmark structures and large-scale deployable bridge system. Chapter 5 presents different sandwich core configurations that are designed to increase the loading capacity of the deployable bridge treadways, followed by explanation of three different test setups and their instrumentations. The experiments objective is to evaluate the cores' compression and shear capacity. Finally, a numerical validation of the experimental results is conducted to assess the models' reliability for testing more complex sandwich cores. Chapter 6 presents the PSO discrete approach for maximizing the strength of the composite laminates and discusses the enhancement achieved by its application on the designed sandwich cores. Last chapter, Chapter 7, presents the conclusions and summary of the design recommendation for designing the sandwich cores in addition to the future work.

<div align="right">

CHAPTER **2**

Literature Review

</div>

2.1 INTRODUCTION

The increasing rate of the world natural disasters emphasized the importance of rapid mobility. Within the past decades, the deployable bridge systems developed by various military armies were the mostly used ones for the post-disaster relief operations. Recently, research efforts started to focus on approaching an effective deployable bridge system in terms of lightweight and high capacity. In this chapter, a detailed review of the in-service armies' metallic deployable and mobile bridge solutions will be presented, followed by a survey of the research conducted for developing composite deployable bridge structure. The chapter ends with a summary of the literature related to optimization of deployable bridges and composite laminates.

2.2 MILITARY BRIDGE SOLUTIONS

Military bridges differ from the traditional bridges connecting the public transportation network in terms of mobility, method of erection and placement. The rapid mobility requirement for military bridges limits their material weight and erection method. The infield damage repair for the military bridges is not practical. Therefore, they are manufactured of multiple modular units that can be easily assembled together or replaced in a minimal time. For the aforementioned reasons, an effective deployable and mobile bridge system shall be characterized by a minimum weight to bearing capacity ratio as well as a quick launching and retrieval assembly.

The military deployable bridge solutions can be classified into three categories based on their mission purpose in the military doctrine. These categories are: Assault bridge solutions, Tactical bridge solutions and Line of communication bridge solutions. The assault bridge solutions are temporary bridges that are designed for gap crossing of the leading troops as rapidly as possible to the front lines. The coverage span of the assault bridges is typically less than 25 m. The tactical bridge solutions are used to cover wider spans up to 40 m and to replace the assault bridges that are required to other gap crossings. The line of communication (LOC) bridges are designed for the long-term use and used to be placed aside to the tactical bridges or to replace them. The LOC

bridges can cover any desired span using abutments. A brief description of seven bridge solutions of the categories that are widely used in post-disaster relief, namely: Assault Bridges and Tactical Bridges, will be presented in the following subsections.

2.2.1 ASSAULT BRIDGE SYSTEMS

I. Close Support Bridge (BR-90)

The Close Support Bridge (CSB) is manufactured by BAE Defense Systems co. (Vickers co.) to serve in the British Royal Army. The CSB system is produced in three classes (i.e. No.10, No.11, and No.12), the three classes are capable of supporting spans of 24.5, 14.5, and 12 m, respectively. The system can be launched by an Automotive Bridge Launching Equipment (ABLE) that is equipped with a crane and assembly platform, or the system can be mounted on a tank and launched by a mechanical system. The Bridge system consists of multiple internal modular units of 1m depth and ramp modules for the end supports. A modular bridge unit is in the shape of the two interconnecting treadway beams that forms one lane with width 4m. The Bridge has a Military Loading Class of MLC70 (i.e. 70 tons) for tanks crossing and MLC100 (i.e.100 tons) for wheeled trucks. The system is made of lightweight Aluminum alloy material, therefore, the time of launching and retrieval is 10 minutes for its shortest class, No.12, which has a weight of 5,445 kg.

Other systems of BR-90 family are: the General Support Bridge (GSB) that is capable of crossing 32m gap and launched by ABLE, the Long Span Bridge (LSB) which covers up to 44m span, and the LSB span can be increased up to 52m by bridge cambering using an axially tensioned Aramid cable attached to the bridge bottom, the system is named, ATLSB. A photograph showing the ATLSB system and the CSB are depicted in Figures 2.1 and 2.2, respectively. (Winney, 1994)

Figure 2.1 Deployed Axially Tensioned Long Span Bridge (ATLSB/BR-90) (Winney, 1994)

Figure 2.2 Close Support Bridge No.10 being launched (Winney, 1994)

II. Wolverine Heavy Assault Bridge (HAB)

The Wolverine Heavy Assault (HAB) bridge system is produced by U.S. and German cooperation. The bridge systems consist of Leguan Bridge manufactured by MAN Mobile Bridges (Germany) and the Wolverine launching system manufactured by General Dynamics Land Systems (U.S.A.). The whole system is mounted over M60 or M1A1 Abrams chassis. The bridge system consists of two parallel tread-way beams, a single treadway is a 1.6m wide and 0.9m depth at the mid-span, whereas the total width of the bridge is 4m. The bridge is of a total length of 26m and can cover a gap of 24m span. The bridge is manufactured from Aluminum alloy material and weighs 10,750 kg. The bridge is designed to a load capacity of 70 tons (MLC70) (kerr, 1990). Figure (2.3) shows a photograph of a HAB bridge system.

Figure 2.3 Wolverine Heavy Assault Bridge being launched (Coker, 2009)

2.2.2 TACTICAL BRIDGE SOLUTIONS

I. Medium Girder Bridge (MGB)

The Medium Girder Bridge is manufactured by Williams Fairey Engineering Limited. The MGB consists of two aluminum alloy girders and a deck is supported in between. The bridge girders form one crossing lane with a total width of 4m. The MGB Bridge has three different categories that are classified based on their span coverage into three classes. A single storey class used to cover a span of 9.9 m and has bridge girders' depth of 0.56m. The double storey class used to cover a gap of 31m span. The total girder depth is increased to 1.65m using truss modular units connected to the bottom of the 0.56m girder. The third storey class can cross a gap of 45.8m span using a link reinforcement to the girder of 2 m depth. All MGB types are of a Military Loading Class (MLC70). The bridge is designed to be deployed using a manpower of 25 within 45 min, therefore, the components assembling the bridge units are designed to be light enough to be carried by 4 men with a weight of 230 kg, except two pieces shall be carried by 6 men. The total MGB bridge weight is 30,850 kg (Coker, 2009; Connors and Foss, 2006). Photographs for the MGB Bridge three classes are showed in figures 2.4, 2.5 and 2.6.

Figure 2.4 MGB single storey bridge with aluminum girders (9.9m span), (Web-4)

Figure 2.5 MGB double storey bridge with truss girder reinforcement (31m span) , (Web-4)

Figure 2.6 MGB Three storey bridge with link reinforcement to the truss girder (45.8m span) , (Web-4)

II. Dry Support Bridge (DSB)

The Dry Support Bridge is a descendant of the MGB bridge solution, the system has been recently produced for the U.S. Army to replace the MGB solutions. The DSB advantages over the MGB system are that: (1) it is mechanically launched, therefore the requirement of ease of construction and minimal manpower are achieved, (2) the technique adopted for assembling the bridge with multiple modular units reduced significantly the number of components, and (3) it has a higher loading capacity of MLC80 for tracked vehicles and MLC110 for wheeled trucks. The bridge consists of two aluminum girders with decking in between and two ramp modules. The deck is connected by means of hinges to the girders, allowing the girder to fold under the deck. A single bridge girder module is of 6m length, 1.19m depth and 4.3m width. The bridge can cross a 40m gap and is being deployed by only a crew of 8 manpower within 90 minutes. The total bridge system excluding the launching mechanism weighs 37,110 kg.

The launching system consists of a hydraulically operated launching system that is mounted on a PLS truck chassis and a set of launching beams. The launching beams are cantilevered across the gap using the hydraulic system, and the manpower is used to suspend then push the assembled modules to the other bank by means of a handling crane. (Connors and Foss, 2005; DiMarco, 2004). The launching and retrieval mechanisms for the DSB Bridge system are illustrated in Figure 2.7. A photograph showing the DSB bridge system being launched is depicted in figure 2.8 (Coker, 2009).

15
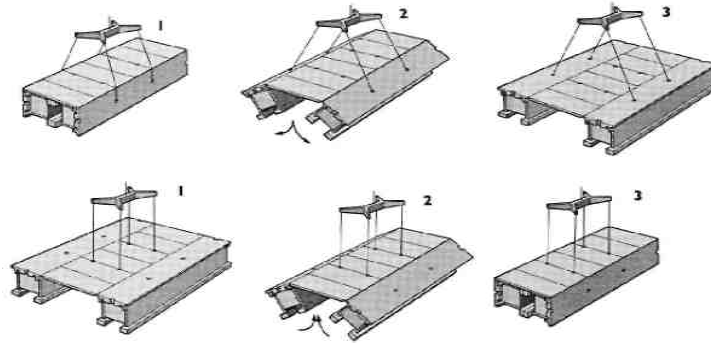
Figure 2.7 Launching and retrieval mechanism of the DSB Bridge system, (Web-5)

Figure 2.8 The DSB being launched across a gap, (Web-5)

2.3   DEPLOYABLE COMPOSITE BRIDGES

In order to increase the rapid mobility in post-disaster relief, efforts had been exerted on the lightweight bridging solutions utilizing composite laminates. A Composite Army Bridge (CAB) had been developed and tested at the University of California, San Diego (UCSD). The CAB system has a length of 14 m and capable of crossing a 12.2 m gap. The bridge system consists of two interconnected tread ways of 1.55 m width which form a lane of 4.0 m wide. Figures 2.9 and 2.10 show a launched CAB system and an isometry that illustrates the bridge components, respectively. CAB system was designed to have a higher loading capacity (i.e. MLC100) than any other single span bridge in the market, while having a bridge weight of 5,775 kg which is the same as the best metallic short span bridge, 'CSB Bridge No.12 system', in addition, almost a similar production cost. To reach the design target, the CAB Bridge tread-way beam is fully designed of Carbon/Epoxy laminates and a balsa core sandwich deck as the main compression bearing element. The bridge geometry profile is designed in the shape of an arched deck for access on and off the

16

bridge in order to have an optimal stress distribution over the bridge fabricated material. Among several deck cores investigated, nothing was better performed similarly to the existing aluminum bridge decks like the balsa core in terms of light weight and high strength. The bridge experienced 20,000 cyclic loading with no sign of any damages (Kosmatka *et al.*, 2000).

Figure 2.9 An Isometry of the Composite Army Bridge (CAB) system, (Kosmatka, 2011)
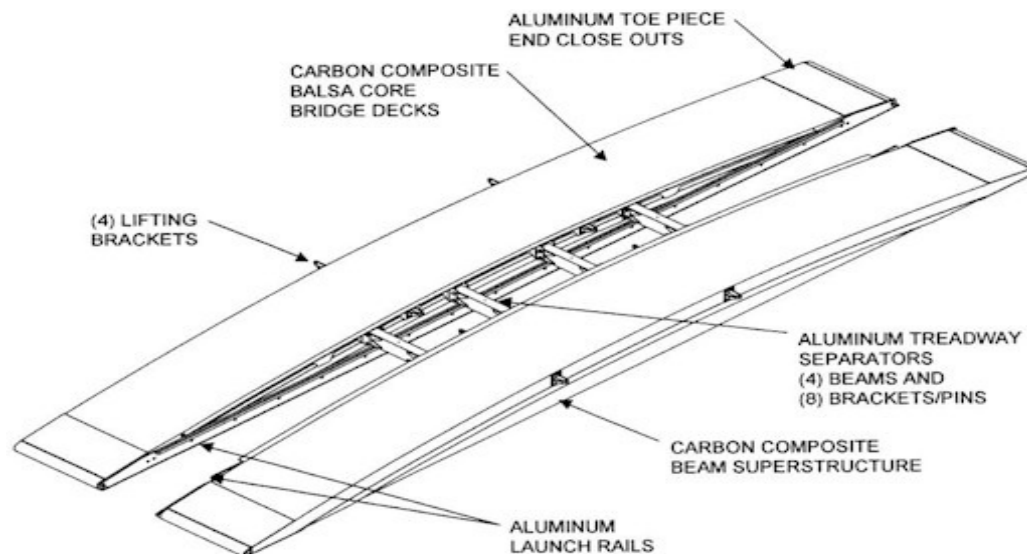
Figure 2.10 An exploded view illustrating the Composite Army Bridge (CAB) components
(Kosmatka *et al.*, 2000)

Another project for testing and developing a light weight bridging system was conducted for crossing short gaps span up to 4 m at University of California, San Diego (Robinson and Kosmatka, 2008). The application purposes of this bridge were versatile, i.e. replacement for damaged bridge decks, decking for long span modular bridges, and quick matting to form access roads and loading ramps for ships and aircrafts. Based on these objectives, the bridge solution is constrained to a profile depth of 100 mm and a maximum weight of 230 kg to be handled by a maximum of four

manpower. As a result, the deck is designed in the shape of a lightweight webbed core Carbon/Epoxy laminates with foam infill. The core system is confined with upper and lower Carbon/Epoxy skins. Four different configurations were experimentally and numerically tested to obtain the best performance system in terms of less weight, maximum shear, and compression capacity (Robinson and Kosmatka, 2008). All configurations were compared with the CAB system's balsa core as the baseline for weight, shear, and compressive strength. The chosen webbed core configuration exceeds the balsa core shear and compressive strength with 1.75 and 1.14 times, respectively and it was lighter in weight by 54%. The bridge could support a Military Loading Class of 30 tons (MLC30) for tracked and wheeled truck (PLS) vehicles. The bridge consists of two parallel tread ways of dimensions (0.76m x 5.6m) per tread-way and forms a track lane of width 2.74m. The final designed weight of the treadway was 205 kg. The bridge treadway was fabricated using the Seemann Composite Resin Infusion Molding Process (SCRIMP), 'a variant of the Vacuum Assist Resin Transfer Molding technique (VARTM)'. A schematic of the SCRIMP technique for treadway epoxy infusion is depicted in Figure 2.11 and a photograph of M113 tracked vehicle during a dynamic test of the bridge system is shown in Figure 2.12.
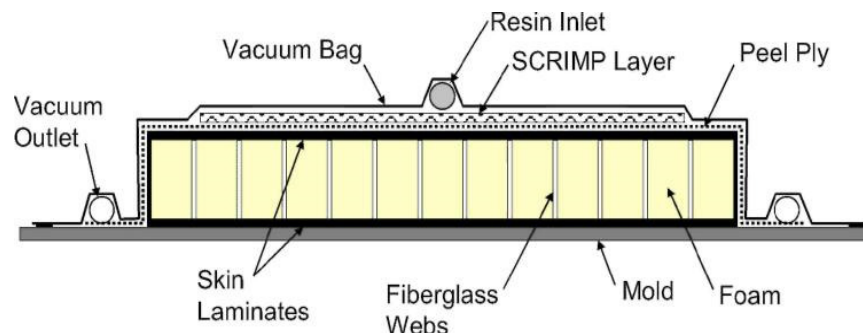
Figure 2.11 Schematic for SCRIMP technique, (Robinson and Kosmatka, 2008)

Figure 2.12 M113 during a dynamic test for the short span composite bridge,
(Robinson and Kosmatka, 2010)

The Canadian forces supported a research by the Military Engineering Group (MERG) at the Royal Military College of Canada for developing, statically and dynamically testing a fiber composite deployable bridge for post-disaster mobility (Wight *et al.*, 2006; Xie, 2007; Landherr, 2008). The bridge consists of two parallel tread ways manufactured from commercially available GFRP pultruded box sections and fiberglass flat plates that are adhesively and mechanically connected together to form a bridge treadway box beam. The bridge box beam length is 10 m and it is tapered at the mid-span with a depth of 0.953 m. The bridge is capable of supporting a gap span of 9.2 m and a Military Loading Capacity of 30 tons (MLC30) for tracked and wheeled vehicles. The total treadway beam weight is 1000 kg. A Photograph showing a crossing test by a Bison (light NATO armored vehicle) on the deployable bridge beam is illustrated in Figure 2.13.

Figure 2.13 The GFRP bridge beam during a crossing test by Bison armored vehicle (9.2 m span), (Landherr, 2008)

2.4   OTHER RESEARCH EFFORTS FOR POST DISASTER MOBILITY

Lederman *et al.* (2014) presented a new type of a tied arched deployable bridge that is launched from a vehicle for disaster aftermath relief operations. The deployable bridge consists of structural pieces stacked together in the shape of a tied arch as shown in Figure 2.14. The stackable assembly is optimized to reduce the packaging size during transportation. The deployment sequence is based on a single actuator that spreads stackable structural pieces; these bridge pieces form a shape of an arch with the aid of sloping cuts in the pieces. The arch is tied with a horizontal cable which is connected to six vertical suspenders along the bridge span. The horizontal tie is tensioned a little during retraction to prevent the bridge from collapse. The vertical suspenders are connected

through pulleys to the horizontal cable for not affecting the position of the suspenders while tensioning. The vertical suspenders provide a better redistribution of the negative moment in the arch when the bridge is loaded and deflected. The load redistribution is analyzed through an experimental testing for a 3m scaled physical model. The aim of this research is to present a deployable bridge of 15m long span and a height of 1.1 m for disaster and relief operation launched from military or nonmilitary vehicles. The deployment sequence concept is examined through a simple physical model of 40cm long of small wooden pieces. This system provides a rapid deployment mechanism, however, it has a limited span coverage and constrained to lightweight wheeled vehicles.
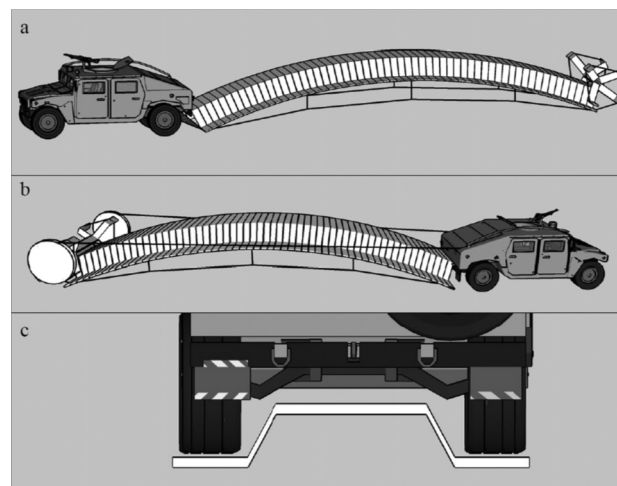
Figure 2.14 Cross section, launching and retrieval Concepts of the 15 m deployable bridge (Lederman et al., 2014)

Hanus *el at.* (2008) Proposed another deployable bridge concept that is able to support heavy vehicle loads. The bridge is categorized as a tactical bridge class based on the military terminology. The bridge concept depends on expanding folded truss components that function as the bridge deck support. The upper deck consists of composite Stay in Place (SIP) forms that are placed over the expanded truss joints; then a concrete mix, as in theatre available material, is casted over the permanent SIP forms. This approach aims to reduce the bridging logistical needs. Recent bridging systems need to transport all assembly components from out of theatre to in theater operation. Figure 2.15 describes the whole deployment sequence of the bridging components. The truss structure while integrated with the composite SIP form and concrete sections are optimized to achieve the minimum weight required. The deck structural behavior and maximum loading capacity are examined, results showed that the deck loading class is (MLC 70). A major setback

20

of this system for the rapid mobility operation is the long period of time needed, until being serviceable for passing vehicles due to concrete pouring operation and curing time.
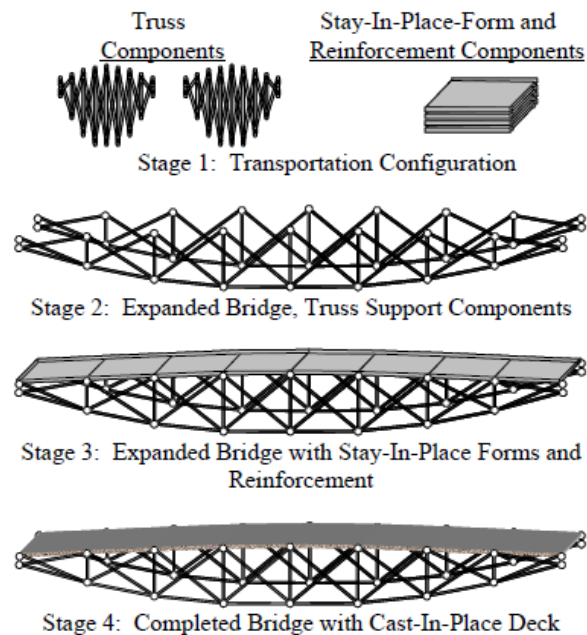
Figure 2.15 Concept of the construction sequence for the deployable bridge using the composite SIP forms (Hanus *et al.*, 2008)

Ario *et al.*, (2013) and Chikahiro *et al.*, (2014) developed a deployable scissors bridge prototype for disasters relief in Japan based on origami folding structure and computer analysis "a Japanese art culture skill in folding papers into geometric decorative shapes". The bridge structural shape is designed by optimizing a domain of a continuum unit cell elements of micro trusses as shown in Figure 2.16, to obtain an outcome of best topology and shape of the structure. The stiffness of the micro-truss members is considered as the design variable to be optimized i.e. *EA*. The objective of the optimization design procedure is to keep safe the local response of the compression buckling that would occur for the micro truss members to achieve a fully stressed design. The design's output is of a rhombic truss, which can be folded in a scissors shape, A FEM is built for the bridge and the model is analyzed in the prototype developing scale. Furthermore, a prototype deployable bridge scale was experimentally tested and its flexural behavior was investigated subject to persons' weight (see figure 2.17). Moreover, the dynamic behavior of the developed prototype was experimented through mode shapes and natural frequencies analysis (Ario *et al.*, 2011).
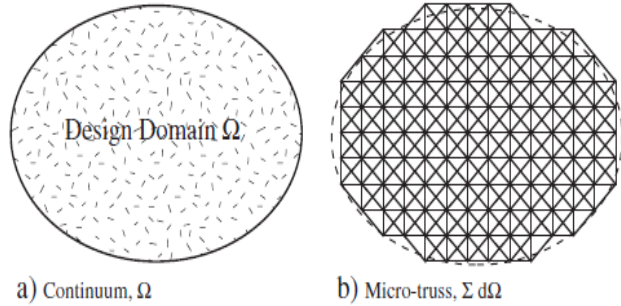
Figure 2.16 Discretization of a continuum body into micro truss elements (Ario *et al.*, 2013)

Figure 2.17. Photograph of the experimental testing of the scissors bridge after been deployed (Ario *et al.*, 2011)

Zhang *et al.*, (2014) presented a hybrid FRP-aluminum space truss bridge system functioned for disaster relief. The bridge is designed as a modular emergency bridge of a 12 m span and composed of successively four modular connected units of width 1.2m. Each unit consists of an aluminum deck supported by FRP and aluminum trussed members. The four modular units are connected together using male jugs and female jaws based on the pre-tightened teeth connection (PTTC) as shown in Figure 2.18a. The investigation of the bridge behavior is conducted primarily for a single treadway, then it is intended to develop a full integrity of two tread ways spaced 0.8 m apart and connected together by transverse braces to form a total width of 3.2 m and a depth of 0.85 m (see Figure 2.18b). In this design, the bridge structure composed of two main parts, an aluminum deck rested over a space truss structure of Hybrid FRP composite tubes. To satisfy the characteristic of a lightweight for ease of transportation, the space truss members of the bridge are manufactured using unidirectional FRP materials, where the space truss tubes are made of HFRP, which are a hybrid of E-glass fiber, carbon fiber, and basalt fiber, and they are used for the lower chord member, the diagonal members are made of GFRP materials, and the vertical members are made of aluminum alloy (see Figure 2.19). The bridge structure is not similar to an analogous space truss structure. The aluminum deck consists of thin plate, longitudinal, and transversal I-beams, the beams are forming the shape of main and secondary grid beams supporting the deck plate. All components are welded to integrate with the Hybrid composite space truss as shown in

22

Figure 2.20. The aluminum alloy category used for the structure is the wrought aluminum 7A05. Finally, the bridge total weight achieved for such structural configuration is 12 kN.

The bridge is designed using the general code for military bridge design (GJB1162-91) in China. The design satisfies sustaining a wheeled vehicle of MLC10, the safety factor for an ultimate limit state design of 1.5, and an allowable deflection between L/150 to L/100.

The bridge flexural properties are experimentally investigated and two FE models are built for results validation using the FE package ANSYS. The experimental study showed a linear behavior under the ultimate limit state loading condition, a measured deflection less than the allowable deflection (80mm) by nearly 40%, and the maximum stresses at the ultimate state level are less than material strength as well as the critical buckling stress. The only drawback is that the structure exhibits a complex unexpected strain distribution through the longitudinal main beams which is considered undesirable to the structure safety and is attributed to the eccentric compression caused by the non-axial concentrated force through the connector. Thus, it seen that the bridge shall be reconsidered and optimized.
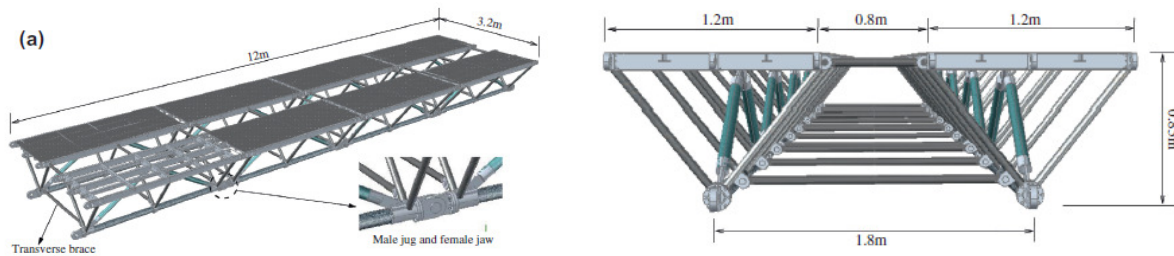
Figure 2.18. Hybrid FRP-aluminum space truss bridge design concept:
a) 3D representation, b) cross section (Zhang *et al.*, 2014)

Trussed members:

E: Lower chord member(HFRP)
F: Diagonal web member(GFRP)
G: Vertical web member(Aluminum)

Cross section of trussed members
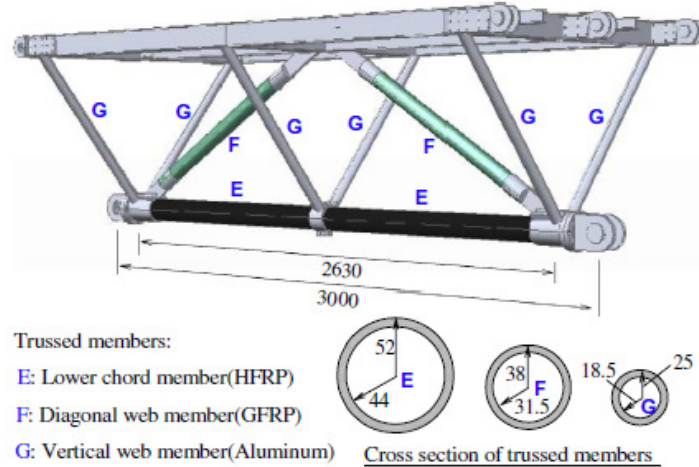
Figure 2.19. Configuration of trussed members (dimensions in mm) (Zhang *et al.*, 2014)

A: Main longitudinal beam;
B: Secondary longitudinal beam;
C: Main cross beam;
D: Secondary cross beam;

Cross section of "I" beams
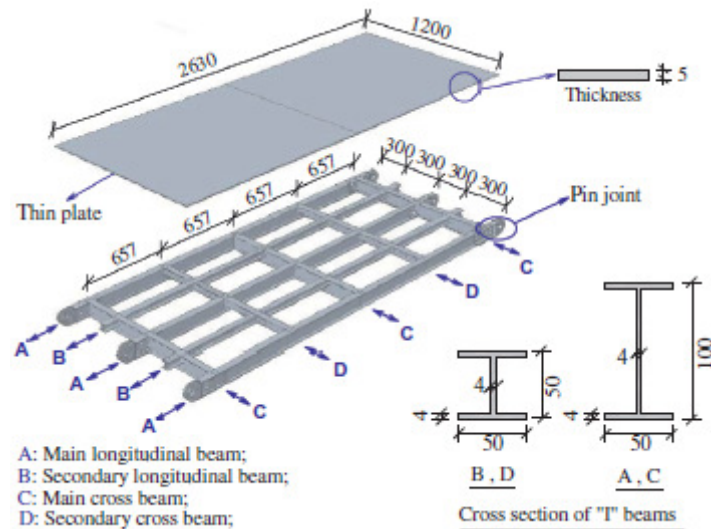
Figure 2.20. Configuration of the bridge and cross section of I beams (Zhang *et al.*, 2014)

2.5 SUMMARY

A comprehensive survey for the state of the art of deployable bridge systems as well as the most current research for developing mobile bridges is presented in this chapter. It can be concluded that, a tendency for using high strength fabricating materials (FRP) along with suitable structural configuration is highly recommended for the rapid mobility of deployable bridges. The achievement of these two requirements will satisfy the current increase in vehicle design loads and the need for effective deployable bridge systems capable of crossing short to long spans in a minimal time. Current metallic deployable bridge systems may no longer withstand serviceable

for those higher specifications. Most of the current researches that had used metals for deployable bridges are functioned for covering short gap spans with high vehicle's capacity, long gap spans with low vehicle's capacity, or for the rescue of people in the aftermath of a disaster. Up to the author's knowledge, no current research focused on the design optimization of these mobile bridge structures to achieve higher performance, whereas, some of the current research emphasized the need of optimizing the deployable bridge structure after it had been studied and developed. Therefore, the main focus of this study is to propose an effective optimization algorithm for the design of these type of bridges as well as to develop different FRP sandwich cores capable of effectively decreasing the weight to capacity ratio of the state of art composite deployable bridges.

Chapter 3 will cover several optimization methods used effectively for structural design optimization. Based on a literature survey, candidate algorithms implementing different optimization techniques are applied and tested on a deployable bridge structure of versatile span coverage. The more effective one is chosen for further investigation and performance enhancement.

3

Structural Design Optimization and Solution Techniques

3.1 INTRODUCTION

This chapter discusses the effectiveness of applying the design optimization of deployable bridge structures. The methodology of choosing, then enhancing and numerically testing the proposed optimization technique is represented. Based on this investigation for the most efficient optimization technique to deployable bridges optimization, Particle Swarm Optimization PSO achieved better results when compared with other algorithms tested. Therefore, it is chosen as the application optimizer in the current study.

3.2 OPTIMIZATION TECHNIQUES

As had been clarified in Chapter 1, the performance of a single optimization technique does not guarantee the same level of efficiency in solving different engineering optimization problems. This is mainly because the engineering problem's nature has a significant influence on the optimizer's performance and its results. There are several optimization algorithms that perform well for simple structural and composite parts design optimization, however, these algorithms may not be able to reach the same level of results quality when tested on complex (large-scale) structures. This could be for many reasons, such as, the increased number of design parameters, the diverse levels of significance of these parameters on the design objective, and the numerical noise caused by the poor parameters. Deployable bridge models, especially when fabricated from composites laminates have these aforementioned characteristics. As a result, different optimization algorithms have to be assessed for design optimization of complex structures. Therefore, the research methodology for an optimal design of deployable bridge structures has to be built on an assessment of effective optimization techniques in the literature. Based on such assessment, a candidate algorithm is chosen for the design optimization process of the deployable bridge treadway.

3.2.1   ASSESSMENT OF OPTIMIZATION SOLUTIONS

Traditionally, optimization methods that involve derivatives (gradient based) in their mathematical computations, such as those proposed by Gellatly and Berke (1971), Venkayya (1971), Schmit and Farshi (1974), Schmit and Miura (1976), and Khan *et al.* (1979) were widely used for structural optimization. These techniques are proven to be effective in solving different engineering optimization problems. However, they could encounter difficulties when solving complex structural models; moreover, simplifying the structural model by including some of the design parameters may reduce the advantage of using optimization. In most cases, structural engineering problems are highly non-linear and any degree of simplification may not be practical. Population-based optimization (PBO) algorithms, also known as swarm intelligence algorithms, proved to offer better and robust solutions with less computational time, however, no grantee for global optima. The PBO algorithms are naturally inspired techniques such as Evolutionary Algorithms (EA). Genetic Algorithms (GA) and Evolutionary Programming (EP) are sorts of EA that is widely used for structural optimization. Artificial Bee Colony (ABC) optimization algorithm is an example of PBO algorithms that mimics the behaviour of bee colonies (Karaboga, 2005). Ant Colony Optimization (ACO) algorithm simulates the real search behaviour of ants starting from their nests to food locations (M. Dorigo and Caro, 1999). Particle Swarm Optimization (PSO) algorithm is another example that is inspired by the school of fish and bird flocks social behavior (Eberhart and Kennedy, 1995).
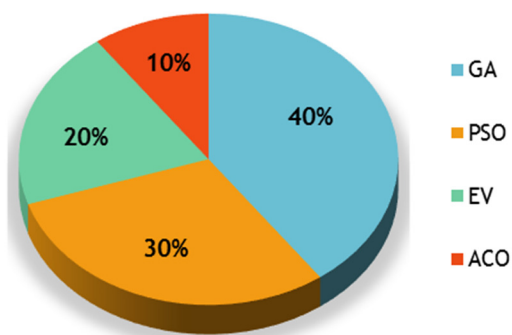
Figure 3.1 Publications distribution for applying meta-heuristic optimization in engineering problems

The distribution of publications that applied population-based techniques (meta-heuristics) to solve different engineering optimization problems in the past decade is shown in Figure 3.1 (Eslami *et al.*, 2012). It is apparently clear that GA and PSO are the most widely used and

investigated compared to ACO and the rest of Evolutionary Algorithms. This could be attributed to their robustness in solving different classes of engineering problems. Based on this, it is decided to assess two PBO algorithms (EAs), namely: GA and PSO, and two gradient-based algorithms, namely: Advanced Zero-Order (AZO) method and First-Order (FO) method built in FEM package ANSYS. A deployable bridge solution that is presented by (Osman, 2006) and being produced by the military for the disaster relief efforts is used as the complex structural problem to be optimized. A comparative analysis of the design optimization results is conducted in terms of better convergence rate and weight/capacity ratio. Furthermore, a comparison with recently in-service deployable bridge solutions is conducted to assess the performance of the most effective technique to achieve rapid mobility solutions. The following subsections briefly describe the GA, AZO, and FO algorithms applied for the design optimization of the proposed deployable bridge system, whereas the PSO will be extensively explained in Chapter 4. More details about GA, PSO, the Advanced Zero-Order and the First-Order method can be found in (Holland, 1975; Yuhui and Eberhart, 1998; ANSYS, 1999), respectively. In the following subsections, the assessment procedure, bridging system, bridge numerical simulation and analysis of the results will be briefly represented.

3.2.1.1 Genetic Algorithms

Genetic Algorithms (GAs) are mathematical algorithms that mimic the natural process of evolution. The natural process is based on the Darwinian principle improved generation reproduction and survival of the fitness by sexual recombination (Koza, 1992). The GAs reproduction plans technique that mimics the evolution process was first introduced by Holland (1975). GAs is employed by generating a random population of potential solutions of the structural optimization problem. Each potential solution is represented in the form of a fixed length chromosome string. Each chromosome consists of a set of characters, called 'genes' (see figure 3.2). The fitness of each chromosome is evaluated against the optimization problem objective function 'minimize or maximize' and its structural design constraints. In general, the GA-based algorithms are capable of evaluating only the unconstrained optimization problems. Therefore, the use of other means 'such as penalization' to deal with the design constraints is a necessity.
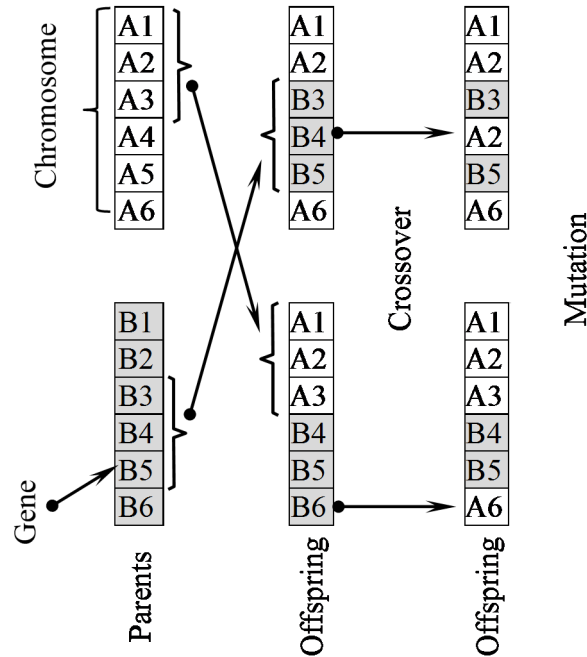
Figure 3.2 Sexual recombination to generate an offspring through crossover and mutation

Basic GA simulates the survival of fitness by performing three operations, which are reproduction, crossover, and mutation. The reproduction operation is responsible for the selection of the best set of chromosomes amongst the generated population to be copied into the new population. This best set of chromosomes is called, 'Elite generation'. A chromosome with a higher fitness has a higher number of offspring based on probability selection criteria' like roulette wheel' (see De Jong, 1975). These best chromosomes exchange their design characteristics to produce the next offspring through crossover and mutation as clarified in Figure 3.2. The crossover operation of chromosomes is a commonly biological operation among parents, while mutation is a scarce operation. Mutation performs a sudden change in the chromosome genes of a randomly selected offspring, this will allow for a new evolutionary genetic material for next offspring production and prevent the stagnation around local minima. The new offspring fitness is evaluated and the process is repeated in order to reach better new generations until a specified criterion is met. More details about the GA mechanism can be found in (Arora, 2012).

The performance of GA is governed by the selection of four operators, the generation size, the elite percentage, the crossover probability and the mutation probability, in this study, the GA operators' values are chosen as 150, 30, 0.7 and 0.01, respectively. The GA mechanism used is

that an offspring with a better fitness replaces only the worst offspring with a real value (continuous design variable).

3.2.1.2 Optimization Methods Built in FE Package (ANSYS)

The concept of the Advanced Zero-Order method is built on the Sequential Unconstrained Minimization Technique (SUMT) (Fiacco and McCormick, 1990). The method starts by converting the structural constrained problem into an unconstrained optimization problem using a penalty function. The method creates fitting for the design data points by the least square method to build response surfaces in each design optimization loop. The ANSYS program allows the user to choose the fitting response equation (i.e. linear, quadratic or quadratic plus cross term fit). Based on the current response surfaces built, the optimizer performs a series of search in the design space to find the minimum of each response surface and create a vector of best design variables. This is done by a series built of an approximate sub-problems of the design variables in order to minimize the objective function. The new design vector is calculated using the following equation:

$$X_j^{K+1} = X_j^K + \eta\left(\hat{X}_j^K - X_j^K\right)$$

where
$$\eta = 1.0 - C^o - C^r.r_j^K$$

(3.1)

such that $\quad 0 < C^o < 0.9 \, , \; 0 < C^r < (1.0 - C^o)$ and $-0.5 < r_j^K < 0.5$

Where η is a constant evaluated as per equation (3.1), C^o is a fraction of the current design variable between the values [0, 0.9]. C^r is a random contribution fraction and r_j^K is a randomly generated number applied to each design variable in the current iteration. The creation of the design variables vector is continued in the same aforementioned procedure until the termination condition is reached.

The First-Order optimization method uses the same procedure of the Advanced Zero-Order method except that, it creates gradients for the objective function and the inequality constraints to each design variable in order to find a search direction to minimize the structural optimization unconstrained problem. The process continues until a termination condition or a convergence criterion is reached. More details about the First-Order method can be found in (ANSYS, 1999).

3.2.2 ASSESSMENT PROCEDURE

The procedure followed for the assessment of the optimization techniques can be clarified as shown in Figure 3.3. The dashed path of flow chart represents the procedure applying the population-based techniques, i.e.GA and PSO, while the solid flow chart path represents the description of the ANSYS gradient based methods.
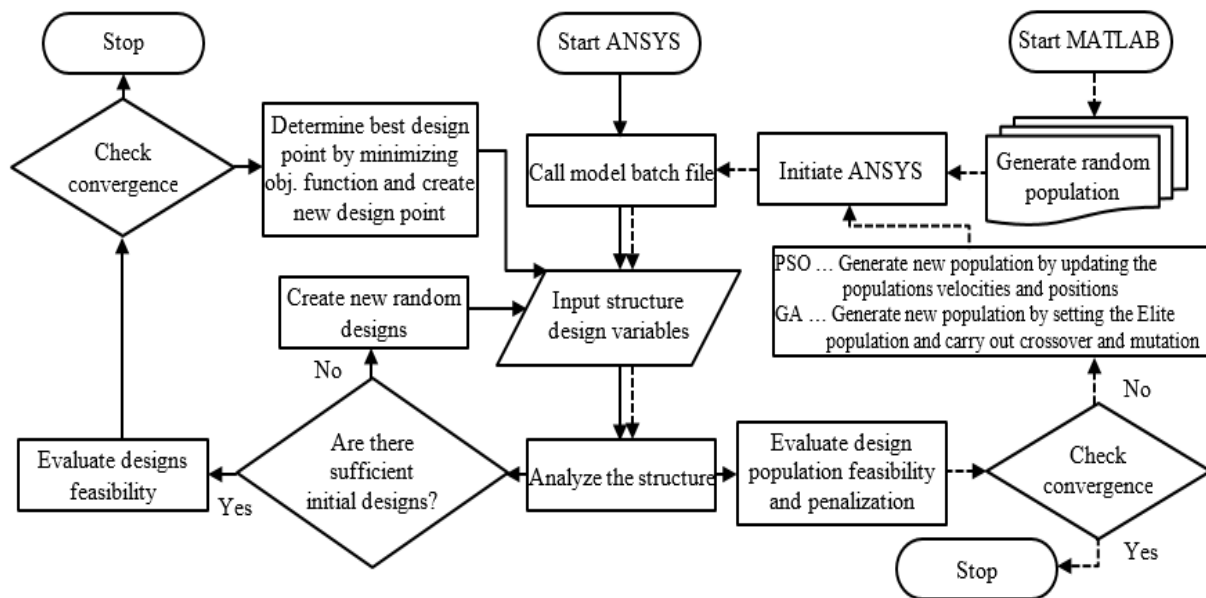
Figure 3.3 Flowchart of the structural design optimization procedure

The structural bridge model is built using ANSYS patch file. In order to apply the PBO algorithms, the ANSYS bridge model is linked to GA and PSO MATLAB built code to evaluate the fitness of the structural model's objective function. Based on the techniques' evaluation of the entire population fitness at each iteration, they create and send the newly generated population for further re-building and re-analyses. The process continues until the termination criteria are met. On the other hand, for each design iteration, a new design vector of a single potential solution is created by the built-in ANSYS gradient based algorithms, and the bridge model is rebuilt for further re-analyses and fitness evaluation by the ANSYS optimizers. The procedure continues until a convergence or a termination condition is met.

3.2.3 THE DEPLOYABLE BRIDGE SYSTEM

The bridge system is designed as a repeated modular unit of 12 m span. Multiple modular units can be assembled to cover different gap spans of 24, 36, and 48 m. The modular units are assembled automatically using pin connections at their attached ends. The structure stability of the bridge systems with a span more than 12 m is achieved through wiring system as shown in figure 3.4, for the 24 m configuration. A single modular unit consists of two parallel treadway beams connected together with flush cross-beams, see figure 3.4. The figure shows an exploded view of a 24 m bridge assembly. Each treadway beam is 1490 mm wide and the whole passing lane width is 4 m.
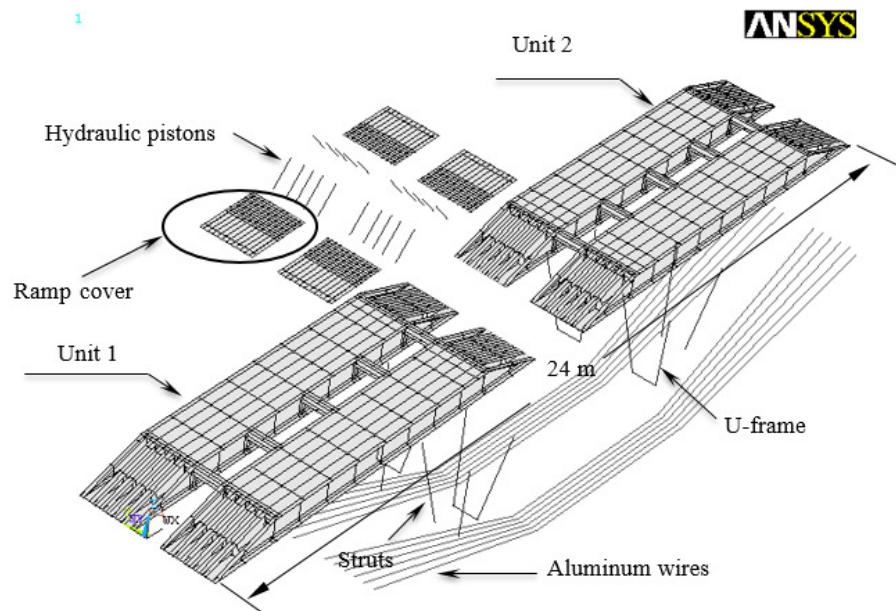
Figure 3.4. An exploded view of the 24 m bridge assembly (Osman, 2006)

The components of the bridge solution can be divided into three main groups defining the system, which are: a) the superstructure (i.e. the treadway beam including the orthotropic deck), b) the supporting ends and ramp covers, and c) the substructure supporting system (i.e. wiring system, U-frame, and struts), see Figure 3.5.a. The treadway beam is formed in the shape of an inverted U-section, as depicted in Figure 3.5.b. The deck surface is stiffened with longitudinal and transverse stiffeners, see Figure 3.5.c. The stiffened ramp covers are folded and outspreaded using 5 hydraulic pistons to form the ramp ends or extend the treadway decking surface for vehicle crossing. Four embedded U-frames and struts inside the treadway beams are outspreaded with the substructure wiring system to maintain the full structure stability.
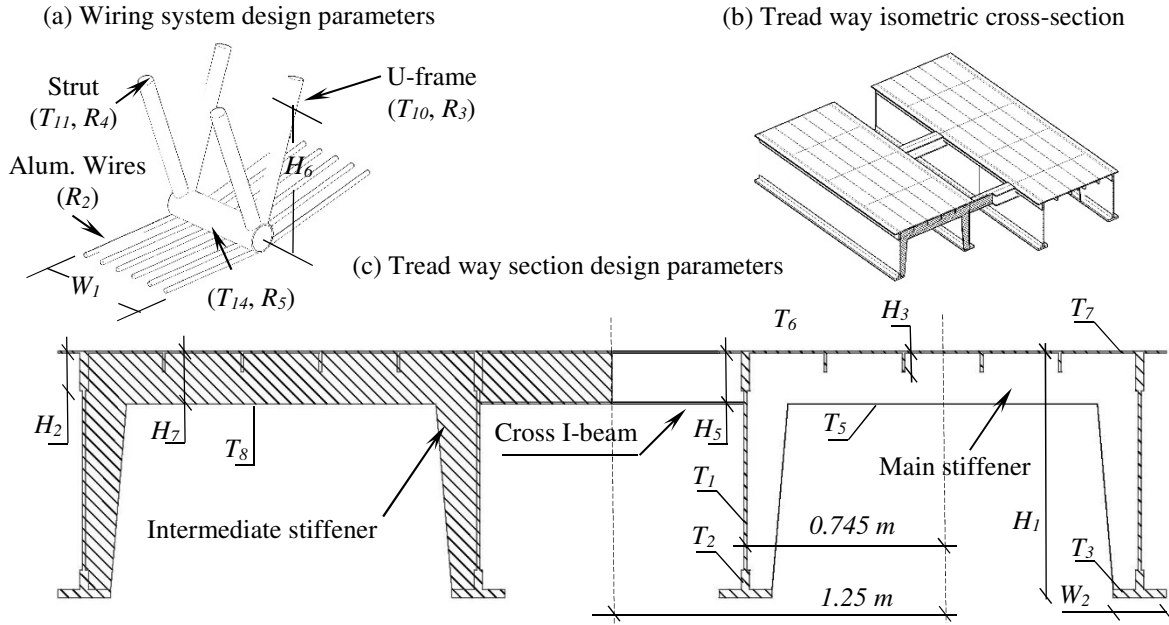
Figure 3.5. Tread-way beams cross-section

The Aluminum alloy 7020-T6 material was chosen for manufacturing the bridge system. The alloy has a density of 2.78 kg/cm^3, passion's ratio of 0.3, modulus of elasticity of 71000 MPa, yield tensile strength of 280 MPa and an ultimate tensile strength of 350 MPa.

These types of mobile deployable bridge systems are widely functioned in harsh conditions for the military gap crossing operations and in the aftermath of natural disasters. Therefore, the guidelines of Trilateral Design and Test Code (TDTC, 2005) which was issued for setting an internationally accepted design limits for this kind of bridges has been followed. The TDTC recommends a safety factor of 1.5 of the ultimate tensile strength or 1.33 of the yield tensile strength for the deployable metallic bridges. The shear strength is taken as 60% of the tensile allowable. The allowable designs for bending stress and shear stress are chosen as the average values 224 MPa and 134.4 MPa, respectively. The TDTC code does not impose a serviceability limit, but a value of 80 mm is taken as a deflection limit to account for any vehicle's misalignment.

The majority of the existing bridge solutions are capable of supporting a military load capacity of 60 tons (MLC60) (Kosmatka et al., 2000). This capacity is often unsatisfactory due to the increasing vehicle design loads. It is noteworthy that a few number of bridge solutions around the world are capable of supporting a load class of (MLC70) or more; for instance, the BR90 Bridge system (Winney, 1994), the LEGUAN system (kerr, 1990), and the CAB system (Kosmatka et al.,

2000). Therefore, the design vehicle load for this bridge is taken as the MLC70 loading class represented by the hypothetical tracked vehicle MLC70 as required by the TDTC. The tracked vehicle patch load has a footprint dimension 5000 mm x 900 mm per track. The design loading conditions are five loading positions for a traveled vehicle: 1) vehicle travel distance is 2000 mm from support end at the beam center line, 2) 5000 mm centric, 3) 7000 mm centric, 4) 9500 mm centric, and 5) 9500 mm eccentric. A uniformly distributed load of 76.274 kPa is applied over a single patch load area. The supporting conditions of the bridge are set as a simple supported.

3.2.3.1 Numerical Simulation

The FEM of the mobile deployable bridge is numerically simulated using the ANSYS Parametric Design Language (APDL). A set of thirty design parameters are chosen to define the mobile bridge's different components and are classified into three groups as follows: 1) the treadway beams' deign parameters, 2) the bridge end supports and ramp covers' design parameters, and 3) the substructure design parameters (i.e. U-frames, struts, compression posts and the wiring system).

The description of the aforementioned thirty design parameters is tabulated in Table 3.1 and they are demonstrated in Figures 3.5.a and 3.5.c. All the treadway plate elements are modeled using Shell181 element. The U-frame and beam struts are modeled using Beam188 element. The aluminum wires, accounting for tension only, are modeled using Link181 element whereas the hydraulic pistons are modeled as compression posts (i.e. no damping is considered) using Link11 element. A subroutine program is developed to create up to 10 automatic meshing trials per single design analysis in order to improve the meshing quality. The average number of elements created for one design analysis is 65200 elements.

3.2.3.2 Numerical Evaluation

The formulation of the optimization problem for the case of minimizing the bridge structural weight $F(x)$ under an imposed strength and deflection constraints $G(x)$ can be as follows:

Minimize:
$$F(x) = \rho_{\text{den}^{\text{elem}}} \sum_{i=1}^{n^{\text{elem}}} A_i(x) \, L_i(x)$$

Subjected to:
$$\frac{G_{i,r}^{Str,l}(x)}{\tilde{G}_i^{Str}} \leq 1 \,, r = 1, 2, \ldots, n^{\text{load}}, \; i = 1, 2, \ldots, n^{\text{elem}}, \; l = S_1, S_2 \text{ or } S_3$$

$$\frac{G_{m,r}^{Def}(x)}{\tilde{G}^{Def}} \leq 1 \,, r = 1, 2, \ldots, n^{\text{load}}, \; m = 1, 2, \ldots, n^{\text{node}}$$

$$x_j^L \leq x_j^i \leq x_j^U \text{ and } j = 1, 2, \ldots, 30$$

(3.2)

where $\rho_{\text{den}^{\text{elem}}}$ is the alloy material density, $A_i(x)$ is the discretized FEM cross-sectional area. $L_i(x)$ is the discretized element length. $G_{i,r}^{Str,j}(x)$ and $\tilde{G}_i^{Str}$ are the calculated and the allowable stress constraints, respectively. $G_{m,r}^{Def}(x)$ and $\tilde{G}^{Def}$ are the calculated and the allowable deflection constraints, respectively. The symbols r and l are the loading conditions and the principal stresses' indices, respectively. x_j^L and x_j^U are the lower and upper bounds of the plate thickness x_j^i assigned to the cross-sectional area numbered i, respectively.

The gradient-based techniques start the optimization analysis from a single feasible initial solution. A random search is created to probe several feasible solutions in the design space. In order to enhance the performance of the Advanced Zero-Order method and the First-Order method optimization processes, five independent iterations are conducted for each method starting from a different initial feasible solution obtained by the random search. The random search started from an initial conventional design of 13.099 tons and the design parameters' values are illustrated in Table 3.1; From 200 random iterations, only 31 feasible design are obtained. The values of the best five feasible designs obtained by the random search in descending order are 11.785, 11.599, 11.287, 11.181 and 10.974 tons.

After applying the Zero-Order optimization's five trials, the best weight results obtained by the method are 9.349, 10.312, 9.904, 10.367, and 10.461 tons. The design parameters' values for the best result (9.349 tons) are illustrated in Table 3.1. It can be clearly seen that starting from a minimum initial feasible design is not a guarantee to obtain the optimal result (i.e. 10.974 tons initial design results in 10.461 tons optimized design). The method succeeded in reducing the weight of the deployable bridge by 28.6%.

Table 3.1 Bridge tread-way beam design parameters

No	D.V.	Parameter Description	Lower Bound	Upper Bound	Initial Design	Zero Order	First Order	GA	PSO
1	H_1	Tread way vertical plates	0.7	1.0	0.9	0.79818	0.83335	0.707	0.77283
2	H_2	Top and bottom ends of v. plates	0.1	0.15	0.15	0.13721	0.13732	0.113	0.14273
3	H_3	Deck longitudinal stiffeners	0.05	0.15	0.05	0.08577	0.1045	0.08	0.06333
4	H_4	Ramp cover long. stiffeners	0.05	0.15	0.15	0.08623	0.050734	0.12	0.10109
5	H_5	Main transverse stiffeners	0.2	0.4	0.2	0.29937	0.27819	0.234	0.2
6	H_6	U-frame vertical beams	1.0	2.0	1.5	1.98183	1.6425	1.89	1.6847
7	H_7	Intermediate transverse stiff.	0.2	0.4	0.2	0.20465	0.22134	0.244	0.28742
8	T_0	Ramp cover long. stiffeners	0.008	0.012	0.01	0.01143	0.011702	0.01	0.00984
9	T_1	Tread way vertical plates	0.008	0.012	0.012	0.00809	0.0081128	0.01	0.008
10	T_2	Thickened ends of v. plates	0.012	0.03	0.03	0.01316	0.012	0.017	0.012
11	T_3	Lower tension flanges	0.02	0.04	0.03	0.02087	0.020122	0.021	0.02212
12	T_4	Ramp cover plate	0.008	0.026	0.008	0.01728	0.018038	0.015	0.0092
13	T_5	Main transverse stiffeners	0.008	0.012	0.01	0.00853	0.0085065	0.008	0.00864
14	T_6	Deck longitudinal stiffeners	0.004	0.01	0.01	0.00409	0.0051978	0.006	0.00495
15	T_7	Deck surface plate	0.008	0.012	0.008	0.00870	0.0080003	0.008	0.00908
16	T_8	Intermediate stiffeners	0.002	0.008	0.008	0.00351	0.0043569	0.005	0.00374
17	T_9	Pistons equivalent alum. C.H.S.	0.006	0.01	0.008	0.00739	0.0085364	0.009	0.00827
18	T_{10}	U-frame C.H.S. vertical beams	0.006	0.01	0.008	0.00987	0.0089027	0.008	0.00715
19	T_{11}	Compression posts C.H.S.	0.006	0.01	0.008	0.00811	0.0079156	0.008	0.00833
20	T_{12}	Deck at connection to ramps	0.01	0.03	0.024	0.01747	0.020441	0.019	0.01776
21	T_{13}	Deck ramped sides	0.016	0.04	0.04	0.01915	0.020178	0.025	0.03476
22	T_{14}	U-frame C.H.S. horizontal beam	0.006	0.01	0.01	0.00793	0.007714	0.09	0.00757
23	T_{15}	Triangular stiff. upper plates	0.008	0.012	0.01	0.00969	0.0091276	0.01	0.01136
24	W_1	U-frame beam	0.3	0.4	0.3797	0.39146	0.39229	0.385	0.3595
25	W_2	Lower tension flanges	0.2	0.36	0.2	0.22600	0.20134	0.2	0.2
26	R_1	Pistons equivalent alum. C.H.S.	0.05	0.07	0.05	0.06227	0.053007	0.056	0.05824
27	R_2	Aluminum wires radius	0.015	0.035	0.015	0.01544	0.015101	0.015	0.015
28	R_3	U-frame C.H.S. vertical beams	0.05	0.07	0.05	0.05068	0.069668	0.06	0.05718
29	R_4	Compression posts C.H.S.	0.05	0.07	0.05	0.06995	0.065975	0.065	0.06158
30	R_5	U-frame C.H.S. horizontal beam	0.05	0.1	0.1	0.08880	0.064682	0.08	0.06372
		Volume (m^3)			4.71214	3.36276	3.3062	3.325	3.2122
		Best weight (tons)			13.0997	9.348584	9.1912	9.245	8.92991
		Weight/capacity ratio			1.0	0.71365	0.70163	0.7057	0.68168
		Computational time (hrs)			--	13.15	102.1	86	60

Note: Design parameters' values are in meters; H: Height; T: Thickness; W: width and R: Outer
All design parameters dimensions are in meters;

The First-Order method is conducted five times using the same initial feasible designs. The best weight results obtained are 10.175, 9.1912, 10.659, 9.3736, and 10.457 tons. The First-Order method results are not synchronized with the Advanced Zero-Order method results in terms of

enhanced solution order obtained by the five trials. The best solution achieved by the First-Order method is more promising with a value of 9.1912 tons and a weight reduction of 29.84 %.

The population-based techniques are then applied by starting with a randomly generated population, unlike the gradient-based methods that use a single initial solution to start. The application of GA resulted in an optimum bridge weight of 9.245 tons with an enhancement of 29.4% from the base conventional design. On the other hand, the application of PSO algorithm resulted in 8.93 tons, improving the base conventional design weight by 31.8%. Design parameters' values obtained by both algorithms GA and PSO are listed in Table 3.1. Figure 3.6 shows the convergence history of the four applied methods. In general, the numerical simulation showed that a tank load positioned at the bridge mid-span and displaced to the side is the critical loading case with a maximum deflection of almost 70 mm value. Figure 3.7 shows the principal stress distribution over the bridge structure and the maximum deflection value at the critical loading case.
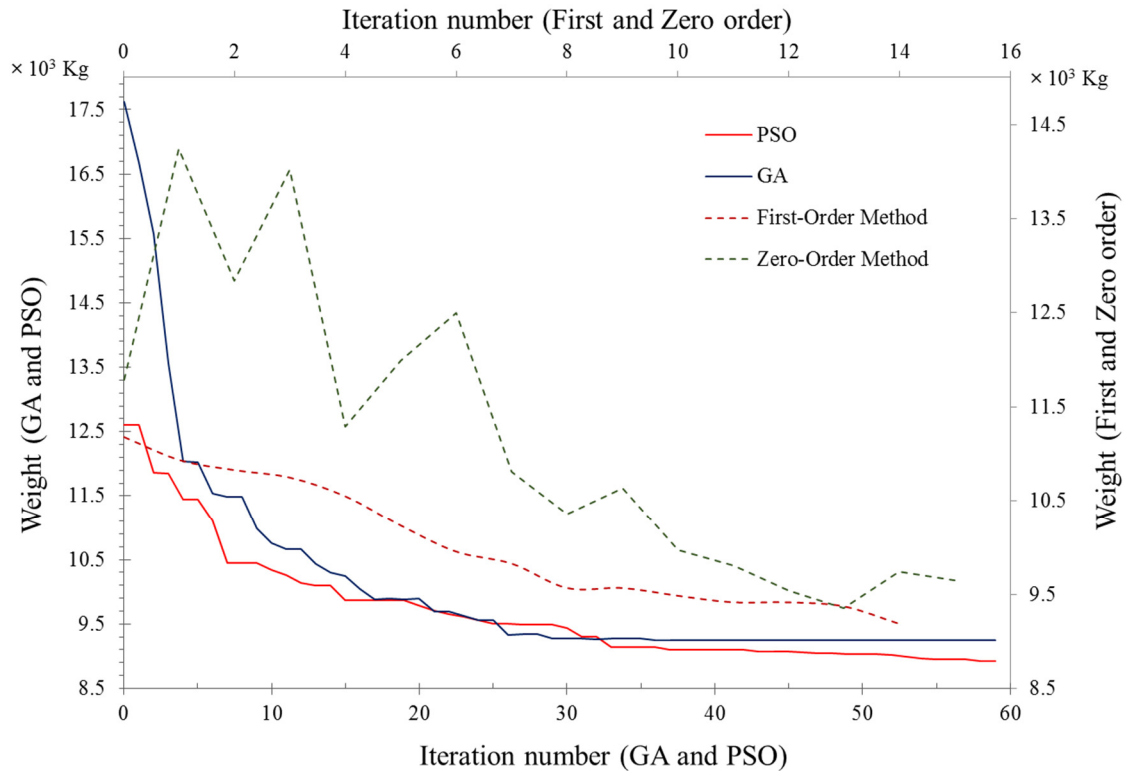
Figure 3.6. Convergence history comparison of the applied methods
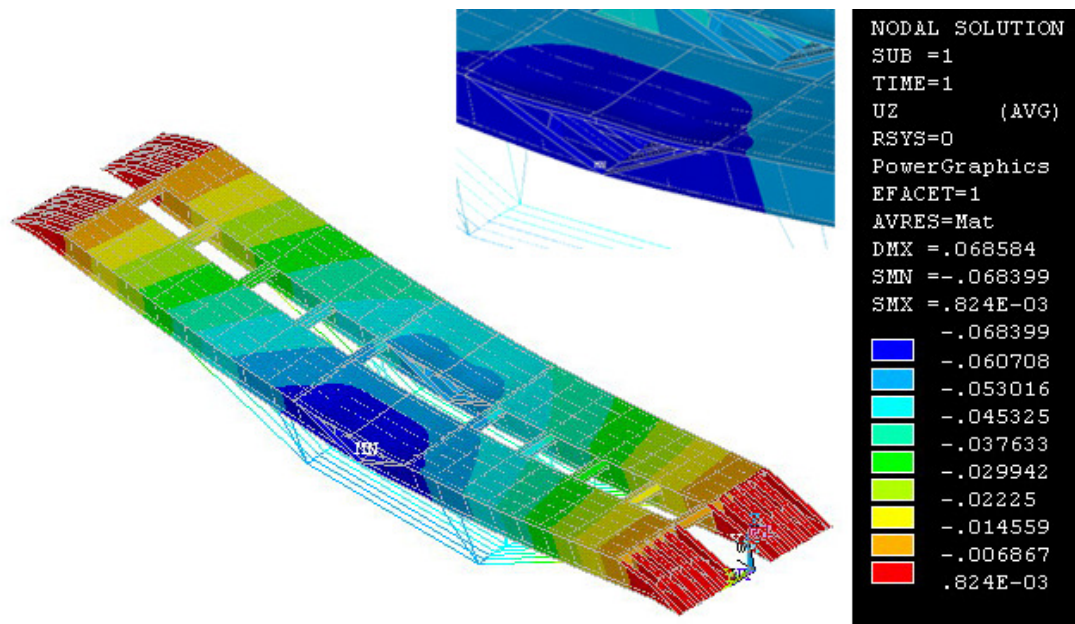
Figure 3.7. Representation of the principal stresses distribution over the bridge structure at the critical loading case (Osman, 2006)

Table 3.2 provides a summary of a comparison between the best optimized design weight of the described deployable bridge and the weight of recently in service army mobile bridges with different span coverages, the comparison shows the success of achieving a lighter mobile bridge system. A considerable decrease in weight is achieved for the configurations of 12m and up to 24m span coverage with a loading class of MLC70. The current design resulted in more than 60% lighter weight for the 12m proposed system compared to the Armored Vehicle Launched Bridge (AVLB) (Connors and Foss, 2006). For the case of the 24m system configuration, the weight is lighter by 16.3% than the Heavy Assault Bridge (HAB) system of class MLC70 reported by Connors and Foss (2006). A lighter design weight is obtained for the 48m configuration than the Medium Girder Bridge (MGB) by approximately 39% and by 49% lighter than the DSB bridge. Moreover, the system assembly is much easier, hence resulting in a shorter launching time.

Table 3.2 Comparison for weight/capacity ratio between current design and other mobile bridges

Gap range (m)	12		18-24			40-48		
Bridge type	This design	AVLB	This design	AVLB	HAB	This design	MGB	DSB
Span coverage (m)	12	15.3	24	18.3	26	48	46	40
Tracked MLC rating	70	70	70	60	70	70	70	80
Wight (tons)	4.5	13.29	9	13.29	10.75	19	31	37

Based on the conducted analysis of results, it is found that PSO performs better for optimizing this type of complex bridge structural systems in terms of convergence rate and best solution, while being second best in terms of computational time. Generally, a promising achievement is found for the application of structural design optimization to reach an effective deployable bridge system for post-disaster rapid mobility through a comparison with recently in service mobile bridges. Therefore, the PSO algorithm is chosen for the composite deployable bridge optimization in this research study.

3.3 SUMMARY

In this chapter, four optimization algorithms from Meta-heuristics (i.e. GA and PSO) and gradient-based techniques (i.e. Zero-order and First-order) are applied for their performance assessment on a deployable bridge structure. The deployable bridge structure is simulated using the direct generation method in ANSYS finite element package. The four optimization algorithms' mechanism are briefly described and coded in MATLAB then integrated with the FE software. Based on the conducted performance assessment, PSO proved to perform better for this kind of bridge structures. Therefore, the PSO algorithm is chosen for further investigation and improvement to suit complex structural problems.

In the following chapter, a representation is illustrated of the candidate algorithm's mechanism, advantages, disadvantages and the modifications developed to minimize, up to a considerable limit, PSO deficiencies in order to adapt an effective structural design optimization of large-scale and complex structures.

CHAPTER 4

Controlled-Diversity Swarm Optimization

4.1 INTRODUCTION

PSO outperforms other PBO algorithms in many aspects based on a comprehensive literature review and the investigation presented in Chapter 3. However, similar to other PBO algorithms, PSO suffers from a premature convergence after few iterations that may result in falling in local minima. This deficiency may affect to a considerable limit the optimization efficiency for complex structural models. Therefore, this chapter aims to present new modifications to PSO in order to enhance the algorithm performance and minimize its deficiency to structural design optimization. The proposed algorithm, Controlled Diversity Particle Swarm Optimizer (CD-PSO), is based on the attraction and repulsion phenomenon of the flock of birds, such that a better balance between exploration and exploitation could be achieved. Further, the modified swarm intelligence optimizer is hybridized with Response Surface Methodology (RSM) as a tool to distinguish the influence level of design parameters to the objective function in complex structural models. Based on a specific criterion, hybrid PSO enhances the swarm search in order to seek for better solutions. CD-PSO performance is evaluated through tests on three benchmark truss structures for the minimum weight design. Finally, the performance of hybrid CD-PSO and its integration with RSM along with original CD-PSO is examined for weight minimization of the deployable bridge model presented in the previous chapter.

4.2 PARTICLE SWARM OPTIMIZATION ALGORITHM

Particle Swarm Optimization (PSO) is an intelligence search technique that is stochastic in nature. First proposed by Eberhart & Kennedy (1995), the PSO algorithm directs the search to the nearest optima simulating the swarm social behavior. The swarm population consists of N_p massless and volume-less particles, where each particle represents a potential solution of the problem.

The algorithm randomly initiates and distributes the particles to probe the promising feasible regions in hyperspace. These particles, forming the swarm cloud, move with changing velocities and share their successful information with other particles while exploring the multi-dimensional hyperspace. Each particle updates its velocity and position based on its own best experience and best experience gained by the whole swarm. Each particle, i, in the swarm, encodes a number of design parameters, n. The particle is represented by a position vector $X_{ij}=\{x_1^i, x_2^i, \dots x_n^i\}$ that is updated using the velocity vector $V_{ij}=\{v_1^i, v_2^i, \dots v_n^i\}$. The equations of the particle's updated velocity and position vectors were given by Yuhui and Eberhart (1998).

$$V_j^{(i,K+1)} = w \cdot V_j^{(i,K)} + c_1 \cdot r_1 \cdot \left({}_P X_j^{(i,K)} - X_j^{(i,K)} \right) + c_2 \cdot r_2 \cdot \left({}_G X_j^{(i,K)} - X_j^{(i,K)} \right) \tag{4.1}$$

$$X_j^{(i,K+1)} = X_j^{(i,K)} + V_j^{(i,K+1)} \tag{4.2}$$

where $X_j^{(i,K)}$ and $V_j^{(i,K)}$ are the current position and velocity of the ith particle in the jth dimension of hyperspace, respectively. The parameter K is the time interval of search history, ${}_P X_j^{(i,K)}$ represents the best experience by the particle which is conceptually resembling an autobiographical memory, and ${}_G X_j^{(i,K)}$ is the best experience gained by the entire swarm. c_1 and c_2 are the cognition and social parameters, respectively, and they were defined by Eberhart and Kennedy (1995) as acceleration factors. The acceleration factors weigh the velocity of each particle to its previous local best or to the global best at the Kth iteration (i.e. a higher value of c_1 contributes more to local best and higher value of c_2 contributes more to a global best). Generally, the acceleration factors are within the range of [0, 4]. r_1 and r_2 are any randomly selected real numbers in the interval of [0, 1]. The updated velocity Equation 4.1 consists of the summation of three terms; the weighted velocity for exploration, the self-cognition learning, and the social learning. In order to balance between exploration and exploitation, the impact of the previous velocities on the current particle velocity $V_j^{(i,K)}$ is weighted by the inertia factor w. Through the entire search history, a large inertia weight is applied at initial travel stages to enable a global exploration of the hyperspace. When the swarm search gets closer to the optimum domain, a small inertia weight is recommended for exploitation. A linear decrease of inertia weight can be achieved using the equation given by Eberhart and Yuhui (2001).

$$w = w_{max} - \left(\frac{w_{max} - w_{min}}{K_{max}} \right) \cdot K \qquad (4.3)$$

where w_{max} and w_{min} are the maximum and minimum inertia weights at the initial and final iterations, respectively, and K_{max} is the maximum number of iterations. The updating velocity scheme of each particle can be illustrated as depicted in Figure 4.1.
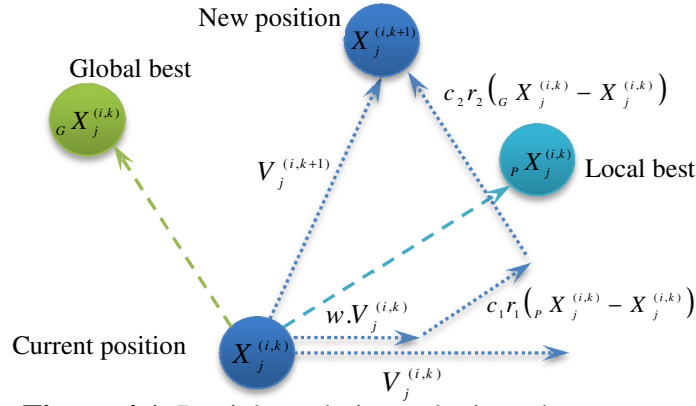
Figure 4.1. Particle updating velocity scheme

4.3   BACKGROUND OF STRUCTURAL OPTIMIZATION USING PSO

PSO proved to perform better than other PBO algorithms in solving different engineering problems in terms of less computational time, few number of parameters setting, ease of execution, and robust performance (Elbeltagi *et al.*, 2005; Hassan *et al.*, 2005). However, based on an early search stagnation of the algorithm, PSO suffers a premature convergence after few iterations. Moreover, it does not appear competitive at later stages for most of the studied cases. Furthermore, achieving an effective design becomes more difficult when the dimensionality of the hyperspace increases in case of complex structural models. Therefore, broad investigations have been developed by researchers to improve the performance of the original PSO.

Li *et al.* (2009) introduced the PSO with the harmony search scheme (HPSO) for truss structures optimization. HPSO is a discrete PSO variant where the harmony search is responsible for dealing with constraint violation instead of penalty functions to reach a better convergence rate. Luh and Lin (2011) developed a modified binary PSO for obtaining the optimal topology of benchmark truss structures. The solution size and shape were then optimized by implementing the attraction

and repulsion of swarm particles (ARPSO) in order to improve the solution quality. Kaveh (2014) proposed the Chaotic Swarming of Particles (CSP) algorithm, in which the particles use the random chaotic search theory to escape from local minima and reach a robust solution. Other research efforts were done earlier by Fourie and Groenwold (2002), Schutte and Groenwold (2003), Perez and Behdinan (2007), and Luh and Lin (2008). Generally, research efforts for developing PSO variants can be classified into four categories based on; parameter tuning, neighborhood topology, learning strategies and hybridization. Learning strategies and hybridization research based algorithms showed the promising convergence results closer to the optimum solution amongst the four categories (Tanweer *et al.*, 2015).

The current study presents a new PSO algorithm that is based on a technique for controlling the attraction and repulsion phenomenon of the swarm. Earlier studies that emulated the flock attraction and repulsion were not effective for structural design optimization after been tested. A control criterion is applied to the proposed algorithm CD-PSO to prevent the swarm's diversity stagnation and to achieve an effective balance between exploration and exploitation. The diversity control technique is presented in which the swarm diversity is regulated using a nonlinear decreasing repulsion surface. The repulsion surface forces the swarm to oscillate between attraction and repulsion in a decaying manner. The controlling technique along with other earlier versions emulated this swarm behavior are comprehensively described in Section 4.4

The concept of CD-PSO is evaluated through a comparison with the classical PSO as well as other four algorithms and the evaluation of the results is presented in Section 4.5; three of them are based on learning strategies (earlier versions of attraction and repulsion) whereas the fourth one is based on hybridization. Moreover, a comparative statistical analysis between the proposed CD-PSO and other algorithms in the literature is conducted. Three benchmark truss structures are selected to validate the effectiveness of the proposed algorithm and the diversity control technique. The results are analyzed and compared in terms of computational time, algorithm stability and solution quality. Finally, in order to achieve better assessment and further enhancement of CD-PSO to optimize large-scale and complex structural models, a hybridized CD-PSO with RSM and original CD-PSO performances are examined on the deployable bridge system proposed in the previous chapter. Original CD-PSO is applied two times, first while considering all the design parameters of the bridge model. The second is applied while considering only the effective design

parameters to the design objective. The hybridization technique and the analysis of results are clarified in Section 4.6.

4.4 CONTROLLED DIVERSITY

4.4.1 CONTROLLING ATTRACTION AND REPULSION OF THE SWARM

The first effort to enhance the classical PSO by simulating the swarm`s attraction and repulsion was done by Riget and Vesterstrøm (2002). The developed algorithm was named Attraction Repulsion Particle Swarm Optimization (ARPSO).In the classical PSO search behavior, the particles attract each other from their random disburse in hyperspace to domains of best solutions. In this attraction phase, all the swarm particles are fully informed about each particle`s best search experience. The full transfer of experience would cause a rapid attraction of the swarm particles, and that would lead to a premature convergence (Reyes-Sierra and Coello, 2006). Riget and Vesterstrøm (2002) proposed a repulsion phase to avoid the premature convergence by inverting the sign of the second and third term in the velocity update formula, Equation 4.1. In the repulsion phase, each particle is disbursed away from its previous best position and the best swarm recorded position. This behavior gives the swarm the ability to discover new domains without trapping into local minima. The diversity term, div , given by the following equation measures the degree at which the swarm particles attract each other or repel.

$$div_{itr=0}^{K_{max}} = \frac{1}{N_p \cdot N_{dv}} \cdot \sum_{i=1}^{N_p} \sqrt{\sum_{j=1}^{N_{dv}} \left(X_j^{(i,K)} - \overline{X}_j^K\right)^2} \qquad (4.4)$$

$$\overline{X}_j^K = \frac{\sum_{i=1}^{N_p} X_j^K}{N_p}$$

where N_P is the population size, N_{dv} is the problem dimensionality, $X_j^{(i,K)}$ is the encoded design variable j for the particle i in the swarm at iteration K. $\overline{X}_j^K$ is the jth value of the design variable mean $\overline{X}$ for all particles at iteration K.

The velocity update formula (4.5) is switched between attraction and repulsion at the following condition:

$$V_j^{(i,K+1)} = w.V_j^{(i,K)} + dir_1 \cdot \left(c_1 \cdot r_1 \cdot \left({}_P X_j^{(i,K)} - X_j^{(i,K)}\right)\right) + dir_2 \cdot \left(c_2 \cdot r_2 \cdot \left({}_G X_j^{(i,K)} - X_j^{(i,K)}\right)\right) \qquad (4.5)$$

Such that:

$$dir_1 = dir_2 = \begin{cases} +1 & \text{if } div \geq d_{high} \\ -1 & \text{if } div < d_{low} \end{cases}$$

When particles attract each other, the diversity decreases until it reaches a lower limit, d_{low}, equals to 5.0×10^{-6}. Consequently, the swarm cloud is switched to the repulsion phase. As a result, the swarm cloud expands and the diversity increases until it reaches an upper limit, d_{high}, equals to 0.25. At this stage, the swarm cloud returns back to attraction again (Riget and Vesterstrøm, 2002).

Pantetal *et al.* (2007) proposed the Attraction Repulsion PSO (ATRE-PSO) which is another version of ARPSO. For this algorithm, in addition to the attraction and repulsion phases, a third phase is considered and identified as the positive conflict phase. In this phase, neither full attraction nor repulsion would occur if the swarm cloud diversity lies between the values of d_{low} and d_{high}. In this case, the velocity update condition is modified as follows:

$$\begin{cases} dir_1 = +1, \ dir_2 = +1 & \text{if } div > d_{high} \\ dir_1 = +1, \ dir_2 = -1 & \text{if } d_{low} \leq div \leq d_{high} \\ dir_1 = -1, \ dir_2 = -1 & \text{if } div < d_{low} \end{cases}$$

Li and Li (2012) proposed the Diversity Guided PSO (DGPSO) in which they added two phases to the ARPSO between full attraction and full repulsion to keep a high swarm diversity. The whole swarm cloud will be shuttling between these phases under the following conditions:

$$\begin{cases} dir_1 = +1, \ dir_2 = +1 & \text{if } div > d_{high} \\ dir_1 = -1, \ dir_2 = +1 & \text{if } \left(d_{low} + d_{high}\right)/2 < div \leq d_{high} \\ dir_1 = +1, \ dir_2 = -1 & \text{if } d_{low} \leq div \leq \left(d_{low} + d_{high}\right)/2 \\ dir_1 = -1, \ dir_2 = -1 & \text{if } div < d_{low} \end{cases}$$

The three aforementioned studies specified two fixed values for d_{low} and d_{high} to switch between phases. These values give promising results when tested over benchmark functions, however, they are unable to assure a promising diversity control of the swarm for structural engineering problems even if they are tuned. In structural engineering problems, the initial population of the swarm is usually smaller than that of benchmark functions to adopt the problem complexities and reduce

computational time. Therefore, the initial swarm diversity could fall below the d_{high} value, and hence forcing the swarm to repel (for the case of ATRE-PSO and DGPSO) without obtaining good solutions in the early stages, which is a major PSO characteristic. Moreover, the swarm diversity may not reach d_{low} at any travel history stage as the swarm population may not precisely resemble; (i.e. the least diversity value of the swarm cloud is predominantly higher than 5.0×10^{-6} in most structural optimization problems). This means that no repulsion would occur, and hence lead the optimizer to perform similarly to the classical PSO.

In this study, a new and more generalized condition is considered for controlling attraction and repulsion of the swarm in the proposed CD-PSO. This is achieved by implementing a nonlinear convex repulsion surface to control the swarm diversity in hyperspace. If the swarm particles are clustering and reach a certain diversity value that falls below the repulsion surface, the swarm search will be switched to the repulsion phase. The repulsion surface location is calculated with reference to the diversity value of the initial population as illustrated in Figure 4.2. In addition, the diversity trajectories for ARPSO and CD-PSO are clarified for a structural case optimization. It can be shown that no repulsion phase could be detected when utilizing the fixed limits, whereas the swarm diversity is regulated using the repulsion surface in which a high, medium and low diversities are achieved as depicted in the scattered plot.

The proposed repulsion surface of CD-PSO is applied in the shape of the following rational function:

$$div \cdot rate \ = \frac{0.381 \cdot div_{\circ}}{1.1^{K\psi}} \tag{4.6}$$

where K is the iteration number, div_{o} is the diversity of the initial random population, and ψ is the factor controlling the rational function convexity. The value of 0.381 is a factor that allows for an acceptable investment of the swarm's early convergence, a sensitive tuning is performed using multiple values from 0.35 to 0.5 until the factor 0.381 is selected. The velocity update formula is switched between attraction and repulsion using the condition:

$$dir_{1} = dir_{2} = \begin{cases} +1 & if \ \ div \geq div \cdot rate \\ -1 & if \ \ div < div \cdot rate \end{cases}$$

Following this strategy, an effective balance between exploration and exploitation will be assured. In other words, a better investment of PSO's early convergence criterion is achieved, while new solution domains are discovered by the repulsion behavior.
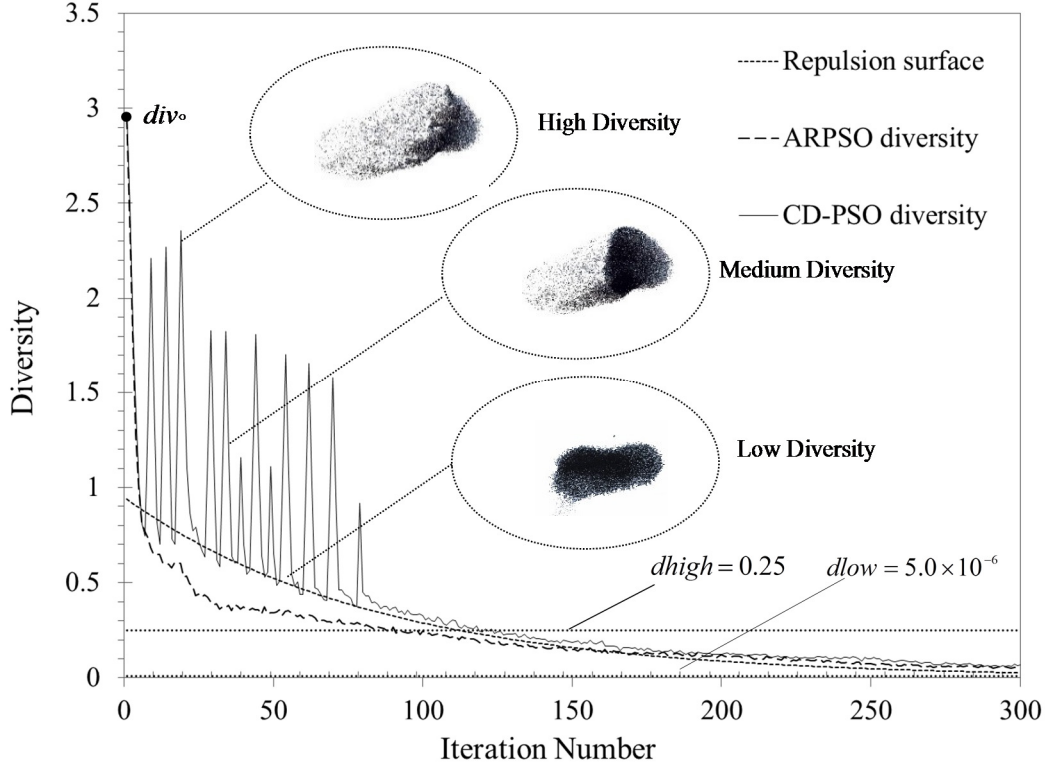
Figure 4.2. The trajectory variation of the classical PSO, ARPSO, and CD-PSO Diversity.

4.4.2   LEVY FLIGHT PSO FOR STRUCTURAL OPTIMIZATION

The Levy Flight Particle Swarm algorithm (LFPSO) was developed by Hakli and Uğuz (2014). The Levy flight is a category of non-Gaussian random processes. These processes are random walks drawn from the Levy stable distribution. The main idea of the LFPSO is to incorporate the Levy flight random movement distribution to PSO when the particle fails to improve its position due to trapping in local minima, such that, a more efficient search in hyperspace can be achieved due to the long jumps made by the particles. The position update formula (4.2) is switched to perform Levy flight random movements using the following equation:

$$X_j^{(i,K+1)} = X_j^{(i,K)} + \alpha \oplus Levy(\beta) \tag{4.7}$$

47

where α is the skewness parameter of the levy distribution which is chosen as a random number, and β is the Levy index that controls the shapes of the probability distribution, such that, smaller β values perform longer particles jumps, hence elongated distribution tails. The product ⊕ means an element-wise multiplication. A more comprehensive explanation of the Levy flight motion is demonstrated by Chechkin *et al.* (2008). LFPSO proved to provide a high diversity distribution to avoid particles' trapping in local minima when it is applied to benchmark functions. In this study, the hybrid LFPSO was reformulated to suit the structural optimization for a comparative statistical analysis with the proposed CD-PSO.

4.5 ASSESSMENT OF CD-PSO ON BENCHMARK STRUCTURES

The effectiveness of the proposed CD-PSO algorithm on structural optimization is assessed through tests on three benchmark truss structures: A 10-member planar truss, a 25-member spatial truss, and a 72-member spatial truss. For the 10, 25 and 72-member structural benchmark problems, the swarm population is chosen as 100, 40 and 40, and the maximum number of iterations is set to 2000, 250 and 200, respectively. Table 4.1 illustrates the CD-PSO operators' values used for running the three optimization tests. The following subsections present a comparison between the numerical results of the proposed CD-PSO algorithm and the results data in the literature.

Table 4.1 Optimization operators of CD-PSO and the rational function convexity factors

Truss benchmark optimization parameters	Operator value
Acceleration factors c_1 and c_2	2.0, 2.0
Maximum inertia weight w_{max}	0.9
Minimum inertia weight w_{min}	0.4
Velocity bounds V_{max} and V_{min}	+10%, -10%
Rational function convexity factor ψ	0.125 and 0.15

4.5.1 PROBLEMS FORMULATION AND FEASIBILITY MANAGEMENT

In general, the optimization problem formulation for the minimum weight $F(x)$ design of the benchmark truss structures under an imposed strength and deflection constraints $G(x)$ can be expressed in a standard formulation as follows:

Minimize: $\quad F(x) = \rho_{\text{den}} \sum_{i=1}^{n^{\text{mem}}} x_i \, L_i$

Subjected to: $\dfrac{G_{i,\text{r}}^{Str}(x)}{\tilde{G}^{Str}} \leq 1$, $r = 1,2,\ldots,n^{\text{load}}$, $i = 1,2,\ldots,n^{\text{mem}}$, $\qquad\qquad$ (4.8)

$\dfrac{G_{m,\text{r}}^{Def}(x)}{\tilde{G}^{Def}} \leq 1$, $r = 1,2,\ldots,n^{\text{load}}$, $m = 1,2,\ldots,n^{\text{node}}$

$x_j^L \leq x_j^i \leq x_j^U$ and $j = 1,2,\ldots,Gr$

where ρ_{den} is the density of the truss steel material, x_i and L_i are the cross-sectional area and length of the truss member numbered i. $G_{i,r}^{Str,j}(x)$ and $\tilde{G}_i^{Str}$ are the calculated and the allowable axial stress constraints, respectively. $G_{m,r}^{Def}(x)$ and $\tilde{G}^{Def}$ are the calculated and the allowable deflection constraints, respectively. The symbol r denotes the loading case number subjected on the truss benchmark. x_j^L and x_j^U are the lower and upper bounds of the cross–sectional areas' grouping Gr, respectively.

In order to transform the structural constrained optimization problem to an unconstrained one. The objective function $F(x)$ in Equation 4.8 needs to be modified. In the present study, a penalty function is applied, such that whenever an infeasible design is detected the result is penalized to a maximized value. Following this technique, the swarm search in hyperspace for feasible solutions will not be misguided. The followed penalization technique can be expressed as follows:

Minimize:

$$\overline{F}(x) = F(x) \cdot \left(1 + \overline{P}\right)^{\eta}$$

where:

$$\overline{P} = \left(\sum_{i=1}^{n^{\text{mem}}} \beta_{i,r}^{Str} + \sum_{K=1}^{n^{\text{node}}} \beta_{K,r}^{Def} \right)$$

(4.9)

Such that:

$$\beta_{i,r}^{Str} = \begin{cases} \lambda_S & \text{if } \lambda_S \geq 0 \\ 0 & \text{if } \lambda_S < 0 \end{cases}$$

$$\beta_{K,r}^{Def} = \begin{cases} \lambda_D & if\ \lambda_D \geq 0 \\ 0 & if\ \lambda_D < 0 \end{cases}$$

and:

$$\lambda_S = \sum_{i=1}^{n^{mem}} \left(\left| \frac{G_{i,r}^{Str}(x)}{\tilde{G}^{Str}} \right| - 1 \right), \ \lambda_D = \sum_{i=1}^{n^{mem}} \left(\left| \frac{G_{K,r}^{Def}(x)}{\tilde{G}^{Def}} \right| - 1 \right)$$

In the modified equation (4.9), the objective function is penalized using the penalty term $\bar{P}$. The objective feasibility violation is calculated using the constraint feasibility term $\lambda_{S,D}$. The penalty term is set to a value greater than zero if any of the design constraints' operators $\beta^{Str,Def}$ is violated for the strength or the deflection. The penalty term value is maximized in case of violation of more than one constraint, while the penalty term exponent η is set to a value greater than one. Choosing the value of the penalty term exponent is very sensitive for the efficient search of feasible solution, therefore, the values 2, 3, and 4 had been tried and 2 was the best selection.

The convergence criterion is met when the difference in solution fitness is less than or equal to 0.001 for 50 consecutive iterations.

4.5.2   10-MEMBER PLANAR TRUSS

Figure 4.3 illustrates the two-dimensional 10-member non-convex cantilevered truss as described by Haug and Arora (1979). The figure shows the truss geometry, the loading pattern, and the material properties. The main design objective is to obtain the minimum weight of the structure while respecting the stress and deflection limits. The stress limits were set as $\pm$ 25 ksi (172.4 MPa), and for deflection, the limits were taken as $\pm$ 2.0 in (51 mm) in the vertical and horizontal directions.
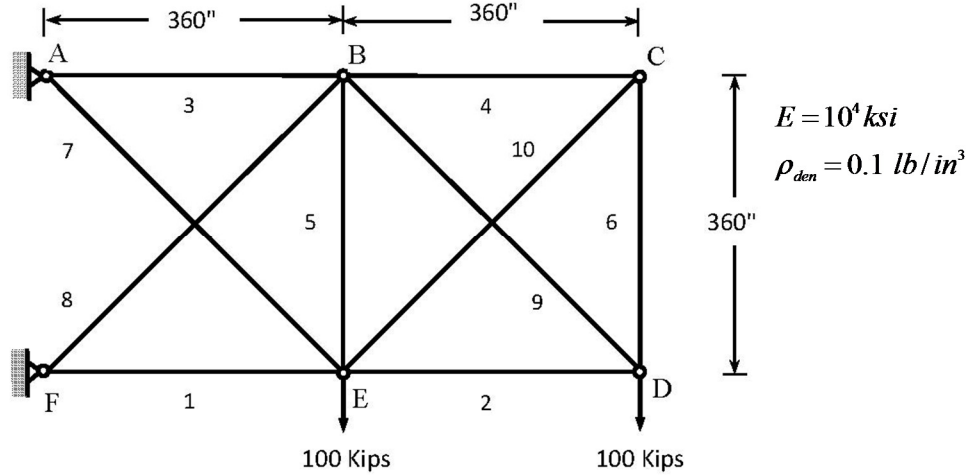
Figure 4.3. A 10-member planar truss

I. CD-PSO Concept Evaluation

The effectiveness of CD-PSO concept is assessed using the 10-member truss benchmark. A comparative analysis is performed between the proposed CD-PSO and the aforementioned algorithms of high diversity control performance, namely: ARPSO, ATRE-PSO, DGPSO and LFPSO along with the standard PSO algorithm. The upper and lower bounds of the design parameter interval (cross-sectional area) are 33.5 in^2 and 0.001 in^2, respectively. The lower bound was chosen to be a value close to zero in order to investigate the algorithm's ability to reach an optimum topology. The analysis showed that, similar to the earlier algorithms, the CD-PSO is able to reach an optimum topology by optimizing members 4, 5 and 10 to the lower bound, while a very small value is reserved for member 6. Figure 4.4 shows a schematic for the final optimized cross-sections for the 10-member truss problem, which is consistent to other studies solved the same problem case, such as Zhou and Rozvany (1993).

Table 4.2 shows the results analysis of the trial with least variance to the mean of best solutions. The stability of algorithms is assessed through 10 independent trials, a swarm population of 100 particles, and a total of 30,000 analyses per trial. The CD-PSO is able to reach the minimum best and average weight values between the tested algorithms. Moreover, the CD-PSO showed a superior performance compared to other tested algorithms with a standard deviation of 0.945, while the standard deviation values for classical PSO, ARPSO, ATRE-PSO, DGPSO, and LFPSO are 21.51, 8.47, 6.03, 6.04, and 5.91, respectively.
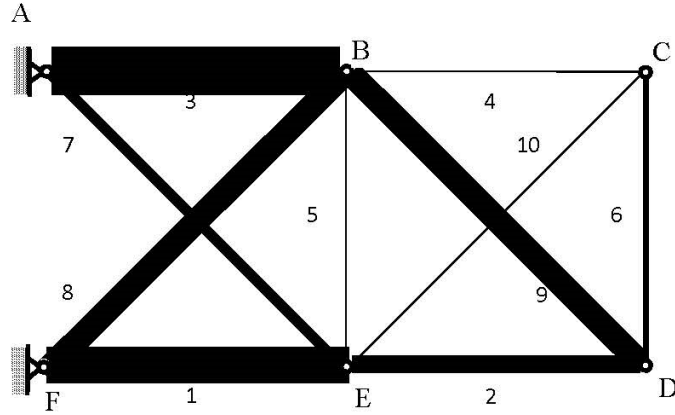
Figure 4.4. The optimized material distribution of 10-member truss.

Table 4.2. Comparative analysis of CD-PSO against other PSO

Design Parameters Evaluation - Cross-sectional area (in^2)						
Members	PSO	ARPSO	ATRE-PSO	DGPSO	LFPSO	CD-PSO
1	23.8750	22.56928	22.80677	23.32701	22.45509	22.79836
2	15.0459	15.39446	14.41803	14.72802	15.245	15.42783
3	29.4439	33.5	33.5	31.32379	30.08818	30.09237
4	0.001	0.001	0.001	0.001	0.001	0.001
5	0.001	0.001	0.001	0.001	0.001	0.001
6	0.0511	0.055231	0.066432	0.102651	0.049562	0.051104
7	7.6016	7.666583	7.794117	7.757325	7.816969	7.667251
8	20.3454	19.13549	20.09236	20.35744	21.0632	20.18758
9	21.7316	21.03506	20.57738	20.96771	21.21304	21.82241
10	0.001	0.001	0.001	0.001	0.001	0.001
Weight (lb)	4,994.187	5,010.275	5,015.984	5,000.327	4,992.614	4,990.583
Average weight (lb)	5,001.643	4,994.206	4,999.202	4,999.895	4,993.136	4,990.823
Standard deviation (lb)	21.5100	8.4721	6.0281	6.0449	5.9085	0.9449
No. of analyses	30,000	30,000	30,000	30,000	30,000	30,000

Note: (lb = 4.45 N)

Figure 4.5 shows the convergence history of CD-PSO average and best penalized weight compared to the best penalized weight of other PSO algorithms. From the figure, it can be seen that the proposed CD-PSO algorithm is able to reach a robust and a better solution quality compared to other algorithms, despite the delay in its convergence rate that is caused by the high hyperspace exploration through attraction and repulsion. It can be also noticed that ARPSO algorithm behaved identically to classical PSO, as the two curves resemble each other, this indicates that ARPSO could not experience any hyperspace exploration through attraction and

repulsion as intended, which is a major drawback for applying the algorithm for structural applications.
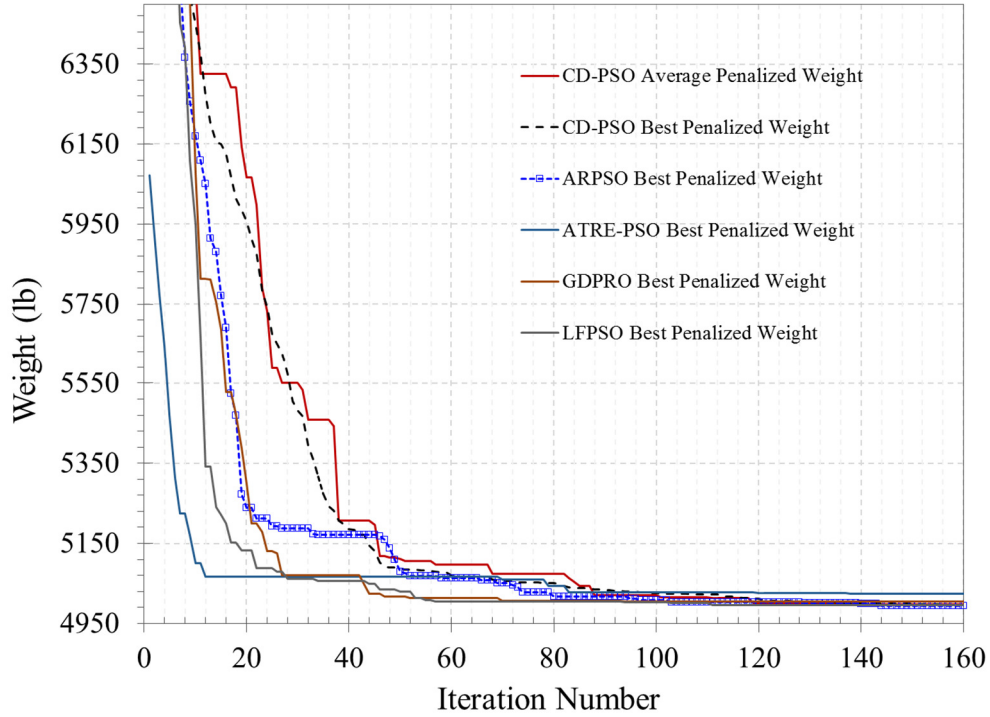
Figure 4.5. Convergence history of CD-PSO compared to other PSO algorithms.

II.   Comparisons with other optimization algorithms

In order to reach a reliable judgment about the performance of CD-PSO, the proposed algorithm is compared to a wide range of data results from other algorithms in past studies. The upper and lower bounds of design parameters for CD-PSO algorithm are modified to 35 in^2 and 0.1 in^2 in order to match the bounds used in the selected studies. The maximum number of iterations is chosen as 2,000 and the swarm population is set to100. The best result obtained by the CD-PSO is converged after 1,319 iterations. Several studies that solved the 10-member truss problem are scanned and re-evaluated against design constraints violation. Only results that satisfy the design constraints to the nearest fifth decimal for deflection and stresses are selected for comparison. Table 4.3 shows the comparative analysis of results of CD-PSO with the selected past studies. The table indicates that CD-PSO algorithm achieved the optimal solution for the 10-member truss benchmark compared to the other studies.

Table 4.3. Results of optimized designs for the 10-member truss problem

Membe	Design Parameters Evaluation - Cross-sectional area (in^2)
	[1]	[2]	[3]	[4]	[5]	[6]	[7]	[8]	[9]	CD-PSO
1	20.03	23.408	23.290	23.760	23.934	23.941	24.07	23.270	23.2740	23.21257
2	15.60	14.904	15.428	14.590	14.733	14.733	13.96	15.190	15.2860	15.23875
3	31.35	30.416	30.500	30.670	30.731	30.73	28.92	30.590	30.0310	30.60087
4	0.100	0.128	0.100	0.1000	0.1000	0.10	0.10	0.1000	0.1000	0.1000
5	0.140	0.101	0.100	0.1000	0.1000	0.10	0.10	0.1000	0.1000	0.1000
6	0.240	0.101	0.210	0.1000	0.1000	0.10	0.56	0.4600	0.5565	0.5402873
7	8.350	8.696	7.649	8.5780	8.5416	8.541	7.69	7.5000	7.4683	7.435041
8	22.21	21.084	20.980	21.070	20.954	20.951	21.95	21.0700	21.1980	20.84516
9	22.06	21.077	21.818	20.960	20.836	20.836	22.09	21.4800	21.6180	21.67716
10	0.100	0.186	0.100	0.1000	0.1000	0.10	0.10	0.1000	0.1000	0.1000
Weight	5112.0	5084.9	5080.00	5076.85	5076.66	5076.67	5076.31	5062.17	5061.6	5061.0339

Note: (lb = 4.45 N)

Gellatly and Berke (1971) [1]; Venkayya (1971) [2]; Dobbs and Nelson (1976) [3]; Schmit and Farshi (1974) [4];
Paulo Rizzi (1976) [5]; Zhou and Rozvany (1993) [6]; Camp *et al.* (1998) [7]; Xia and Liu (1987) [8];
Haug and Arora (1979) [9].

4.5.3 25-MEMBER SPATIAL TRUSS

The second example considers the design of a 25-member transmission tower spatial truss. The truss benchmark was first designed by Gellatly (1966) and Schmit and Farshi (1974). The structure geometry and material properties are illustrated in Figure 4.6. The 25 truss members are categorized into 8 groups of members' design. Two loading patterns are considered for the design as shown in Table 4. The spatial truss optimization problem is subjected to stress limits of $\pm$ 40 ksi (275.8 MPa) and deflection limits of $\pm$ 0.35 in (8.8 mm) for all truss joint directions. The upper and lower bounds for the eight design groups defining the truss members' cross-sectional areas are taken as 3.4 in^2 and 0.01 in^2, respectively.

Table 4.5 shows the comparative analysis of optimized design of CD-PSO and other evolutionary-based algorithms for the 25-member truss problem. The table illustrates that the CD-PSO algorithm is able to reach a result that is consistent with the best results reported in the literature with a maximum difference of 0.12 percent. Meanwhile, the algorithm showed a superior stability performance with a standard deviation of 0.2533 lb, which is less than all other algorithms. The average weight using the CD-PSO from a set of best feasible designs of twenty independent

trials is 545.32 lb, which is the second least average weight obtained by all the tested algorithms (when applicable). The computational time required to achieve the optimum design is competitive compared to other published results with a number of analyses per trial equals to 10,000, whereas it is 9,875 for the truss designed by Kaveh and Talatahari (2009) using a hybrid algorithm of PSO and ACO, and it is 9,596 truss analysis by Schutte and Groenwold (2003) using a modified PSO. Moreover, CD-PSO computational time is less by about 51% and 43% compared to Camp (2007) and Kaveh *et al.* (2014), respectively. Figure 4.7 shows the convergence history of the CD-PSO and classical PSO best penalized weight.

Table 4.4. Loading patterns for the 25-member spatial truss.

Load case	Joint number	Load value in kips (kN)		
		F_x	F_y	F_z
1	1	1 (4.45)	10 (44.5)	-5 (-22.25)
	2	0	10 (44.5)	-5 (-22.25)
	3	0.5 (2.225)	0	0
	6	0.5 (2.225)	0	0
2	1	0	20 (89)	-5 (-22.25)
	2	0	-20 (-89)	-5 (-22.25)
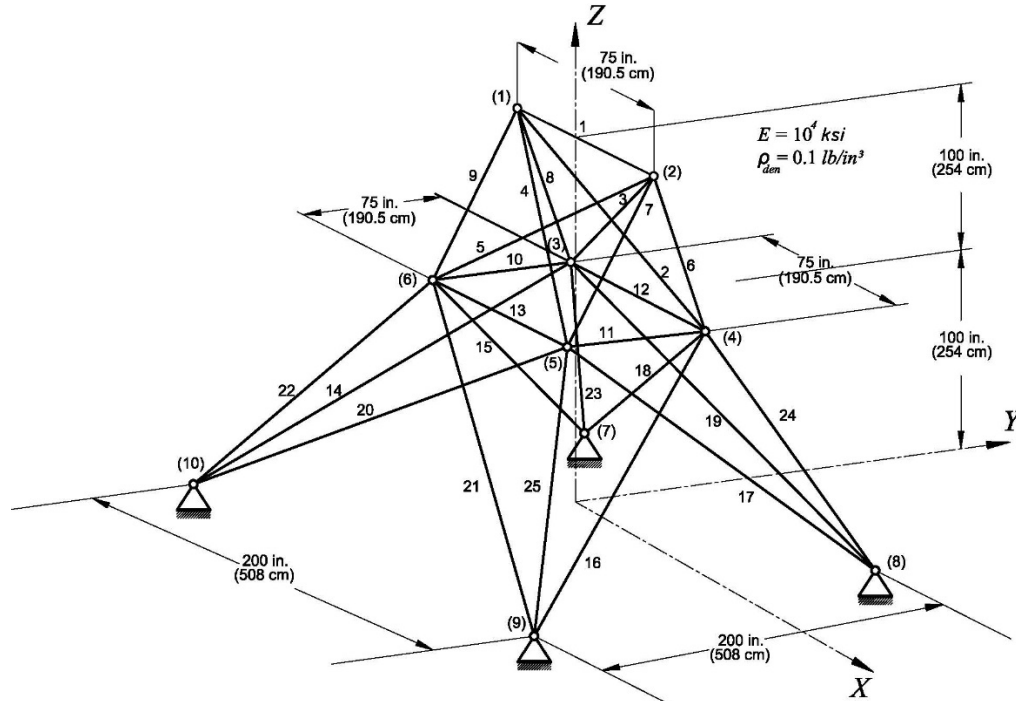
Figure 4.6. A 25-member spatial truss.

Table 4.5. Results of CD-PSO and other evolutionary-based algorithms for the 25-member Design Parameters Evaluation - cross-sectional area (in^2)

Element Group	Members	GA [1]	ACO [2]	BB-BC [3]	HS [4]	PSO [5]	HPSACO [6]	BB-BC [7]	RO [8]	CSP [9]	CD-PSO
G1	1	0.010	0.010	0.010	0.047	0.010	0.010	0.010	0.0157	0.010	0.0100
G2	2-5	2.0119	2.000	2.092	2.022	2.052	2.054	1.993	2.0217	1.910	2.0124
G3	6-9	2.9493	2.966	2.964	2.950	3.001	3.008	3.056	2.9319	2.798	3.0380
G4	10-11	0.010	0.010	0.010	0.010	0.010	0.010	0.010	0.0101	0.010	0.0100
G5	12-13	0.0295	0.012	0.010	0.014	0.010	0.010	0.010	0.0108	0.010	0.0100
G6	14-17	0.6838	0.689	0.689	0.688	0.684	0.679	0.665	0.6562	0.708	0.6979
G7	18-21	1.6798	1.679	1.601	1.657	1.616	1.611	1.642	1.6793	1.836	1.6312
G8	22-25	2.6759	2.668	2.686	2.663	2.673	2.678	2.679	2.71626	2.645	2.6431
Best Weight (lb)		545.80	545.53	545.38	544.38	545.21	544.99	545.16	544.65	545.09	545.077
Average weight (lb)		N/A	546.34	545.78	N/A	546.84	545.52	545.66	546.68	545.20	545.32
Standard deviation (lb)		N/A	0.940	0.491	N/A	1.478	0.315	0.367	1.6124	0.487	0.2533
No. of analyses/trial		N/A	16,500	20,566	15,000	9,596	9,875	12,500	13,880	17,500	10,000

Note: (lb = 4.45 N)

Cao (1996) [1]; Camp and Bichon (2004) [2]; Camp (2007) [3]; Lee & Geem (2004) [4];
Schutte and Groenwold (2003) [5]; Kaveh and Talatahari (2009) [6]; Kaveh and Talatahari (2009) [7];
Kaveh and Khayatazad (2012) [8]; Kaveh *et al.* (2014) [9].
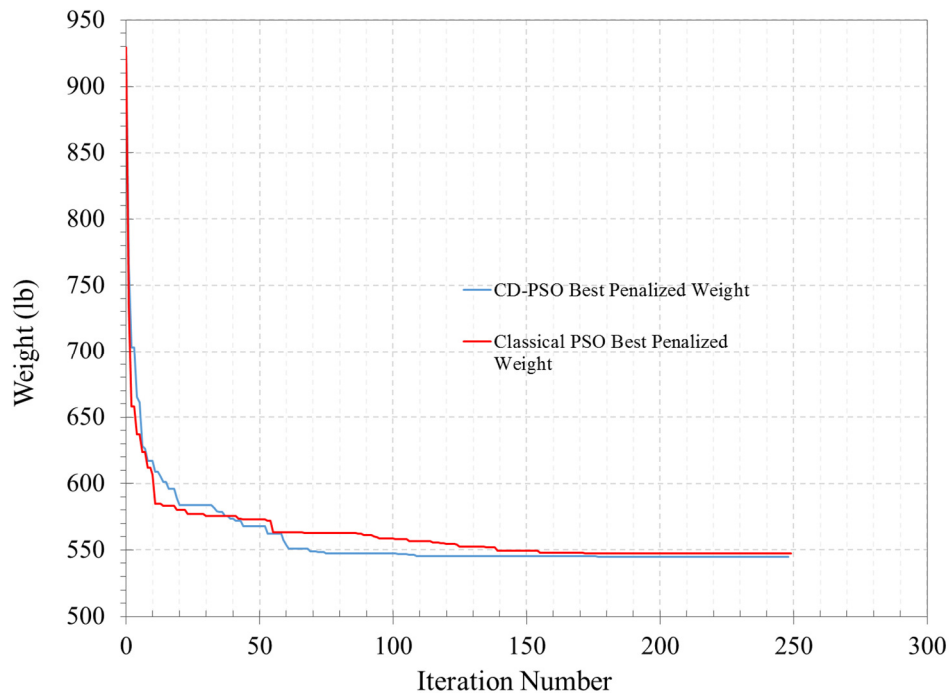
Figure 4.7. Convergence history of CD-PSO and classical PSO best for the 25-member spatial truss.

4.5.4   72-MEMBER SPATIAL TRUSS

The design example of the 72-member spatial truss shown in Figure 4.8 has been widely used in continuous optimization literature. The design example was first presented by Venkayya *et al.* (1968). The truss problem contained 16 independent design parameters and two different loading patterns. Table 4.6 describes the two loading patterns considered for the design of the 72-member truss. The stress limits are set as $\pm$ 25 ksi (172.4 MPa) and the deflection limits are taken as $\pm$ 0.25 in (6.3 mm) in the vertical and horizontal directions. Table 4.7 shows a comparison between the CD-PSO results and other evolutionary-based algorithms in the literature. The comparison demonstrates that CD-PSO has more robust performance compared to other studies. The proposed algorithm led to the optimal average weight with the least standard deviation of 0.28322 lb (obtained using 20 independent trials). The number of analysis runs per trial required to obtain the optimum value using the CD-PSO is 8000, which is considerably less than the number required by other algorithms. Moreover, the best solution obtained from the CD-PSO algorithm is very close to the best solutions obtained by Camp (2007), and Kaveh and Ghazaan (2014) with a maximum difference of 0.065 percent. Figure 4.9 shows a faster convergence rate of CD-PSO compared to the classical PSO best penalized weight.

Table 4.6. Loading patterns of the 72-member spatial truss.

Load case	Joint number	Load value in kips (kN)		
		F_x	F_y	F_z
1	1	5 (22.25)	5 (22.25)	-5 (-22.25)
2	1	0	0	-5 (-22.25)
	2	0	0	-5 (-22.25)
	3	0	0	-5 (-22.25)
	4	0	0	-5 (-22.25)
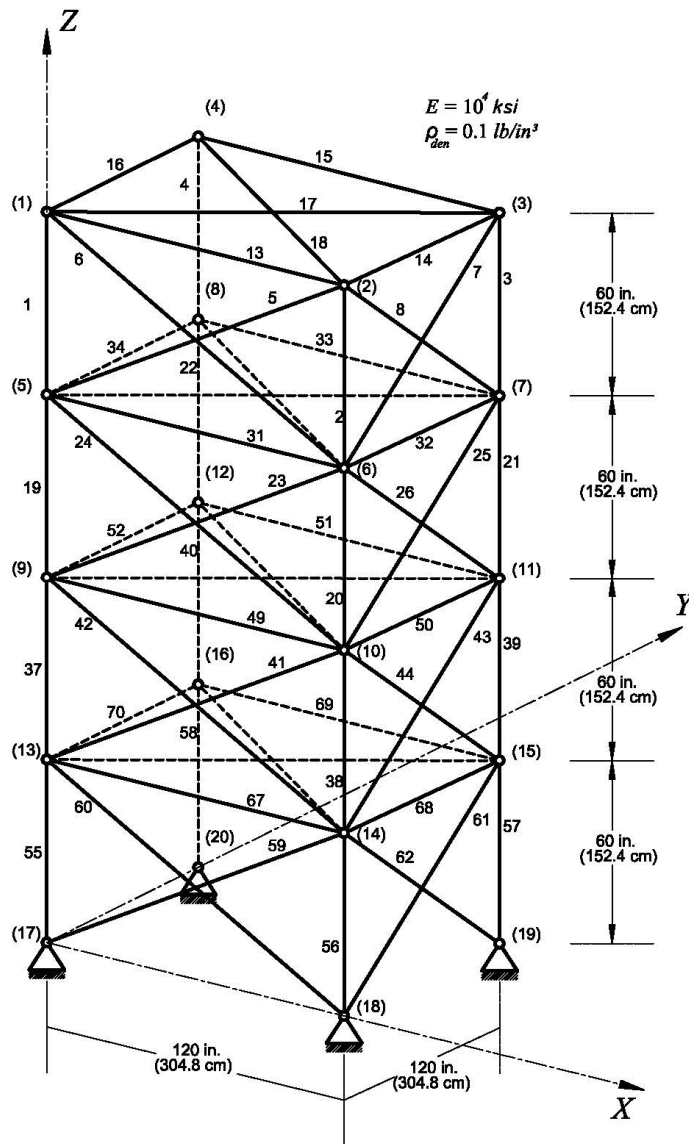
Figure 4.8. A 72-member spatial truss.

58

Table 4.7. Results of CD-PSO and other evolutionary-based algorithms for the 72-member truss.

Element Group	Members	PSO [1]	GA [2]	ACO [3]	BB-BC [4]	RO [5]	ECBO [6]	CD-PSO
				Design Parameters Evaluation - Cross-sectional area (in^2)				
G1	1-4	0.1615	0.1557	0.156	0.1565	0.1576	0.1560	0.155757
G2	5-12	0.5092	0.5501	0.550	0.5507	0.5222	0.5572	0.550307
G3	13-16	0.4967	0.3981	0.390	0.3922	0.4356	0.4259	0.432478
G4	17-18	0.1000	0.1000	0.102	0.1000	0.1004	0.1000	0.530810
G5	19-22	0.5142	0.5177	0.561	0.5209	0.5730	0.5312	0.590520
G6	23-30	0.5464	0.5227	0.492	0.5172	0.5499	0.5173	0.517241
G7	31-34	0.1000	0.1000	0.1	0.1004	0.1004	0.1000	0.100024
G8	35-36	0.1000	0.1000	0.100	0.1012	0.1001	0.1000	0.100297
G9	37-40	1.3079	1.2830	1.303	1.2476	1.2522	1.2819	1.268199
G10	41-48	0.5193	0.5028	0.511	0.5269	0.5033	0.5091	0.493895
G11	49-52	0.1000	0.1000	0.101	0.1000	0.1002	0.1000	0.100000
G12	53-54	0.1095	0.1049	0.107	0.1005	0.1001	0.1000	0.100000
G13	55-58	1.7427	1.8562	1.948	1.8577	1.8365	1.8519	1.909074
G14	59-66	0.5185	0.4933	0.508	0.5059	0.5021	0.5141	0.511367
G15	67-70	0.1000	0.1000	0.101	0.1000	0.1000	0.1000	0.100000
G16	71-72	0.5619	0.6749	0.592	0.5922	0.5971	0.5271	0.100223
Best Weight (lb)		381.91	380.32	380.24	379.85	380.458	379.77	380.0192
Average weight (lb)		N/A	N/A	383.16	382.08	382.553	380.39	380.3777
Standard deviation (lb)		N/A	N/A	3.66	1.912	1.221	0.8099	0.28322
No. of analyses/trial		8,000	15,000	18,500	19,621	19,084	18,000	8,000

Note: (lb = 4.45 N)

Perez and Behdinan (2007) [1]; Cao (1996) [2]; Camp and Bichon (2004) [3]; Camp (2007) [4];

Kaveh and Khayatazad (2012) [38]; Kaveh and Ghazaan (2014) [6];
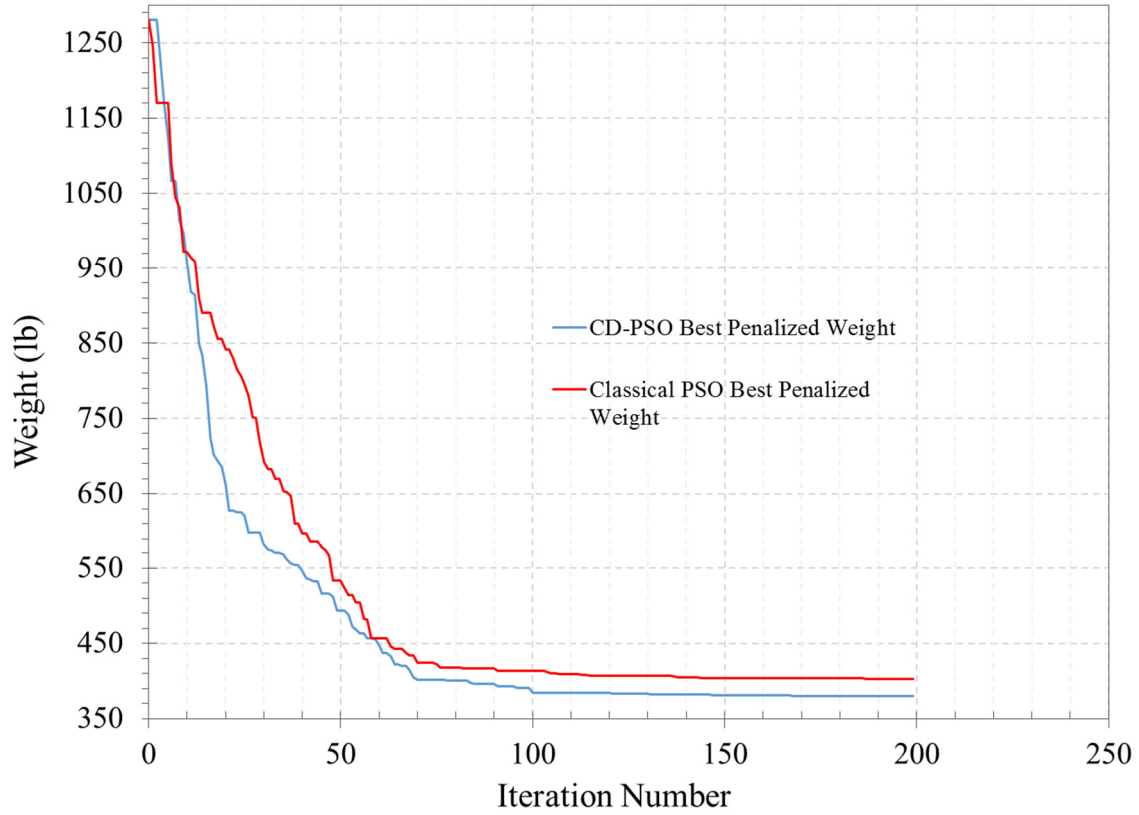
Figure 4.9. Convergence history of CD-PSO and classical PSO best for the 72-member spatial truss.

4.6   ASSESSMENT OF HYBRID AND ORIGINAL CD-PSO

The majority of optimization techniques are tested on benchmark truss structures. Therefore, they succeed to reach promising results in terms of algorithms stability, convergence rate, and solution quality. However, these techniques may not be able to reach the same level of results robustness when tested on large scale structures. In these structures, the increased number of design parameters, the diverse levels of significance of these parameters on the design objective, and the numerical noise caused by the poor parameters would play an instrumental role in this shortcoming of available techniques.

In general, to overcome these setbacks, previous research studies used a multi-step design optimization procedure for complex structural models, where the response surface methodology (RSM) is applied as a priory of an optimization operation. The RSM builds Meta-models that are used as surrogates of the actual computational expensive structural simulation model when a large number of evaluations are needed. The method is conducted in consecutive steps and can deal only

with continuous design optimization of complex structures. In the current research, CD-PSO and hybridized CD-PSO with RSM are studied and applied on a large-scale structure, namely the deployable bridge described in Chapter 3, in order to perform the optimization operation in a single step, reduce the computational cost, and propose the method as a candidate for discrete optimization of complex structural models. The RSM technique and its integration with CD-PSO technique are clarified in the coming subsection.

The numerical results of testing CD-PSO and hybrid CD-PSO are compared with classical PSO and GA results that are obtained in chapter 3 while considering all the design parameters. Moreover, they are compared with classical PSO-S results ("S" stands for significant design parameters), where only design parameters with sufficient influence on minimizing the weight of the bridge structure are considered. These design parameters are determined through sensitivity analysis of random trials. This will confirm the effectiveness of CD-PSO and the hybrid CD-PSO in probing wide feasible areas in hyperspace to speed up the convergence rate and achieve promising results.

4.6.1   RESPONSE SURFACE METHODOLOGY (RSM)

The response surface methodology (RSM) is an integration of mathematical and statistical techniques that is generally used as a prior procedure to the planning of a complex optimization operation. The method proposed by Box and Wilson (1951) can be applied when the analysis of physical or numerical design problems involves a considerable number of design parameters. The main function of RSM is to distinguish the influence of these design parameters on the design objective. This would help the designer to eliminate the parameters with minor influence in order to simplify the optimization process.

In general, the RSM integrates both the Design of Experiments (DOE) and the Response Surface Analysis (RSA) techniques. First, the DOE is conducted to create multiple design trials that randomly experiment the design parameters for a further classification. Out of this sampling pool of design trials, a set of feasible designs is built through FE analysis for every design point in the sampling pool. Random, Quasi-Random, Factorial, Placket-Burman designs, Latin hypercube sampling and orthogonal arrays (Taguchi or Fisher) are examples of DOE sampling techniques (Myers *et al.*, 2009; Giunta *et al.*, 2003; Santner *et al.*, 2013; and Koehler and Owen, 1996). The second step conducts a Response Surface Analysis (RSA) to interpolate the available data in order

to predict locally or globally the influence level of design parameters on the objective function as well as to recognize the correlation between design parameters and their combined impact on the design objective. The RSA constructs a response mathematical Metamodel that uses the DOE results. On the basis of response surface analysis, the metamodeling technique gives an approximate equation that relates the design parameters x_i (inputs) to the design objective F (output) for a particular structural model:

$$F = f(x_1, x_2, ..., x_n) + \varepsilon \tag{4.10}$$

where f is the approximate response function, ε is the statistical error term having a normal distribution with a mean of zero, n is the number of design parameters. Several Meta-model formation methods are available for constructing the statistical or mathematical models such as polynomial regression methods, artificial neural networks, multivariate adaptive regression splines and high-dimensional model representation (Koziel and Yang, 2011). Using a particular metamodeling technique is very critical to check precisely its goodness of fit and prediction capability. Based on the problem complexity and nature, it was found that most of the metamodeling techniques work efficiently for Linear Regression Models (LRM) (Mukhopadhyay et al., 2015). Therefore, a General Linear Regression Model (GLRM) is chosen in this study in its First-order format. Hence, the generated mathematical model becomes easier to be optimized using gradient-based algorithms in order to reduce the computational cost. Figure 4.10 illustrates a schematic drawing for the procedure.

This model would clarify the relation between the design parameters $\{x_1^i, x_2^i, ... \ x_n^i\}$ and feasible design objective F. The main advantages of RSM are that: the procedure does not need design sensitivity, and it is not sensitive to numerical noise (Poloni et al., 2002).
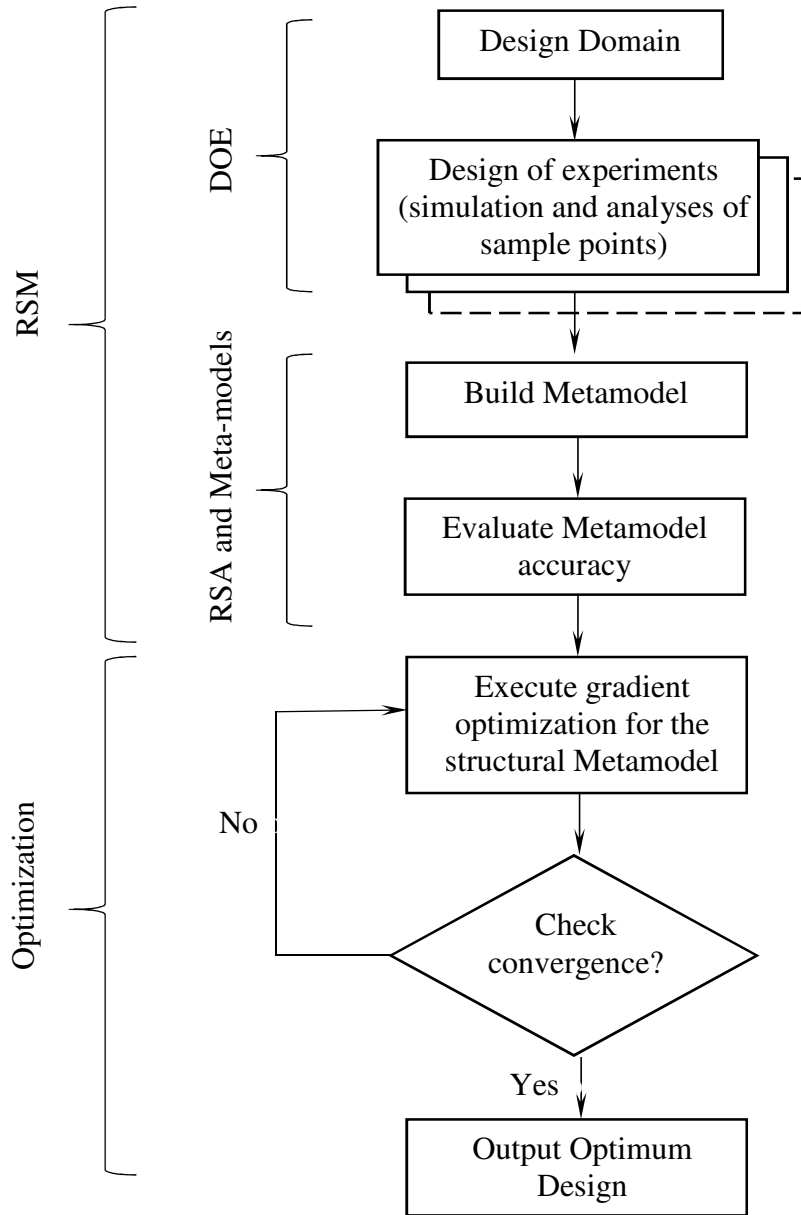
Figure 4.10. Schematic illustration of using DOE and RSA for multi-step design optimization

4.6.2 HYBRID CD-PSO

In this study, RSM is integrated with CD-PSO as a statistical guide search tool within the design optimization procedures and not as a priory. The RSM code was written in MATLAB in order to integrate easily with CD-PSO code, the hybrid algorithm is then integrated with FE package ANSYS to analyze the potential designs of the bridge structure. Consequently, build a linear regression model (LRM) that represents the correlation between design parameters and their

influence on the design objective. The strategy of RSM implementation within the CD-PSO can be described as follows:

Step 1. Generate random population using the following equation:

$$x_j^{(i,K+1)} = x_j^L + r_j^{(i,K)}\left(x_j^U - x_j^L\right) \qquad (4.11)$$

where $r_j^{(i,K)}$ is a random value between 0 and 1, x_j^U and x_j^L are user–defined upper and lower bounds of the design parameter x_j . In this step, all the design parameters are considered for structural design optimization.

Step 2. Disburse the swarm cloud in hyperspace to probe the good solutions and control the swarm attraction and repulsion using the equations (4.2), (4.5), and (4.6). A matrix of only feasible design points for the repelled particles is created. These data will be considered as the random samples forming DOE in hyperspace. In this case, the particle's encoded parameters are of random values and not driven by the optimization formulas.

Step 3. Conduct a sensitivity analysis for the feasible design points using RSM, namely, DOE and RSA, when any of the following conditions is satisfied:

    a) If the best fitness is not improved,

    b) If no repulsion phases occur,

    c) Or if the solution diverges from the global best within a specific number of trials (chosen as $1/6^{th}$ of the travel history),

Step 4. Construct a First-order linear regression models (Kutner *et al.*, 2004):

$$y_i = b_\circ + \sum_{j=1}^{N_{dv}} b_j \cdot x_j^i + \varepsilon_i \qquad (4.12)$$

where ε is the error observed in the feasible response y_i for the ith particle data, and b is the regression coefficients of the jth dimension in hyperspace. The value of b represents the change in the design objective resulting from one unit change in the design parameter after fixing all the other parameters, whereas b is expressed in the same unit of the design parameter. In order to integrate Equation 4.12 with CD-PSO in MATLAB, the equation has to be defined in a matrix form as follows:

$$\underset{N_{sample} \times 1}{\mathbf{Y}} = \underset{N_{sample} \times (N_{dv}+1)}{\mathbf{X}} \cdot \underset{(N_{dv}+1) \times 1}{b} + \underset{N_{sample} \times 1}{\varepsilon} \qquad (4.13)$$

Where:

$$Y_{N_{sample} \times 1} = \begin{bmatrix} y_1 \\ y_2 \\ \vdots \\ y_{N_{sample}} \end{bmatrix}, \quad X_{N_{sample} \times (N_{dv}+1)} = \begin{bmatrix} 1 & x_{11} & x_{12} & \cdots & x_{1N_{dv}} \\ 1 & x_{21} & x_{22} & \cdots & x_{2N_{dv}} \\ \vdots & \vdots & \vdots & & \vdots \\ 1 & x_{N_{sample}\,1} & x_{N_{sample}\,2} & \cdots & x_{N_{sample}\,N_{dv}} \end{bmatrix},$$

$$b_{(N_{dv}+1)\times 1} = \begin{bmatrix} b_0 \\ b_1 \\ \vdots \\ b_{N_{dv}} \end{bmatrix}, \text{ and } \varepsilon_{N_{sample}\times 1} = \begin{bmatrix} \varepsilon_1 \\ \varepsilon_2 \\ \vdots \\ \varepsilon_{N_{sample}} \end{bmatrix}$$

where Y is a vector of the design objectives' values, X is a matrix of a column of 1 and columns of N_{dv} parameters, in which it represents the design matrix of a set of value combinations of encoded design parameters, N_{sample} is the number of feasible design points generated during repulsion, b is a vector of regression coefficients, and ε is a vector of the error observed.

Step 5. Estimate the regression coefficients, fitted values, and residuals of errors of the model

a) The matrix b can be calculated as follows:

$$b_{(N_{dv}+1)\times 1} = (X'X)^{-1} \cdot X'Y \tag{4.14}$$

where $\acute{X}$ is the transpose of matrix X.

b) Calculate the hat matrix H using:

$$H_{N_{sample} \times N_{sample}} = X (X'X)^{-1} \cdot X' \tag{4.15}$$

c) Calculate the vector of fitted values $\hat{Y}$ and the vector of residual terms e using:

$$\hat{Y}_{N_{sample}\times 1} = Xb = HY \tag{4.16}$$

$$e_{(N_{dv}+1)\times 1} = Y - \hat{Y} = \left(1 - H\right)Y \tag{4.17}$$

d) Calculate matrix of standardized regression coefficients β using:

$$\beta_i = b_i \frac{std\left(x_{ij}\right)}{std\left(y_i\right)} \tag{4.18}$$

where $std(x_{ij})$ is the standard deviation of the design parameter x of the ith particle in the jth dimension in hyperspace, and $std(y_i)$ is the design parameter's associated design response of the ith particle. β coefficients help to distinguish the importance of relatives changes between design parameters and their effect on the design objective in terms of standard deviation neglecting their units difference (if any).

<u>Step 6.</u> Calculate the sums of squares for the analysis of variance (ANOVA) in matrix terms, as follows:

$$SSE = é.e = Ý.(1-H).Y \tag{4.19}$$

$$SSR = Ý.\left(H - \left(\frac{1}{N_{sample}}\right).J\right).Y \tag{4.20}$$

$$SSTO = ÝY - \left(\frac{1}{N_{sample}}\right).ÝJY \tag{4.21}$$

where SSE is the sum of squares of errors, SSR is the sum of squares of residuals, $SSTO$ is the total sum of squares of residuals SSR and errors SSE, I is an identity matrix, and J is a N_{sample} x N_{sample} unity matrix.

<u>Step 7.</u> Check the strength of association between the design parameters and the design response using coefficient of multiple of determination R^2 and R^2_{adj}:

$$R^2 = \frac{SSR}{SSTO} \tag{4.22}$$

$$R^2_{adj} = 1 - \left(\frac{N_{sample}-1}{N_{sample}-N_{dv}-1}\right).\left(\frac{SSR}{SSTO}\right) \tag{4.23}$$

where R^2 is the amount of variation around the mean explained by the model, R^2_{adj} is the amount of variation around the mean explained by the model and adjusted to the number of design parameters in the model, such that R^2_{adj} value decreases when the number of design parameters with insignificant influence on the design response increases. R^2 and R^2_{adj} should have a value between 0 and 1. A close value of R^2 and R^2_{adj} to one attributed to a good fit of the model to the design points in hyperspace.

<u>Step 8.</u> Conduct a significance testing to predict the probability of how each design parameter is represented by the model at 95% confidence interval. The mathematical equations for the significant testing in a matrix form and the assessment conditions can be found at (Kutner *et al.*,

2004).

<u>Step 9.</u> Normalize the unstandardized coefficients of all the design parameters with respect to the design parameter that has the highest influence on the design objective, given the design parameters with the highest influence an assumed value of 100%.

<u>Step 10.</u> Classify the design parameters according to their associated normalized coefficients according to Table 4.8. The values in Table 4.8 are considered as a measure of the design parameters' influence on the design objective.

Table 4.8. Influence classification of the effect of design parameters on the design objective

Influence classification	ω (%)
Very significant	$10 \leq \omega \leq 100$
Significant	$5 \leq \omega < 10$
Minor	$2 \leq \omega < 5$
Negligible	$0 \leq \omega < 2$

<u>Step 11.</u> Based on the design parameter's classification in step 10. A decision is made, such that all design parameters with poor influence or with a model relation less than 95% confidence will be mutated and fixed to their corresponding values in the global best. The remaining parameters will be updated using equations (4.1) and (4.2) to allow the swarm particles to find better positions in hyperspace to the end of travel history.

<u>Step 12.</u> Before continuing the search, disperse randomly the swarm particles to allow a wide scan for the design space under the effect of only the significant design parameters. Figure 4.11 shows a flowchart drawing of the hybrid CD-PSO algorithm with RSM. A pseudocode for the CD-PSO algorithm is created to clarify Hybrid CD-PSO algorithm and it is illustrated in appendix B-1.
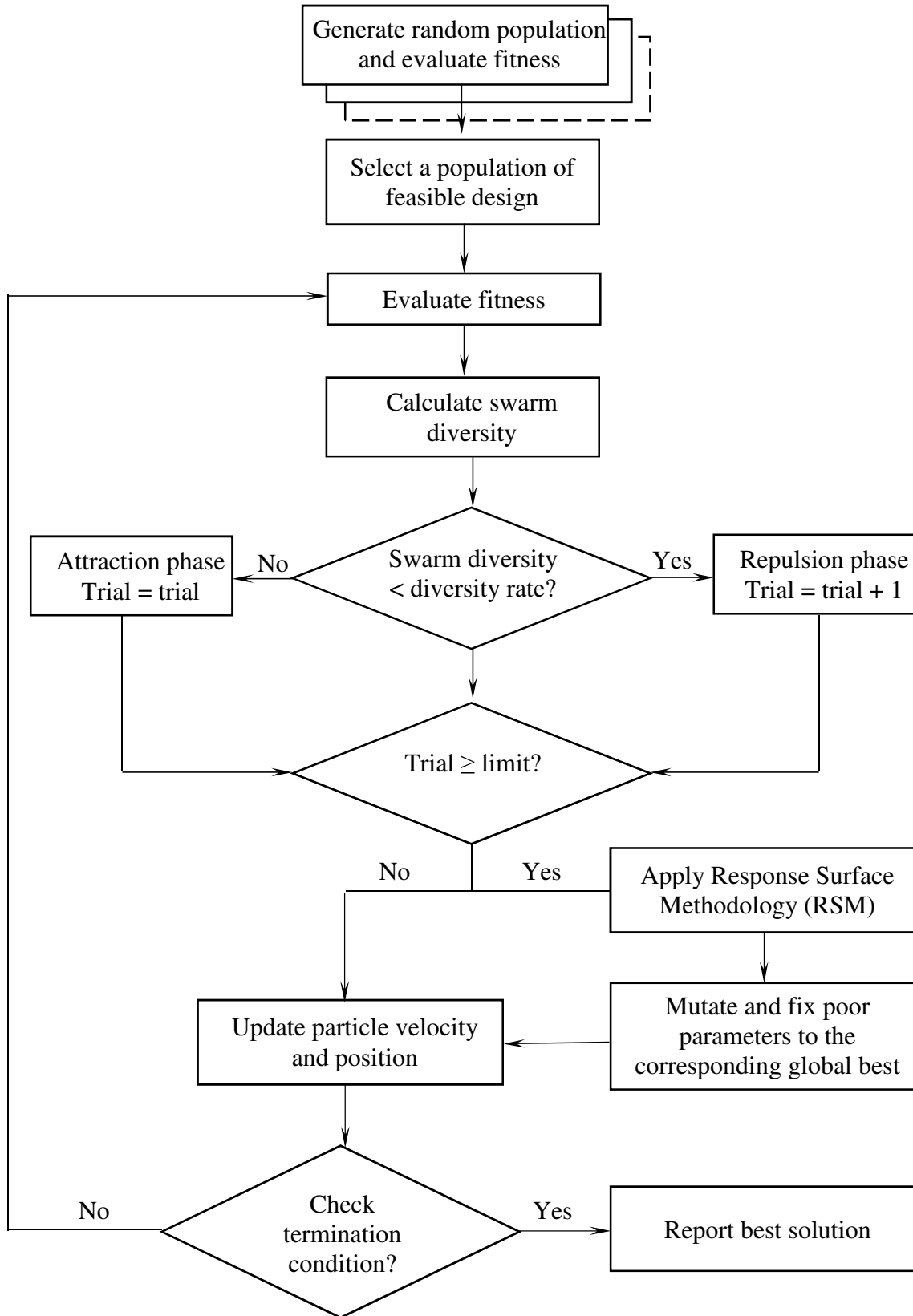
Figure 4.11. Flowchart illustration of hybrid CD-PSO with RSM

4.6.3 NUMERICAL RESULTS

The application of GA resulted in a bridge weight of 9.245 tons (20381 lb) with an enhancement of 29.4% from the base conventional design 13.099 tons (28878 lb). On the other hand, the application of PSO-A while considering the whole set of design parameters resulted in 8.929 tons (19685 lb), hence, an improvement of 31.8% from the base conventional design weight is achieved. Design parameters' values obtained by both algorithms GA and PSO-A are listed in Table 4.9.

In order to apply PSO-S ("S" stands for significant design parameters) for minimizing the weight of the bridge structure. The previously obtained 31 feasible designs in section 3.2.3.2 are used to create a pool of design points for further sensitivity analysis of the design parameters. The aforementioned steps from 4 to 10 are applied to estimate the influence of the design parameters on the design objective through constructing a linear regression model. Table 4.10 shows the unstandardized, standardized, and the probability value of how each design parameter is represented by the model. The regression model developed showed a strength of association R^2_{adj} of 0.9998, which indicates an excellent fit of the model to the design points in hyperspace. The design parameters' coefficients are normalized to a percent value of the highest unstandardized coefficient and denoted as ω in Table 4.10. Amongst the whole design parameters, it was found that eighteen design parameters have sufficient influence more than 2% on the design objective based on the classification listed in Table 4.8. Moreover, significant design parameters with a probability value not less than 95% confidence interval are only considered for velocity updates when applying PSO-S. Finally, the application of PSO-S resulted in a bridge weight of 10.306 tons (22720 lb) and a minimized weight/capacity ratio of only 21.326 %. On the other hand, CD-PSO achieved a decrease in weight/capacity ratio of 33.2 percent based on a deployable bridge weight of 8.773 tons (19342 lb), while Hybrid CD-PSO with RSM achieved the best reduction in weight/capacity ratio by 34.3 percent with a total bridge weight of 8.606 tons (18972 lb). Table 4.9 shows the parameters' values of the best design achieved by CD-PSO and hybrid CD-PSO with RSM, while Table 4.11 lists the LRM coefficients and percent of parameters significance achieved by Hybrid CD-PSO with RSM. Finally, Figure 4.12 shows the convergence history of the four applied techniques.

Table 4.9 Optimization results of CD-PSO and other applied algorithms for the deployable bridge model

NO	Design parameters (m)	Lower Bound	Upper Bound	Initial Design	GA	PSO-A	PSO-S	CD-PSO	CD-PSO + RSM
1	H_1	0.7	1.0	0.9	0.707	0.77283	0.89221	0.76235	0.75981
2	H_2	0.1	0.15	0.15	0.113	0.14273	0.15	0.1461	0.10038
3	H_3	0.05	0.15	0.05	0.08	0.06333	0.15	0.07743	0.07368
4	H_4	0.05	0.15	0.15	0.12	0.10109	0.15	0.08149	0.06402
5	H_5	0.2	0.4	0.2	0.234	0.2	0.2	0.23324	0.27107
6	H_6	1.0	2.0	1.5	1.89	1.6847	1.5	1.73718	2.000
7	H_7	0.2	0.4	0.2	0.244	0.28742	0.2	0.27827	0.38648
8	T_0	0.008	0.012	0.01	0.01	0.00984	0.00886	0.00897	0.00826
9	T_1	0.008	0.012	0.012	0.01	0.008	0.00943	0.008	0.008
10	T_2	0.012	0.03	0.03	0.017	0.012	0.02111	0.012	0.01207
11	T_3	0.02	0.04	0.03	0.021	0.02212	0.02169	0.02149	0.02065
12	T_4	0.008	0.026	0.008	0.015	0.0092	0.00801	0.01149	0.01601
13	T_5	0.008	0.012	0.01	0.008	0.00864	0.012	0.0088	0.00903
14	T_6	0.004	0.01	0.01	0.006	0.00495	0.004	0.00504	0.00503
15	T_7	0.008	0.012	0.008	0.008	0.00908	0.008	0.008	0.00804
16	T_8	0.002	0.008	0.008	0.005	0.00374	0.00384	0.0032	0.00204
17	T_9	0.006	0.01	0.008	0.009	0.00827	0.00732	0.00742	0.00698
18	T_{10}	0.006	0.01	0.008	0.008	0.00715	0.006	0.00708	0.00661
19	T_{11}	0.006	0.01	0.008	0.008	0.00833	0.00697	0.00928	0.006
20	T_{12}	0.01	0.03	0.024	0.019	0.01776	0.03	0.01886	0.01636
21	T_{13}	0.016	0.04	0.04	0.025	0.03476	0.04	0.03521	0.0285
22	T_{14}	0.006	0.01	0.01	0.09	0.00757	0.00878	0.006	0.00683
23	T_{15}	0.008	0.012	0.01	0.01	0.01136	0.0099	0.00953	0.01109
24	W_1	0.3	0.4	0.3797	0.385	0.3595	0.3797	0.37802	0.37336
25	W_2	0.2	0.36	0.2	0.2	0.2	0.2	0.20594	0.200
26	R_1	0.05	0.07	0.05	0.056	0.05824	0.05	0.05	0.05488
27	R_2	0.015	0.035	0.015	0.015	0.015	0.015	0.015	0.015
28	R_3	0.05	0.07	0.05	0.06	0.05718	0.05	0.06357	0.05596
29	R_4	0.05	0.07	0.05	0.065	0.06158	0.05	0.0583	0.06105
30	R_5	0.05	0.1	0.1	0.08	0.06372	0.1	0.07867	0.08542
	Volume, m³ (ft³)			4.71214 (166.407)	3.325 (117.421)	3.2122 (113.438)	3.70722 (130.919)	3.15595 (111.4515)	3.09583 (109.3283)
	Best weight, tons, (lb)			13.0997 (28878)	9.245 (20381)	8.929916 (19685)	10.30607 (22720)	8.773541 (19342)	8.606407 (18972)
	Normalized Weight/capacity ratio (W/C)			1.0	0.70574	0.68168	0.78674	0.66795	0.65699
	Computational time (hrs)			--	86	60	60	60	60

Note: Design parameters 'values are in meters; H: Height; T: Thickness; W: width and R: Outer radius

Table 4.10 The feasible design samples' linear regression model and design parameters weight

NO	Parameter symbols	Parameters Description	Unstandardized Coefficients			Standardized Coefficients β	t-test	Sig.
			b	Std. Error	ω %			
Bridge Model								
	Intercept		-72.966	1.330	--	0	-54.826	1.68E-96
1	H_1	Tread way main vertical plates	40.925	0.468	2.533	0.212	87.401	4.97E-124
2	H_2	Top and bottom ends of v. plates	30.056	2.967	1.860	0.028	10.128	1.99E-18
3	H_3	Deck longitudinal stiffeners	29.002	1.401	1.795	0.0276	20.688	2.05E-44
4	H_5	Main transverse stiffeners	11.854	0.505	0.733	0.0476	23.454	2.41E-50
5	H_7	Intermediate transverse stiff.	2.846	0.568	0.176	0.0067	5.005	1.64E-06
6	W_2	Lower tension flanges	72.508	0.859	4.488	0.1779	84.357	6.48E-122
7	T_1	Tread way vertical plates	884.959	25.313	54.784	0.0520	34.960	4.82E-71
8	T_2	Thickened ends of v. plates	741.630	5.605	45.911	0.2659	132.31	6.19E-149
9	T_3	Lower tension flanges	1165.80	7.687	72.170	0.2286	151.64	3.61E-157
10	T_5	Main transverse stiffeners	510.226	32.705	31.586	0.0227	15.600	2.00E-32
11	T_6	Deck longitudinal stiffeners	1080.56	22.758	66.893	0.0633	47.478	3.37E-88
12	T_7	Deck surface plate	1615.34	30.435	100	0.0696	53.074	1.28E-94
13	T_8	Intermediate stiffeners	230.858	16.890	14.291	0.0301	13.667	1.50E-27
14	H_4	Ramp cover long. stiffeners	12.447	1.186	0.770	0.0135	10.491	2.33E-19
15	T_0	Ramp cover long. stiffeners	151.902	35.818	9.403	0.0112	4.240	4.02E-05
16	T_4	Ramp cover plate	285.911	6.481	17.699	0.0804	44.109	5.31E-84
17	T_{12}	Deck at connection to ramps	330.645	6.141	20.469	0.0687	53.837	1.91E-95
18	T_{13}	Deck ramped sides	-3.287	4.898	-0.203	-0.0012	-0.671	0.5032
19	T_{15}	Triangular stiff. upper plates	328.874	31.023	20.359	0.0146	10.600	1.22E-19
20	H_6	U-frame vertical beams	1.862	0.121	0.115	0.0379	15.371	7.41E-32
21	W_1	U-frame beam	-0.891	1.147	-0.055	-0.0021	-0.777	0.4381
22	T_9	Pistons equivalent alum. C.H.S.	159.807	27.811	9.893	0.0080	5.746	5.47E-08
23	T_{10}	U-frame C.H.S. vertical beams	175.639	25.567	10.873	0.0136	6.869	1.94E-10
24	T_{11}	Compression posts C.H.S.	168.840	27.981	10.452	0.0081	6.034	1.36E-08
25	T_{14}	U-frame C.H.S. horizontal beam	107.429	27.709	6.650	0.0058	3.876	0.0001
26	R_1	Pistons equivalent alum. C.H.S.	14.837	6.901	0.918	0.0038	2.149	0.033278
27	R_2	Aluminum wires radius	824.569	6.895	51.045	0.2884	119.58	7.73E-143
28	R_3	U-frame C.H.S. vertical beams	30.847	5.451	1.909	0.0104	5.658	8.32E-08
29	R_4	Compression posts C.H.S.	22.137	6.155	1.370	0.0058	3.596	0.000446
30	R_5	U-frame C.H.S. horizontal beam	4.1831	2.429	0.258	0.0040	1.721	0.0872

Rows 1–13 are labeled **Group 1**; rows 14–21 are labeled **Group 2**; rows 22–30 are labeled **Group 3**.

Note: H: Height; T: Thickness; W: width and R: Outer radius

Table 4.11 Hybrid CD-PSO linear regression model coefficients and design parameters weight

NO	Parameter symbols	Parameters Description	Unstandardized Coefficients			Standardized Coefficients β	t-test	Sig.
			b	Std. Error	ω %			
Bridge Model								
	Intercept		-69.642	1.226	--	0	-56.823	1.14E-93
1	H_1	Tread way main vertical plates	38.401	0.288	2.415	0.2422	133.367	6.17E-141
2	H_2	Top and bottom ends of v. plates	25.283	2.005	1.590	0.0311	12.612	2.59E-24
3	H_3	Deck longitudinal stiffeners	25.789	0.719	1.622	0.0721	35.859	2.85E-69
4	H_5	Main transverse stiffeners	11.271	0.380	0.709	0.0642	29.641	1.09E-59
5	H_7	Intermediate transverse stiff.	3.512	0.493	0.221	0.0136	7.119	6.59E-11
6	W_2	Lower tension flanges	66.391	0.733	4.176	0.2607	90.581	2.48E-119
7	T_1	Tread way vertical plates	1042.731	22.422	65.582	0.1176	46.505	6.92E-83
8	T_2	Thickened ends of v. plates	691.554	4.681	43.495	0.4293	147.744	1.12E-146
9	T_3	Lower tension flanges	1162.452	7.477	73.111	0.2707	155.473	1.53E-149
10	T_5	Main transverse stiffeners	465.322	19.583	29.266	0.0557	23.761	3.82E-49
11	T_6	Deck longitudinal stiffeners	1158.402	14.155	72.857	0.1442	81.836	1.07E-113
12	T_7	Deck surface plate	1589.972	34.821	100.000	0.0951	45.662	6.52E-82
13	T_8	Intermediate stiffeners	280.257	16.064	17.627	0.0310	17.446	7.35E-36
14	H_4	Ramp cover long. stiffeners	11.236	0.771	0.707	0.0304	14.565	4.26E-29
15	T_0	Ramp cover long. stiffeners	106.215	20.788	6.680	0.0108	5.109	1.13E-06
16	T_4	Ramp cover plate	310.887	4.884	19.553	0.1714	63.653	7.40E-100
17	T_{12}	Deck at connection to ramps	315.765	4.780	19.860	0.1209	66.066	6.78E-102
18	T_{13}	Deck ramped sides	15.827	3.627	0.995	0.0105	4.364	2.58E-05
19	T_{15}	Triangular stiff. upper plates	375.707	21.726	23.630	0.0359	17.293	1.64E-35
20	H_6	U-frame vertical beams	1.647	0.086	0.104	0.0359	19.087	1.61E-39
21	W_1	U-frame beam	1.181	0.822	0.074	0.0027	1.436	0.1532921
22	T_9	Pistons equivalent alum. C.H.S.	173.855	23.214	10.934	0.0199	7.489	9.37E-12
23	T_{10}	U-frame C.H.S. vertical beams	156.977	16.083	9.873	0.0176	9.760	3.22E-17
24	T_{11}	Compression posts C.H.S.	136.859	23.145	8.608	0.0137	5.913	2.79E-08
25	T_{14}	U-frame C.H.S. horizontal beam	45.458	20.516	2.859	0.0050	2.216	0.02845
26	R_1	Pistons equivalent alum. C.H.S.	32.353	5.327	2.035	0.0139	6.073	1.29E-08
27	R_2	Aluminum wires radius	771.500	4.549	48.523	0.3474	169.612	1.97E-154
28	R_3	U-frame C.H.S. vertical	25.078	4.316	1.577	0.0121	5.811	4.53E-08
29	R_4	Compression posts C.H.S.	28.128	4.379	1.769	0.0123	6.423	2.31E-09
30	R_5	U-frame C.H.S. horizontal beam	3.641	1.691	0.229	0.0044	2.154	0.03311

Group 1: rows 1–13
Group 2: rows 14–21
Group 3: rows 22–30

Note: H: Height; T: Thickness; W: width and R: Outer radius
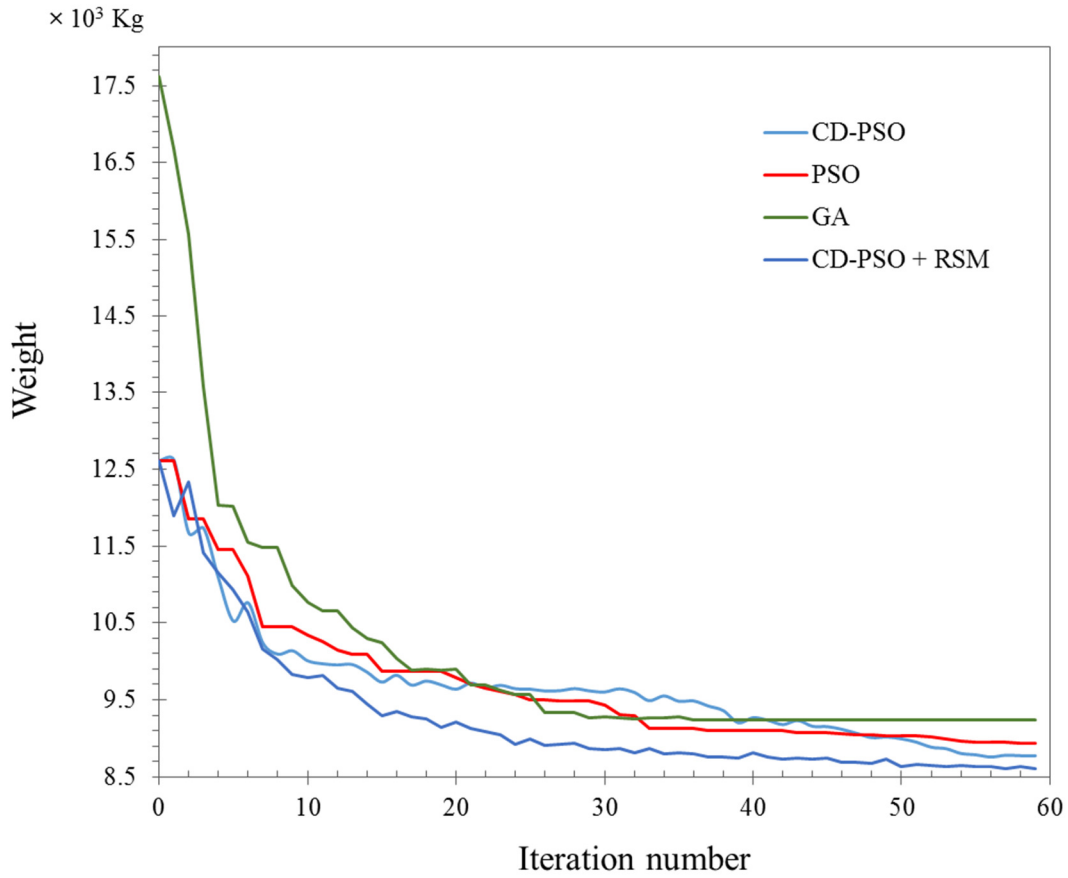
Figure 4.12. Convergence history for the 24 m (78.74 ft) deployable bridge structure.

4.7   CONCLUSIONS

4.7.1   CD-PSO APPLICATION ON BENCHMARK STRUCTURES

In this study, a Controlled Diversity Particle Swarm Optimizer (CD-PSO) for the design optimization of structures is developed. The algorithm simulates the flock attraction and repulsion through regulating the swarm diversity using a non-linear decreasing convex repulsion surface. Earlier studies simulated the phenomenon, namely: ARPSO, ATRE-PSO, and DGPSO, as well as a hybrid Levy PSO algorithm, are reformulated to suit structural optimization. A test on 10-member benchmark structure is conducted for CD-PSO and the aforementioned reformulated algorithms to assess the proposed algorithm strategy. The comparison results proved CD-PSO preciseness with a standard deviation difference of 84.00% to LFPSO that is ranked second in stability performance. Furthermore, the CD-PSO achieved the most robust solution despite a slight delay in convergence rate due to high hyperspace exploration.

73

Three benchmark structures (10, 25, and 72-member trusses) are utilized to evaluate the effectiveness of the algorithm compared to other meta-heuristic results in the literature. A robust design is reached for the 10-member planar truss compared to others that were re-evaluated in literature with no constraint violation to the nearest fifth decimal. The comparative analysis conducted for the test results of the 25, and 72-member spatial trusses showed that CD-PSO possesses a superior algorithm stability with standard deviations of 0.2533 lb and 0.2832 lb which are lower than the best standard deviation result in past studies by 19.58% and 65.03%, respectively. Moreover, the competitive and better solutions achieved by CD-PSO along with the low computational cost promote the algorithm to be an effective choice for structural design optimization using a meta-heuristic algorithm that is stochastic in nature.

4.7.2 HYBRID AND ORIGINAL CD-PSO APPLICATION ON DEPLOYABLE BRIDGE STRUCTURE

In a second phase, a more challenging performance assessment of the proposed algorithm CD-PSO is conducted for complex structural models where large design parameters are considered. Moreover, the algorithm is hybridized with Response Surface Methodology RSM to redirect the swarm search in hyperspace under the influence of only efficient design parameters when specific criteria are met, whereas the poor parameters are mutated to their global best values. The performance of both techniques (i.e. CD-PSO and hybrid CD-PSO) is examined for the minimum weight design of a deployable bridge structure of 24m span. Both algorithms performed better in term of solution quality when compared to genuine GA, PSO-A while involving all design parameters, and PSO-S where only effective parameters are taken into account. Hybrid CD-PSO achieved the minimum normalized weight/capacity ratio of 65.69 percent and the rapid convergence rate, whereas CD-PSO ranked second in solution quality and explored a higher volume of hyperspace before it has converged. A 66.795 percent of normalized weight/capacity ratio is achieved by CD-PSO. It is worth mentioning that all the optimization computations and the deployable bridge simulation for the second phase were made on the supercomputer "Briarée", managed by Calcul Québec and Compute Canada. The operation of this supercomputer is funded by the Canada Foundation for Innovation (CFI), the ministère de l'Économie, de la science et de l'innovation du Québec (MESI) and the Fonds de recherche du Québec - Nature et technologies (FRQ-NT).

4.8   SUMMARY

In this chapter, the controlled diversity particle swarm CD-PSO and its hybrid version with RSM are proposed. CD-PSO showed a satisfactory performance for the application of large-scale structural design optimization. However, hybrid CD-PSO is more recommended for complex structural optimization where a high varying influence of design parameters on the design objective exists. From the analysis of the results, it can be shown that deployable bridge decks contribute to more than 20% of the total bridge weight. Moreover, the design of these bridge decks as the main bearing element of compression in deployable bridge structures is very critical, to which it is the main focus of this study. Therefore, CD-PSO is chosen for maximizing the strength and stiffness of the proposed bridge deck sandwich cores, whereas hybrid CD-PSO is kept for future size and shape optimization of a scaled deployable bridge treadway. The following chapter will present two different sandwich cores designed for the bridge deck, as well as demonstrate the experimental program for testing the cores along with its numerical validation.

5

Developing and Testing of New Composite Decks

5.1 INTRODUCTION

In the recent decades, many research studies investigated replacing the deteriorated metallic or concrete deck bridges with alternatives of composite FRP decks, such as Lopez *et al.* (1997), Brown and Zureick (2001), Davalos *et al.* (2001), Zetterberg *et al.* (2001), Williams *et al.* (2003), Link (2003), Keller and Gürtler (2005), Zhou *et al.* (2005), Liu (2007), Osei-Antwi *et al.* (2013), Keller *et al.* (2014), Zhu and Lopez (2014), and Tuwair *et al.* (2015). On the other hand, Kosmatka *et al.* (2000) and Robinson and Kosmatka (2008) investigated alternatives of high performance CFRP deck systems that are characterized by higher strength to weight ratio for the application in the Composite Assault Bridge (CAB) and the Composite Joint Assault Bridge (CJAB) deployable systems, respectively. As a result of the increased demand for disaster aftermath bridge rapid mobility, the current research investigates the performance of two alternatives of sandwich CFRP cores which provides increased capacity to weight ratio compared to the core system of the CAB bridge. Moreover, the CFRP cores' design configuration is compared with two reproduced webbed CFRP cores using the same design configuration and manufacturing procedure that are recently developed by Robinson and Kosmatka (2008).

In this chapter, a review of different manufacturing techniques is presented followed by a comparison between all the processing methods advantages and disadvantages. The design of the proposed sandwich cores as well as a detailed description of each core are demonstrated; the CAB bridge deck core and the two CFRP webbed cores developed by Robinson and Kosmatka (2008) are briefly described. Followed by a description of the experimental test setups and the instrumentations developed to evaluate the cores' compression and shear strength; the experimental results are then clarified. A finite element progressive failure analysis for the proposed sandwich cores is performed. Finally, a numerical validation of the experimental results is summarized.

5.2   COMPOSITE PROCESSING METHODS

This section reviews the composite processing methods used for building the structural components, in addition to the techniques that are used to impregnate the resin successfully inside a sandwich core construction.

The methods presented are, 1) wet layup, 2) Resin Transfer Molding (RTM), 3) Vacuum Assisted Resin Transfer Molding (VARTM), 4) Film resin infusion, 5) Out of Autoclave processing, 6) Filament winding, and 7) Pultrusion processing. A description of each process including advantages disadvantages, and schematic illustration is presented and finally a comparison between all processing methods is summarized.

5.2.1   WET LAYUP

The wet layup method or the hand laminating process is the basic technique for the manufacture of low-cost composite components. The wet layup is a primitive method used for many years in the boat building industry. In addition, it is still widely used for the production of prototypes. The method consists of laying the dry reinforcing fibers and fabrics on a single sided smooth and rigid mold. A catalyzed resin is applied to the preform using hand tools such as a roller or a brush, hence force the resin to infuse into the fibers to remove any trapped air. The process is repeated for each placed reinforcing fabric until the required thickness is built up.

A major advantage of this method is the low-cost of its simple application procedure, tooling and materials. On the contrary, other methods require special tools to seal and air tight the mold and fabrics. In addition, the method is suitable for use with many fabric materials and resins (i.e. GFRP, CFRP, epoxy resin, polyester resin …etc.). The main disadvantages of the wet layup method are the poor quality control which highly dependent on the skill of the applicator, the exposure to potentially harmful emissions and styrene evaporation into the atmosphere, and the difficulty of controlling the part thickness, hence the fiber volume fraction and surface quality. In general, a skilled operator can achieve a fiber volume fraction between 40% and 45% (complete fiber wetting). In order to reach thick laminates, many stops have to be taken after laying a certain number of layers to allow the exothermic heat to dissipate before placing additional layers. Due to the limited quality of the manufactured component, the laminate is used in very low stress applications and in the structural

locations where dimensional accuracy is not critical. A schematic illustration of the process is presented in Figure (5.1).
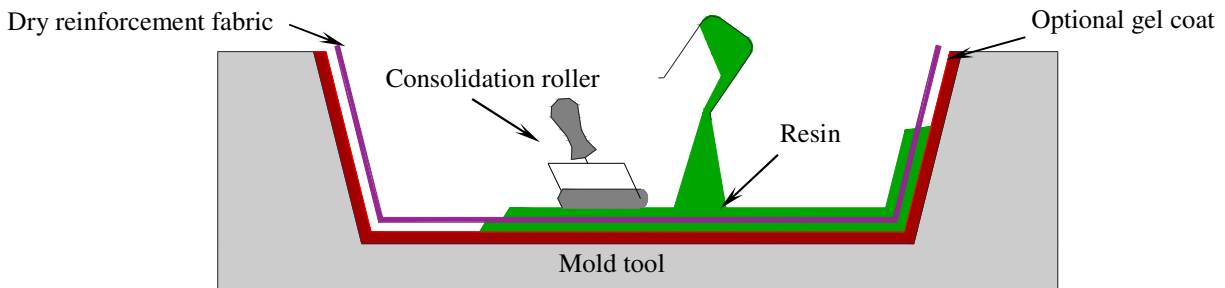
Figure 5.1. Schematic of the Wet Layup Method

5.2.2   RESIN TRANSFER MOLDING (RTM)

The Resin Transfer Molding (RTM) method is used for producing mass production components of small to medium size parts. The process starts by placing the reinforcing fibers in between two stiff mold halves having the shape of the preform. The two halves of the molds are clamped from their ends in order to hold them together and to apply the required pressure on the preform. Then, the resin is infused into the preform and between the molds using injection (positive pressure) with the aid of a small vent to allow the flow of any trapped air and replace it with the infused resin, or using suction (negative pressure) from one side. Based on the part size, time of infusion and fiber density, the infusion process is chosen to satisfy the objective of full fiber wetting and remove any cavity within the preform. The curing of resin is performed by the aid of catalysts and curing agents, in some cases heated molds are used to quickly cure the part. Finally, the part is demolded and removed in order to be replaced by the next dry preform. A fiber volume fraction of 50% to 60% can be achieved using the RTM process. In addition, the used molds need to be very stiff to resist any possible deformation that may happen as a result of the high pressure applied. Therefore, this limits the use of this process for the production of small to medium sized parts, whereas the application for large structural parts will be costly.

The advantages of the RTM process are: high fiber volume fraction, very good surface quality of the part, and excellent environmental control. The disadvantages are the limitation of the part size, and expensive tooling. Figure 5.2 illustrates a schematic drawing of the RTM process.
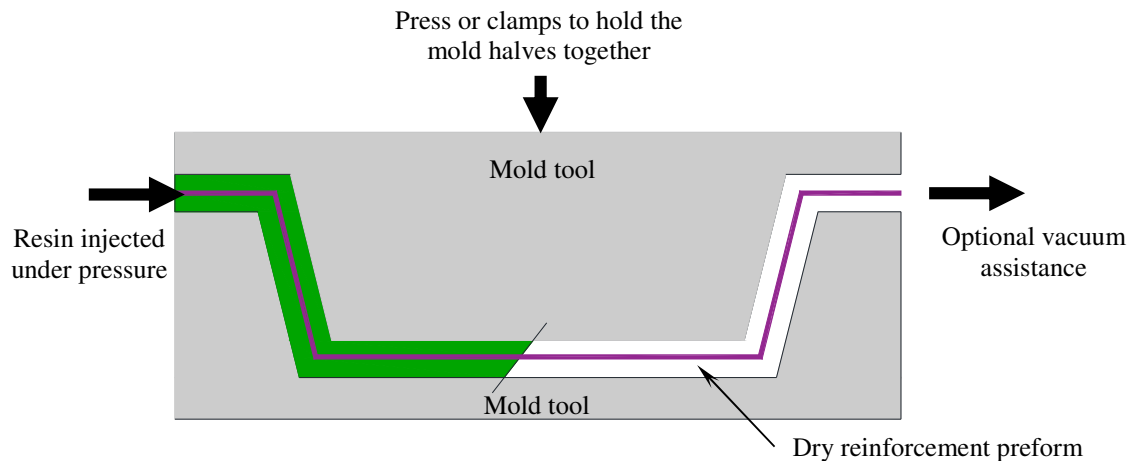
Figure 5.2. Schematic of the Resin Transfer Molding Process (RTM)

5.2.3 VACUUM ASSISTED RESIN TRANSFER MOLDING (VARTM)

The Vacuum Assisted Resin Transfer Molding Process (VARTM) is similar to the RTM process except that it uses a single sided mold and the other side is a flexible plastic membrane (Bagging film) which is sealed around the mold perimeter. The VARTM process uses only the vacuum (negative pressure) to impregnate the resin into the longitudinal direction of the reinforcing fibers under the atmospheric pressure. Therefore, the pressure differential is low which enables the process to produce relatively large structural components. The main advantages of the VARTM process are: a safe contaminated system for epoxy infusion, molds of less stiffness can be used resulting in lower costs, an acceptable fiber volume fraction from 45% to 55% are achieved. The main disadvantage of using VARTM is the process sensitivity to the strategy of infusion used (i.e. resin feed lines, the number of feed inlets) which sometimes makes it complex to perform. In addition, only resins of low viscosity below 40 P can be used.

The Seaman Composite Resin Infusion Molding Process (SCRIMP) is a variant of the VARTM technique. The SCRIMP process uses a distribution mesh in between the bagging film and the mold to allow the resin flow through the fiber thickness and not through the reinforcing fabrics planar direction. Therefore, larger structural components can be manufactured using the SCRIMP process such as wind turbines and boat hulls. Another added advantage is that low to medium viscosity resins can be used. Both VARTM and SCRIMP have the disadvantage of having only one good surface finish. Figure (5.3) illustrates a schematic for the SCRIMP technique.
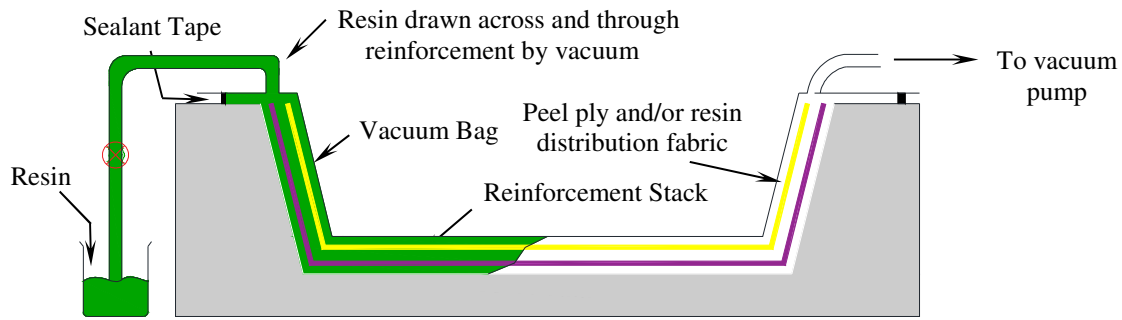
Figure 5.3. Schematic of Seaman Composite Resin Infusion Molding Process (SCRIMP), a variant of the VARTM process

5.2.4 FILM RESIN INFUSION MOLDING (FRIM)

The Film Resin Infusion Molding (FRIM) process uses a similar procedure of VARTM except that thin semi-solid resin films are used to wet the dry fabrics instead of the infusion. For ease of application, the resin layers are catalyzed and kept frozen to delay the chemical reaction to a certain shelf life. The resin films are interleaved with the reinforcing fiber layers. The whole lay-up is sealed and vacuum bagged to remove air from the dry fabrics. Further, vacuum pressure and heat are applied to melt the resin films and permeate into the dry fabrics, then kept to cure. Figure 5.4 shows a schematic drawing for the FRIM process. The main advantages of this process are the high fiber volume fraction that can be accurately achieved, high laminate mechanical properties due to the cure in elevated temperature, safe application environment, and relatively lower cost than prepreg (i.e. pre-impregnated fabrics with partially cured resin which kept frozen to a certain shelf life). On the other hand, the tools used must be able to withstand the applied elevated curing temperature (60 – 100) C°.
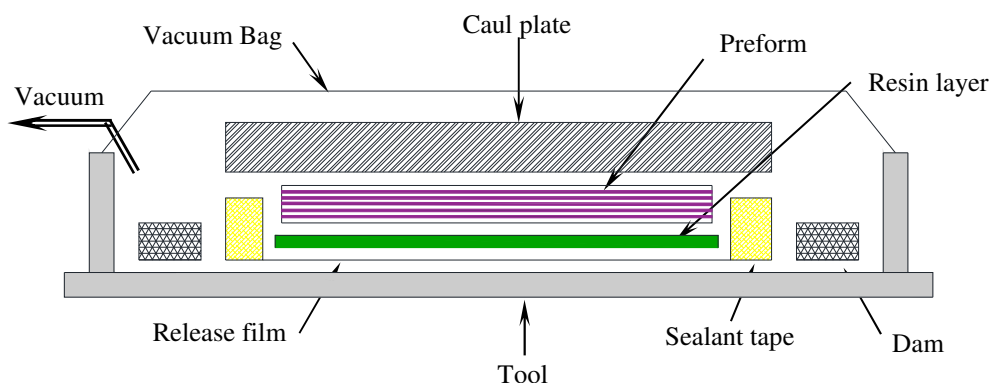
Figure 5.4. Schematic of the Resin Film Infusion Molding Process (FRIM)

5.2.5 OUT OF AUTOCLAVE (OOA) AND AUTOCLAVE PROCESS

The autoclave processing has been the highest quality manufacturing process of composite parts for many years to the moment. It is the typical manufacturing process in aerospace industry and sporting goods. The process consists of the layup of prepreg fabrics in the shape of the preform which is then sealed and vacuum bagged around the perimeter of a rigid mold. The whole assembly is placed inside the Autoclave while a pressure from 75 to 100 psi and an elevated curing temperature are applied. The composite component is connected to an external vacuum pump to remove any gasses produced from the chemical reaction of the resin. The autoclave is a highly cost process, especially for producing large structural parts due to the need of large autoclave size. Therefore, Out of Autoclave (OOA) processing is now under consideration. Typically the OOA process is exactly the Autoclave process except that the composite component has to be cured under temperature without using the Autoclave for applying pressure. The requested pressure for OOA under pump vaccum is almost 1/6 of the autoclave pressure. Excellent fiber volume fraction from 55% to 60% can be achieved using OOA. Figure 5.5 shows a schematic drawing of the OOA processing method.
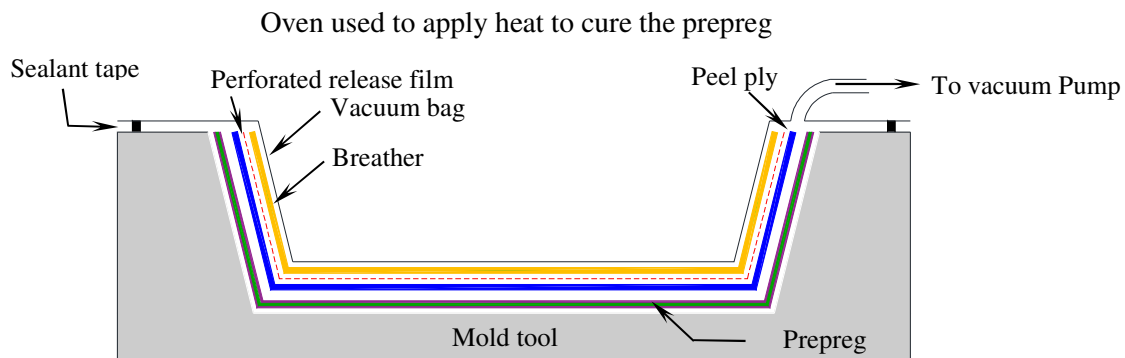
Figure 5.5. Schematic of the Out of Autoclave Process (OOA)

5.2.6 FILAMENT WINDING PROCESS

The Filament Winding Process is typically used for manufacturing composite hollow sections such as pipes, tanks, and pressure vessels. The fiber winding operation is very simple in which a continuous reinforcing fibers are passed through a resin bath (wet winding) or passed dry for a further wetting process after being wound around a rotating mandrel. The reinforcing fibers angle is controlled by the traversing speeds of the mandrel synchronized with its rotation. A schematic of the Filament Winding process is shown in Figure 5.6. The advantages of the Filament winding process

are: fiber cost is minimized since no process to convert the reinforcing fibers into fabric forms, the resin content can be controlled with the fiber tows using dies, and good material properties can be achieved for complex structural shapes. The main disadvantages are the process is limited to certain shapes, and placing the fibers along the component longitudinal direction is difficult.

Dies

Fiber tows

Rotating Mandrel

Resin bath
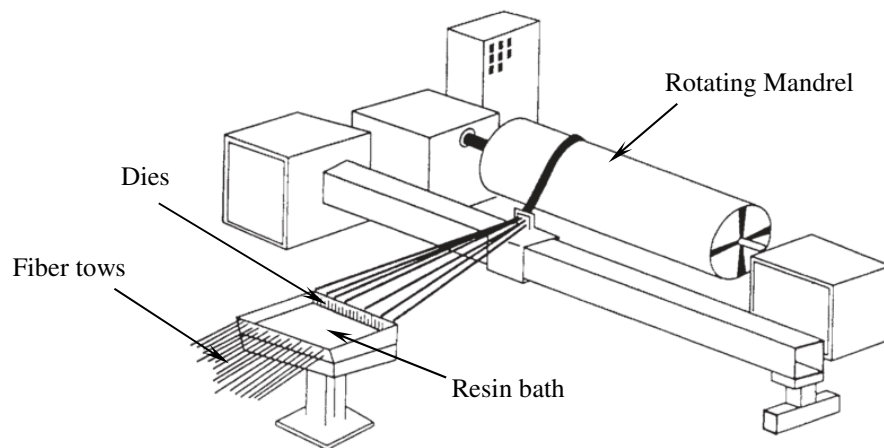
Figure 5.6. Schematic of the Filament Winding Process (Hoa, 2009)

5.2.7 PULTRUSION PROCESS

The pultrusion process is used for producing standard structural shapes such as I-beams, angles, rods, plates, and reinforcing rebar of concrete. The structural component is produced in one single step, such that, fibers tows are placed on fiber racks then pulled and routed through series of guides to a low viscosity resin bath; after that, the wetted reinforcing fibers are aligned to form the required compacted structural profile and enter a heated die to cure. After the structural profile has been shaped and became solid, it is cut into lengths for further storage and shipment. As the pultrusion process takes place in a single step it is characterized by fast component production in the rate of meters per minute which makes it a relatively cheap process. On the other hand, the rapid production process reflects in a limited quality control on the structural component. Typically the process is mostly unidirectional, however fabrics can be added to the structural profile to have different fiber orientation, which is reflected in the process and material costs. Figure 5.7 illustrates a schematic drawing of the pultrusion process.
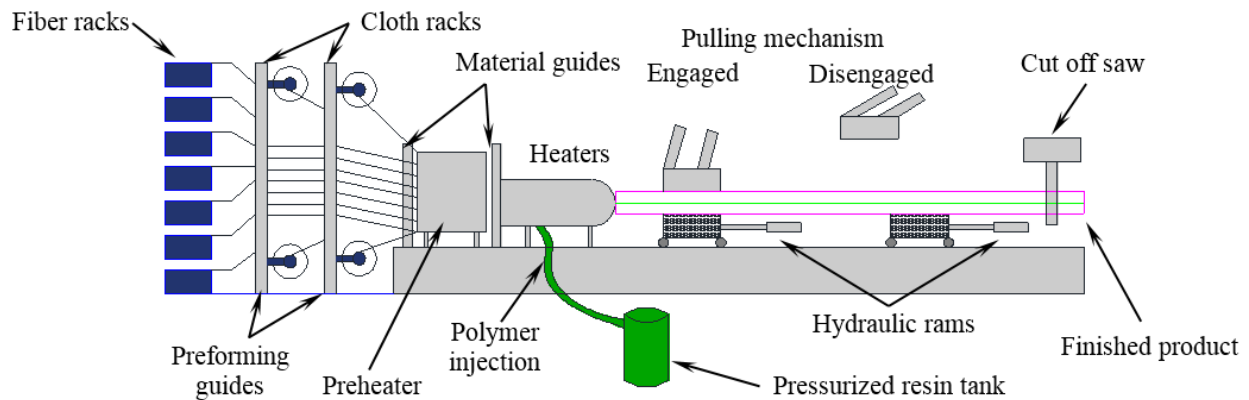
Figure 5.7. Schematic of the Pultrusion process

5.2.8 COMPARISON OF MANUFACTURING PROCESSES

A comparison of the aforementioned composite processing methods is summarized in Table 5.1 based on their relative equipment cost, material cost, the capability of customization, and the quality of the manufactured components. The hand lamination processing is considered the lowest cost manufacturing technique. However, the produced component quality is significantly dependent on the manufacturer skills and generally it results in low fiber volume fraction which makes it not applicable for deployable bridge applications. The RTM processing results in a high-quality component and production rate. The requirement of large stiff molds makes the process very expensive for producing large structural components for the bridges application. However, only specific bridge components in a bridge treadway can be effectively produced using the RTM method, such as the treadway transverse stiffeners. The VARTM, SCRIMP, and FRIM processing techniques provide a very good quality component with low to medium material cost, and the ability to manufacture large and complex structural components. The OOA is a promising processing technique that offers a relatively excellent part quality with a minimized cost compared to the Autoclave processing. It provides mostly all the advantages of the aforementioned processing methods. However, the relatively high cost achieved of a heated chamber to cure large structural parts make the process impractical as well as the long time needed to cool down the temperature in order to replace the component with a new one limits its application. Out of the whole reviewed processing methods, the VARTM, SCRIMP and FRIM are found to be the most practical processing techniques for manufacturing the sandwich deck cores. In particular, the SCRIMP processing method is selected based on its successful use in producing other deployable bridge cores in the literature

83

such as in Kosmatka *et al.* (2000) and Robinson and Kosmatka (2008). Moreover, an effective assessment can be achieved of the proposed cores compared with the recently developed.

Table 5.1. A comparison of different composite material processing methods

Manufacturing Process	Material Cost	Ability to Customization	Dimensional Tolerance	Equipment cost	Fiber volume fraction (V_f)	Component quality
Wet Layup	L	H	M	L	40% - 45%	Poor
RTM	L	M	L	H	50% - 55%	V. good
VARTM & SCRIMP	L	H	L	M	45% - 55%	Good
FRIM	M	H	L	M	50% - 55%	Good
OOA	M-H	H	L	M	55% - 60%	Excellent
Filament Winding	L	L	L	M	55% - 60%	V. good
Pultrusion	L	L	M	M	55% - 60%	V. good

Relative value: H=high, M=medium, and L=mow

5.3   EFFECTIVE COMPOSITE BRIDGING

Previous research studies investigated the utilization of composite deck cores for the deployable bridge treadways, such as Kosmatka *et al.* (2000) and Robinson (2008). Based on the high capacity/weight ratio achieved, the sandwich cores were used as alternative systems to the existing extruded aluminum deck cores of the deployable bridges for rapid post-disaster mobility. Over a wide range of investigated cores by Kosmatka *et al.* (2000), none performed well as the developed balsa core in terms of two-way bending strength, compressive strength, shear strength, and cost. Furthermore, it is worth mentioning that the balsa core experienced within the CAB deployable bridge program more than 20,000 actual or simulated load crossing with no sign of a damage. In terms of one directional bending application, all Robinson and Kosmatka (2008) webbed cores with foam infill achieved higher compression and shear strengths than the balsa core and are lighter by 28%. The foam infill between the core webs was used to increase their buckling capacity. However, some of the cores failed due to buckling of the webs in the compression tests.

In the current study, the buckling capacity of the cores is increased using a better geometrical shapes of the CFRP sandwich construction. These structural shapes are designed by placing honeycomb foam beams wrapped with the reinforcing fabrics in different configurations to minimize

the unsupported length of the core webs. The coming subsections will present a detailed description of each core configuration and clarify the design strategy of the deck cores.

5.3.1 DECK DEVELOPMENT

A designed sandwich core for decking a bridge beam structural assembly shall sustain adequate shear and compressive strengths, whereas the bending strength of the deck is supported by the full deck configuration (i.e. upper and lower skins and core designed web laminates). Therefore, the design of any tested core configuration shall adjust the failure to occur in shear of the core rather than bending in the skins. In the current study, the proposed cores performance are deigned to match the balsa core base-line of the CAB system, for further performance evaluation the failure modes of the cores are compared with the reproduced webbed cores of Robinson and Kosmatka (2008) for short span bridging. The balsa core of the CAB bridge system achieved an ultimate cross-sectional shear strength of 3,100 kPa (450 psi) and compression strength of 9,240 kPa (1,340psi), (Kosmatka *et al.*, 2000). In order to match the balsa core base-line for one way bending application, the webbed cores developed by Robinson were designed to carry an approximate shear load of 255 kN/m (1,457 lb/in) and a compressive load of 462 kN/m (2,639 lb/in) per each web spaced at 51 mm. Similarly, an approximate shear load of 142 kN/m (811 lb/in) and a compression load of 257 kN/m (1468 lb/in) shall be carried by the each laminate web of the first sandwich core construction (A1-HC-W), the core is constructed of honeycomb beams and vertical webs .A shear load of 319 kN/m (1822 lb/in) and a compression load of 578 kN/m (3301 lb/in) are recommended for the second sandwich core construction (A2-HC- CP). The core structural geometry is an integration between honeycomb beams, trapezoidal beams and corrugated fiber plates.

5.3.2 CORES DESCRIPTION AND MANUFACTURING

The balsa core of the CAB deployable bridge presented by Kosmatka *et al.* (2000) consists of two face sheets forming the upper and lower skins and two balsa sheets of thickness 38 mm (1.5 in) for each in between. The balsa core material was chosen to have a 248 kg/m^3 (15.5 pcf) density. The total balsa core thickness was 92 mm (3.606 in). The two skins were fabricated from 11 plies of 5-Harnesss (5H) satin weave 12k carbon fiber fabric, in addition to unidirectional stitched 50k carbon plies at the bridge mid-span and treadway center. The laminate resulted in 8mm (0.301in) skin thickness. The two balsa sheets are adhesively bonded in the mid plane of core to 2 splitter plies of 5H woven fabrics with of 0.678 kg/m^2 (20 oz/yd^2). The SCRIMP technique (a variant of VARTM)

was used to infuse the balsa core with the resin, where a matrix of holes was drilled through the balsa thickness to allow the resin flow from the upper skin to the splitter plies and the lower skin. The balsa cores moisture content level were kept by treating the core surfaces with a sealant. The whole core assembly resulted in a final density of approximately 290 kg/m^3 (18 pcf) and nearly 22 kg/m^2 (4.5 psf) of core areal weight. The performance evaluation of the balsa core results in a compressive strength of 9240 kPa (1340 psi) and shear strength of 3100 kPa (450 psi). The developed core behaves well for bi-directional application due to the isotropic property of balsa wood. The core design configuration is shown in Figure 5.8.
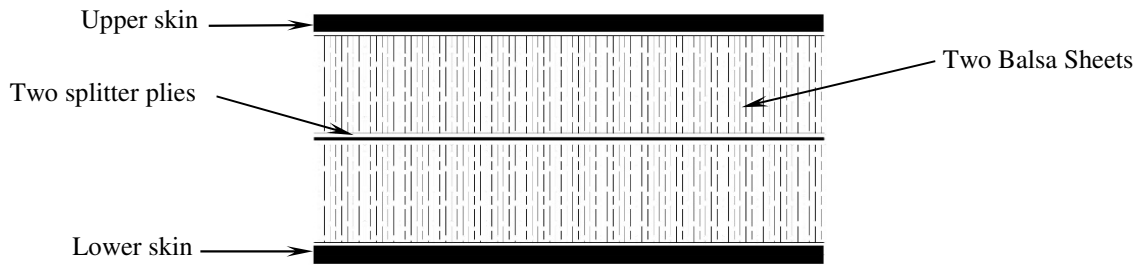
Figure 5.8. Balsa core applied for CAB deployable bridge

The webbed core specimen (C4-TC) designed by Robinson and Kosmatka (2008) was reproduced and fabricated using manual wrapping of two unidirectional carbon layers oriented at ±45° around rectangular polyisocyanurate foam beams of density 48 kg/m^3 (3pcf). The service temperature of the foam is 149 C$^\circ$ which was adequate for a post-cure temperature applied to the specimen at 64 C$^\circ$ for 24 hours. The cross section of the foam beams were 50 mm x 76 mm (1.95 in × 3.0 in). The wrapped UD carbon fibers created two layers of 0.82 kg/m^2 (24 oz/yd^2) and angle-ply orientation of $[\pm 45_1]_T$ around a single beam. A web of thickness 4.0 mm was placed in between every two wrapped foam beams as a filler. The webs were fabricated from UD layers of $[0, \pm 45]_{2T}$ fiber architect and of density 1.22 kg/m^2 (72 oz/yd^2). The core assembly resulted in a final areal weight of 14.8 kg/m^2 (3.03 psf) and dry fiber areal weight of the webs of 3.26 kg/m^2 (96 oz/yd^2).

The second webbed core specimen (C5-CC) was refabricated using manual wrapping of two UD carbon fibers oriented at $[\pm 45]_T$ of 0.82 kg/m^2 (24 oz/yd^2) around only three sides of trapezoidal polyisocyanurate foam beams of density 96 kg/m^3 (6pcf). The trapezoidal foam beams dimensions are 60 mm × 35 mm × 76 mm depth (2.35 in × 1.35 in × 3.0 in deep). The web filler thickness is built through the assembly of 6 layers of UD carbon fibers in between the attached trapezoidal foam

beams with $[\pm 45]_{3T}$ fiber architect. The core web dry fiber areal weight is 3.26 kg/m^2 (96 oz/yd^2). The total web laminate thickness is 4.0 mm. The total core areal weight is 18.6 kg/m^2 (3.81 psf).

The core specimens C4-TC and C5-CC design configurations developed by Robinson and Kosmatka (2008) are shown in Figures 5.9 and 5.10, respectively.
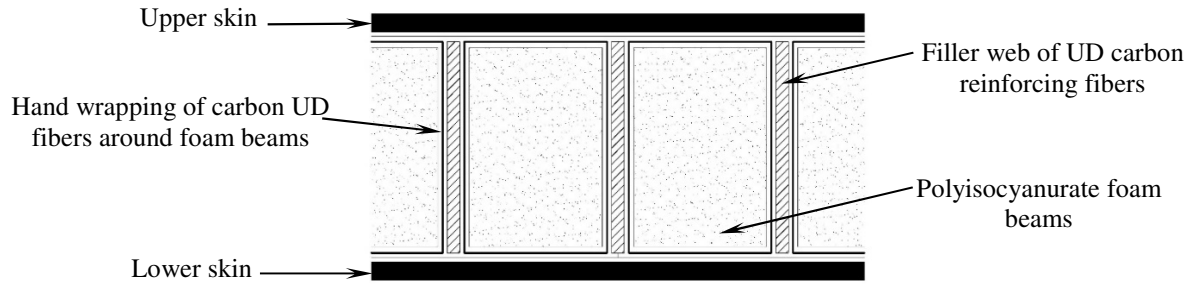
Figure 5.9. CFRP webbed core with foam infill (C4-TC)
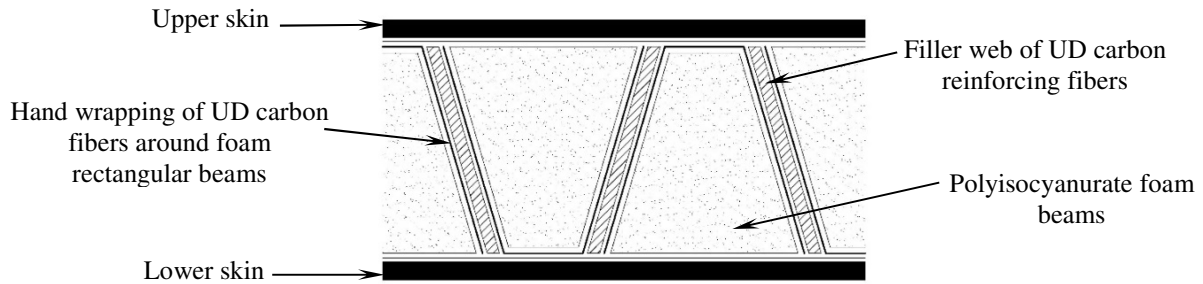
Figure 5.10. CFRP webbed core with trapezoidal shape (C5-CC)

In the current study, two different designed core configurations are proposed. Each core configuration is approximately 76 mm thick (face skins are not included) and all are fabricated from carbon/epoxy laminates. The common configuration of the cores consists of several honeycomb beams placed parallel to each other. The beams are fabricated by manual wrapping of unidirectional carbon layers with different ply orientation around the hexagonal shaped polyisocyanurate foam beams. The honeycomb beams are placed between two upper and lower carbon/epoxy skins to hold the whole core together. The following is a detailed description of the proposed sandwich cores.

- **Core 1: (A1-HC-W)**

The first core consists of manual wrapping of 6 unidirectional carbon fabrics of 0.41 kg/m^2 (12 oz/yd^2) per layer around 64 kg/m^3 (4 pcf) honeycomb polyisocyanurate foam beams with 76 mm depth and 41.5 mm hexagonal side length. The 6 wrapped layers are oriented to build a balanced and symmetric laminate around the foam beam of $[0_1, \pm 45_1]_S$ fiber architect. A spray adhesive is used to

hold the carbon layers together during wrapping. Every two honeycomb beams are separated by vertical carbon fiber webs. Eight plies are used to build up the thickness of the web filler, the webs are fabricated from the same unidirectional fibers and assembled in $[0_2, \pm45_1]_S$ of a laminate plies orientation. The zero angle is set perpendicular to the upper and lower skins to increase the web compression capacity. The space between the web and the two adjacent honeycomb beams are filled with triangular shapes of the same foam material. The maximum dry fiber areal weight of the core is 3.26 kg/m^2 (96 oz/yd^2). The total core areal weight is 14.11 kg/m^2 (2.89 psf). Figure 5.11 shows an illustration of the core configuration.

- **Core 2: (A2-HC-CP)**

The second configuration is composed of the assembly of three constructed items, which are, wrapped honeycomb beams, wrapped trapezoidal beams, and two back to back carbon laminate preforms. The wrapped honeycomb beams consists of manual wrapping of 4 unidirectional carbon layers of 0.41 kg/m^2 (12 oz/yd^2) and $\pm$ 45 fiber orientation around 64 kg/m^3 (4 pcf) honeycomb polyisocyanurate foam beams, as well as two unidirectional layers of 0.41 kg/m^2 (12 oz/yd^2) oriented in $0°$ angle normal to the skins and attached to every side of the wrapped honeycomb foam beam in order to increase the compression and bending capacities of its hexagonal side. The wrapped trapezoidal beams are fabricated of wrapping two UD carbon layers of 0.41 kg/m^2 (12 oz/yd^2) and $\pm$ 45 ply orientation around trapezoidal shaped foam beams. The two back to back corrugated preforms are fabricated of 0.41 kg/m^2 (12 oz/yd^2) unidirectional carbon layers, such that a single corrugated preform laminate construction is of two UD layers oriented $\pm$ 45 degrees. The wrapped trapezoidal beams are placed from their short side into the open cells of the corrugated preform, whereas the wrapped honeycomb beams are placed inside the closed cells of the corrugated preforms with the hexagonal construction. The whole integration of the honeycomb beam, trapezoidal beam and the corrugated carbon preforms are placed in between the upper and lower skins of the sandwich core. The core assembly resulted in a laminate construction of $[\pm45_2, 0_2, \pm45_2]_T$ fiber orientation as core webs of the honeycomb sides. This fiber architect resulted in a web thickness of 4.0 mm, in addition, a horizontal laminate of $[\pm45_2]_S$ fiber architect is constructed and connects every two honeycomb beams. The maximum dry fiber areal weight of the honeycomb beam side is 4.07 kg/m^2 (120 oz/yd^2). The total core areal weight achieved is 10.74 kg/m^2 (2.2 psf). An illustration of the core configuration is presented in figure 5.12.
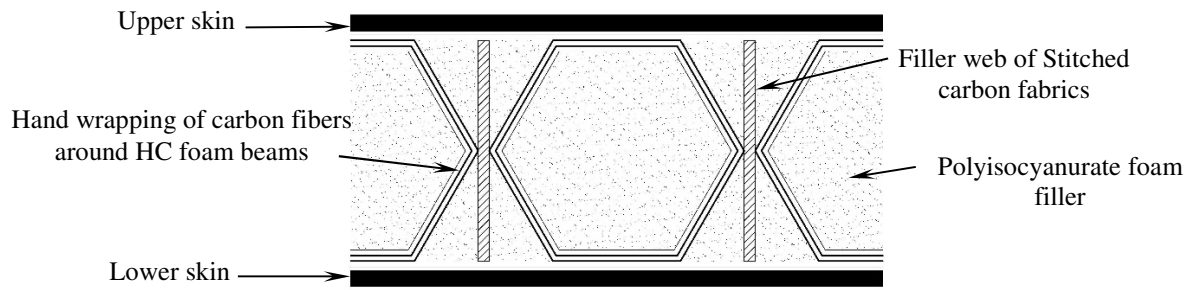
Figure 5.11. An illustration of core A1-HC-W design configuration
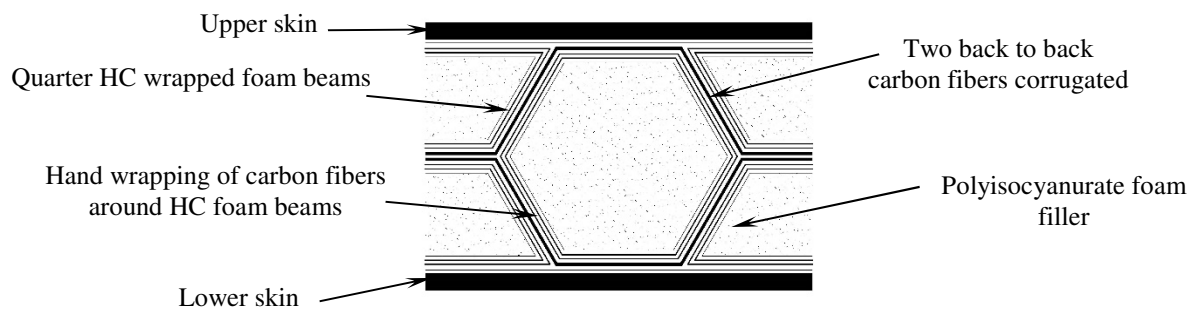
Figure 5.12. An illustration of core A2-HC-CP design configuration

Photographs of the A1-HC-W and A2-HC-CP fabricated specimens are shown in Figures 5.13 and 5.14, respectively. Figures from C.1 to C.4 show photographs of both cores in different steps of the assembling procedure.
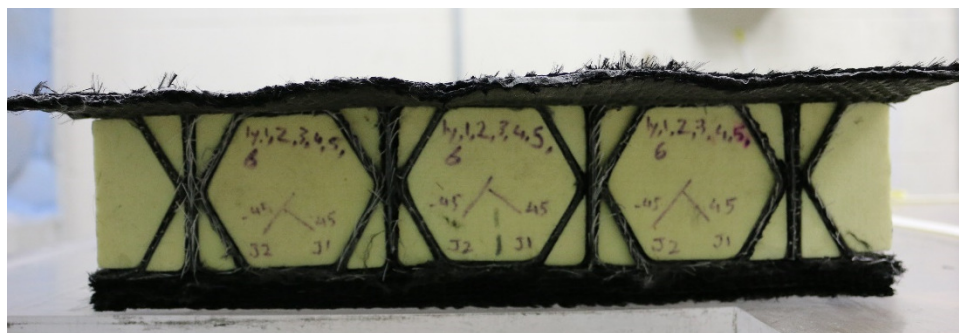
Figure 5.13. A photograph of the A1-HC-W fabricated core specimen
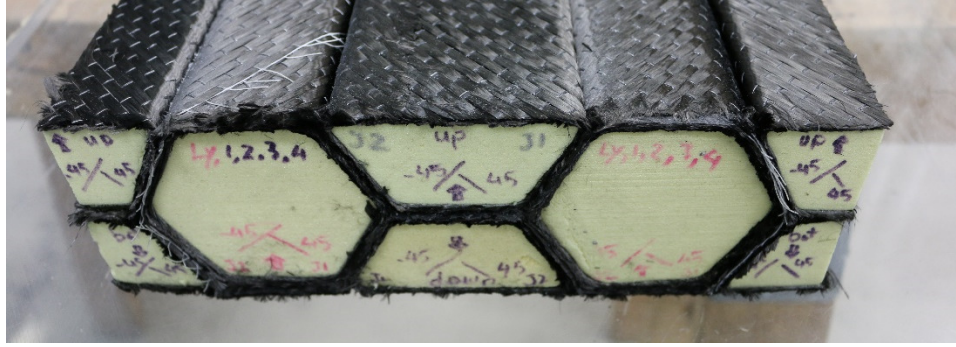
Figure 5.14. A photograph of the A2-HC-CP fabricated core specimen

A summary of the whole cores design configurations including their different fibers architecture, dimensions and foam specifications are illustrated in detail in table 5.2.

As previously mentioned, the purpose of the current study is to evaluate the compressive and shear strength of the proposed core designs. Therefore, only 10 layers were applied for each of the upper and lower deck skins for the tested samples in compression to ensure a sufficient fixed boundary condition of the core laminate webs. A total of 22 layers and 6 layers were applied for the compression side and the tension side of deck, respectively, for the tested samples in shear, in order to ensue shear failure in the core as opposed to bending failure in the skins will occur. All the manufactured core samples were set for post cure at 64 C° for 24 hours after cured in the room temperature, as shown in Figure 5.15. The SCRIMP processing method was used to infuse the core specimens with resin. Figures 5.16.a and 5.16.b show a schematic of the infusion strategies followed for the specimens (A1-HC-W) and (A2-HC-CP), respectively, whereas Figure 5.17 shows a photograph of a sample during infusion.
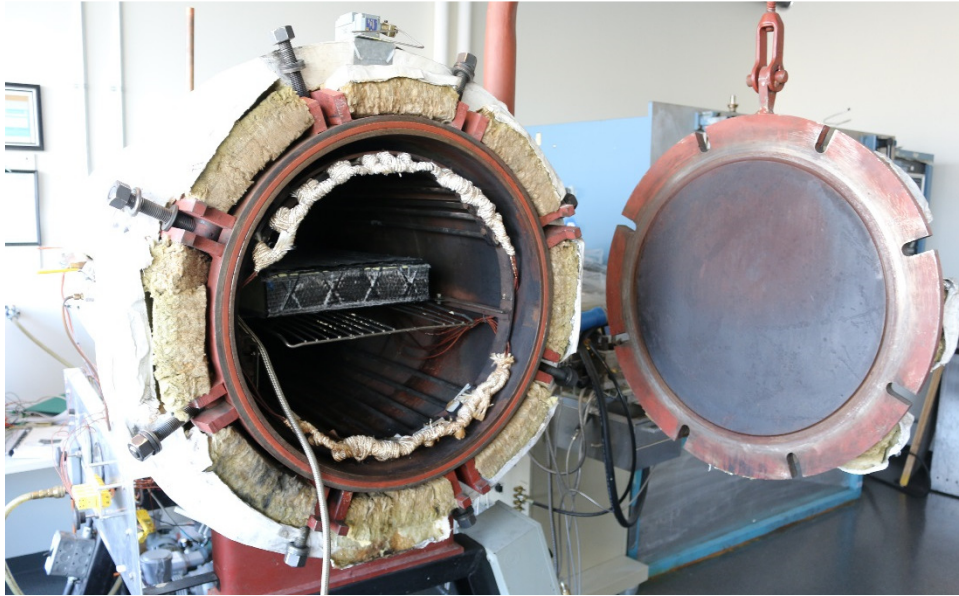
Figure 5.15. A photograph of the A1-HC-W being post cured in Autoclave
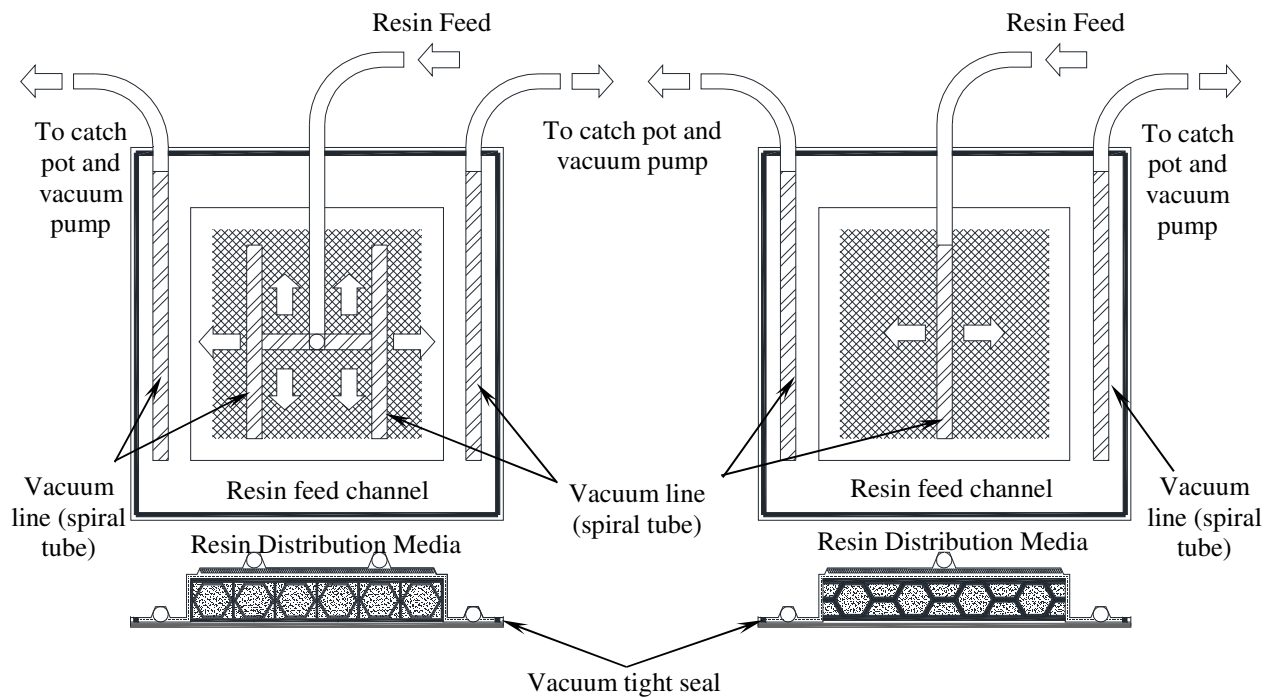
Figure 5.16. A schematic of the infusion strategy used for the core specimens
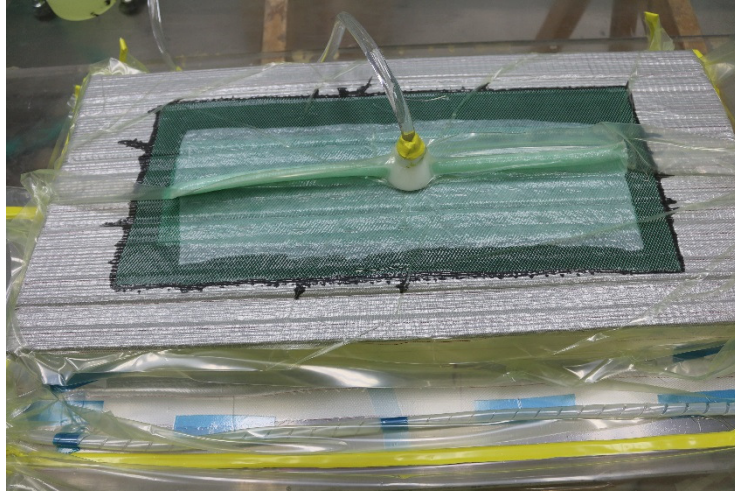
Figure 5.17. A photograph of the A2-HC-CP specimen being infused with resin

Fiber volume fraction of 45% ± 4% is achieved for the tested specimens. The fiber volume fraction V_f was measured through microscopic analysis of a part of the manufactured samples. Figure 5.18 shows microscopic photographs for an analyzed sample.
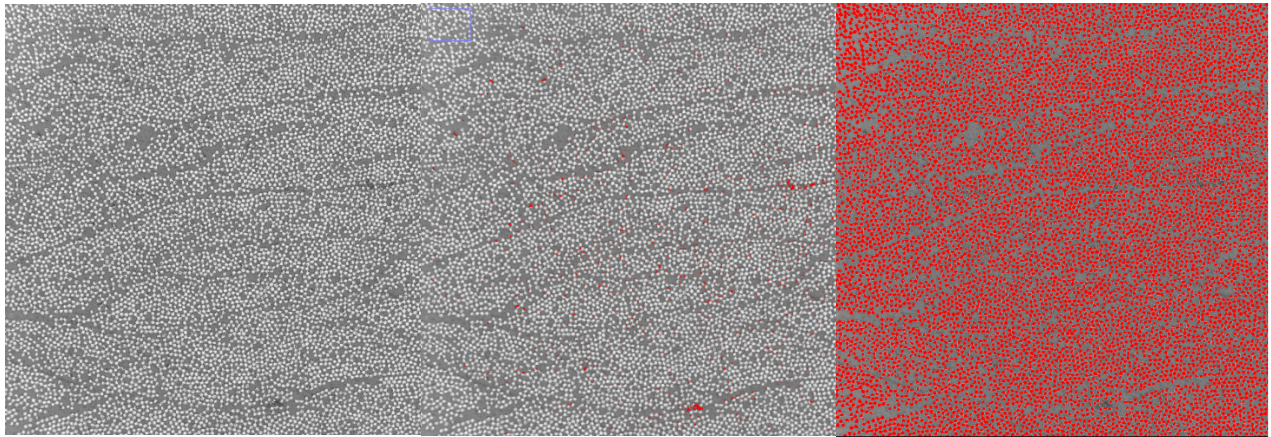
a) Microscopic photograph   b) Voids detection   c) fibers detection

Figure 5.18. A photograph of an analyzed microscopic sample

Table 5.2. Sandwich cores design configuration details

Sandwich core type	Skins thickness (mm)	Filler web ply orientation	Core Ply orientation	dimensions of tested samples (W x H x T) mm	Fiber type	Filler fiber	Core wrap fiber	Max. dry fiber areal weight/web	Total dry fiber areal weight per specimen width	Max. Web thickness [mm]	Foam infill	V_f
Balsa core	8 mm Top 8 mm Bottom	NA	NA	NA	Carbon	G519-12K 5H woven fabric $[0_2]_T$-(18 oz/yd^2)	NA	36 oz/yd^2	36 oz/yd^2	NA	15 pcf Balsa wood	53.5 ± 2.5
C4-TC	4 mm Top 4 mm Bottom	$[0, +45, -45]_{3T}$ /web	$[\pm 45_1]_T$ /core	164 x150 x 97 Flatwise compression	Carbon	Tyfo SCH-11UP UD fibers (72 oz/yd^2)	Tyfo SCH-11UP UD fibers (24 oz/yd2)	96 oz/yd^2	288 oz/yd^2	4.0	PVC (48 kg/m3)	42.5 ± 2.5
C5-CC	4 mm Top 4 mm Bottom	$[\pm 45_3]_T$ /web	$[\pm 45_1]_T$ /core	208 x150 x 96 Flatwise compression	Carbon	Tyfo SCH-11UP UD fibers (72 oz/yd^2)	Tyfo SCH-11UP UD fibers (24 oz/yd^2)	96 oz/yd^2	270 oz/yd^2	4.0	P600 (96 kg/m3)	42.5 ± 2.5
A1-HC-W	8 mm Top 4 mm Bottom	$[\pm 45, 0_2]_S$ /web	$[\pm 45_2, 0]_S$ /cell	180x762x 90-Flexural 180x150x 90-Fcomp.	Carbon	Tyfo SCH-11UP Unidirectional (12 oz/yd2)	Tyfo SCH-11UP Unidirectional (12 oz/yd2)	96 oz/yd^2	252.6 oz/yd^2	3.2 0.399 mm/layer	P400 (64 kg/m3)	45.0 ± 4.0
A2-HC-CP	8 mm Top 4 mm Bottom	$[\pm 45_2]_S$ /curr.	$[\pm 45_2]_T$ $[0_2, \pm 45_2]_T$ /cell	122x762x 90-Flexural 122x150x 90-Fcomp.	Carbon	Tyfo SCH-11UP Unidirectional (12 oz/yd2)	Tyfo SCH-11UP Unidirectional (12 oz/yd2)	120 oz/yd^2	153.03 oz/yd^2	4.0 0.399 mm/layer	P400 (64 kg/m3)	45.0 ± 4.0

5.3.3 DESIGN AND BUCKLING ANALYSIS

The proposed structural configurations of the sandwich cores using the honeycomb beams characterize the design with an increased buckling capacity compared with the vertically aligned webbed cores with foam infill. Figure 5.19 shows that each inclined or vertical web of cores A1-HC-W and A2-HC-CP has shorter unsupported length (without foam infill), whereas, the webbed cores have vertical webs of full core depth. In addition, shear and compression forces are distributed on several vertical and inclined webs and the compression forces are spilt into two resultant components in the in-plane and out-of-plane surface of the web laminate.

(a) A1-HC-W   (b) A2-HC-CP
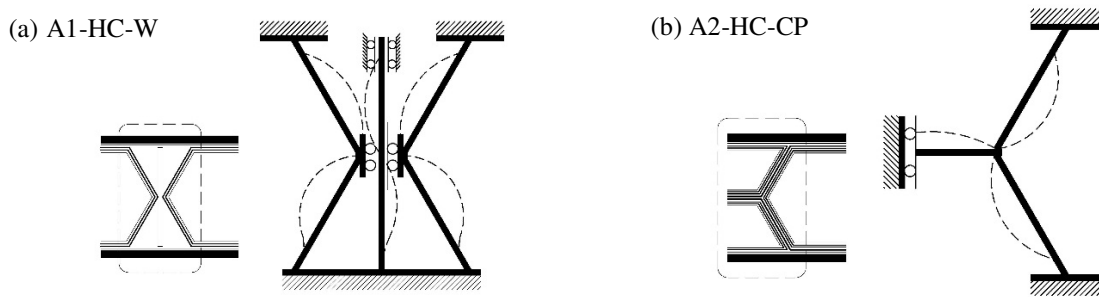
Figure 5.19 Schematic of the possible local buckling modes of the sandwich cores

The in-plane loads would result in lesser compression load values, whereas as additional out-plane load component is created. The foam infill in the current study acts as an elastic foundation of the core webs. The foam contribution in increasing the buckling capacity of the webs in not significantly efficient compared with the buckling capacity achieved by the structural geometry itself for the case of the proposed deck cores of approximately 90 mm depth. However, the foam infill plays an instrumental role in creating a nonlinear distributed load all over the inclined webs length in order to balance up to a considerable limit the created out-of-plane load resultant, such that a response load is created and composed of two components which are: an induced force from the web laminate bending stiffness and an force caused by the foam distributed load. This would significantly decrease the bending stress created on the webs due to that out-of-plane load. An illustration of the generated nonlinear distributed load over the inclined webs is shown in Figure 5.20.
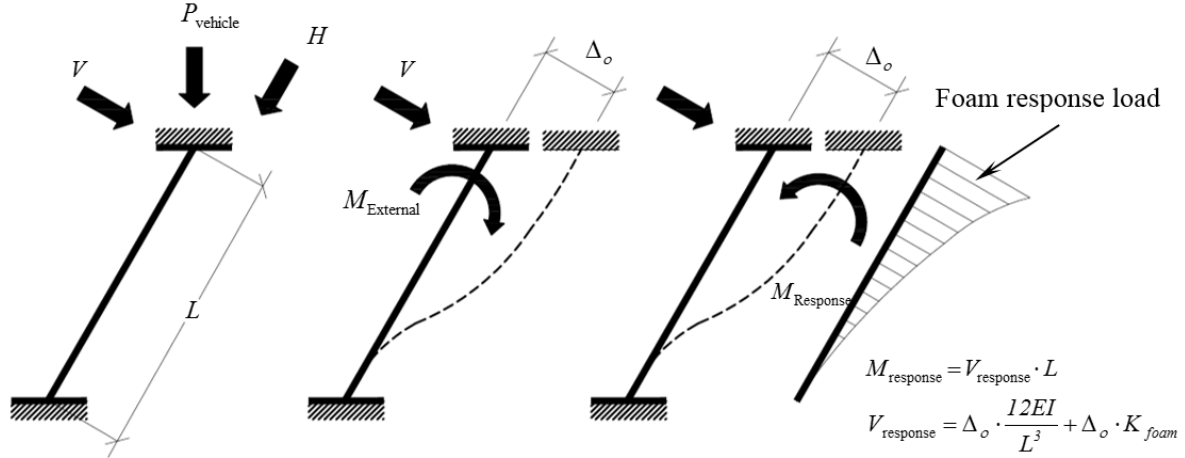
Figure 5.20 An illustration of the out-of-plane acting loads and the generated load response by the foam and web stiffness

$$M_{response} = V_{response} \cdot L$$

$$V_{response} = \Delta_o \cdot \frac{12EI}{L^3} + \Delta_o \cdot K_{foam}$$

5.4 EXPERIMENTAL TEST SETUPS

The performance of the proposed cores compressive strength, and shear strength was experimentally evaluated. In order to assess the compression strength capacity in the direction perpendicular to the deck surface, a flatwise compression test (ASTM C365-11a) was conducted, and the shear strength capacity was quantified by applying three points loading test (ASTM C393-11). The cores configurations A1, and A2 were fabricated in two panels per configuration of 760 mm × 380 mm (30 in × 15 in), and 760 mm × 300 mm (30in × 11.8 in) dimensions, respectively. Each panel was cut using an abrasive diamond blade into the required dimensions and number of specimens as illustrated in Table 5.2.

5.4.1 MATERIAL CHARACTERIZATION

The carbon fiber material and epoxy formulation used to fabricate the deck cores were donated by Fyfe Composites Co. in California, USA. The laminate mechanical properties were characterized through performing multiple coupons tests. The fiber tensile, and compressive strengths and its corresponding ultimate strains were obtained by conducting a tensile test for coupons of $[0_5]_T$, and $[\pm45_2]_T$ fiber orientation in accordance to ASTM D3039 and ASTM D3518, respectively. The tests were performed on MTS machine of 250 kN capacity, whereas, the fibers and matrix compressive strength and ultimate strain were quantified by testing coupons in accordance to ASTM D3410 on MTS machine of 100 kN capacity. The matrix and reinforcing fibers ultimate tensile and strain properties for coupons of $[90_5]_T$ fiber architect were evaluated on

HOSKIN machine of 5 kN capacity to obtain precise results. Figures 5.21.a, b, and c show photographs of testing the material coupons' tensile, compressive, and matrix properties, respectively. Table 5.3 presents the material mechanical properties. Figures C.5 to C.10 in appendix C show the compressive, tensile, and shear stress-strain relationship of the tested coupons.

a) Tensile testing on MTS machine of 250 kN capacity

b) Compressive testing on MTS machine of 100 kN capacity

c) Fiber matrix testing on HOSKIN machine of 5 kN capacity

Figure 5.21. Photographs of testing the coupon samples using different machines

Table 5.3. carbon/epoxy material characteristics

Property			Tested (SCRIMP)	Manufacturer (Wet layup)	ASTM method
Tension [0°]	Tensile modulus	E_{1t} (GPa)	119.0845 GPa	95.8 GPa	D3039
	Poisson ratio	v_{12}	0.38045	NA	
	Ultimate tensile	X_t (MPa)	1580.065 MPa	986 MPa	
	Ultimate tensile strain	ε_{1t} (µε)	0.013691 µε	NA	
Tension [90°]	Tensile modulus	E_{2t} (GPa)	6.4054 GPa	NA	D3039
	Poisson ratio	v_{21}	0.0204	NA	
	Ultimate tensile	Y_t (MPa)	16.14 MPa	NA	
	Ultimate tensile strain	ε_{2t} (µε)	0.002325 µε	NA	
Compression [0°]	Compression modulus	E_{1c} (GPa)	96.590	NA	D3410
	Ultimate compression	X_c (MPa)	322.105 MPa	NA	
	Ultimate compressive strain	ε_{1c} (µε)	0.0031273 µε	NA	
Compression [90°]	Compression modulus	E_{2c} (GPa)	7.45637 GPa	NA	D3410
	Ultimate compression	Y_c (MPa)	90.2869 MPa	NA	
	Ultimate compressive strain	ε_{2c} (µε)	0.015575 µε	NA	
Shear [±45°]	Shear modulus	G_{12} (GPa)	4.2813 GPa	NA	D3518
	Ultimate in-plane shear	S (MPa)	34.916 MPa	NA	
	Ultimate shear strain	γ_{12} (µε)	0.04908415	NA	
Dry Areal weight kg/m^2 (oz/yd^2)			0.393 (11.6)		
V_f			46.75% ± 3%		
Material / Manufacturer			Tyfo SCH-11UP/ Fyfe Composites Co.		

5.4.2 SHEAR USING THREE POINTS LOADING TEST

The proposed cores were fabricated as beams of sandwich construction in order to evaluate its shear strength under the application of beam bending. The sandwich core beams were tested against bending of three points loading, such that the core shear strength, core to face shear strength, and shear stiffness were quantified. The sandwich cores were designed to ensure a shear failure would occur rather than flexure in the upper and lower laminate skins. This was done by having facing skins of sufficient thicknesses that were able to carry flexural compression and tensile forces in the skins before the core fails in shear; at the same time, not too thick such that, the transverse shear forces will not be carried to a considerable extent by the skins. Furthermore, as the face thickness to core thickness ratio for all specimens is less than 0.1, a core failure was adjusted in shear satisfying the recommendations of C363 (2011). In the proposed core design, the facing skins were fabricated from the same carbon/epoxy material that is balanced and symmetric.

The three points loading test was conducted using a Tenuis Olsen machine of 500 kN capacity. The core beam specimen was supported over two rigid steel plates of a hinged-roller boundary condition with wide rubber pads and spaced 610 mm (24 in). In order to prevent any local failure of core under the machine loading crosshead, a rectangular steel plate of 152 mm × 352 mm (6 in × 13.9 in) dimension rested on a wide rubber pads was placed to transfer the machine monotonic load to the specimen as well as to avoid any cutting into the upper skin. The loads versus specimen deflection were recorded with a minimum of 100 data points. The test setup is shown in Figure 5.22.

A total of 9 strain gauges of 5 mm (0.2 in) gauge length were installed to each tested specimen, 6 were placed in the upper skin and the rest were installed in the lower skin. In the upper skin, each strain gauge was placed every one third of the specimen width at the two opposite quarter spans from the supports, whereas the other 3 strain gauges were placed by the same manner on the lower skin surface at the mid-span. A total of six displacement potentiometers were placed in the tested specimen. A set of two displacement potentiometers were placed at each support and attached to a flat steel bar at the upper skin; similarly two displacement potentiometers were placed below the core mid-span at the lower skin. The instrumentations of 6 strain gauges in the quarter spans displaced from the beam centerline as well as the two displacement potentiometers at mid-span were functioned to measure any relative strains and displacements between the sides in order to

98

detect any occurrence of torsion during loading. A Plot of the load-deflection data was conducted to detect any significant fraction of failure occurred by finding the significant transition point at a change of 10% or more in the slope. Figure 5.23 shows an illustration for the three points loading test setup.
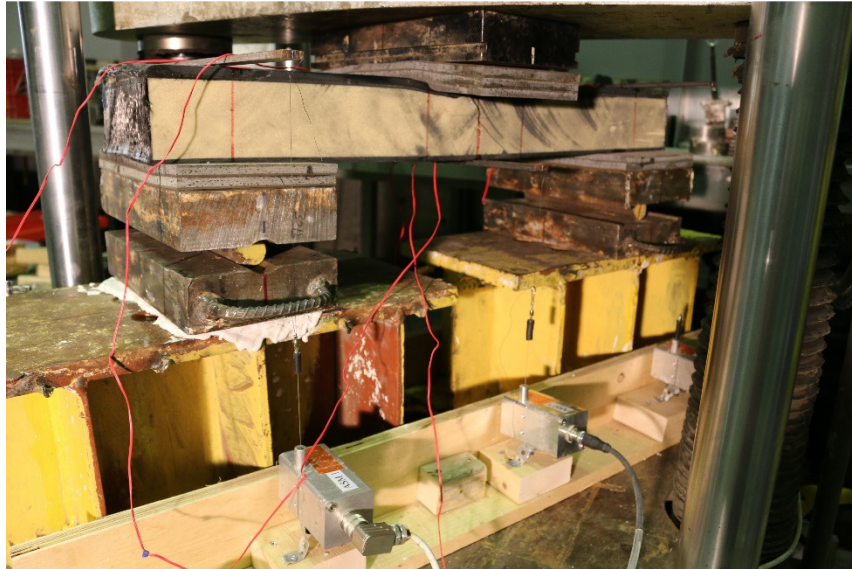
Figure 5.22. A photograph of a core beam during a three point load test
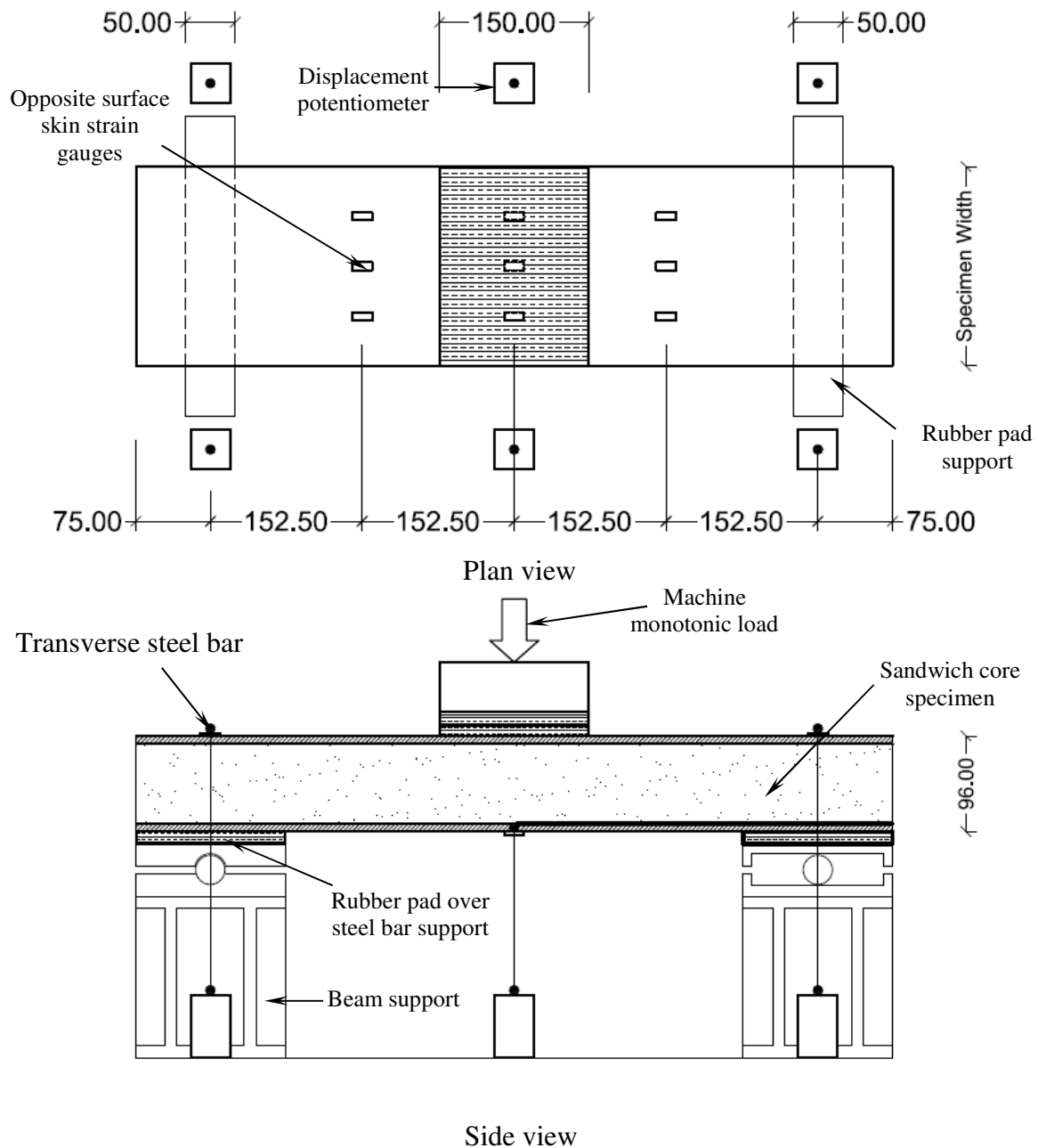
Figure 5.23. Illustration of the three points loading test set up and the instrumentation with the displacement potentiometers and the strain gauges locations

5.4.3 FLATWISE COMPRESSION TEST

The purpose of this test is to determine the compressive capacity and the compression modulus of the sandwich cores in a direction normal to the cores' skin, such that, assurance of no core failure may occur from the passing heavy loads of wheeled or tracked vehicles. The test consists

of applying a uniaxial monotonic load over the sandwich core skin from a Tenuis Olsen machine of 500 kN capacity. The specimens were placed in between a steel flat loading platen of 350 mm × 350 mm (13.8 in × 13.8 in) dimension and a steel base welded over steel I-beam cross-section. The specimens were leveled to the steel platens' surfaces using drystone layer with high compressive strength (50 MPa) in order to ensure a uniform load distribution, smooth and parallel surface of the tested specimens. A self-aligning spherical seat was placed on the top of the upper flat loading platen to transfer the machine testing load. Four displacement potentiometers were placed at the four sides' center of each specimen and attached to upper flat loading platen in order to measure the core average deformation. The vertical alignment of the displacement potentiometers stroke wires was adjusted using laser alignment rays. A photograph of the test setup is shown in Figure 5.24.

Figure 5.24 Flatwise compression test setup of the reproduced C4-TC core

The expected failure modes of the specimens are: (a) crushing of the web, (b) only for the specimen with vertical web, failure at the joint between web and skin may occur. A population of three core specimens per designed configuration was tested to validate the obtained results.

5.5　TEST RESULTS AND DISCUSSIONS

5.5.1　SHEAR USING THREE POINTS LOADING TEST

The potential failure modes of the core specimens are: (a) crushing of the core webs, (b) separation of the facing skins from core due to shear, and (c) only for specimen A1-HC-W failure may occur at the joint between the vertical web and the skins. For core A1-HC-W the failure mode observed was a delamination failure due to interlaminar shear between the core and upper skin. This type of failure occurs when the core laminate webs have the sufficient thickness to carry the shear stresses, and the contact between the core and skin surfaces is weaker. A photograph showing the failure mode in a cross section cut of the core beam just near the supports is presented in Figures 5.25. Core A2-HC-CP was cut at two different locations, such that each cut would provide a different core structural shape. The first cut was done to provide a core cross-section of two back to back trapezoidal shapes which act as a framed structure with columns inclined to the outside. The second cut considered a full honeycomb shape within the core cross-section. The first cut failed in delamination at the corners between the core layers and the skins due to interlaminar shear, as shown in Figure 5.26.a. On the other hand, the second core cut failed in a different interlaminar shear path, in which the failure occurred between the ±45 and 0 layers point of contact starting from the free edge of the core and splitting the upper half of the honeycomb core laminate, as shown in Figure 5.26.b.

The failure modes of cores A1-HC-W and A2-HC-CP can be explained by the illustration presented in Figure 5.27. For core A2-HC-CP, the shear flow followed a path from the inclined web laminate into the skin and the failure occurred at the weakest point inside the laminate web between the ±45 and 0 layers. Although manual wrapping of fibers was performed around both the honeycomb beams and the trapezoidal shaped beams in order to distribute the shear flow all over the skin, the shear forces were more concentrated to flow into the corrugated shape of the core, this flow concentration caused a delamination failure in the web layers and the failure followed the path of corrugation before a delamination between the core and the whole skins occurred. This can be attributed to the unequal distribution of the continuous layers from the web to the skin, as only two layers of the web thickness of ±45 ply orientation were wrapped around the trapezoidal shape, whereas 6 layers of the web including the corrugated preform layers were

wrapped around the honeycomb beam at their contact with the skin. In the same manner, the shear flow of the frame structure developed by the trapezoidal shapes was concentrated to the edges of the core between the two honeycomb halves and the skin.

On the contrary, core A1-HC-W experienced shear flow that is equally distributed into the skin laminate resulting in a full delamination failure due to interlaminar shear between the core and the skin, and the designed laminate $[\pm 45, 0_2]_S$ of the vertical webs as well as the $[\pm 45, 0_1]_S$ laminate of the honeycomb beam side were with an adequate thickness to resist the shear stresses. An illustration of shear distribution of core A1-HC-W is shown in Figure 5.27.b.

Interlaminar shear failure
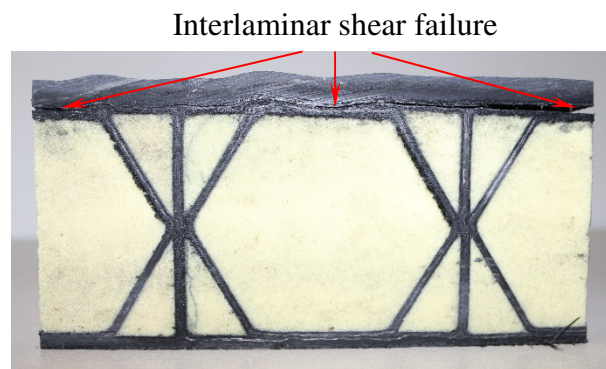
Figure 5.25 Photograph of the shear failure mode of core A1-HC-W during three points loading test

Interlaminar shear failure   Interlaminar shear failure

(a)   (b)
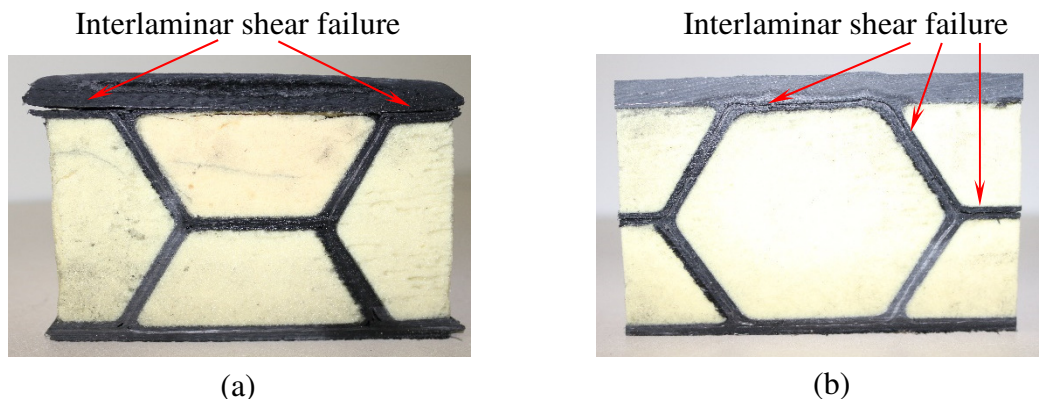
Figure 5.26 Photograph of the shear failure mode of core A2-HC-CP during three points loading test

Both cores A1-HC-W and A2-HC-CP achieved a similar shear strength to the balsa core of the CAB deployable bridge system with a difference of 4.5% to 0.8%, respectively. However, they had achieved a higher shear strength to areal weight ratio ranging from 1.5 to 2.04 times of the

balsa core system, respectively. Furthermore, it is expected that equal redistribution of web laminate layers to wrap both the trapezoidal shaped and the honeycomb shaped beams, along with changing the design of the web laminate of core A2-HC-CP from [±45, 0] ply orientation to a uniformly [±45] angle ply laminate would increase the shear strength, and at the same time the web laminate thickness has to be increased for not sacrificing the compressive strength of the core.

(a) A2-HC-CP   (b) A1-HC-W
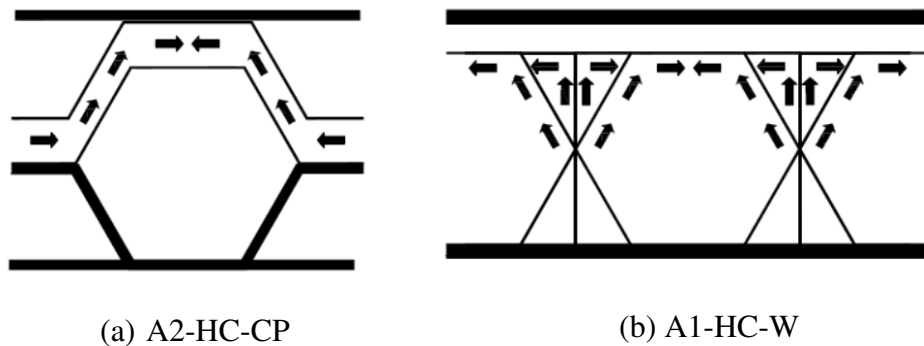
Figure 5.27 Illustration of intelaminar shear failure modes of cores A1-HC-W and A2-HC-CP

Table 5.4 summaries the three points loading test results of cores A1-HC-W, and A2-HC-CP compared with the balsa core system. It can be noticed that both core has better stiffness than the balsa system.

Table 5.4. A comparison of three points loading test results

Core	Failure Load (kN)	Shear Strength (kPa)	Average deflection (mm)	Failure mode	Shear Strength/Areal Weight Ratio	Normalized ratio
Balsa Core	103 kN	3100	5.1	Core shear	14	1.0
A1-HC-W	95.5 kN	2958	4.79	Skin/Core delamination due to interlaminar shear	21	1.50
A2-HC-CP	68 kN	3075	4.55	Skin/Core delamination due to interlaminar shear	28.6	2.04

It is worth noting that, a difference in the reading of mid-span strain gauges of core A1-HC-W on both sides of the centerline was observed when reaching a value of 2500 kPa (363 psi) , as shown in Figure 5.28, as well as a difference in the readings of displacement potentiometers at the mid-span. This may be attributed to a differential stiffness between both sides of the core webbed

laminate structure due to a difference in their fiber volume fraction V_f which is typically caused by unbalanced resin distribution.
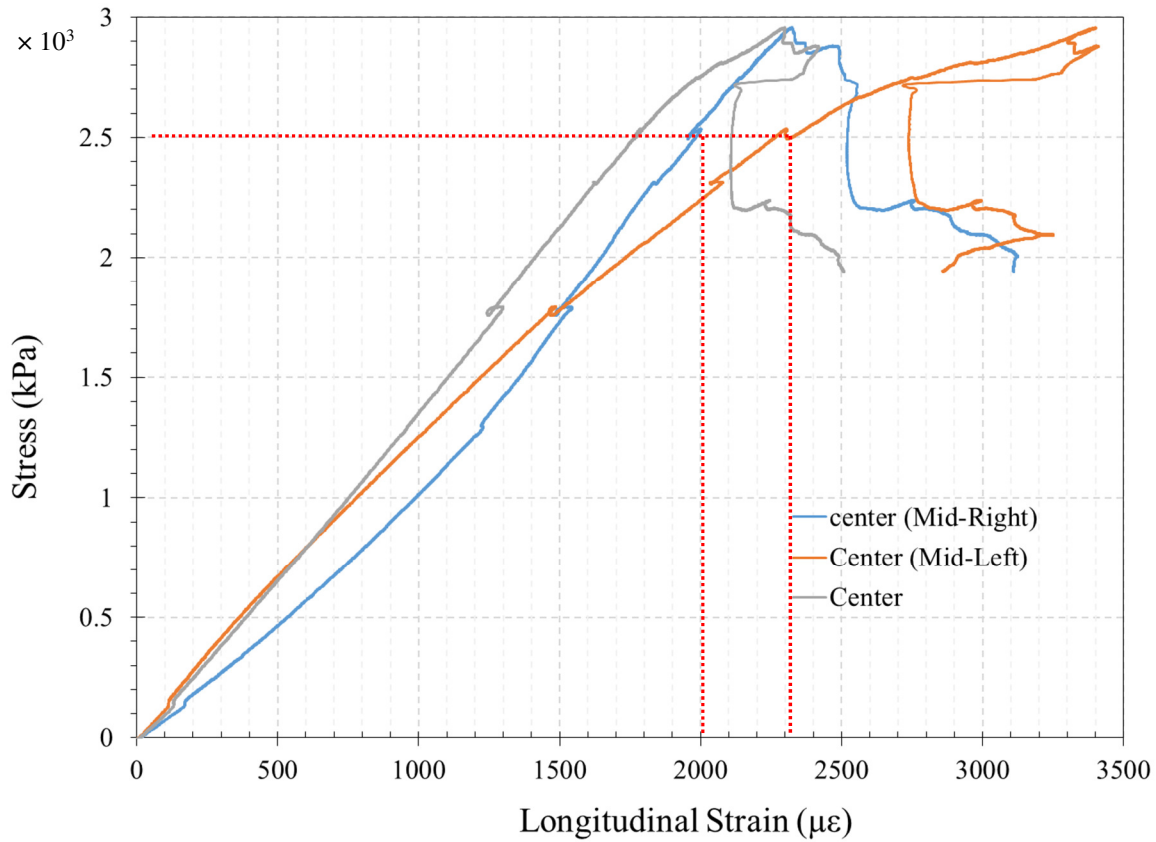
Figure 5.28 Stress-Strain relation-ship of core A1-HC-W in the mid-span location

5.5.2 FLATWISE COMPRESSION TEST

It was observed that, neither crushing of the webs nor failure of the joints between the skin and the core webs occurred during the compression test for both specimens A1-HC-W and A2-HC-CP. However, a delamination failure due to in-plane shear between the bottom skin and the core corners took place, resulting in a total separation of the core web laminate and the skin joint, followed in some samples by a full separation of the honeycomb halves at the edges from the core. However, no single sign of damage was observed for the rest of the web laminated structure inside the core. As a result, it is recommended to fully wrap the edge honeycomb halves of the core, as well as overlapping the upper and lower skins at core sides to prevent this premature delamination failure. This is highly expected to increase the compressive strength of both cores. A photograph

showing the failure mode and the location of failure is presented in Figure 5.29 for both cores A1-HC-W and A2-HC-CP.

It can be noticed that the buckling failure mode was avoided in all samples due to the high critical buckling load achieved by the core structural geometry as described in Section 5.3.3.
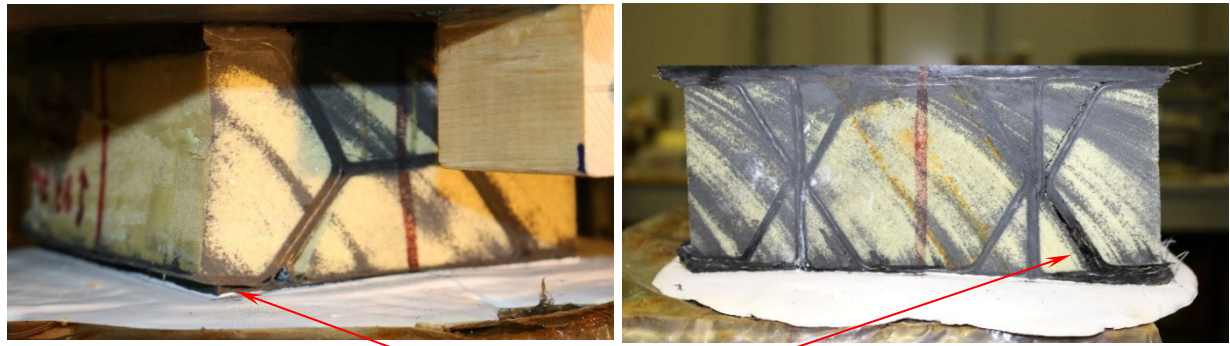
In plane shear failure

Figure 5.29 Photograph illustrating the in-plane shear failure of cores during the compression test

Despite the premature failure observed for both cores, the core A1-HC-W achieved nearly similar compressive strength to the balsa system with a difference of 6.55%. In addition, it has the best stiffness with an average core deformation of 0.55 mm. The compressive strength to areal weight ratio compared with balsa core was increased to 1.44 times the balsa system. On the other hand, the premature failure of A2-HC-CP resulted in a minimum core compressive strength. However, the core has a similar compressive strength to areal weight ratio and it was stiffer than the balsa system. Table 5.5 summaries a comparison of the flatwise compression test results.

Table 5.5. A comparison of flatwise compression test results

Core	Failure Load (kN)	Average Deformation (mm)	Compression Strength (kPa)	Failure mode	Compression Strength /Areal Weight Ratio	Normalized ratio
Balsa Core	254 kN	2.8	9240	Crushing	42	1.0
A1-HC-W	225 kN	0.55	8635	Side Honey Comb / Skin interlaminar shear	61.2	1.44
A2-HC-CP	87 kN	1.05	4442	Side Honey Comb/ Skin interlaminar shear	41.4	0.99

106

5.5.3 COMPARISON WITH CFRP WEBBED CORES

The cores C4-TC and C5-CC developed by Robinson and Kosmatka (2008) achieved a compression strength of 16100 kPa (2330 psi) and 15300 kPa (2220 psi), respectively. These values were obtained by fabricating the cores using Shell Epon 862 epoxy with Lindride 6 hardener. Due to the difficulty in obtaining the same material and epoxy formulation used by Robinson and Kosmatka (2008) to develop all the core specimens, the webbed cores were reproduced using the current study characterized material in order to constraint the evaluation of cores to the deck structural shape. From a strength point of view, the web laminate thickness is governed by the compressive strength (Robinson and Kosmatka, 2008). Therefore, only the compression test was conducted for the webbed cores and the current study cores for re-evaluation. Despite the premature failure occurred for cores A1-HC-W and A2-HC-CP as a result of the delamination failure at corners as previously explained, it was found that both cores A1-HC-W and A2-HC-CP achieved higher compressive strength than C5-CC by 2.11 and 1.08 times, and better compressive strength to areal weight ratio by 2.78 and 1.88 times, respectively, whereas their compressive strength was less than core C4-TC by 25.09% and 61.9%, respectively. However, it has a more stiffness by 2.3 times than that of core C4-TC.

With respect to the design recommendation explained earlier for wrapping the honeycomb halves at the edge of the bridge deck and overlapping the upper and lower skins on the edge sides, the failure mode will be transformed to be either a skin/core delamination or crushing of the core webs. Therefore, an expected higher compressive strength will be achieved for both cores, such that the webs will be efficiently functioned to carry the compressive stresses. Based on a Classical Lamination Theory (CLT) analytical analysis of A1-HC-W and A2-HC-CP web laminates, and using Tsai-Wu and Maximum Stress failure theories, it is expected that core A1-HC-W is able to resist an average compression strength obtained from the two failure theories of 18872 kPa (2737 psi), which is higher than the compression strength of core C4-TC by 1.62 times using the current study material and resin formulation, and by 1.17 times of the result obtained by Robinson and Kosmatka (2008). In addition, a higher compression strength to areal weight ratio of 1.21 times is predicted compared with the result obtained by Robinson and Kosmatka (2008). The core A2-HC-CP is expected to resist an average compressive strength of the two failure theories of 12060 kPa (1749 psi), this value provides a similar compressive strength to areal weight ratio of core C4-TC

presented by Robinson and Kosmatka (2008). A summary of the compression test results of the CFRP cores is illustrated in Table 5.6. In addition, a comparison is presented in Table 5.7 of the predicted compressive strength when the aforementioned design recommendation is satisfied for the proposed cores with the webbed core results of Robinson and Kosmatka (2008).

Table 5.6. A comparison of compression to areal weight ratio between Robinson and Kosmatka (2008) reproduced cores and the current study

Core	Failure Load (kN)	Average Deformation (mm)	Compression Strength (kPa)	Web thickness (mm)	Failure mode	Compression Strength /Areal Weight Ratio	Normalized ratio
C5-CC	101 kN	1.985	4101	4.2	Web Buckling	22	1.0
C4-TC	273 kN	1.278	11654	4.0	Web Crushing	78.6	3.57
A1-HC-W	225 kN	0.55	8635	3.2	Side Honey Comb/ Skin interlaminar shear	61.2	2.78
A2-HC-CP	87 kN	1.05	4442	4.0	Side Honey Comb/ Skin interlaminar shear	41.1	1.88

Table 5.7. A comparison of predicted compression strength results of the proposed core with the webbed cores presented by Robinson and Kosmatka (2008)

Core	Failure Load (kN)	Compression Strength (kPa)	Web thickness (mm)	Compression Strength /Areal Weight Ratio	Normalized ratio
C5-CC	242 kN	15300	4.2	82	1.0
C4-TC	400 kN	16100	4.0	111	1.35
A1-HC-W	530 kN	18872	3.2	134	1.63
A2-HC-CP	236 kN	12060	4.0	112	1.37

108

5.6 NUMERICAL SIMULATION

A progressive failure analysis for the three points loading and the flatwise compression tests was performed using a three dimensional finite element simulation of the deck cores. The numerical results obtained, namely: failure modes, deflections, strains, compressive, and shear capacities, were compared and validated with the experimental results in order to assess the reliability of the model for further complex and fatigue analysis in later studies. The progressive failure analysis included stress analysis, failure analysis and material property degradation under incremental loadings, such that geometrical and material nonlinearities were performed. The stress analysis was conducted using a three dimensional FE modeling in ANSYS software, the core models were built using the ANSYS Parametric design language (APDL). The failure analysis and the material property degradation were based on Hashin failure criteria (Hashin, 1980) and a set of degradation rules which were implemented in the ANSYS patch code.

5.6.1 FINITE ELEMENT MODELING

The FE geometry of the proposed cores was created using the eight node "SOLID185" ANSYS brick element to visualize accurately the laminate damage degradation in every layer within the thickness. A homogeneous structural element geometry was considered for modeling the polyisocyanurate foam and the rich resin area in each core, whereas a structural layered element geometry was chosen to define the carbon/epoxy laminate with different ply orientation. In order to achieve a highly accurate interlaminar stresses of the composite laminates, every web laminate was constructed using layered solid elements of specific ply orientation that were stacked together in the thickness direction. The interface connection between the carbon/epoxy element layers and the surface of the foam volume is considered as a glued surface, such that no contact element is considered to simulate the overlap shear failure between the two surfaces as the failure value has to be experimentally quantified. However, a delamination failure at the outer surface of the carbon/epoxy laminate would represent the separation between the two surfaces. An average value for tensile and compressive young's modulus of 13625 kPa (1976 psi), shear modulus of 5512 kPa (799 psi), and Poisson ratio of 0.04 were used for defining the 64 kg/m^3 (4 pcf) foam beams properties. The tensile, compressive, and flexural modulus of the resin matrix was set to an average value of 3.17 GPa. All the aforementioned properties were obtained from the manufacturer, whereas the carbon/epoxy material properties and ultimate strength values used were listed earlier

in Table 5.3. Table 5.8 illustrates the ultimate strength values for the 64 kg/m^3 (4 pcf) polyisocyanurate foam and the resin matrix. After building the core models, a mesh sensitivity analysis was performed which resulted in a converged mesh element size of 2.5 mm (0.1 in) in order to reduce the computational time. The mapped meshing type was used for modeling the majority of the core geometry except the rich resin complex volumes that were meshed using a tetrahedral shapes, as shown in Figure 5.30. The three dimensional type of analysis aims to represent accurately the dimensional stresses

Table 5.8. Ultimate strength properties of the foam and resin matrix and resin matrix

Property	Epoxy resin	(64 kg/m^3) Polyisocyanurate foam
Compressive strength	86200 kPa	524 kPa
Tensile strength	72400 kPa	479 kPa
Shear Strength	123400 kPa	362 kPa
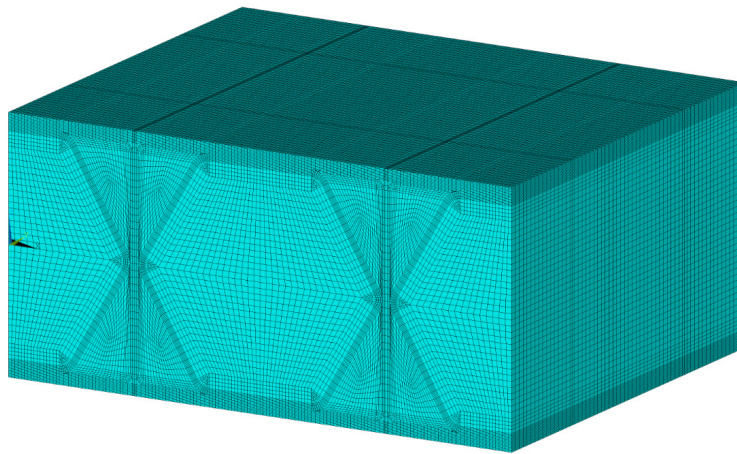
Figure 5.30 Finite element mapped meshing of A1-HC-W core

5.6.2 PROGRESSIVE DAMAGE MODELING

A progressive damage modeling is an iterative procedure that conducts three steps in a single iteration. The procedure starts with stress analysis, based on the model complexity the analysis can be conducted using FE or analytical modeling. The second step detects the model elements failure by applying a suitable failure criterion to the element resultant stresses. Eventually, a material property degradation for the failed element is applied. An illustration for the progressive damage modeling is presented in the flowchart in Figure 5.31.
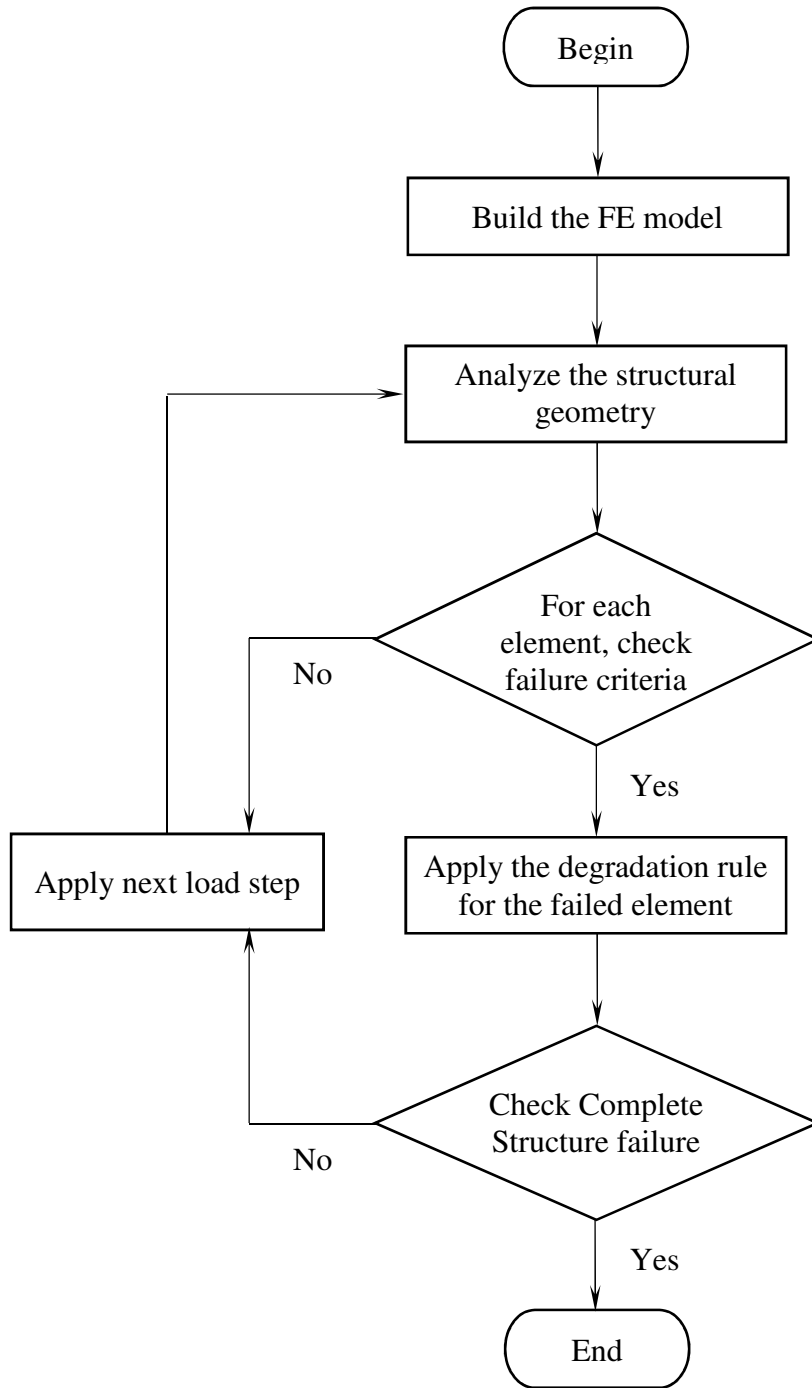
Figure 5.31 Flowchart illustrating the progressive failure model

In the current study, a ply-by-ply stress analysis was performed using FE ANSYS patch code. The failure analysis of composite materials is very complex due its multiple failure mechanisms. Therefore, choosing failure criteria that are able to clearly distinguish between numerous modes of failure are exigent. In the present study, Hashin polynomial failure criteria as

they were modified by Shokrieh *et al.* (1996) were selected for the failure analysis. The selection was based on its simplicity, successful use in simple composite models such as in (Kermanidis, 2000), and ease of implementation to the FE ANSYS code. The Hashin failure criteria consist of seven stress-based interaction equations. The failure modes identified by these equations are matrix tensile, matrix compressive, fiber tensile, fiber compressive, fiber-matrix shear, delamination in tension, and delamination in compressions failures. The failure criteria as presented by Shokrieh *et al.* (1996) are shown in equations 5.1, 5.2, 5.3, 5.4, 5.5, 5.6, and 5.7:

For Matrix Tensile Failure (MTF), If $\sigma_y^{act.} > 0$:

$$\left(\frac{\sigma_y^{act.}}{Y_t}\right)^2 + \left(\frac{\sigma_{xy}^{act.}}{\sigma_{xy}^{ult}}\right)^2 + \left(\frac{\sigma_{yz}^{act.}}{\sigma_{yz}^{ult}}\right)^2 \geq 1 \qquad (5.1)$$

For Matrix Compressive Failure (MCF), If $\sigma_y^{act.} < 0$:

$$\left(\frac{\sigma_y^{act.}}{Y_c}\right)^2 + \left(\frac{\sigma_{xy}^{act.}}{\sigma_{xy}^{ult}}\right)^2 + \left(\frac{\sigma_{yz}^{act.}}{\sigma_{yz}^{ult}}\right)^2 \geq 1 \qquad (5.2)$$

For Fiber Tensile Failure (FTF), If $\sigma_x^{act} > 0$:

$$\left(\frac{\sigma_x^{act.}}{X_t}\right)^2 + \left(\frac{\sigma_{xy}^{act.}}{\sigma_{xy}^{ult}}\right)^2 + \left(\frac{\sigma_{xz}^{act.}}{\sigma_{xz}^{ult}}\right)^2 \geq 1 \qquad (5.3)$$

For Fiber Compressive Failure (FCF), If $\sigma_x^{act} < 0$:

$$\left(\frac{\sigma_x^{act.}}{X_c}\right)^2 \geq 1 \qquad (5.4)$$

For Fiber-Matrix Shear-out Failure (FMSF), If $\sigma_x^{act} < 0$:

$$\left(\frac{\sigma_x^{act.}}{X_t}\right)^2 + \left(\frac{\sigma_{xy}^{act.}}{\sigma_{xy}^{ult}}\right)^2 + \left(\frac{\sigma_{xz}^{act.}}{\sigma_{xz}^{ult}}\right)^2 \geq 1 \qquad (5.5)$$

For Delamination In Tension (DIT), If $\sigma_z^{act} > 0$:

$$\left(\frac{\sigma_z^{act.}}{Z_t}\right)^2 + \left(\frac{\sigma_{xz}^{act.}}{\sigma_{xz}^{ult}}\right)^2 + \left(\frac{\sigma_{yz}^{act.}}{\sigma_{yz}^{ult}}\right)^2 \geq 1 \tag{5.6}$$

For Delamination In Compression (DIC), If $\sigma_z^{act} < 0$:

$$\left(\frac{\sigma_z^{act.}}{Z_c}\right)^2 + \left(\frac{\sigma_{xz}^{act.}}{\sigma_{xz}^{ult}}\right)^2 + \left(\frac{\sigma_{yz}^{act.}}{\sigma_{yz}^{ult}}\right)^2 \geq 1 \tag{5.7}$$

Where the nominators σ_{ij}^{act} are the calculated on-axis stress components of an element in each ply in the *ij* direction and the dominators are their associated ultimate strengths. The on-axis stress components are presented in the schematic drawing in the element level in Figure 5.32
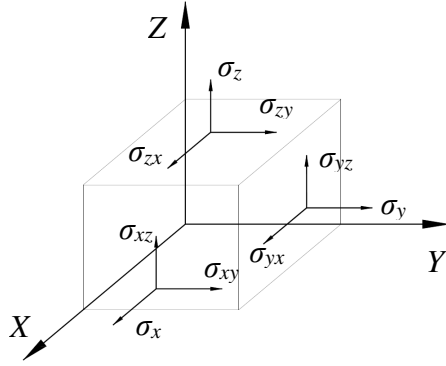
Figure 5.32 On-axis stress components on a layered composite element

5.6.3 MATERIAL DEGRADATION RULES

As illustrated in the schematic flowchart of Figure 5.31, the model starts to check all the failure criteria element by element and ply-by-ply. When any failure criterion is detected a material degradation is applied to that particular element. The degradation rule consists of multiplying the governing material property of the failure by a reduced factor in order to disable the element from carrying a certain load in the next steps. The degradation rule for a matrix tensile or compressive failure is to reduce the properties E_y, and υ_{xy}, such that the matrix cannot carry any subsequent load. For a fiber tensile or compressive failure, all the properties E_x, E_y, E_z, G_{xy}, G_{xz}, G_{yz}, υ_{xy}, υ_{yz}, and υ_{xz} are suddenly reduced, which means no any type of loads can be carried by the failed element. In the case of fiber-matrix shear failure only the loads in the fiber and transverse to fibers

direction can be carried, this is achieved by reducing the values of G_{xy}, and v_{xy}. The delamination failure in tension or compression has two modes, the first mode affects the carrying capacity of the laminate in the z direction, and the second mode affects the interlaminar shear carrying capacity between the layers. Therefore, the properties E_z, G_{yz}, G_{xz}, v_{yz}, and v_{xz} must be reduced.

5.6.4 SHEAR TEST SIMULATION

A finite element simulation of the three points loading test was performed for the cores A1-CH-W and A2-CH-CP. The boundary conditions applied to the core structure were hinged and roller supports spaced 610 mm (24 in), and similar to that conducted in the experimental testing. A linearly increasing load protocol was applied in the center of the top skin to an area equals to the rectangular steel loading plate contact with the specimen. An incremental value of 5 kN up to a total load of 350 kN is applied on the beam. Only quarter of the beam geometry was created and two planes of symmetry are assumed in order to reduce the computational time.

The progressive failure modeling of both cores A1-HC-W and A2-HC-CP showed an agreement with the delamination failure mode due interlaminar shear detected in the experimental work, such that the stress-component σ_{yz} has the highest value and the major contribution in the delamination failure. Figures 5.33.a, b, and c show the damage propagation predicted by the core A1-HC-W model before failure during a three points loading application at the load steps 90 kN, 95 kN, and 100 kN, respectively. The pictures show a quarter section of the core where a delimitation failure is propagating between the core and the skin surfaces. In addition, a comparison between the numbers of the accumulated failed elements by each failure criterion per load step is presented in the charts for the three different load steps. Figure 5.34.a, and 5.34.b present the failed elements under delamination in tension and compression of both cores A1-HC-W and A2-HC-CP, respectively. It can be noticed that the progressive model was able to depict the observed mode of failure in the experimental test. In addition, Figure 5.35 shows the degraded elements between the core structure and the upper skin, which resulted in a partial separation just near the machine loading foot print.

In the finite element validation, the total core failure is recorded at 10 percent change in the slope of the load-deflection curve. A summary of the validation results of the FE element progressive model degradation with experimental work is presented in Table 5.9.
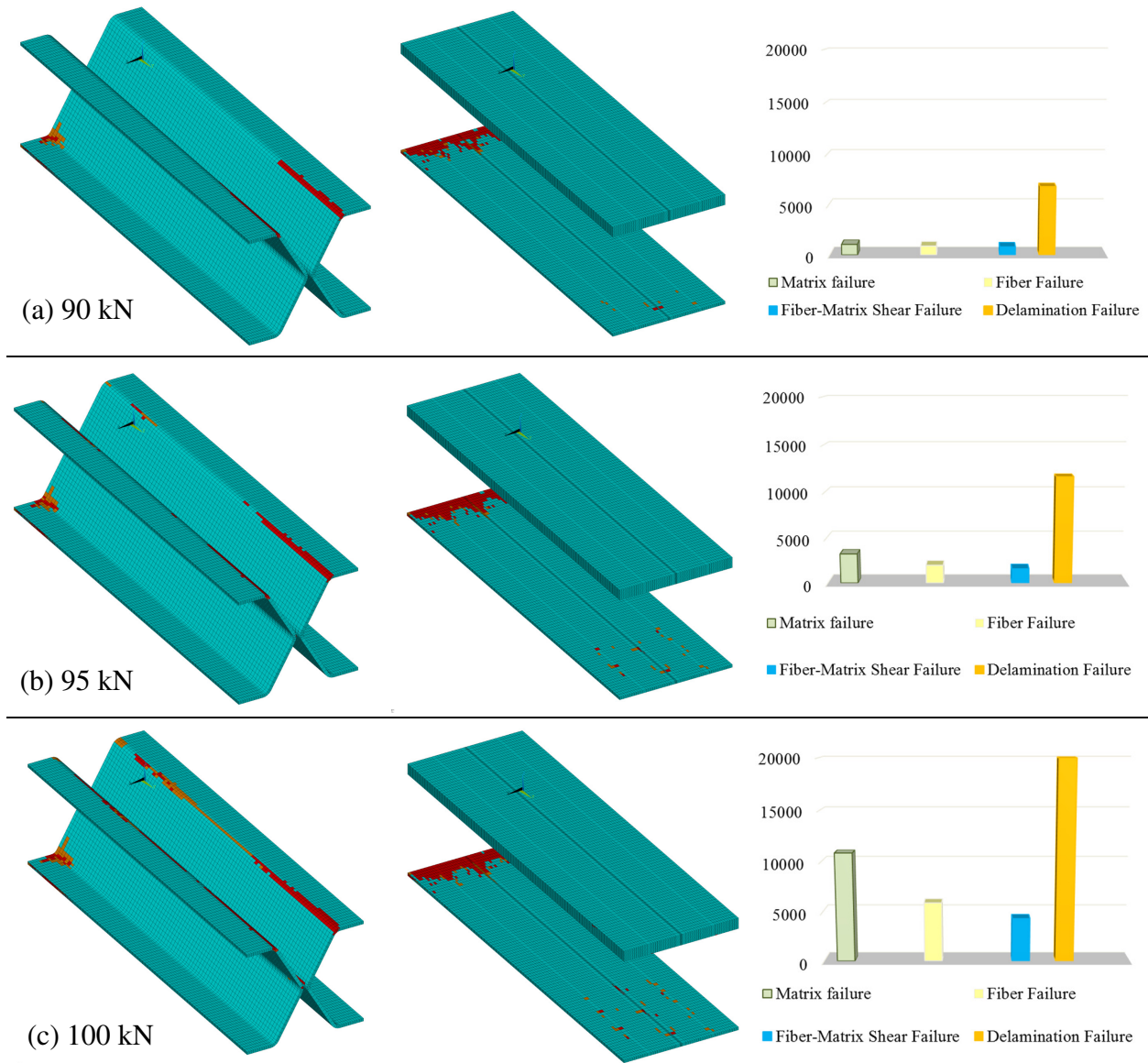
Figure 5.33 Illustration of the progressive damage predicted by the model in a three points loading simulation at different load steps

Table 5.9. FE progressive modeling and experimental validation results of three points loading test

Core type	Shear Strength			Deformation			Mid-span strain			¼ Span strain		
	Exp. (kPa)	FE (kPa)	Diff. (%)	Exp. (mm)	FE (mm)	Diff. (%)	Exp. ($\mu\varepsilon$)	FE ($\mu\varepsilon$)	Diff. (%)	Exp. ($\mu\varepsilon$)	FE ($\mu\varepsilon$)	Diff. (%)
A1-HC-W	2958	3118	5.1	4.79	5.45	12.1	2561	2299	-11.4	-1330	-1135	-17.1
A2-HC-CP	3075	3230	4.8	4.55	4.63	1.76	1713	1881	9.8	-1298	-1410	8.6

115

Figure 5.34 Pictures showing failure validation under delamination in tension and compression of both cores A1-HC-W and A2-HC-CP in three points loading test
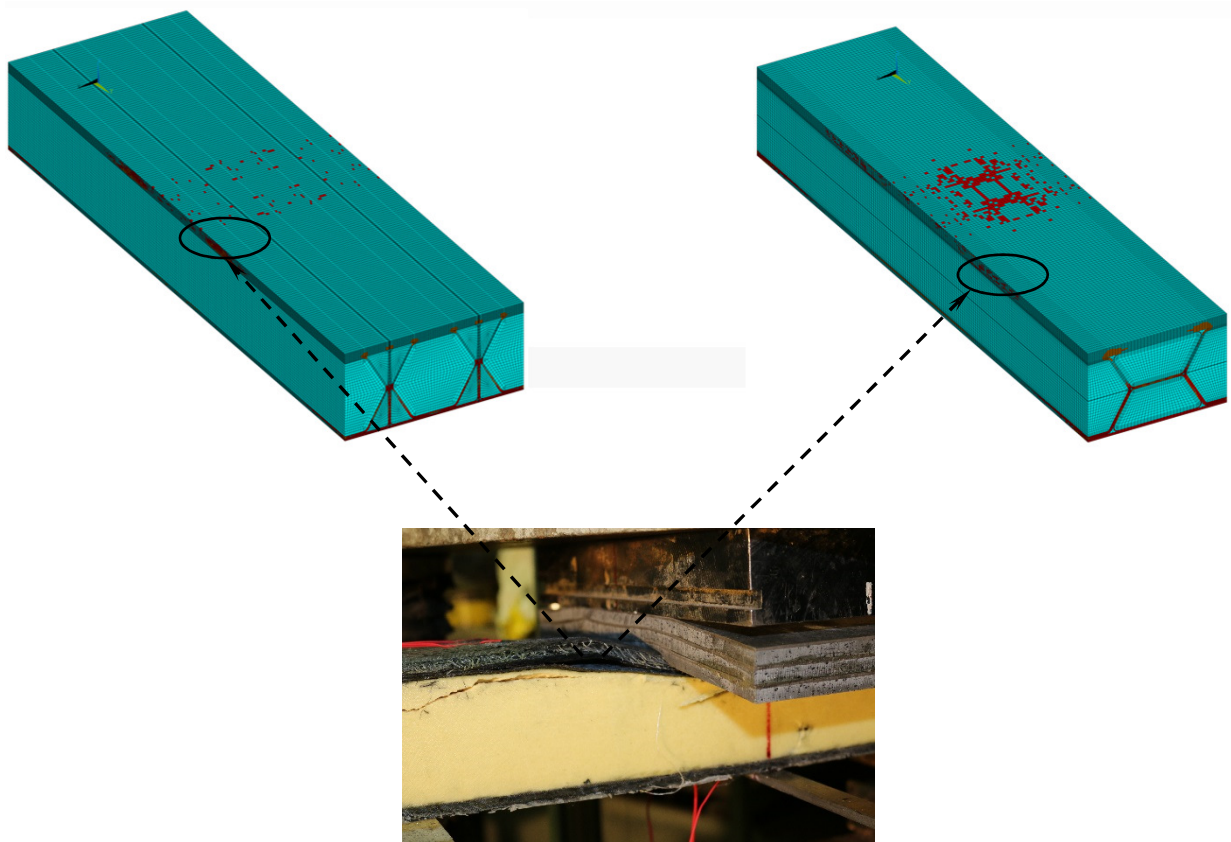
Figure 5.35 Partial separation of the upper skin and core cross-section due to delamination failure just near the machine loading foot print

5.6.5   COMPRESSION TEST SIMULATION

In the progressive failure simulation of a compression test, the lower skin nodes of each core FE model were prevented from the translation in x, y, and z directions. A linearly increasing pressure load protocol was applied on the upper skin of each core. All the upper skin surface nodes were coupled together in the three dimensional translation in order to simulate the rigid body motion of the loading steel flat plate. The progressive damage failure criteria were applied. The simulation of the compression test progressive failure was conducted to validate the premature failure occurred for both core corners due to the interlaminar shear delamination. The degraded failure analysis and FE simulation proved that both cores A1-HC-W, and A2-HC-CP would fail due to a delamination separation between the honeycomb corners and the skin, which supports the design recommendation for a full confinement of the core at the sides. A comparison between the experimental results and FE progressive simulation is listed in Table 5.10, which showed a good agreement with the experimental work. Figure 5.36 presents the number of failed elements counts at different load steps, it can be noticed that the delamination in shear is the dominant failure mode. Figure 5.37 illustrates the degraded failure of core A1-HC-W during flatwise compression. Figure 5.38 presents the degraded failure models of both cores under flatwise compression and the observed location of delamination failure due to interlaminar shear at failure load.

Table 5.10. FE progressive modeling and experimental validation results of Flatwise compression test

Core type	Compressive Strength			Deformation		
	Exp. (kPa)	FE (kPa)	Diff. (%)	Exp. (mm)	FE (mm)	Diff. (%)
A1-HC-W	8635	9259	6.7	0.55	0.8	31
A2-HC-CP	4442	4830	8.7	1.05	1.15	9.5
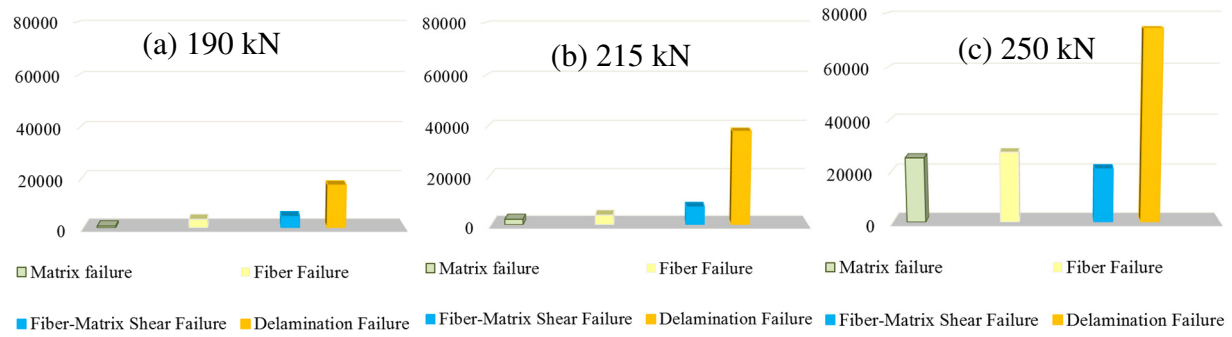
Figure 5.36 Plot charts of the number of failed elements counts at each failure criterion

(a) 190 kN

(b) 215 kN

(c) 250 kN
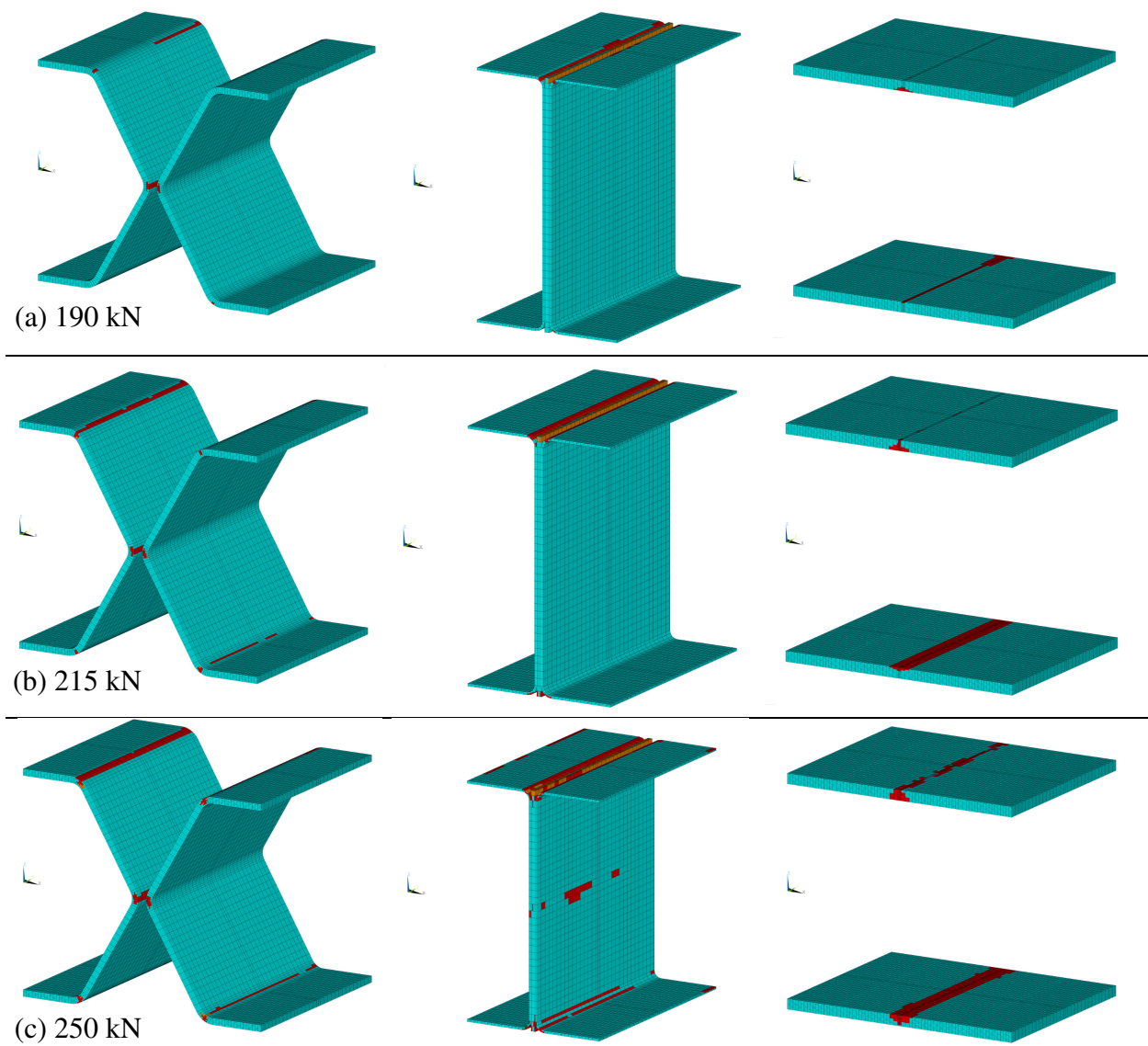
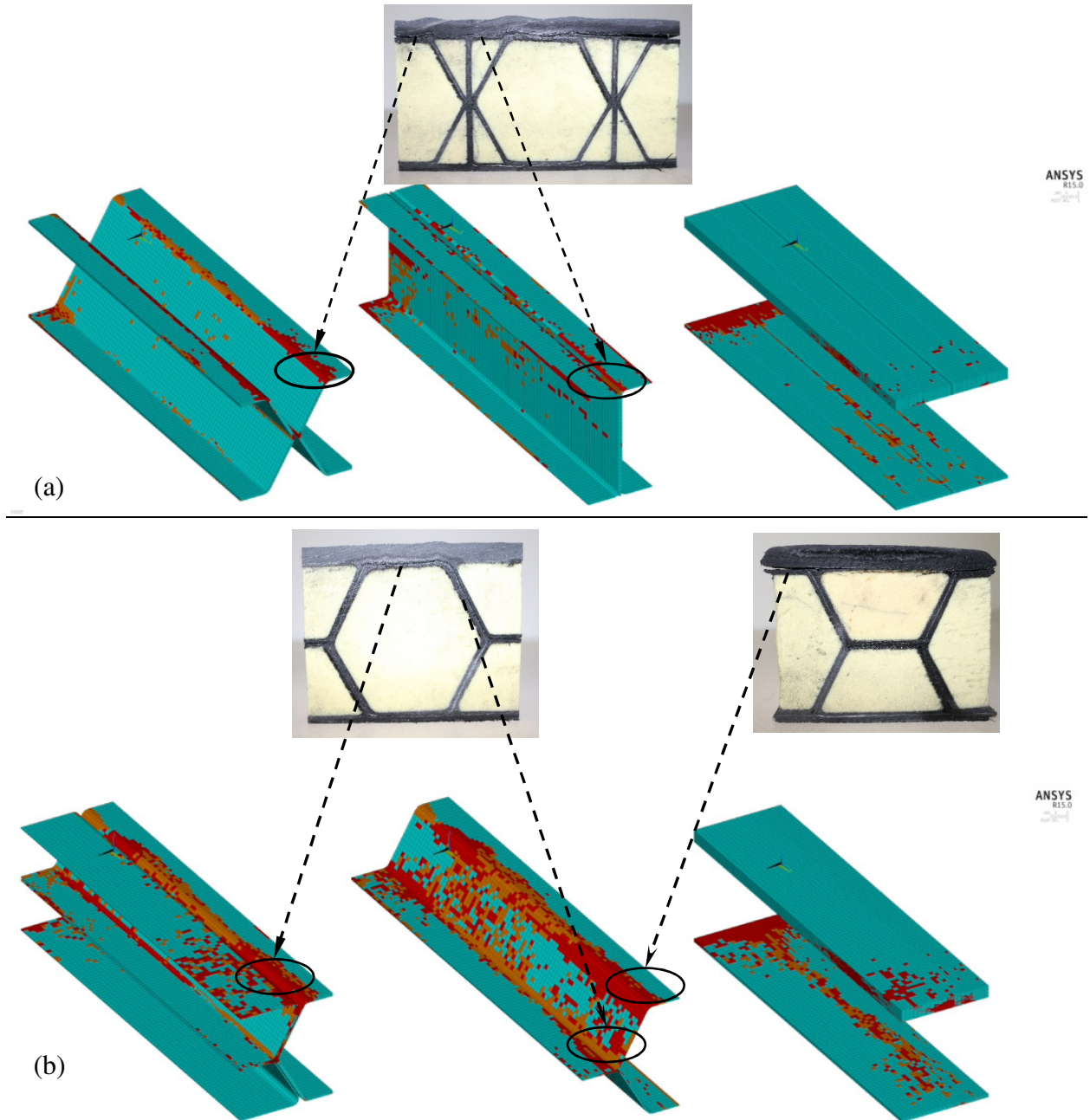**Figure 5.37** Illustration of A1-HC-W degraded model in a compression test at different load steps
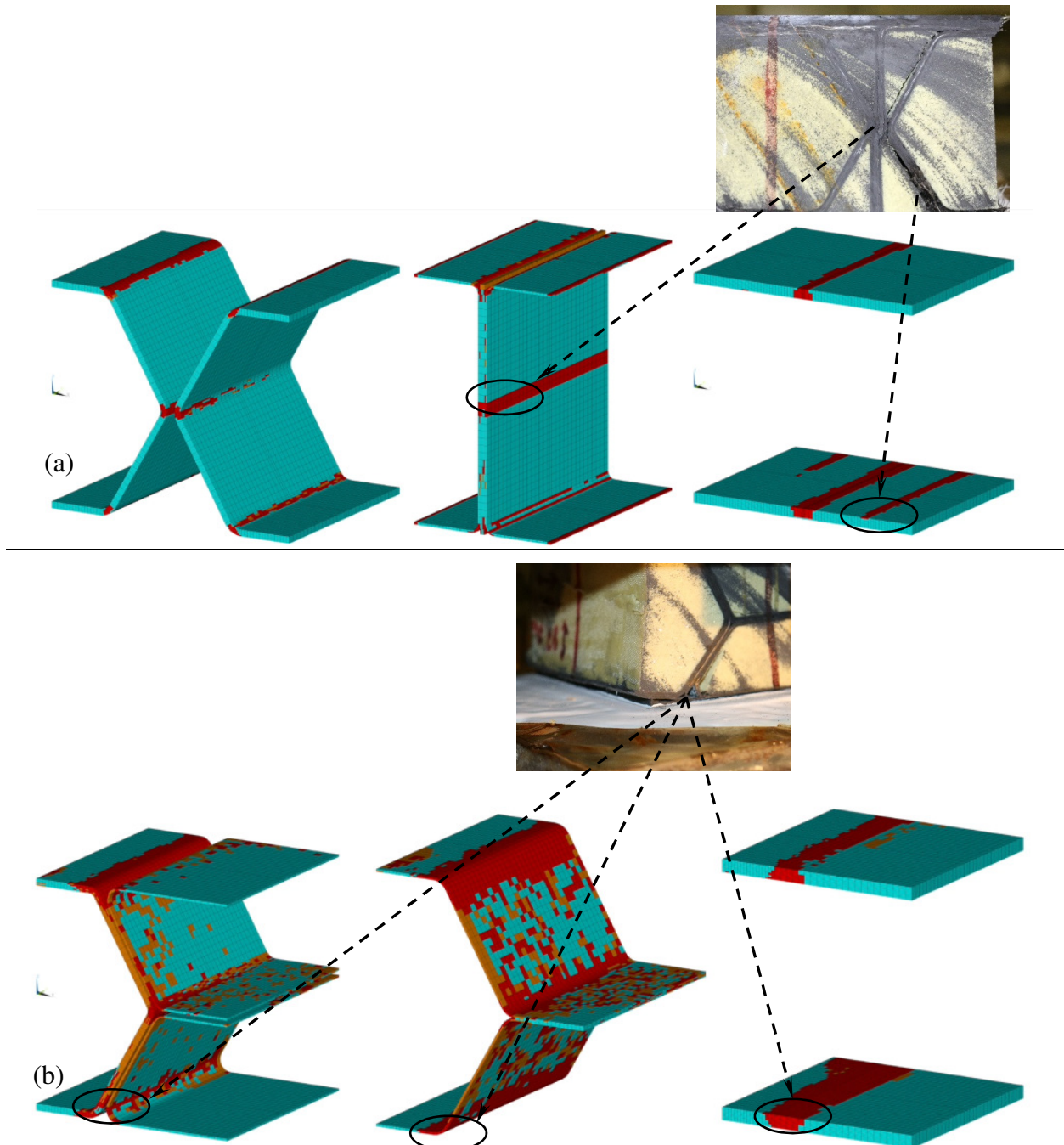
Figure 5.38 Pictures showing failure validation under delamination in tension and compression of both cores A1-HC-W and A2-HC-CP in the flatwise compression test

120

5.7 SUMMARY AND DESIGN RECOMMENDATIONS

Based on the experimental testing results and the degraded numerical validation, guidelines are presented for the design of light weight composite cores with honeycomb beams that are configured in different structural geometries. In addition, performance charts and presented for the designer in order to select the appropriate honeycomb bas ed sandwich core out of a variety of core selections in the literature.

For the shear strength, it is worth noting that the similar shear performance achieved by cores A1-HC-W and A2-HC-CP with the balsa system was based on a carbon/epoxy laminate that is nearly of 35 MPa shear strength capacity, see Figure 5.36. On the other hand, the carbon fibers and resin formulation used to fabricate the webbed cores developed by Robinson and Kosmatka (2008) provided a 386 MPa shear strength. Core A1-HC-W failed due to delamination of interlaminar shear between the core and the skin surfaces. This mode of failure represents the maximum shear strength that can be carried by this core structural configuration. Another epoxy formulation that could provide only an average value of shear strength between the two previously mentioned values would expect to highly increase the shear strength of the fabricated core. In addition, the material cost and consequently fabrication cost would not be highly increased when compared to the webbed cores that were fabricated using a special epoxy formulation.

The fabrication of core A1-HC-W experienced three different trials using the SCRIMP technique with different infusion strategies until a succesful infusion was achevied, this resulted in a consumption of large amounts of resin and reinforcing fiber materials. The difficulty of having a successful infusion of core A1-HC-W using the SCRIMP technique can be attributed to the existence of several non straight and vertical flow baths, i.e. core webs, within the core cross-section. Moreover, the successful trial achieved a non uniform distribution of the resin all over the core cross-section width, which resulted in a variable fiber volume fraction, hence a relative difference in webs stiffnesses. The torsional moment detected at the end of the core shear test can be attributed to the existence of variation of webs stiffness. Therefore, it is recommended to fabricate the sandwich composite cores that have a similar construction of flow paths using the FRIM, or OOA processing methods. For the FRIM processing method, no special tools is used other than that used for the SCRIMP technique. Using the resin films to infuse the core webs will

ensure a highly uniform resin distribution and full wetting of the inside core fibers, and at the same time, the capability of manufacturing large-scale structures will be maintained. The OOA would provide the highest quality of fiber/epoxy laminates within the core cross-section, and its applicable for manufacturing these type of cores as the service temperature of the used foam is higher than 150 C$^{\circ}$. This would make it possible to use the prepregs. The only concern for the FRIM and OOA application is the relative cost of material, which can be minimized through an optimized laminate thickness.

Both the honeycomb and the trapezoidal shaped beams of core A2-HC-CP were wrapped with different number of carbon layers in order to construct the web laminate thickness and to distibute the shear forces into the skin in both sides of the web. Despite doing this, the core failed in delamination due to interlaminar shear for both core cuts; and it was found that the distibuted number of continuous layers from the webs into the skin has a high contribution in the equal distribution of shear forces. Therefore, for core webs spaced 80 mm as in core A2-HC-CP, it is recommended to equally interleave the continous fibers from the webs into the skin, such that a concentration of shear forces over a single side of the skin can be avoided.

From the flatwise compression test, it was found that both cores A1-HC-W and A2-HC-CP would experience a premature failure due to delamination of interlaminar shear at the core sides. In addition, the core laminate webs will not function to its ultimate compressive capacity. Finding this, a full confinement of the core sides is recommended by overlapping the upper and lower skins at the core sides as well as the full wrapping of the side foam beams. This will ensure higher compressive stresses of the core webs. By satisfying this recommendation and the consideration of full web compressive capacity, core A1-HC-W and core A2-HC-CP would achieve 2.04 and 1.3 times increase in compressive capacity than the balsa core, and lighter by nearly 36% and 49%, respectively. In addition, core A1-HC-W would have 1.17 times increase in the compressive capacity than core C4-TC, which is considered the highest compressive strength achieved for a deployable bridge deck core in the literature.

In order to aid for the core selection from a strength prespective, a plot of the shear strength, compressive strength of the cores A1-HC-W and A2-HC-CP as well as the predicted compressive strength after satisfying the recommendation of wrapping the core sides is presented in Figure 5.39, the values are compared to the balsa-baseline performance and all webbed cores presented

by Robinson and Kosmatka (2008). When light weight is a major term of core selection for the designer, a plot in Figure 5.40 could be used to present the strength performance of each core reference to its areal weight, the proposed cores performance/areal weight ratio are plotormalized to the balsa core system as the base-line performance and the values are compared with all webbed cores presented by Robinson and Kosmatka (2008).

The progressive failure modeling conducted in this study showed a good agreement with experimental testing results, in addition it provided a full picture of the carbon/epoxy laminate degradation within the core strucutre through the whole testing history. Figure 5.41 shows a validation plot of experimental and numerical strength performance to core areal weight ratios, the plot shows both testings are of a close agreement and both proposed cores exceeds the balsa base-line performance except for the compressive strength/areal weight ratio of core A2-HC-CP that has a similar balsa-core performance. however, the numerical results are slightly higher than the experimental as it represnts a perfectly ideal case that is does not exist in real tests in terms of coherent laminate stiffness and filled resin rich areas.
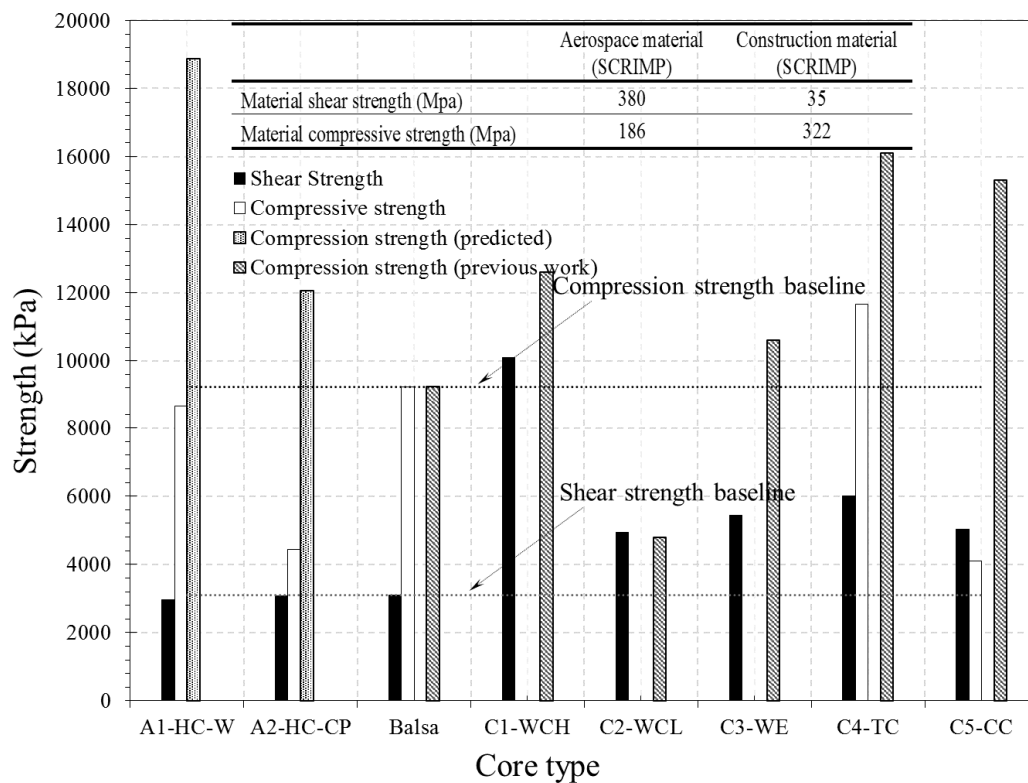
Figure 5.39 Plot of shear and compressive strength performance of different sandwich cores

123
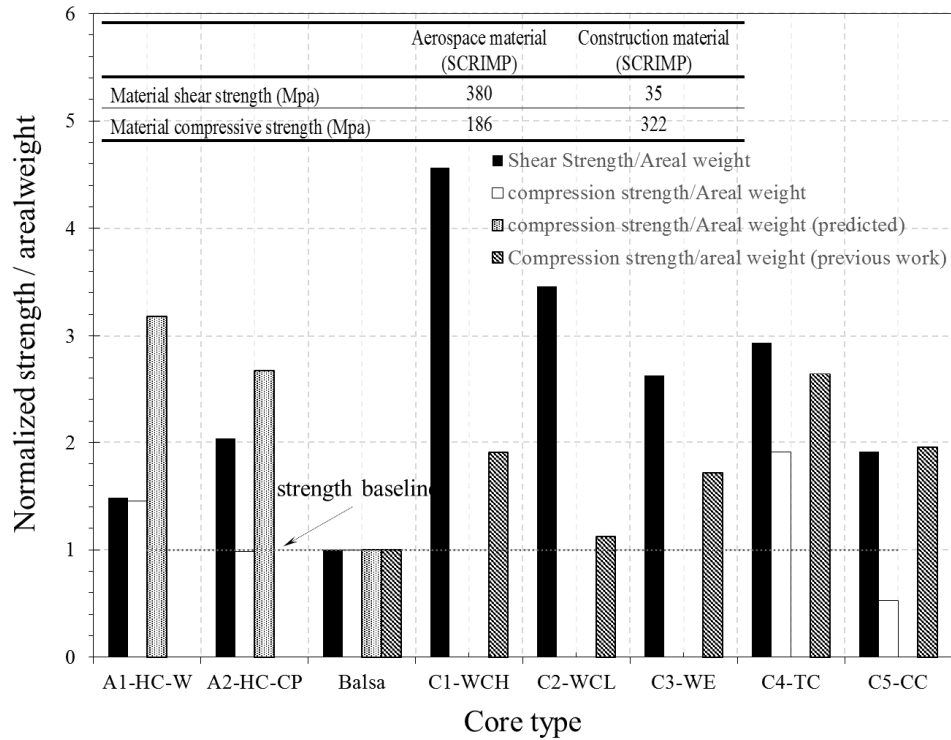
Figure 5.40 Plot of shear and compressive strength to core areal weight ratio normalized to balsa
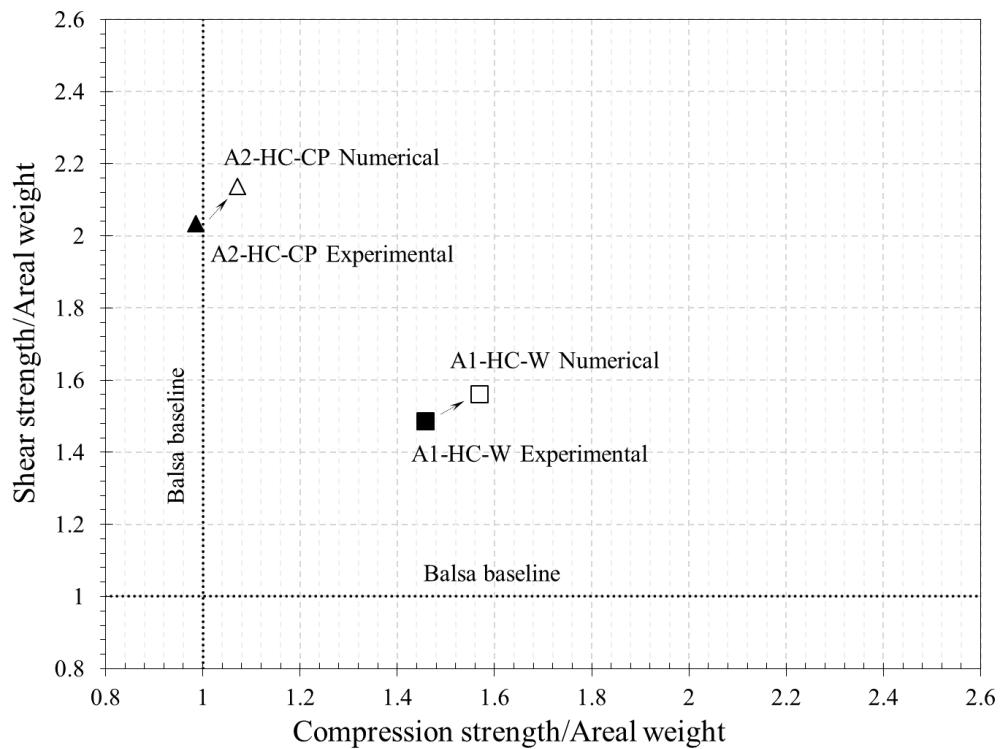
Figure 5.41 Plot of experimental and numerical strength performance to core areal weight ratios

In general, cores A1-HC-W, and A2-HC-CP were tested against one-way bending application. However, core A2-HC-CP was designed for a bi-directional bending capability, such that the corrugated preform laminate within the core cross-section carries the bending loads in the transverse direction. If a specific lateral bending capacity is recommended, tuning of the corrugated preform fabric thickness and plies orientation have to be considered. Core A2-HC-CP will be tested in a later work for bi-directional bending applications. On the other hand, It has to be noted that all the proposed cores are assumed to serve under normal climate conditions. Therefore, no residual stresses due to temperature and humidity are taken into consideration.

Finally, it is worth mentioning that, the material characterization through coupons testings and the post cure of the fabricated material were conducted in the mechnaical laboratories in Concordia University, whereas, the flatwise compression and shear strengths were examined in the structures laboratory of concordia univeristy.

5.8   CONCLUSIONS AND PERFORMANCE CRITERIA

An assessment of the expected weight savings by the findings of this study is performed through replacing the balsa core system of the CAB deployable bridge with the proposed sandwich composite cores. The deck structure of the CAB system has a weight of 21.73 kN (4884 lb) which represents almost 39% of the bridge total weight which is 56.63 kN (12730 lb). The CAB system is capable of supporting a military loading class of MLC100 (Kosmatka et al., 2000). Both cores A1-HC-W and A2-HC-CP meet the shear strength of the balsa system using the characterized material, at the same time, both cores comply with the TDTC requirement of 1.8 safety factor of the maximum applied working compression load, namely: the MLC100 tracked vehicle pad load in case of the CAB system. Moreover, at least a value more than 2.2 margin of safety factor is achieved by the core A2-HC-CP which has the minimum compressive strength. Therefore, the expected weight saving for replacing the balsa system by the current sandwich composite cores A1-HC-W and A2-HC-CP is ranging from 36% to 51% of the deck structure's weight, which represent 14% to 20% of the CAB deployable bridge weight, respectively.

Strength Optimization of Composite Deployable Bridge Decks

6.1   INTRODUCTION

The use of composite materials in many structural applications is found to be very advantageous as they provided high strength to weight ratio. Although composites are excellent replacement of metallic materials in the application of deployable bridges, as proved in Chapter 5, the analysis and design of composite structures is very complex compared with the metallic structures. A remarkable benefit of using composites is the capability of varying the material orthotropic properties to meet a specific structural need. In addition, minimizing weight and cost are other factors that can be taken into consideration, laminate stacking sequence (ply orientation) is the main design variable to control and achieve these designs objectives. The possibility of reaching an effective design while satisfying multiple failure criteria and the difficulty of obtaining the best design values out of a large set of design variables make design optimization the efficient tool for satisfying the design requirement. For a deployable bridge application, structural laminates in the composite decks are subjected to multiple loading conditions that cannot be represented in a laboratory test except in the scaled structure prototypes. For instance, a biaxial load in tension and compression can significantly decrease the compressive strength of a unidirectional composite laminate. Therefore, the maximum strength design optimization of sandwich composite decks while considering different types of loading conditions is investigated in this Chapter. Standard PSO and the proposed algorithm CD-PSO are modified to meet the discrete nature of composites design. Moreover, the CD-PSO is integrated with the Harmony search technique and a fly-back mechanism to handle the constraints violation and redirect the swarm search into feasible regions. The developed algorithm is named HCD-PSO. A computationally efficient analytical model implementing the Classical Lamination Theory (CLT) is developed. The stacking sequence of the

laminate fibers is considered as the design variable to maximize the margin of failure with respect to the applied loadings. The failure analysis is conducted using the Tsai-Wu failure criterion.

In this chapter, the design approach of composite laminates and the design safety factors recommended by the Trilateral Design and Testing Code (TDTC, 2005) for deployable bridges are clarified. Analysis of the maximum applied loads of different MLC vehicle classes on a deployable bridge structure of 12 m is presented and the corresponding applied loads on the sandwich core are demonstrated. Following, the stress and strain laminate analysis using the Classical Lamination Theory (CLT) in composite plates is briefly described. The optimization problem formulation for the maximum strength design of composites using the HCD-PSO algorithm is represented. Finally, the standard PSO and CD-PSO are applied and a comparison of the results is summarized.

6.2   DESIGN APPROACH

The design approach of the composite deployable bridges follows a Limit State Design provisions (LSD), the design criteria deals with the relationship of:

    (a) Stresses and strains occurring in a structural material under an external applied loads,

    (b) Stresses and strain capacities of the structural material element,

    (c) Separation between the actual stresses and strains values and the structural material capacity by an acceptable factor of safety.

The relationship concept for the imposed load and the material resistance can be clarified as in Figure 6.1 in the shape of bell curves distribution along with the design limits, in which, the design loads (working loads) are taken as the maximum expected static loads of the hypothetical vehicles based on TDTC requirements or real vehicle loads of the same loading class, these working loads take into account the impact, side-slope and eccentricity factors. The design properties of the composite materials are determined from coupon tests and derived using a standard statistical tests of the test data values. The B-basis allowable property is the statistical test that is used to derive the material design property of sandwich composite cores, in which 90% reliability of the fabricated material will not fail at the allowable strength value. This is represented as follows

$$\sigma_{B-basis} = \sigma_{av.} - (N \cdot S_{dv})$$
(6.1)

where $\sigma_{B\text{-}basis}$ is the B-basis allowable property, $\sigma_{av.}$ is the average strength test value, N equals to 3.0407 for five tested coupons and S_{dv} is the standard deviation of the tested values. The TDTC specified a safety factor of 1.8 for B-basis allowable or 50% of the ultimate fiber strain for the material resistance. The margin of safety (*M.S.*) shown in Figure 6.1 can be defined as the separation factor between the maximum working load and the factored material resistance based on B-basis allowable, *M.S.* can be defined as:

$$M.S. = \left(\frac{\sigma_{all.}}{\sigma_w \cdot F.S.} \right) - 1 \tag{6.2}$$

where $\sigma_{all.}$ is the allowable stress for a given lamina (B-basis allowable), $\sigma_{w.}$ is the actual stress for a given lamina at working load, and *F.S.* is an applicable factor of safety.
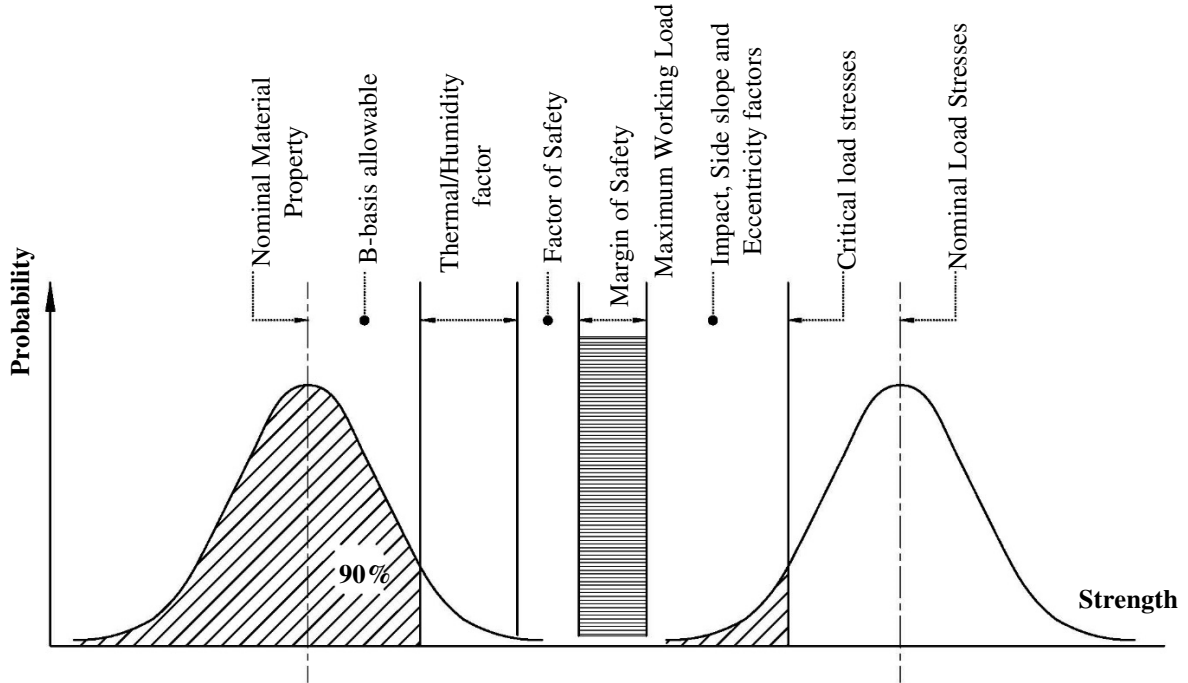
Figure 6.1 Design approach definition (Kosmatka *et al.*, 2000)

6.2.1 LOADS ANALYSIS

A deployable bridge system is subjected to many unusual operational services, such as, crossing a gap of high vertical slope between the near and the far banks, the transverse slope misalignment between the near and the far banks, the eccentric vehicle loads for normal crossing of the road, and the travelling vehicle impact loads. The aforementioned service conditions, may induce high different stresses all over the bridge cross-section, and the stresses may become higher when

several service conditions are combined together. Therefore, the Trilateral Design and Testing Code for Military Bridging and Gap Crossing Operations (TDTC, 2005) outlined specific load factors in order to include the effect of these service conditions into the design of deployable bridges. The strength design optimization of composite cores in the current study is in compliance with these design provisions. Table 6.1 summaries the load factors applied to nominal vehicle loads.

Table 6.1: Factors applied to nominal load

Loading class	Impact factor		Side-slope	Eccentricity
	Moment	Shear		
MLC30	1.15	1.05	1.26	
MLC50	1.15	1.06	1.26	
MLC70	1.15	1.2	1.26	
MLC100-(wheeled)	1.15	1.2	1.09	1.13
MLC100-(Tracked)	1.15	1.2	1.07	1.03

The MLC30, MLC50, MLC70, MLC100 hypothetical wheeled and tracked loads are specified by the TDTC for the deployable bridge design at these loading classes, The real loads of the PLS truck (MLC30), M113 track (MLC30), M1-A1 Abrams (MLC70) towing M1-A1 Abrams (MLC70) vehicles as well as the aforementioned TDTC hypothetical loads are applied to calculate the moment and shear all over the bridge span. Then the maximum values of moment and shear envelopes are plotted versus each vehicle position on the bridge span. All the load factors, namely: Impact, side-slope, and eccentricity, are included within the plotted values. The MLC100 Hypothetical tracked vehicle achieved the maximum bending moment and shear values on the bridge cross-section. Figures 6.2, and 6.3 show the shear and moments' envelopes, respectively, of the passing vehicles loads of class MLC70 and MLC100, whereas, Figures 6.4, and 6.5 show the shear and moments' envelopes, respectively, of the passing vehicles loads of class MLC30 and MLC50.
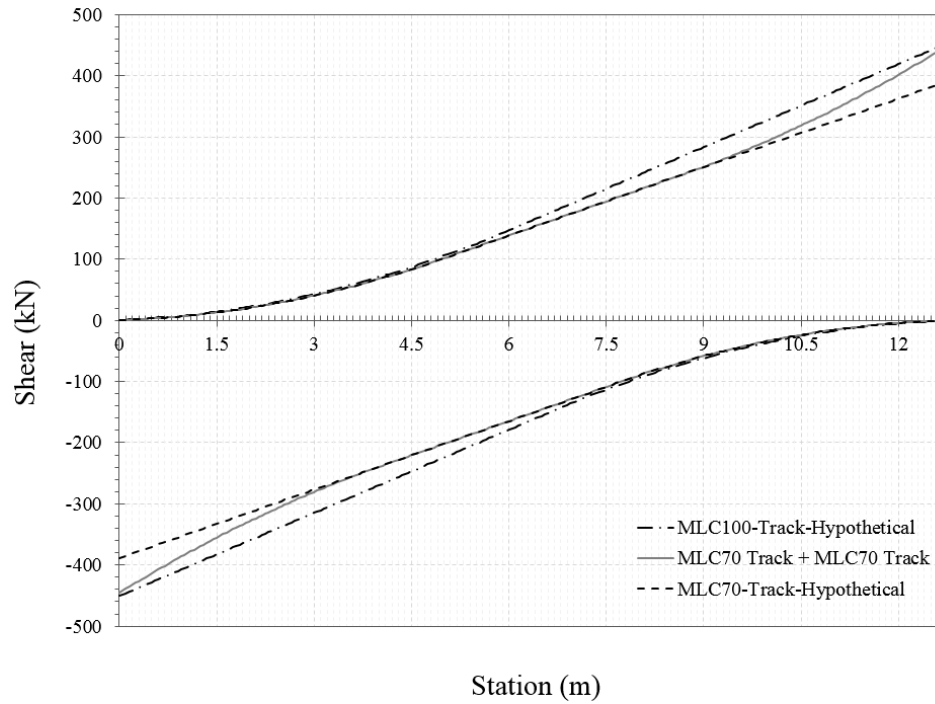
Figure 6.2 Shear envelope of MLC70 and MLC100 design loads on a 12.7 m bridge design span
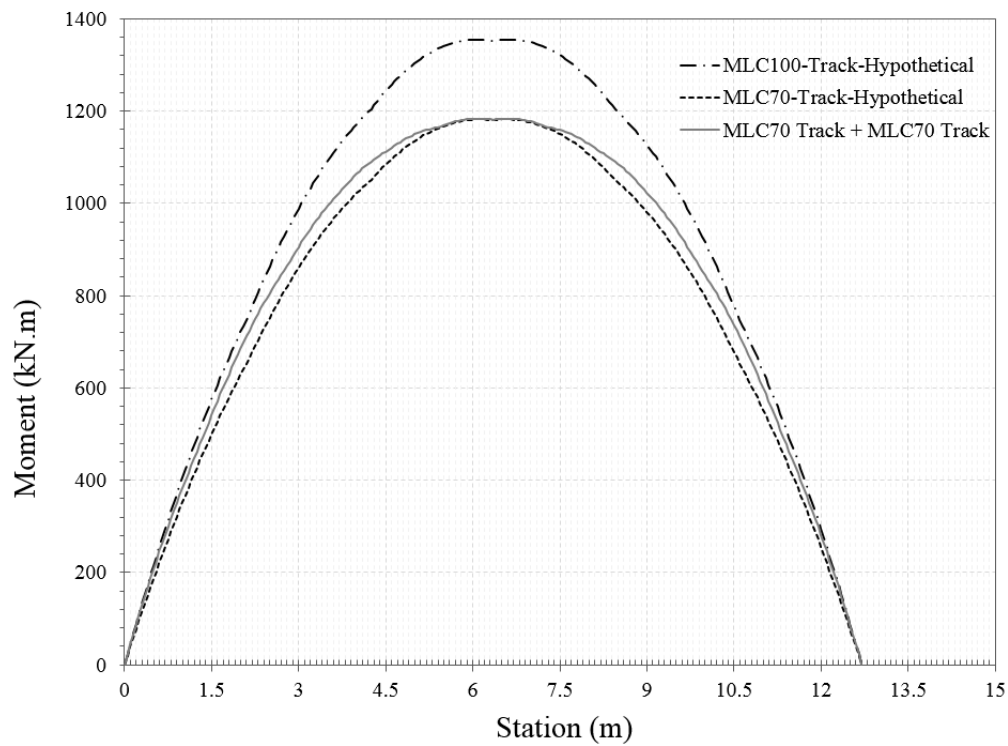
Figure 6.3 Moment envelope of MLC70 and MLC100 design loads on a 12.7 m bridge design span

130
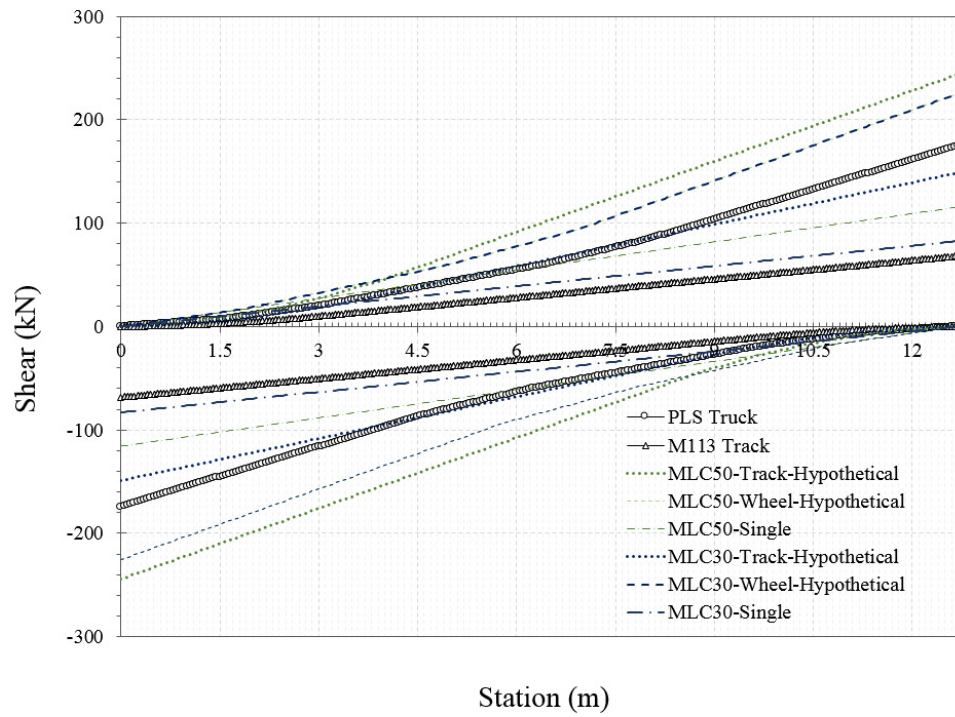
Figure 6.4 Shear envelope of MLC30 and MLC50 design loads on a 12.7 m bridge design span
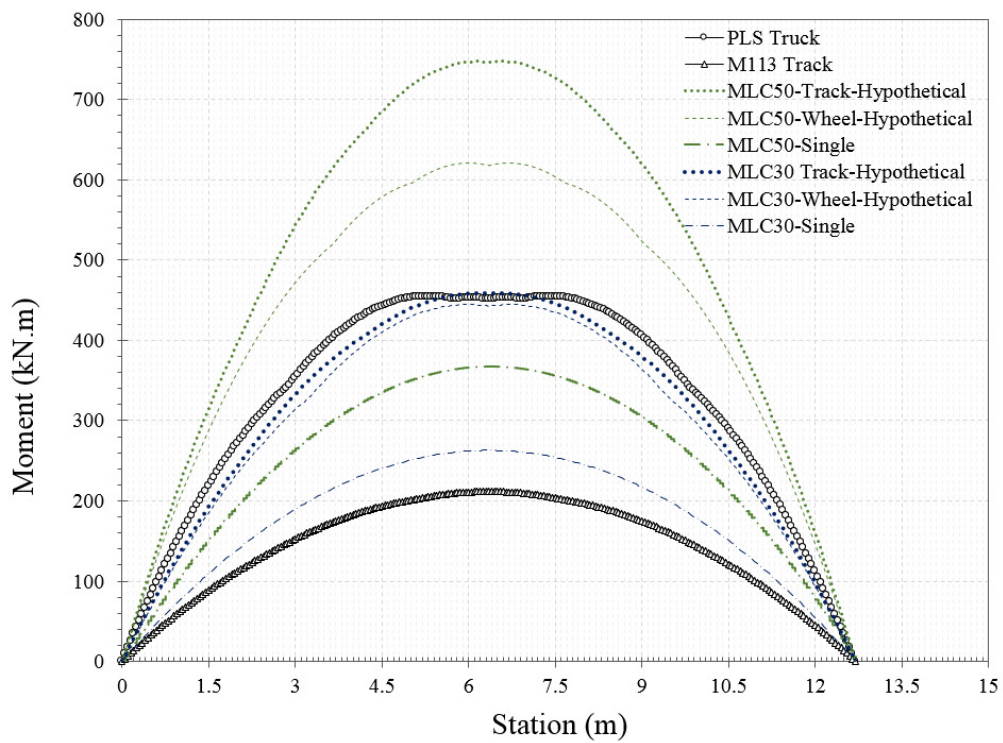
Figure 6.5 Moment envelope of MLC30 and MLC50 design loads on a 12.7 m bridge design span

131

A web laminate in a sandwich core construction of a deployable bridge is subjected to mainly three types of external loadings, which are: a compression load due to bridge bending in the treadway longitudinal direction (i.e. edgewise compression), a compression load normal to the deck skin (i.e. Flatwise compression) and shear load between the deck supporting stiffeners due to the passing vehicle axle loads. The compression and shear loads calculated in Chapter 5 to match the baseline performance of balsa core are considered for the strength design optimization in this chapter, whereas the compression load induced due to bridge bending in its longitudinal direction is calculated based on the maximum value of the generated moment envelopes shown in Figure 6.3 and an assumed treadway depth of 650 mm. Figure 6.6 represents a schematic of a thin laminated composite shell subjected to forces and moment resultants. The load components N_x, N_y, and N_{yx} in the figure represent the aforementioned calculated loads, whereas other load values are set to zero including the load component M_x that is produced from the out-of-plane load component as a result of the opposed response of the web laminate stiffness and foam infill, see Section 5.3.3. Tables 6.2 illustrates the bi-axial and shear load values applied on a core web laminate of cores A1-HC-W and A2-HC-CP.
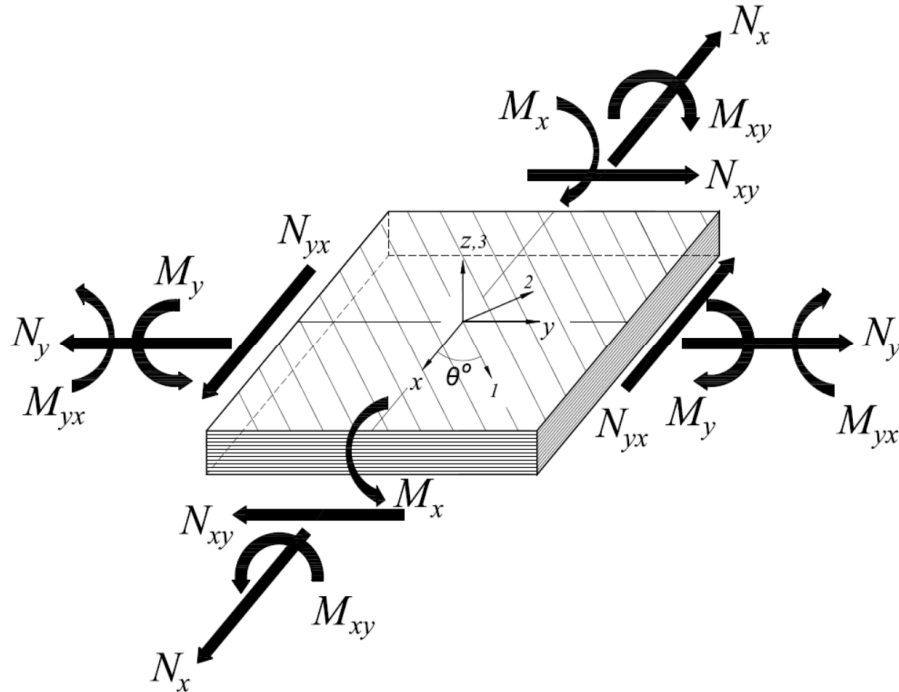
Figure 6.6 illustration of a thin composite laminate plate subjected to forces and moments resultants

Table 6.2: External applied loads on a composite deck laminate at different stations

Station	A1-HC-W			A2-HC-CP		
	N_x (kN/m)	N_y (kN/m)	N_{yx} (kN/m)	N_x (kN/m)	N_y (kN/m)	N_{yx} (kN/m)
5 cm	257	0	142	578	0	319
Mid-span	257	248	0	578	419	0

6.2.2 LAMINATE ANALYSIS

In the current study, an analytical model is developed in MATLAB and uses the Classical Lamination Theory (CLT) to calculate the stress and strain components in a thin composite laminate. The developed optimizer HCD-PSO change iteratively the laminate layers stacking sequence until a maximum strength design satisfying the termination conditions is achieved. A ply-by-ply failure analysis using Tsai-Wu failure criterion is conducted. A symmetric laminate is considered for the strength design using the analytical model. For every lamina (k) in the z coordinate of the web composite laminate, the stresses in the global coordinate system x, y, and z and their relationship to the mid-surface strains and curvatures are calculated from the following fundamental equations (Hyer, 2009).

$$\begin{Bmatrix} \sigma_x \\ \sigma_y \\ \tau_{xy} \end{Bmatrix}^{(k)} = \begin{bmatrix} \overline{Q}_{11} & \overline{Q}_{12} & \overline{Q}_{16} \\ \overline{Q}_{21} & \overline{Q}_{22} & \overline{Q}_{26} \\ \overline{Q}_{61} & \overline{Q}_{62} & \overline{Q}_{66} \end{bmatrix}^{(k)} \cdot \begin{Bmatrix} \varepsilon_x^\circ + z \cdot k_x^\circ \\ \varepsilon_y^\circ + z \cdot k_y^\circ \\ \tau_{xy}^\circ + z \cdot k_{xy}^\circ \end{Bmatrix} \tag{6.3}$$

where σ_x and σ_y are the normal stresses, τ_{xy} is the shear stress, ε_x°, ε_y° and γ_{xy}° are the mid-surface strains, k_x°, k_y° and k_{xy}° are the mid-surface curvatures, and $\overline{Q}_{ij}^{(k)}$ is the off-axis reduced stiffness matrix of the lamina (k) of thickness h_k. Figure 6.7 illustrates an enlarged view of a laminate cross-section clarifying the nomenclature.
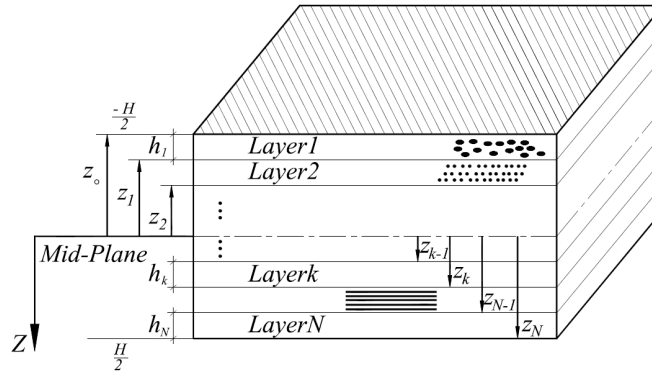
Figure 6.7 illustration of an enlarged view of a laminate cross-section

The applied forces and moments per unit width of the laminate are expressed in terms of the induced stresses as follows:

$$\{N_x \quad N_y \quad N_{xy}\} = \int_{-H/2}^{H/2} \{\sigma_x \quad \sigma_y \quad \sigma_{xy}\} \cdot dz$$

$$\{M_x \quad M_y \quad M_{xy}\} = \int_{-H/2}^{H/2} \{\sigma_x \quad \sigma_y \quad \sigma_{xy}\} \cdot z \cdot dz$$

(6.4)

From Equation 6.3 and 6.4, the relation between the applied loads and the mid-surface strains and curvature is identified as:

$$\begin{Bmatrix} N \\ M \end{Bmatrix} = \begin{bmatrix} A_{ij} & B_{ij} \\ B_{ij} & D_{ij} \end{bmatrix} \cdot \begin{Bmatrix} \varepsilon^\circ \\ k^\circ \end{Bmatrix}$$

(6.5)

where N is the vector of the applied forces, and M is the vector of the applied moments, ε° and k° are vectors of the mid-surface strains and curvatures, respectively. A_{ij} is the elastic stiffness matrix, B_{ij} is the coupling stiffness matrix, and D_{ij} is the bending stiffness matrix of dimensions 3×3. The generated 6×6 matrix is called the *ABD* stiffness matrix, in which all the laminate stiffness components are defined in terms of the off-axis reduced stiffness matrix $\overline{Q}_{ij}^{(k)}$ as follows:

$$A_{ij} = \sum_{k=1}^{N} \overline{Q}_{ij}^{(k)} \cdot \left(z_k - z_{(k-1)} \right), \qquad i = 1,2,6$$

$$B_{ij} = \frac{1}{2} \cdot \sum_{k=1}^{N} \overline{Q}_{ij}^{(k)} \cdot \left(z_k^2 - \left(z_{(k-1)} \right)^2 \right), \qquad i = 1,2,6 \qquad (6.6)$$

$$D_{ij} = \frac{1}{3} \cdot \sum_{k=1}^{N} \overline{Q}_{ij}^{(k)} \cdot \left(z_k^3 - \left(z_{(k-1)} \right)^3 \right), \qquad i = 1,2,6$$

The reference strains ε° and k° are calculated using the *abd* matrix which is the inverse of the *ABD* laminate stiffness matrix multiplied by the applied forces and moments, as follows:

$$\begin{Bmatrix} \varepsilon^\circ \\ k^\circ \end{Bmatrix} = \begin{bmatrix} a_{ij} & b_{ij} \\ b_{ij} & d_{ij} \end{bmatrix} \cdot \begin{Bmatrix} N \\ M \end{Bmatrix} \qquad \text{, such that } [abd] = [ABD]^{-1} \quad (6.7)$$

134

Hence the off-axis stresses σ_x, σ_y and τ_{xy} at each layer of the laminate are computed using Equation 6.3. by performing a tonsorial transformation of trigonometric functions, the on-axis stresses σ_1, σ_2 and τ_{12} at each layer (k) are calculated as follows:

$$
\begin{Bmatrix} \sigma_1 \\ \sigma_2 \\ \tau_{12} \end{Bmatrix}^{(k)} = \begin{bmatrix} m^2 & n^2 & 2mn \\ n^2 & m^2 & -2mn \\ -mn & mn & m^2 - n^2 \end{bmatrix} \cdot \begin{Bmatrix} \sigma_x \\ \sigma_y \\ \tau_{xy} \end{Bmatrix}^{(k)}
\tag{6.8}
$$

where m and n equal to $\cos\Theta$ and $\sin\Theta$, respectively. By knowing the on-axis stresses, the Tsai-Wu failure criterion is applied as described in the coming section.

6.2.3 FAILURE ANALYSIS

The Tsai-Wu failure criterion is chosen for the maximum strength design in the current study due to its simplicity in this application, as well as its better ability of predicting the failure in a multiple applied loading condition which is the case of the composite core web laminates. For the state of plane stress analysis the failure occurs using Tsai-Wu criterion when the calculated stresses reach the ultimate stresses σ_{imax} , such that the following equation is satisfied (Tsai and Wu, 1971):

$$
F(\sigma_1, \sigma_2, \tau_{12}) = F_1\sigma_{1\max} + F_2\sigma_{2\max} + F_{11}\sigma_{1\max}^2 + F_{22}\sigma_{2\max}^2 + F_{66}\tau_{12\max}^2 + 2F_{12}\sigma_{1\max}\sigma_{2\max} = 1 \tag{6.9}
$$

Therefore, the strength ratio to reach the ultimate stresses is identified as follows:

$$
F_1 \cdot S_R \cdot \sigma_1 + F_2 \cdot S_R \cdot \sigma_2 + F_{11} \cdot S_R^2 \cdot \sigma_1^2 + F_{22} \cdot S_R^2 \cdot \sigma_2^2 + F_{66} \cdot S_R^2 \cdot \tau_{12}^2 + 2F_{12} \cdot S_R^2 \cdot \sigma_1\sigma_2 = 1 \tag{6.10}
$$

Which can be shown in the form of a quadratic equation as:

$$
A \cdot S_R^2 \cdot + B \cdot S_R - 1 = 0 \tag{6.11}
$$

Where coefficients A, and B are equal to:

$$
A = F_{11} \cdot \sigma_1^2 + F_{22} \cdot \sigma_2^2 + F_{66} \cdot \tau_{12}^2 - 2F_{12} \cdot \sigma_1 \cdot \sigma_2
$$
$$
B = F_1 \cdot \sigma_1 + F_2 \cdot \sigma_2
$$

The terms F_1, F_2, F_{11}, F_{22}, F_{66}, and F_{12} are calculated as follows:

$$F_1 = \left(\frac{1}{X_t} + \frac{1}{X_c}\right), \qquad\qquad F_{11} = -\left(\frac{1}{X_t \cdot X_c}\right)$$

$$F_2 = \left(\frac{1}{Y_t} + \frac{1}{Y_c}\right), \qquad\qquad F_{22} = -\left(\frac{1}{Y_t \cdot Y_c}\right) \qquad (6.12)$$

$$F_{66} = \left(\frac{1}{S}\right)^2 \qquad\qquad F_{12} = -\frac{1}{2}\sqrt{F_{11} \cdot F_{22}}$$

where X_t and X_c are the ultimate tensile and compressive strength in the fiber direction, Y_t and Y_c are the ultimate tensile and compressive strength perpendicular to the fiber direction, and S is the ultimate in-plane shear strength. Finally in order to achieve a feasible solution, the stress at every point within the laminate thickness has to satisfy the following inequality constraint:

$$F(\sigma_1, \sigma_2, \tau_{12}) < 1 \qquad (6.13)$$

Figure 6.8 shows the typical Tsai-Wu quadratic failure envelope with the condition of stress state at different points on the failure envelope. It could be noticed that the initiation of the failure mechanism is highly affected by an acting bi-axial loading, such that the cracks initiation could be accelerated or slow based on the type of bi-axial loading compared to on-axis compressive or tensile loading. In Figure 6.8.a and Figure 6.8.b, it can be noticed that a lamina subjected to on-axis compressive load and lateral tensile load would fail due to initiated cracks faster than a lamina subjected only to an axial compression load, respectively. Similarly, the crack is slowly initiated in a lamina subjected to on-axis tensile loading and lateral compressive load than a lamina subjected to only an off-axis tensile load, as shown in Figure 6.8.c, and Figure 6.8.d, respectively.
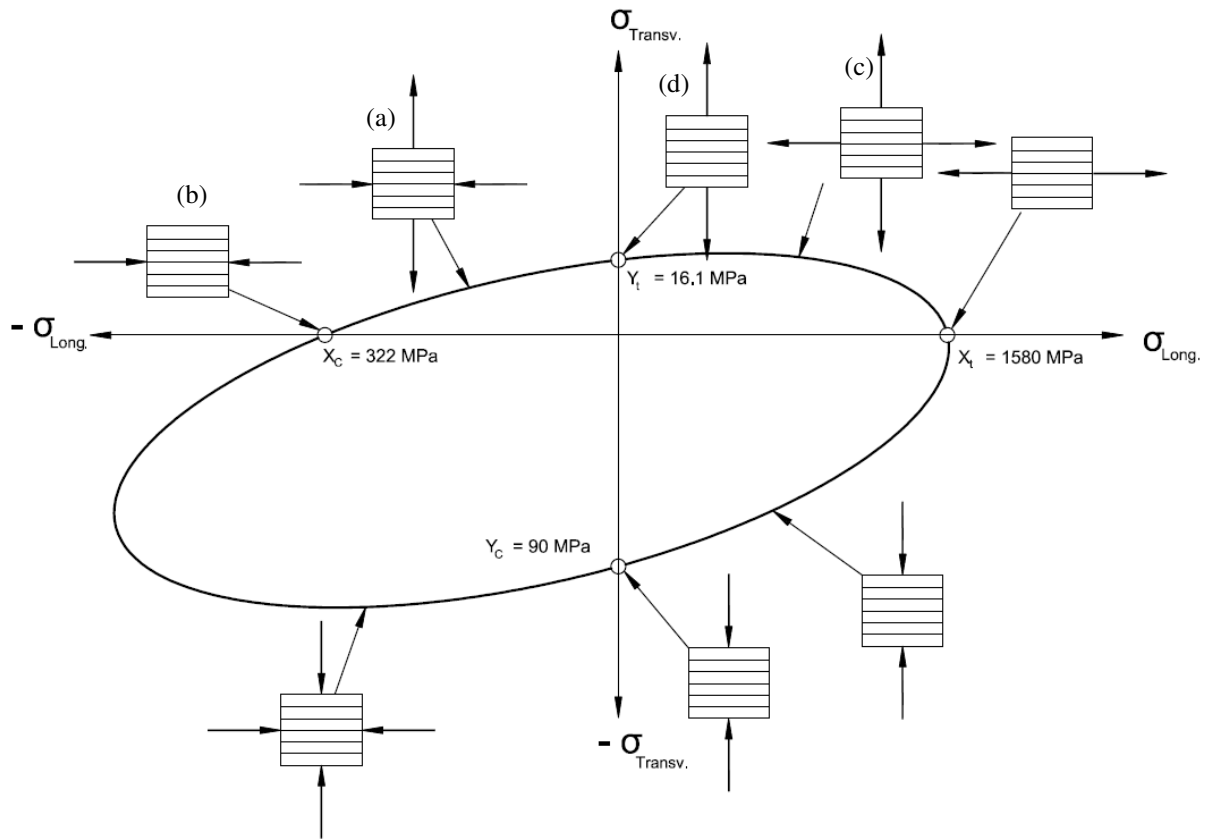
Figure 6.8 Illustration of Tsai-Wu quadratic failure envelope

6.3   DISCRETE CD-PSO FOR LAMINATED STRUCTURES

Many structural design optimization problems were solved in the continuous design space, from a practical point of view a discrete design space is more convenient to be handled especially when the structure is fabricated from composite laminates, as a simple example if the design optimization problem considers the minimum weight design of a structure constructed from prefabricated members, the cross-sectional properties shall be chosen from a tabulated list of prefabricated structural members. Similarly, for altering the orthotropic property of a structural composite laminate, the plies angle orientation shall be chosen from a list of possible angles orientation that can be implemented using the appropriate manufacturing method. Dealing with a discrete design space is more complex than a continuous space, where the potential feasible solutions are limited and an optimization algorithm with high exploration capability is required while at the same time the exploitation shall not be sacrificed. Therefore, a discrete version of CD-PSO is created in order

to invest its proved high dimensionality exploration as well as to assess its performance in the search of a discrete design space. Moreover, enhancements for dealing with the feasibility constraint violation are added to CD-PSO, such that the fly-back mechanism is implemented to redirect the swarm diversity to search back in the feasible regions when a violation of the design feasibility constraint is occurred (Venter and Sobieszczanski-Sobieski 2003).whereas the violation of the variables boundary constraints is handled using the heuristic search of the swarm particles (HPSO) (Li *et al.* 2007), Figure 6.9 presents the two possibilities of a particles' violation to even the problem specific constraint or the variables' boundary constraint. This algorithm is called, HCD-PSO. Eventually, the algorithm HCD-PSO performance with the fly-back mechanism to the strength design optimization of composite laminates is compared with original PSO, and the Heuristic Particle Swarm Optimization (HPSO).
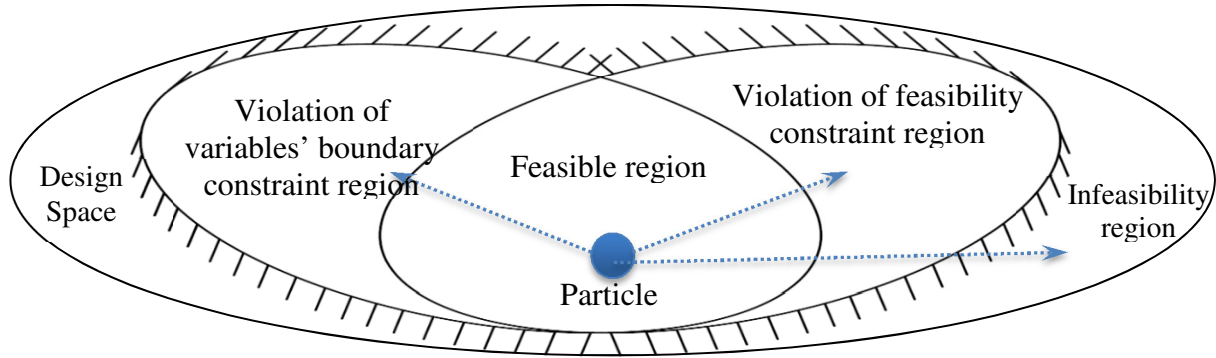
Figure 6.9 illustration of the possibilities of a particles' violation to the problem feasibility constraint or the variables' boundary constraint

6.3.1 DISCRETE FORMULATION OF CD-PSO

In the strength design optimization of a composite laminates the design variables are selected from a list of discrete values of ply orientations. The objective function is maximizing the strength ratio of the Tsai-Wu failure criterion subjected to a feasibility constraint of a strength ratio greater than or equal to one, the discrete optimization formulation can be formulated as follows:

Maximize: $\min S_R\left(x^1, x^2, ..., x^d\right),$ $d = 1, 2, ..., N_{dv}$

Subjected to: $-90^\circ \leq g_q\left(x^1, x^2, ..., x^d\right) \leq 90^\circ,$ $d = 1, 2, ..., N_{dv}$ (6.14)

$$S_R \geq 1,$$
$$q = 1, 2, ..., M$$

$$x^d \in S_d = \{X_1, X_2, ..., X_{Dis}\}$$

where $S_R(x^1, x^2, ..., x^d)$ is the strength ratio function in terms of a set of design variables $x^1, x^2, ...,$ x^d. A single design variable x^d has a scalar value that belongs to a vector S_d which includes all the scalar values $\{X_1, X_2, ..., X_{Dis}\}$ corresponding to every discrete variable value. The inequality $g(x^1, x^2, ..., x^d)$ is the constraints functions. The symbols N_{dv} and M are the numbers of design variables and inequality functions, respectively, the symbol Dis is the number of all available discrete variables.

The vector S includes scalar numbers arranged in an ascending order equal to the number of discrete design variables, such that each discrete variable is given an order of a scalar number in S, which can be represented as:

$$S_d = \{X_1, X_2, ..., X_j, ..., X_{Dis}\}, \qquad 1 \le j \le Dis$$

Where, a mapped matrix $T(j)$ is created to represent the indices of its corresponding discrete variables in each particle, such that in every iteration the scalar numbers are substituted by the discrete variables' values for further revaluation, in this way the position of each particle in hyperspace can be described by a vector X_{ij}

$$X_{ij} = \{x_1^i, x_2^i, ..., x_d^i\}, \qquad i = 1, ..., N_P$$

where $d \in N_{dv}$ and d is the dimension of the ith particle with discrete design variables, and N_p is the number of population of the swarm particles, as previously described in Chapter 3. The particle's updated velocity and position Equations 4.1, and 4.2 are reformulated to the following:

$$V_j^{(i,K+1)} = w \cdot V_j^{(i,K)} + c_1 \cdot r_1 \cdot \left({}_P X_j^{(i,K)} - X_j^{(i,K)} \right) + c_2 \cdot r_2 \cdot \left({}_G X_j^{(i,K)} - X_j^{(i,K)} \right) \qquad (6.15)$$

$$X_j^{(i,K+1)} = INT(X_j^{(i,K)} + V_j^{(i,K+1)}) \qquad (6.16)$$

Where all the updating velocity terms $X_j^{(i,k)}$, ${}_P X_j^{(i,k)}$, ${}_G X_j^{(i,k)}$ are inputs from the scalar mapped matrix $T(j)$ that includes all the swarm particles encoded data at the Kth iteration.

139

6.3.2 HEURISTIC CONTROLLED DIVERSITY PARTICLE SWARM HCD-PSO

As illustrated earlier in Figure 6.9, the possibility of a constraint violation by a travelling particle can be any of the following: violation of the problem specific constraint and this is handled by the fly-back mechanism which will be explained in the coming subsection, violation of the variables' boundary constraint which is handled by the heuristic search implemented to the PSO, or violation for both constraints such that the particle will be completely located in the infeasible region of the design space, given this, the two techniques are activated to handle the constraints violation. In general, the heuristic particle swarm optimizer for dealing with the violation of the variables' boundary is based on the Harmony search algorithm proposed by Geem *et al.*, (2001). Every particle in the swarm has a vector of scalar values $X_{ij} = \{x_1^i, x_2^i,...,x_d^i\}$, the scalar x_d^i is a component of this vector, if $x_d^i < x^L$ (lower bound) or $x_d^i > x^U$ (upper bound) then the scalar x_d^i is regenerated by randomly choosing a corresponding component from $_PX_d^k$ at the current k^{th} iteration. This can be expressed by the following equation:

$$x_d^{(i,K)} = {}_P x_d^{(t,K)}$$
$$t = INT\left(rand\left(1,N_P\right)\right)$$

(6.17)

Where $_Px_d^{(t,k)}$ is a corresponding scalar in the dth of dimension of the vector $_PX_d^{(i,k)}$ having the local best values of all swarm particles at the kth iteration.

6.3.3 FLY-BACK MECHANISM FOR HCD-PSO

The fly-back mechanism was first introduced by Venter and Sobieszczanski-Sobieski, (2003), the method redirects the updated velocity vector of a violated particle to a usable feasible region. A modification is made to Equation 6.15 by re-setting the weight velocity term and only includes the self-cognition, and the social learning of the particle. This strategy will redirect the resultant velocity vector of the equation to point back to the feasible region, as shown in Figure 6.10. The modified equation can be represented as follows:

$$V_j^{(i,K+1)} = c_1 \cdot r_1 \cdot \left({}_P X_j^{(i,K)} - X_j^{(i,K)}\right) + c_2 \cdot r_2 \cdot \left({}_G X_j^{(i,K)} - X_j^{(i,K)}\right)$$

(6.18)
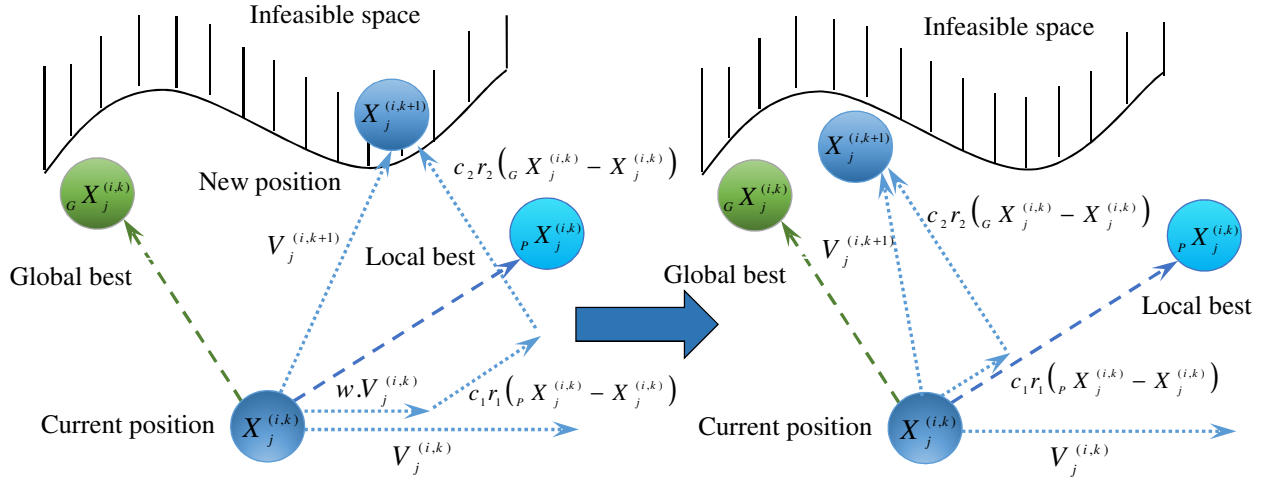
Figure 6.10 illustration of the fly-back mechanism

6.4 ASSESSMENT OF HCD-PSO

A carbon/epoxy laminate is considered for the assessment of the developed algorithm HCD-PSO. The pre-characterized material property in Chapter 5 is used for the composite plate. The composite plate in subjected to different in-plane loadings as previously described in Figure 6.4. The fiber angle orientation (θ°) considered in this study for the composite plate layers are chosen in the range between $\{-90^\circ, 90^\circ\}$ with steps of 15° degrees, such that the set of discrete design variables is as follows $\{-90^\circ, -75^\circ, -60^\circ, -45^\circ, -30^\circ, -15^\circ, 0^\circ, 15^\circ, 30^\circ, 45^\circ, 60^\circ, 75^\circ, 90^\circ\}$.the composite laminate plate is of dimensions $1000\,\text{mm} \times 1000\,\text{mm}$ ($39.4\,\text{in} \times 39.4\,\text{in}$) and of thickness $8.8\,\text{mm}$ ($0.35\,\text{in}$). In the current assessment two different in-plane loadings are considered, which are: bi-axial loading, and bi-axial and shear loadings. The discrete PSO, HPSO, and HCD-PSO are applied for the strength design optimization trials. The chosen number of iterations for all techniques is 200 iterations, the swarm population number is 50 particles, and the clamping velocity factor is 0.4, the cognition and social learning factors are taken equal to 0.4. The weighting velocity factor ω is a linearly decreasing value between 1.0 and 0.4. Figure 6.11 shows the convergence history of the maximized strength ratio of the composite plate under N_x, and N_y loadings. It can observed that HPSO and HCD-PSO obtained similar strength ratio values. However, HCD-PSO converged relatively faster. Table 6.3 presents the optimal ply angles orientation achieved of four optimization runs per each tested algorithm and their average strength ratios. Similarly, Figure 6.12 presents the convergence history of the strength ratio of the

composite plate subjected to bi-axial N_x, and N_y and shear N_{xy} loading conditions. Table 6.4 presents the optimal ply orientations obtained under the application of bi-axial and shear loadings.
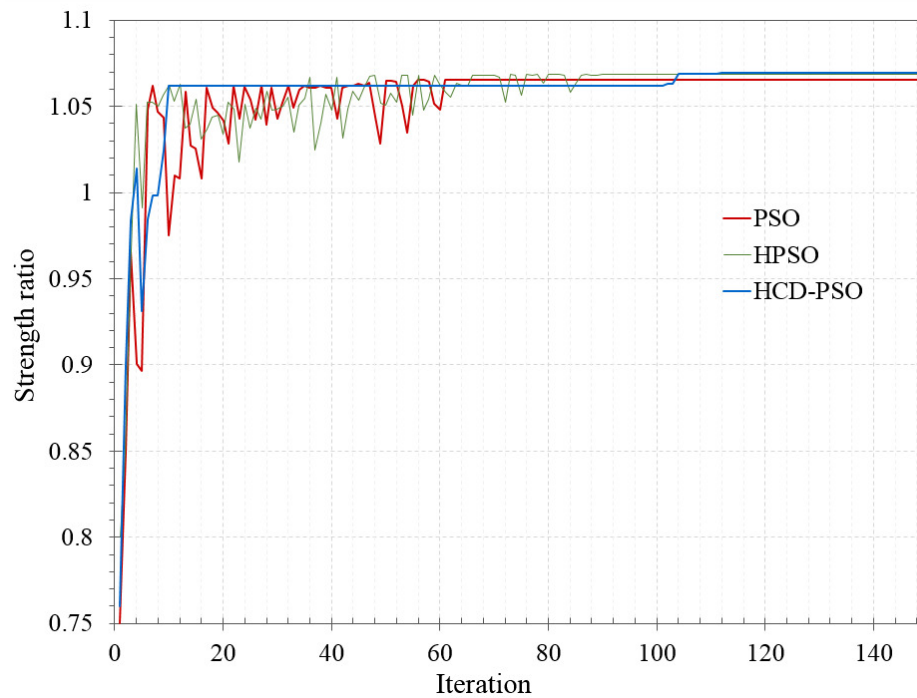
Figure 6.11 Convergence history of the strength ratio for the different PSO versions under the application of bi-axial loading condition.

Table 6.3: Optimum design configuration results obtained for bi-axial loading conditions

Loading Case (kN/m)			Optimization technique	Optimal ply angles orientation (degrees)	Average strength ratio (S_R)
N_x	N_y	N_{xy}			
			PSO	[-60,0,-45,30,45,45,30,-30,-45,30,-45]ₛ [-15,15,-15,75,-15,15,-45,90,30,-60,45]ₛ [-45,15,15,-45,90,-30,30,15,60,15,-60]ₛ [-45,15,90,60,-30,15,15,15,-75,15,-45]ₛ	1.065
1500	1000	-	HPSO	[-15,15,-15,45,45,-60,-75,15,60,-45,-15]ₛ [45,-75,-15,15,90,15,15,-30,60,-45,-15]ₛ [-15,15,-15,45,45,-60,-75,15,60,-45,-15]ₛ [45,-75,-15,15,90,15,15,-30,60,-45,-15]ₛ	1.069
			HCD-PSO	[15, 60,45,75,-45,-60,15,-45,-15,-15,15]ₛ [15, -45,-60,-15,75,60,45,15,15,-15,-45]ₛ [-15, 90,15,75,-15,-75,15,45,15,-15,-45]ₛ [30,45,-15,45,-15,-60,-15,90,-15,75,-15]ₛ	1.07

142
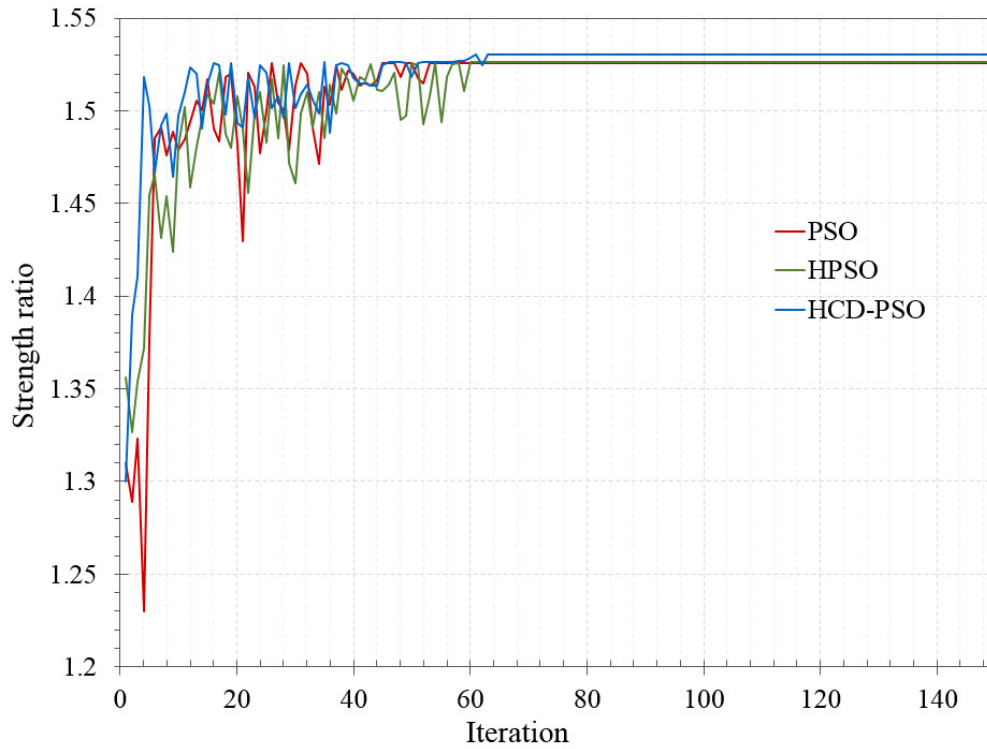
Figure 6.12 Convergence history of the strength ratio for the different PSO versions under the application of bi-axial and shear loading conditions

Table 6.4: Optimum design configuration results obtained for bi-axial and shear loadings

Loading Case (kN/m)			Optimization technique	Optimal ply angles orientation (degrees)	Average strength ratio (S_R)
N_x	N_y	N_{xy}			
1000	750	300	PSO	[0,-15,-15,-15,-15,-60,-15,90,-90,90,-45]$_s$ [45,0,-75,-30,-30,-75,-30,-30,-30,15,-75]$_s$ [-15,90,-90,-15,-15,-15,-15,-75,-30,-15,90]$_s$ [30,-45,-60,-60,15,90,-45,-45,0,-30,0]$_s$	1.5256
			HPSO	[-45,30,-45,-30,-60,15,-60,0,30,-45,-60]$_s$ [-45,0,-60,-60,-60,-15,30,30,0,-60,-45]$_s$ [-60,-45,-60,-45,30,-60,15,-45,-45,15,15]$_s$ [-45,-60,-60,15,-45,-45,30,-60,15,-45,15]$_s$	1.5263
			HCD-PSO	[-60,-45,15,-45,-45,-60,-60,15,30,-45,15]$_s$ [-30,-30,0,-45,-75,-30,75,0,-30,45,-60]$_s$ [-45,15,0,-60,-30,-60,-45,-60,30,-45,30]$_s$ [-30,-45,15,30,-45,-45,0,0,-60,90,-60]$_s$	1.5305

143

6.5   HCD-PSO APPLICATION ON COMPOSITE CORE DECKS

The designed core web laminate of core A1-HC-W was of $[0_1, \pm45_1]_S$ and $[0_2, \pm45_1]_S$ fiber architect for the honeycomb sides and the vertical filler web between honeycombs, respectively. For core A2-HC-CP the web laminate fiber architect was of $[\pm45_2, 0_2, \pm45_2]_T$ angles orientation. This conventional design of core web laminates provides an average strength ratio of 2.203 and 1.305 for the cores A1-HC-W and A2-HC-CP, respectively, due to the application of an in-plane compressive load only, in which it would results in an expected compressive capacity of 18872 kPa (2737 psi) and 12060 (1749 psi) for both cores, respectively, as previously described in Chapter 5. For a field application, a practical assumption is to consider the different loading conditions subjected on the web laminate at the same time during a vehicle crossing as described in Section 6.2.1. Therefore, the designed composite laminate will achieve a realistic strength ratio that is capable of providing the code provisions of safety factor and an acceptable margin of safety. For instance, a web laminate of core A1-HC-W at the location just near the bridge support is subjected to a combined loading of shear N_{xy} and compression N_x as presented in Table 6.2. By recalculating the strength ratio of the core web laminate subjected to these loadings, an average value of 1.86 strength ratio is achieved from failure analysis using Tsai-Wu and Maximum Stress failure criteria, similarly the web core laminate subjected to a compressive bi-axial loading at the mid-span location of the bridge would achieve an average strength ratio of 1.264, which may significantly affect the compliance with code provisions for a recommended safety factor. Therefore, a strength design optimization is exigent.

The developed discrete HCD-PSO is applied for the strength design optimization of cores A1-HC-W and A2-HC-CP considering the loading cases presented in Table 6.2. Table 6.5 illustrates the optimal ply angles orientation and the obtained strength ratio correspondingly per each loading case. Figure 6.13 presents the convergence history of the optimum strength ratio achieved for cores A1-HC-W and A2-HC-CP while applying each loading condition.

Table 6.5: Optimum design configuration results obtained of cores A1-HC-W and A2-HC-CP for different loading conditions

Loading Case (kN/m)			Core type	Optimal ply angles orientation (degrees)	Average strength ratio (S_R)
N_x	N_y	N_{xy}			
-257	0	142	A1-HC-W	[-30,75,-30,-15]$_s$ [-30,-15,-30,75]$_s$ [-30,75,-30,-15]$_s$ [-30,-15,-30,75]$_s$	2.2313
-257	-248	0	A1-HC-W	[60,-30,-30,60]$_s$ [-45,-45,45,45]$_s$ [45,45,-45,-45]$_s$ [45,-45,-45,45]$_s$	1.9194
-578	0	319	A2-HC-CP	[-30,60,-15,-30,-15]$_s$ [-45,-15,-15,60,-15]$_s$ [-15,-15,60,-30,-30]$_s$ [60,-15,-15,-30,-30]$_s$	1.2851
-578	-419	0	A2-HC-CP	[0,45,-45,45,-45]$_s$ [-45,45,0,-45,45]$_s$ [0,-45, 45,45,-45]$_s$ [-45,45,0,-45,45]$_s$	1.21
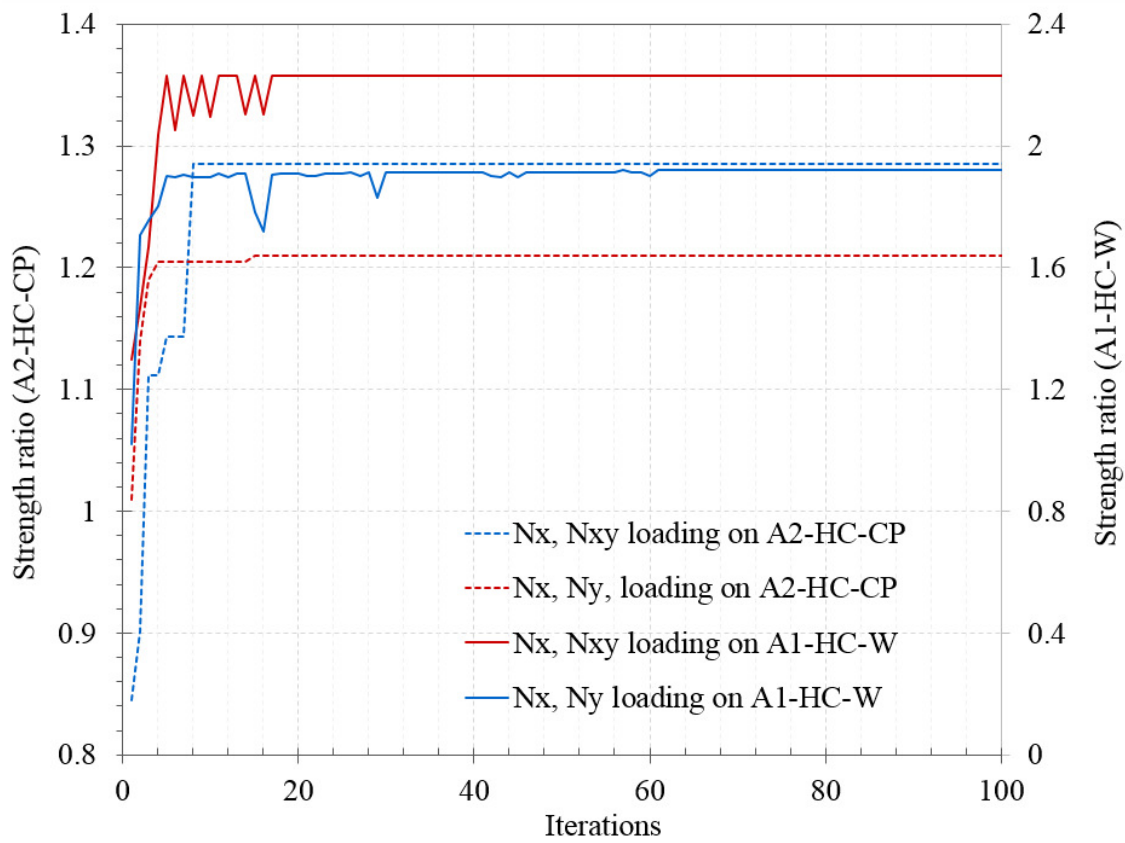
Figure 6.13 Convergence history of the strength ratio for cores A1-HC-W and A2-HC-CP for different loading conditions

6.6 SUMMARY AND CONCLUSIONS

In this Chapter, a discrete optimization algorithm HCD-PSO is developed for the strength design of composite laminates. A mapped matrix is used to encode integer values corresponding to the list of available discrete variables which are arranged in an ascending order. This mapped matrix is used to covert the search of the swarm from the continuous design space into the discrete design space. The optimization algorithm HCD-PSO is based on the Controlled Diversity, the Harmony search, and the fly-back techniques. The Controlled Diversity particle Swarm CD-PSO is responsible for achieving high dimensionality exploration as a result of the emulation of the swarm repulsion phase, which is controlled by a nonlinear convex repulsion surface, whereas the Harmony search technique is set to handle the variables' boundary constraint violations and the fly-back mechanism is used to redirect the swarm particles into usable feasible regions through their search history. The integration of the two techniques with the CD-PSO optimizer is

146

comprehensively described. The algorithm convergence rate was evaluated on a composite laminate plate and the results are compared with the performance of developed PSO, and HPSO discrete versions. The HCD-PSO showed an efficient convergence rate evolving a smooth search in hyperspace. Therefore, it is concluded that the technique is an efficient candidate for the discrete optimization of large-scale composite structures. An effective performance evaluation of composite cores may need specific laboratory tests that are difficult to be setup, for instance experimentally testing a composite core under multiple loading conditions such as bi-axial and shear forces cannot be represented expect when a scaled bridge beam is tested. A multiple loading application on a composite laminate plate may affect in decreasing or increasing the strength ratio based on the designed fiber orientation compared with a laminate plate subjected to a single loading. Therefore, the design of the composite core shall comply with these loading combinations which would results in variety of potential designs with different strength ratios. As a result, HCD-PSO is applied for the strength design optimization of the core web laminates under multiple loading conditions in order to ensure a high strength ratio that would meet the design provisions of specific safety factors and acceptable margins of safety at the critical locations of the bridge composite structure. The HCD-PSO achieved an increase in the strength ratio of core A1-CH-W from 1.86 to 2.23 under the application of compressive and shear loading at the location just near the bridge support, whereas, a strength ratio of 1.91 was obtained with an increase of 1.5 times of the conventional design under the application of bi-axial compressive loading at the bridge mid-span.

7
Summary, Conclusions and future work

This research has proposed the Controlled Diversity Particle Swarm Optimizer (CD-PSO) as an efficient tool for the minimum weight/capacity ratio design of deployable bridge structures, the study described the development and testing of two sandwich composite cores which are compared with the balsa core system of the Composite Assault Bridge (CAB) and other two composite webbed cores that were part of core alternatives for decking the Composite Joint Assault Bridge (CJAB). Finally, the discrete Heuristic Controlled Diversity Particle Swarm Optimizer (HCD-PSO) for the maximum strength design of composite laminated plate was developed.

7.1   OPTIMIZATION OF DEPLOYABLE BRIDGES

Based on the wide range of optimization techniques used effectively for structural design optimization. The performance of selective algorithms of this research study case was assessed, these algorithms are: Particle Swarm Optimizer (PSO) and Genetic Algorithm (GA) from heuristic-based algorithms, and First-Order Method (FO) and Zero-Order Method (ZO) from gradient-based algorithms. The PSO was the suitable technique to achieve rapid convergence rate, better solutions and competitive computational time.

A comprehensive investigation was conducted of PSO advantages and disadvantages. Further, the CD-PSO has been developed to cope the possibility of falling in local minima which considered as the major drawback of PSO. The algorithm implemented a novel technique for better emulation of the swarm attraction and repulsion, such that the swarm diversity in exploring the design space behaves in an oscillating wave manner. An assessment of CD-PSO on different truss benchmark structures was performed, the results were compared with wide range of available results in the

literature and the robustness of CD-PSO solutions was proved. The new algorithm was applied another time for the minimum weight/capacity ratio design of the deployable bridge implementing size and shape optimization. An enhanced normalized weight/capacity ratio of 66.795 percent with the conventional design was achieved compared with PSO and GA and having 5.35 and 2.01 percent difference, respectively. Moreover, the CD-PSO was hybridized with the Response Surface Methodology (RSM) in order to outfit the algorithm with a tool to handle complex structural models such as deployable bridges, where large number of design parameters is considered and the relationship between these design parameters and the design objective cannot be easily known. The Hybridized algorithm (CD-PSO + RSM) proved its effectiveness in distinguishing the significance of design parameters on the design objective. This helped in evolving the search for better solutions and a best minimum weight/capacity ratio of 65.69 was achieved.

7.2   COMPOSITE DEPLOYABLE BRIDGE DECKS

Because of the high weight percentage representation of decks in the deployable bridge design, the current study investigated deck core alternatives to the currently in-service composite cores, such that the decks represents more than 20% of the metallic deployable bridges weight, and about 40% of the composite deployable bridges weight. This research proposed two composite cores alternatives to the balsa system of the CAB deployable bridge and the composite webbed cores of the CJAB deployable bridge. The composite cores A1-HC-W and A2-HC-CP structural shape were designed based on different configurations assembly of honeycomb foam beams wrapped with FRP. The two core systems C4-TC and C5-CC of the webbed cores in the Literature were reproduced using the same material of the current study to set a baseline of the performance assessment. In a comparison with the balsa core, both proposed cores in this study achieved similar shear strength, and exceed the balsa core shear strength-to- areal weight ratio with at least 1.5 times for the core A2-HC-CP which has the lesser value of the two proposed systems. A progressive failure FE simulation was conducted and it was found with a good agreement with the proposed cores failure mode, shear capacity, deflection, and strains, which can be considered a viable tool for further fatigue simulation of the bridge deck and structure.

Despite the premature failure observed in the proposed cores compressive strength test, they obtained a satisfactory compressive strength capacity that complied with the TDTC code provision of achieving 1.8 safety factor of the design compressive load. Moreover, they provided a margin of safety more than 2.2 under the application of a tracked vehicle load of 100 tons (MLC100). However, core A2-HC-CP achieved similar compressive strength/areal weight ratio with the balsa system, whereas, core A1-HC-W exceed the balsa performance with 1.44 times. The progressive failure FE modeling showed a good agreement with the experimental test results which was very efficient is studying the premature failure mode observed.

The experimentally tested compressive performance of the proposed cores was compared with the reproduced webbed core systems C4-TC and C5-CC. both cores achieved better compressive strength and compressive strength to areal weight ratios than core C5-CC, and less than C4-TC. A design recommendation was set to prevent the premature failure occurred and to reach the analytically calculated compressive capacity, it is expected to exceed the compressive capacity of all composite cores presented in the literature after satisfying this design recommendation.

It is worth noted that, the balsa system as well as the webbed core systems in literature were manufactured using carbon fiber materials and epoxy formulation that are specially used in aerospace industry which reflected on the super mechanical properties achieved such as 386 MPa of shear strength, whereas the proposed cores were fabricated using carbon fiber materials and epoxy formulation used commonly in the construction industry that resulted in nearly 35 MPa of shear strength. Given this, the proposed cores are promoted for decking civilian bridges as well with a relatively lower cost as opposed to currently developed cores for the CAB and CJAB deployable bridges. In addition, it was shown that weight saving of 14% to 20% can be realized in the CAB deployable bridge by replacing the balsa deck system with the proposed cores A1-HC-W and A2-HC-CP, respectively.

7.3   STRENGTH DESIGN OPTIMIZATION OF COMPOSITE CORES

A composite sandwich core is subjected to multiple loading conditions at the same time during a vehicle passing load along a deployable bridge span. Assessing a sandwich core performance is very complex under multiple loading conditions in laboratory tests except for a

scaled or full structural bridge model which in turn found to be very expensive. On the other hand, achieving an effective design of composite laminates subjected to multiple loadings is difficult while the stacking sequence has to be chosen from a wide range of permissive ply orientations in order to reach the recommended strength and ensure the prevention of failure. Therefore, increasing the strength ratio of any laminated structure subjected to multiple loading conditions using the mathematical optimization is exigent and found to be a natural tool. The design optimization using the developed CD-PSO algorithm was applied for the maximum strength design of proposed sandwich cores. A discrete version of the CD-PSO was created in order to introduce a practical design of composite laminated plates. The implemented stress and strain analysis theory of composites was briefly described, and the failure analysis criterion used as for the strength design of the composite cores was clarified. The discrete CD-PSO was outfitted with the Harmony search technique and the fly-back mechanism to handle the constraints violation and named HCD-PSO. This algorithm integration showed a good convergence rate when tested on a composite laminated plate subjected to different in-plane loading conditions. Further, the HCD-PSO was applied for increasing the strength ratio of the proposed cores web laminate while subjected to multiple loading conditions. The results showed an increase in the strength ratio of both cores, such that core A1-HC-W strength ratio increased by 1.2 and 1.5 under the application of axial and shear loading at location just near the bridge support, and bi-axial loading at the bridge mid-span, respectively.

7.4 CONTRIBUTIONS

The contributions of this research study can be summarized as follows:

- An efficient controlled diversity particle swarm optimizer CD-PSO with robust stability is developed for the structural design optimization through a better emulation of the attraction and repulsion phenomenon of swarm of birds.

- An efficient hybrid CD-PSO optimizer with RSM for the optimal design of large-scale structures and deployable bridges is proposed, the performance of the methodology was assessed with classical PSO and GA and showed better solution, and rapid convergence.

- Novel Light weight with high shear and compressive strength composite core decks are developed for decking the deployable bridges of high carrying capacity of 100 tons. Both cores showed higher performance in terms of strength to areal core weight ratio when

151

compared with the balsa system of the CAB bridge except for the compressive strength to areal weight ratio of core A2-HC-CP which should a similar balsa performance.

- Design recommendations are presented to enhance the compression performance of the proposed composite cores through the full wrapping of cores sides with carbon/epoxy laminates.

- Performance charts are proposed for the designer to aid in the core deck selection out of a wide variety of composite cores in literature.

- Recommendations for manufacturing the proposed composite cores are suggested, such that core A1-HC-W is preferred to be fabricated using the FRIM or OOA processing methods, and A2-HC-CP with the SCRIMP method.

- An efficient progressive failure modeling is implemented by the integration of FE modeling of the sandwich cores and modified Hashine failure criteria. The model closely captured the observed failure modes, failure locations, and the shear and compressive capacities of the sandwich cores.

- An effective discrete optimization technique HCD-PSO is developed for the maximum strength design of composite laminates subjected to different loading conditions. The optimizer is linked with an analytical model for the strain-strain analysis of composite laminated plates using the CLT as well as quantification of the laminate strength ratio using Tsai-Wu failure criterion. The HCD-PSO technique showed a remarkable enhancement of the laminated structure strength ratio after handling the constraint violation with the fly-back mechanism and the Harmony search technique.

7.5   LIMITATIONS

The following are the limitations of this study:

- More investigation is needed for CD-PSO and the hybridized version with RSM to quantify their solution stability for solving complex structural models.

- The proposed cores are assumed to serve under normal climate conditions. Therefore, no residual stresses due to temperature and humidity are taken into consideration.

- More investigation is needed to quantify the composite cores performance under fatigue loadings.

- The developed sandwich cores were tested only in a one-way bending, whereas, other tests are needed to quantify the performance in two-way bending application for the core A2-HC-CP.

7.6 FUTURE WORK

Based on the findings of this study a second phase is expected to prolong and it will cover the following scopes:

- The proposed composite cores will be used for decking a deployable bridge system. A sandwich core will be chosen as a candidate deck to sustain the compression in top of a one-quarter scale FRP bridge beam.
- Multiple objective discrete optimization will be performed for the minimum weight and cost design of the whole deployable bridge treadway.
- The flexural performance, safety factors and margins of safety will be evaluated based on the Trilateral Design and Test Code for Military Bridging and Gap Crossing operations' requirements. The evaluation will include a moment and shear proof tests by simulating the axle load distribution of a vehicle using a whiffle tree structure.
- Core A2-HC-CP will be tested for two-way bending application, such that the composite deck will be manufactured with a dimension covering the treadway suggested width and a deck length supported on two transverse stiffeners (bulk heads).
- Extend the performance assessment of the proposed cores experimentally against fatigue and validate the results using a progressive failure modeling.
- Assess the performance of the whole developed and optimized scaled deployable bridge treadway against fatigue and cyclic loadings experimentally.
- Validate the fatigue performance of the scaled deployable bridge treadway through a progressive failure modeling.

APPENDIX A

Table A.1. World Wide Summary of Deployable Single Solid bridge component

Country	Model	Length (m)	Width (m)	Height (m)	Weight (Kg)	Capacity (Kg)
Brazil	*XLP-10 AVLB*	11.2	2.70	0.87	2,750	20,000
Poland	*SMT-1*	11.00	3.00	0.80	2,300	40,000
Russia	*MTU*	12.30	3.27	1.00	-	50,000
Sweden	*Brodiv-941*	15.00	4.00	0.75	7,000	50,000
Switzerland	*Bru Pz68*	18.23	3.79	1.00	6,600	50,000
United kingdom	*#9*	13.40	4.18	0.91	9,144	60,000
	#11	16.00	4.00	-	-	70,000
	#12	13.50	4.00	0.71	5,650	70,000

Table A.2. World Wide Summary of Deployable Multiple Components Bridges(F=folding, L=layered)

Country	Model	Length (m)	Width (m)	Height (m)	Weight (Kg)	Capacity (Kg)
China	*Type 84 (F)*	18.00	3.20	-	8,000	40,000
Czech & Slovakia	*MT-55 (55)*	18.00	3.34	0.90	6,500	50,000
France	*AMX-30 (F)*	22.00	3.95	-	8,500	50,000
	AMX-13 (13)	14.30	3.16	1.12	4,630	25,000
Germany	*BLG-60 (F)*	21.60	3.20	0.80	6,000	50,000
	BRLPZ-1 (L)	22.00	4.00	1.00	9,940	50,000
	Krupp-MAN (L)	26.00	4.01	1.10	10,000	60,000
Italy	*Astra A26 (F)*	21.40	4.10	1.00	-	54,000
Japan	*Type 67 (F)*	12.00	3.50	0.90	-	40,000
Netherlands	*Centurion (F)*	19.20	4.02	-	-	-
Russia	*MTU-20 (3F)*	20.00	3.30	1.00	7,000	60,000
UK	*#8 (F)*	24.38	4.17	0.91	12,200	60,000
	#10 (F)	26.00	4.00	-	-	70,000
USA	*M60 (F)*	19.20	4.00	0.90	14,470	60,000

APPENDIX B

Begin;
Generate random population of N_p Particles;
Calculate particles diversity;
Initiate swarm diversity control function *div.rate*;
For each particle $i \in N_p$, evaluate fitness;
Trial=0;
Switch=0;

    If Swarm diversity <*div.rate*;
        Switch to repulsion phase;
        Trial=Trial+1;
    else;
        Keep attraction phase;
    End;
    Initiate the value of inertia weight *w*;
    For each particle:
        Set Pbest $_PX_j^{(i,K)}$ as the best position for particle *i*,
        If the fitness is better than Pbest;
        Pbest(i)= fitness(i);
    End;
    Set Gbest $_GX_j^{(i,K)}$ as the best position for all particles;
    Calculate particle velocity;
    Check velocity bounds;
    Update particle position;
    Check particle encoded parameter bounds;
    If $_GX_j^{(i,K)} - {}_GX_j^{(i,K-1)} < 0.001$;
        Switch=Switch+1;
    End;
    If Trial=$\frac{1}{6}K_{max}$ OR Switch=$\frac{1}{6}K_{max}$;
        Initiate RSM analysis;
        Categorize parameters reference to influence rate;
        Mutate poor parameter to the Gbest equivalent;
        Fixing mutated poor parameter value;
    End;
    If $X_j^{(i,K)} > X_j^U$;
        $X_j^{(i,K)} = X_j^U$;
    End;
    If $X_j^{(i,K)} < X_j^L$;
        $X_j^{(i,K)} = X_j^L$;
    End;
Check if termination condition is True;
End;
End;
End;

APPENDIX C
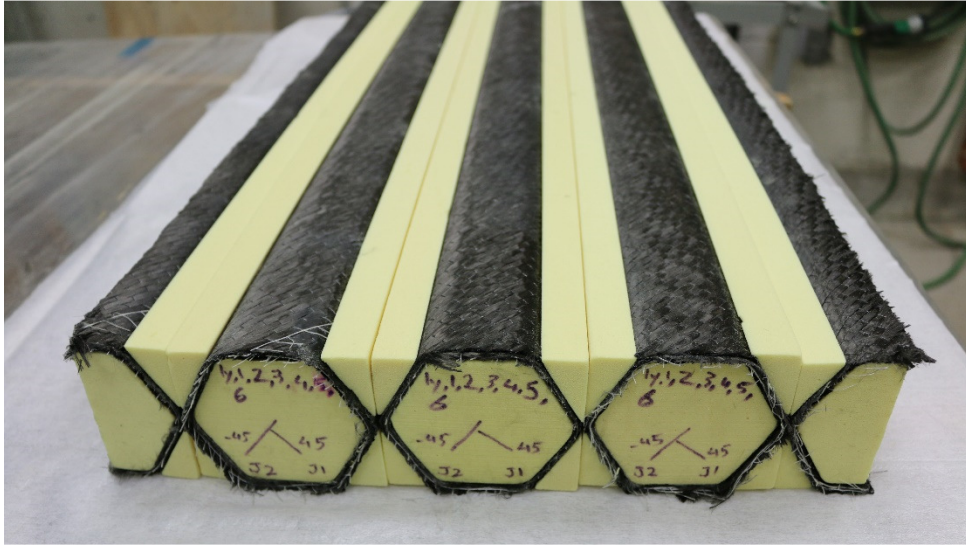
Figure C.1 A photograph of assembling the wrapped honeycomb beams and the triangular foam filler of core A1-HC-W

Figure C.2 A photograph of the polyisocyanurate foam beams assembly of core A2-HC-CP

Figure C.3 A photograph of the wrapped honeycomb beams, trapezoidal beams, and the corrugated preform assembly of core A2-HC-CP

Figure C.4 A photograph of the sandwich construction in between the skins of core A2-HC-CP

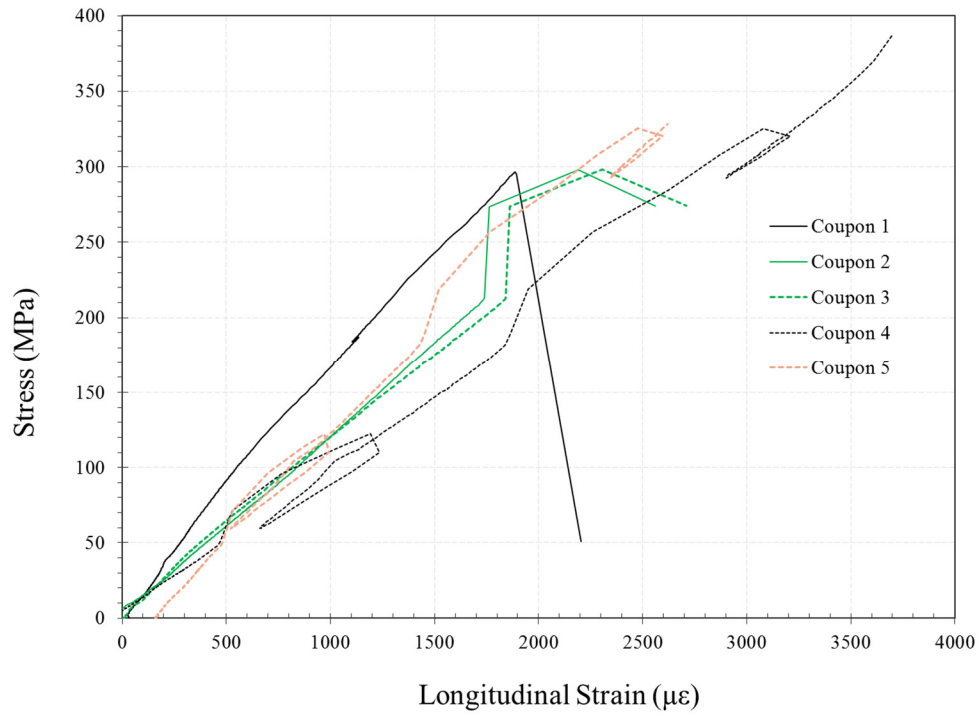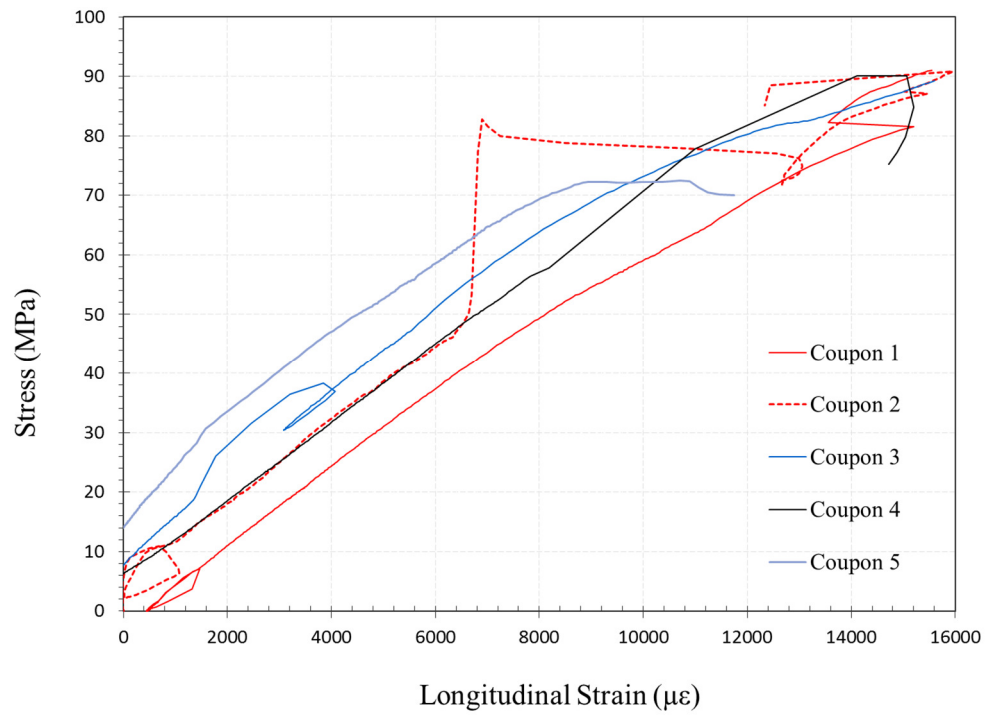**Figure C.5** Compressive Stress-Strain curves of coupons at $[0_5]_T$

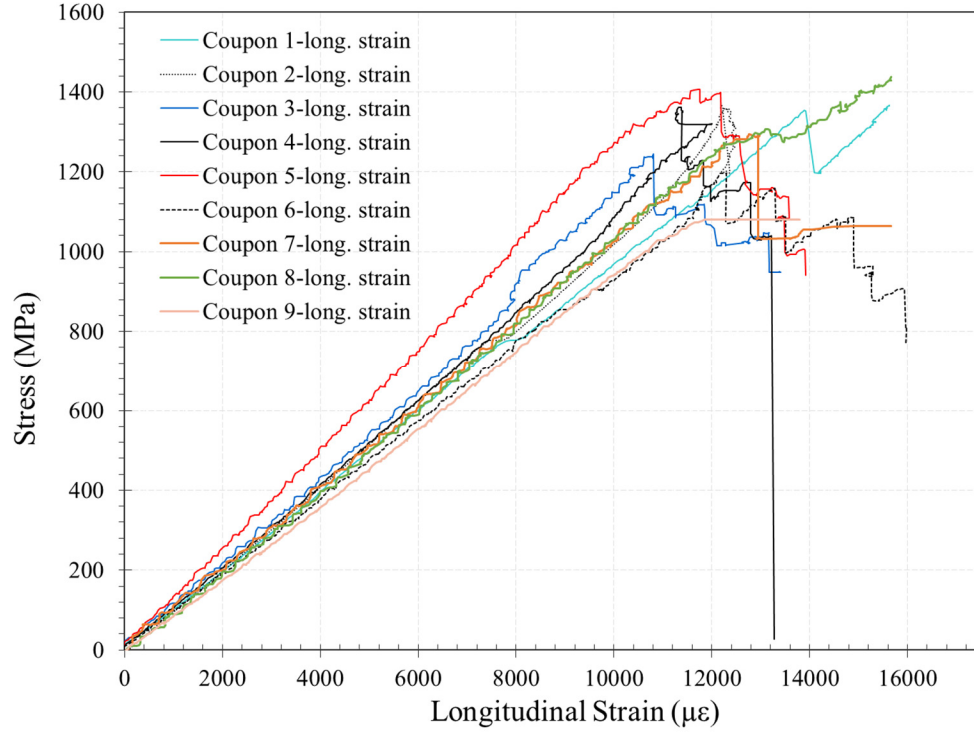**Figure C.6** Compressive Stress-Strain curves of coupons at $[90_5]_T$

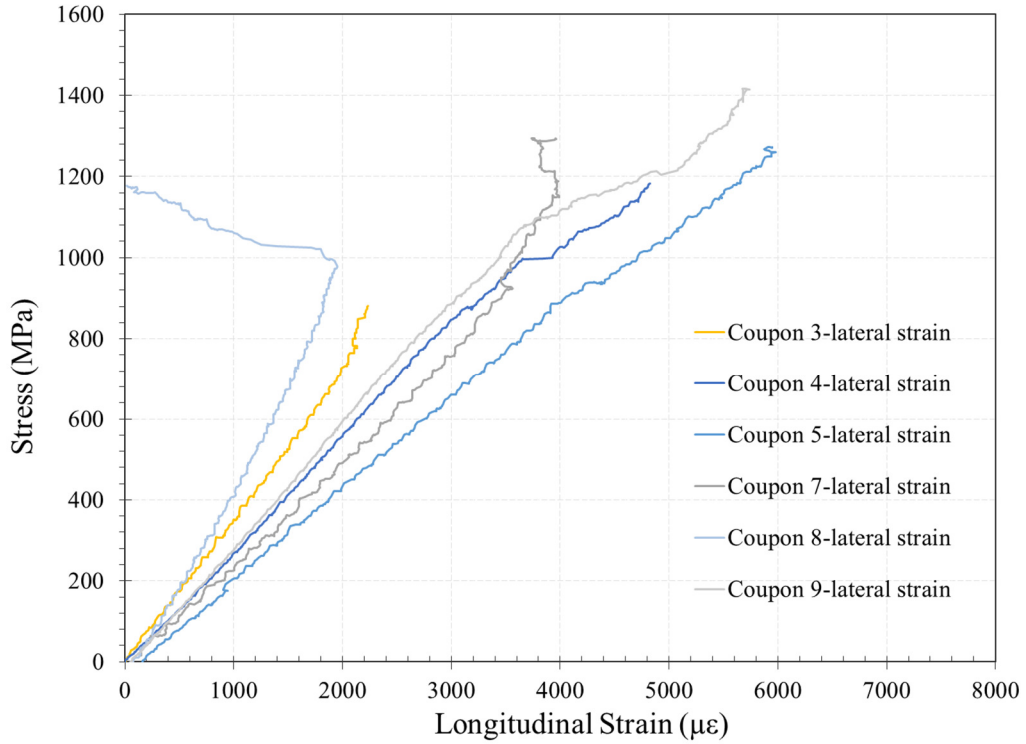**Figure C.7** Tensile Stress-Strain curves in fiber direction of coupons at $[0_5]_T$

Figure C.8 Tensile Stress-Strain curves perpendicular to fiber direction of coupons at $[0_5]_T$
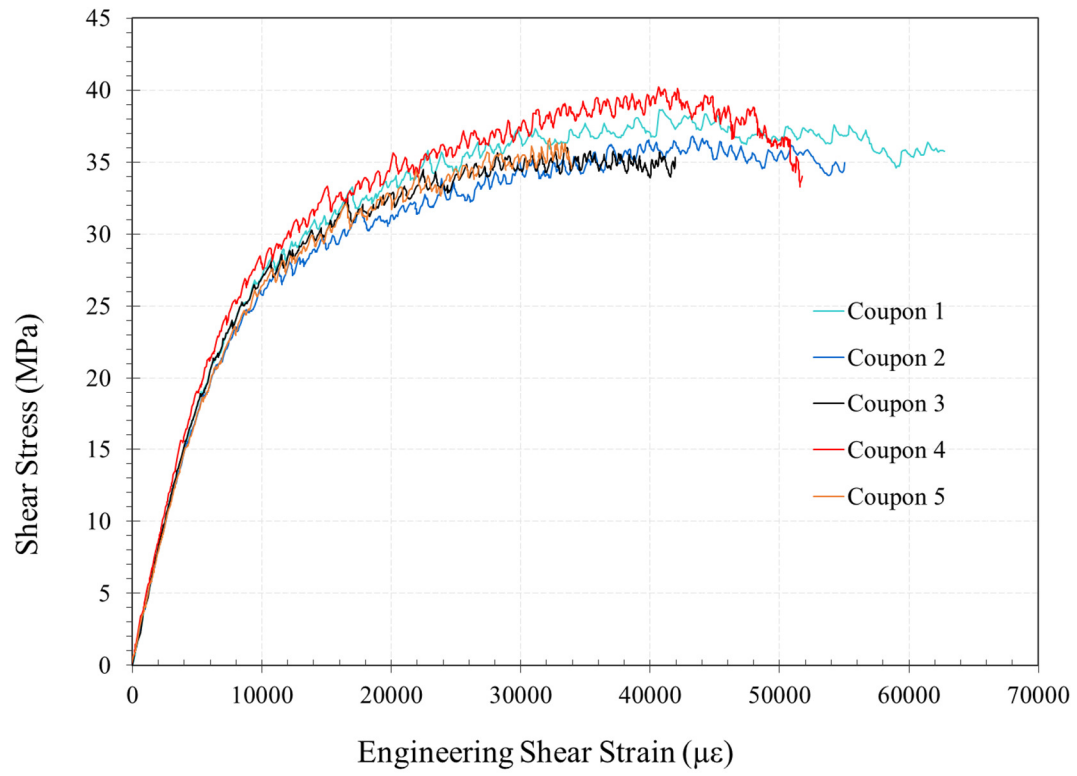
Figure C.9 Stress-Strain curves of in plane shear response for coupons at $[\pm45_4]_T$

REFERENCES

ANSYS, U. M. (1999). Structural Analysis Guide (Version Version 5.6).

Ario, I., Chikahiro, Y., and Tanaka, Y. (2011). Dynamic analysis for the prototype of a new type of Mobilebridge TM. Proceedings of the 7th anuual Europian Nonlinear Dynamic Conference. ENOC 2011. July 2011.

Ario, I., Nakazawa, M., Tanaka, Y., Tanikura, I., and Ono, S. (2013). Development of a prototype deployable bridge based on origami skill. Automation in Construction, 32, 104-111.

Arora, J. (2012). Introduction to optimum design. MA, USA & Oxford, UK: Academic Press.

Below, L., Palmer, M., Lindow, D., and Kellogg, D. (2003). Bridging Study: Phase 2. US Army Maneuver Support Center, Fort Leonard Wood, MO.

Bischmann, P. (1985). River Crossing in the Central Region. NATO's Sixteen Nations, 3, 76.

Box, G. E., and Wilson, K. (1951). On the experimental attainment of optimum conditions. Journal of the Royal Statistical Society. Series B (Methodological), 13(1), 1-45.

Brown, R. T., & Zureick, A.-H. (2001). Lightweight composite truss section decking. Marine Structures, 14(1–2), 115-132.

C363, A. (2011). C393/C393M − 11, Standard test method for core shear properties of sandwich constructions by beam flexure (Vol. 15.03): American Society for Testing and Materials. West Conshohocken, PA.

C364, A. (2012). C394/C394M − 12, Standard Test Method for Edgewise Compressive Strength of Sandwich Constructions (Vol. 15.03): American Society for Testing and Materials. West Conshohocken, PA.

C365, A. (2011). C395/C395M − 11a, Standard Test Method for Flatwise Compressive Properties of Sandwich Cores (Vol. 15.03): American Society for Testing and Materials. West Conshohocken, PA.

Camp, C. (2007). Design of Space Trusses Using Big Bang–Big Crunch Optimization. Journal of Structural Engineering, 133(7), 999-1008.

Camp, C., and Bichon B. (2004). Design of Space Trusses Using Ant Colony Optimization. Journal of Structural Engineering, 130(5), 741-751.

Camp, C., Pezeshk, S., and Cao, G. (1998). Optimized Design of Two-Dimensional Structures Using a Genetic Algorithm. Journal of Structural Engineering, 124(5), 551-559.

Cao, G. (1996). Optimized design of framed structures using a genetic algorithm. Ph.D. Thesis, The University of Memphis, Ann Arbor.

Chechkin, A. V., Metzler, R., Klafter, J., and Gonchar, V. Y. (2008). Introduction to the theory of Lévy flights, Anomalous Transport: Foundations and Applications, pp. 129-162.

Chikahiro, Y., Ario, I., Nakazawa, M., Ono, S., Holnicki-Szulc, J., Pawlowski, P., and Graczykowski, C. (2014). An experimental study on the design method of a real-sized Mobile Bridge for a moving vehicle. Mobile and Rapidly Assembled Structures IV, 136, 93.

Cluff, L. (2007). Effects of the 2004 Sumatra-Andaman earthquake and Indian Ocean tsunami in Aceh province. bridge-washington-national academy of engineering, 37(1), 12.

Coker, C. (2009). New Options on Military Bridging. Military Technology, 33(3), 42.

Connors, S. C., and Foss, C. F. (2005). Jane's Military Vehicles and Logistics 2005-2006: Jane's Information Group Limited.

Connors, S. C., and Foss, C. F. (2006). Jane's Military Vehicles and Logistics 2005-2006: Jane's Information Group Limited.

Das, S., and Suganthan, P. N. (2011). Differential evolution: A survey of the state-of-the-art. Evolutionary Computation, IEEE Transactions on, 15(1), 4-31.

Davalos, J. F., Qiao, P., Frank Xu, X., Robinson, J., and Barth, K. E. (2001). Modeling and characterization of fiber-reinforced plastic honeycomb sandwich panels for highway bridge applications. Composite structures, 52(3–4), 441-452.

De Jong, K. A. (1975). Analysis of the behavior of a class of genetic adaptive systems. Ph.D. Thesis. University of Michigan, Ann Arbo.

DiMarco, A. (2004). Bridging the gap: Modernizing Army bridge units. Engineer, Prof. Bull., U.S. Army Maneuver Support Center, 2, 20-21.

Dobbs, M., and Nelson, R. (1976). Application of optimality criteria to automated structural design. AIAA journal, 14(10), 1436-1443.

Eberhart, R. C., and Kennedy, J. (1995). A new optimizer using particle swarm theory. Proceedings of the sixth international symposium on micro machine and human science. New York, NY. 39-43

Eberhart, R. C., and Yuhui, S. (2001). Particle swarm optimization: developments, applications and resources. Proceedings of the 2001 Congress on the Evolutionary Computation.

Elbeltagi, E., Hegazy, T., and Grierson, D. (2005). Comparison among five evolutionary-based optimization algorithms. Advanced Engineering Informatics, 19(1), 43-53.

Eslami, M., Shareef, H., Khajehzadeh, M., and Mohamed, A. (2012). A survey of the state of the art in particle swarm optimization. Research Journal of Applied Sciences, Engineering and Technology, 4(9), 1181-1197.

Fiacco, A. V., and McCormick, G. P. (1990). Nonlinear programming: sequential unconstrained minimization techniques: Siam, (Vol. 4).

Fourie, P., and Groenwold, A. (2002). The particle swarm optimization algorithm in size and shape optimization. Structural and Multidisciplinary Optimization, 23(4), 259-267.

Gellatly, R. A. (1966). development of procedures for large scale automated minimum weight structural design: DTIC Document.

Gellatly, R. A., & Berke, L. (1971). Optimal Structural Design: DTIC Document.

Giunta, A. A., Wojtkiewicz, S. F., and Eldred, M. S. (2003). Overview of modern design of experiments methods for computational simulations. Proceedings of the 41st AIAA aerospace sciences meeting and exhibit, AIAA-2003-0649.

Haklı, H., and Uğuz, H. (2014). A novel particle swarm optimization algorithm with Levy flight. Applied Soft Computing, 23(0), 333-345.

Hanus, J., Bank, L., and Oliva, M. (2008). Investigation of a Structural FRP Stay-in-Place Form for a Prototype Military Bridge System. ACI Special Publication, 257, 53-70.

Hashin, Z. (1980). Failure criteria for unidirectional fiber composites. Journal of applied mechanics, 47(2), 329-334.

Hassan, R., Cohanim, B., De Weck, O., and Venter, G. (2005). "A comparison of particle swarm optimization and the genetic algorithm." Proceedings of the 1st AIAA multidisciplinary design optimization specialist conference, 18-21.

Hassan, T., Reis, E. M., and Rizkalla, S. H. (2003). Innovative 3-D FRP sandwich panels for bridge decks. Proceedings of the Fifth Alexandria International Conference on Structural and Geotechnical Engineering.

Haug, E. J., and Arora, J. S. (1979). Applied optimal design: mechanical and structural systems: John Wiley & Sons.

Hetényi, M. (1946). Beams on elastic foundation. The University of Michigan Press;G. Cumberlege, Oxford university press, Ann Arbor; London.

Hoa, S. V. (2009). Principles of the manufacturing of composite materials: DEStech Publications, Inc.

Holland, J. H. (1975). Adaptation in natural and artificial system: an introduction with application to biology, control and artificial intelligence. University of Michigan Press, Ann Arbor.

Jang, S. H., Hwang, I. W., Kwon, B. C., Kim, S. T., and Choi, Y. H. (2012). Structural optimization based on static design criteria of a long span mobile bridge using genetic algorithm. Applied Mechanics and Materials, Trans Tech Publ, 4732-4741.

Karaboga, D. (2005). An idea based on honey bee swarm for numerical optimization: Technical report-tr06, Erciyes university, engineering faculty, computer engineering department.

Kaveh, A. (2014). Chaos Embedded Metaheuristic Algorithms Advances in Metaheuristic Algorithms for Optimal Design of Structures: Springer International Publishing. pp. 369-391.

Kaveh, A., and Ghazaan, M. I. (2014). Enhanced colliding bodies optimization for design problems with continuous and discrete variables. Advances in Engineering Software, 77, 66-75.

Kaveh, A., and Khayatazad, M. (2012). A new meta-heuristic method: Ray Optimization. Computers & structures, 112–113, 283-294.

Kaveh, A., Sheikholeslami, R., Talatahari, S., and Keshvari-Ilkhichi, M. (2014). Chaotic swarming of particles: A new method for size optimization of truss structures. Advances in Engineering Software, 67(0), 136-147.

Kaveh, A., and Talatahari, S. (2009a). "Hybrid algorithm of harmony search, particle swarm and ant colony for structural design optimization. Harmony search algorithms for structural design optimization, Springer, Berlin Heidelberg, 159-198.

Kaveh, A., and Talatahari, S. (2009b). Size optimization of space trusses using Big Bang–Big Crunch algorithm. Computers and Structures, 87(17), 1129-1140.

Keller, T., and Gürtler, H. (2005). Quasi-static and fatigue performance of a cellular FRP bridge deck adhesively bonded to steel girders. Composite Structures, 70(4), 484-496.

Keller, T., Rothe, J., De Castro, J., and Osei-Antwi, M. (2013). GFRP-balsa sandwich bridge deck: Concept, design, and experimental validation. Journal of Composite for Construction, 18(2), 04013043.

Kermanidis, T., Labeas, G., Tserpes, K., and Pantelakis, S. (2000). "Finite element modeling of damage accumulation in bolted composite joints under incremental tensile loading." Proceedings of the Third ECCOMAS Congress, 11-14.

kerr, j. v. (1990). "U.S.-German cooperative efforts in military bridging." Army RD&A Bulletin, Headquarters Department of U.S. army, USA, 1-4.

Khan, M., Willmert, K., & Thornton, W. (1979). An optimality criterion method for large-scale structures. AIAA journal, 17(7), 753-761.

Koehler, J., and Owen, A. (1996). "9 Computer experiments." Handbook of Statistics, 13 261-308.

Kosmatka, J. (2011). Composite bridging for military and emergency applications. 8th annual proceeding, Annual Int. Conf. on Composites/Nano Engineering.

Kosmatka, J. B., Grippo, W., Policelli, F., Charbonnet, S., Randolph, B., and Hegimier, G. (2000). Advanced composites for bridge infra-structure renewal- phase II DARPA: University of California San Diego. pp. 326.

Kovács, G., and Spens, K. M. (2007). Humanitarian logistics in disaster relief operations. International Journal of Physical Distribution & Logistics Management, 37(2), 99-114.

Koza, J. R. (1992). Genetic programming: on the programming of computers by means of natural selection: MIT press. Vol. 1.

Koziel, S., and Yang, X. (2011). Computational optimization, methods and algorithms. Springer. Vol. 356.

Kutner, M. H., Nachtsheim, C. J., Neter, J., and Wasserman, W. (2004). Applied linear regression models. McGraw-Hill Irvin.

Landherr, J. (2008). Dynamic analysis of a FRP deployable box beam.

Lederman, G., You, Z., and Glišić, B. (2014). A novel deployable tied arch bridge. Engineering Structures, 70(0), 1-10.

Lee, K. S., and Geem, Z. W. (2004). A new structural optimization method based on the harmony search algorithm. Computers & structures, 82(9–10), 781-798.

Li, L. J., Huang, Z. B., and Liu, F. (2009). A heuristic particle swarm optimization method for truss structures with discrete variables. Computers and structures, 87(7–8), 435-443.

Li, N., & Li, Y. X. (2012). A Diversity Guided Particles Swarm Optimization. Advanced Materials Research, Trans Tech Publ, 532, 1429-1433.

Link, C. (2003). Development of panel-to-panel connection for use with a pultruded fiber-reinforced-polymer bridge deck system. Civil & Environmental Engineering. Blacksburg, Virginia Polytechnic Institute & State University. MS.

Liu, Z. (2007). Testing and analysis of a fiber-reinforced polymer (FRP) bridge deck. Virginia Polytechnic Institute and State University.

Lopez-Anido, R., Ganga Rao, H. V., Vedam, V., and Overby, N. (1997). Design and evaluation of a modular FRP bridge deck. marketing technical regulatory sessions of the composites institutes international composites expo, 3-Edition.

Luh, G.-C., and Lin, C.-Y. (2008). Optimal design of truss structures using ant algorithm. Structural and Multidisciplinary Optimization, 36(4), 365-379.

Luh, G.-C., and Lin, C.-Y. (2011). Optimal design of truss-structures using particle swarm optimization. Computers & structures, 89(23–24), 2221-2232.

M. Dorigo, and Caro, G. D. (1999, 1999). Ant colony optimization: a new meta-heuristic. Proceedings of the 1999 Congress on Evolutionary Computation. Washington, DC., pp. 1470–1477.

Mukhopadhyay, T., Dey, T. K., Dey, S., and Chakrabarti, A. (2015). Optimisation of Fibre-Reinforced Polymer Web Core Bridge Deck—A Hybrid Approach. Structural Engineering International, 25(2), 173-183.

Myers, R. H., Montgomery, D. C., and Anderson-Cook, C. (2009). Response surface methodology: product and process optimization using designed experiments: John Wiley & Sons, New York.

Navy, U. S. (2005). US Navy 050127-N-0057P-268 tsunami rescue effort near Banda Aceh, Sumatra, Indonesia,. from https://commons.wikimedia.org/wiki/File:US_Navy_050127-N-0057P-268

NOAA. (1998). Mitch: The Deadliest Atlantic Hurricane Since 1780. Retrieved Sept. 30, 2014, from http://www.ncdc.noaa.gov/oa/reports/mitch/mitch.html

Nor, N. M. (2011). Simulation analysis of a foldable carbon fiber reinforced polymer bridge prototype. National Postgraduate Conference (NPC), IEEE, 1-4.

Nor, N. M., Agusril, S., Alias, M. Y., Mujahid, A. A. Z., and Shohaimi, A. (2012). Dynamic Analysis of Sandwiched Composite Foldable Structure under Heavy Vehicle Load. Applied Mechanics and Materials, Trans Tech Publ, 110, 2331-2336.

Osei-Antwi, M., de Castro, J., Vassilopoulos, A. P., & Keller, T. (2013). FRP-balsa composite sandwich bridge deck with complex core assembly. Journal of Composites for Construction, 17(6).

Osman, A. (2006). Optimum Design or Orthotropic Metallic Deck Bridges. M. Sc. Thesis, Military Technical College, Egypt.

Pant, M., Radha, T., and Singh, V. P. (2007). A Simple Diversity Guided Particle Swarm Optimization. IEEE Congress on the Evolutionary Computation. CEC 2007.

Paulo, R. (1976). optimization of multi-constrained structures based on optimality criteria. 17th Structures, Structural Dynamics, and Materials Conference: American Institute of Aeronautics and Astronautics.

Perez, R. E., and Behdinan, K. (2007). Particle swarm approach for structural design optimization. Computers and structures, 85(19–20), 1579-1588.

Poloni, C., Pediroda, V., Clarich, A., and Steven, G. (2002). The use of Design of Experiments (DOE) and Response Surface Analysis (RSA) in PSO. Product and System Optimization (PSO) (pp. 3). Copenhagen.

Repetski, E. J. (2003). Assessment of Bridging Requirements and Current Bridging Capabilities for use of Legacy Heavy Forces Inside the Contemporary Operational Environment: DTIC Document.

Reyes-Sierra, M., and Coello, C. C. (2006). Multi-objective particle swarm optimizers: A survey of the state-of-the-art. International journal of computational intelligence research, 2(3), 287-308.

Riget, J., and Vesterstrøm, J. S. (2002). A diversity-guided particle swarm optimizer-the ARPSO. Dept. Comput. Sci., Univ. of Aarhus, Aarhus, Denmark, Tech. Rep, 2, 2002.

Robinson, M., and Kosmatka, J. (2010). Experimental dynamic response of a short-span composite bridge to military vehicles. Journal of Bridge Engineering, 16(1), 166-170.

Robinson, M., and Kosmatka, J. (2008a). Development of a Short-Span Fiber-Reinforced Composite Bridge for Emergency Response and Military Applications. Journal of Bridge Engineering, 13(4), 388-397.

Robinson, M., and Kosmatka, J. (2008b). Light-weight fiber-reinforced polymer composite deck panels for extreme applications. Journal of Composites for Construction, 12(3), 344-354.

Robinson, M. J. (2008). Simulation of the vacuum assisted resin transfer molding (VARTM) process and the development of light-weight composite bridging. PhD Thesis, UCSD, San Diego, California.

Russell, B. R., and Thrall, A. P. (2012). Portable and rapidly deployable bridges: Historical perspective and recent technology developments. Journal of Bridge Engineering, 18(10), 1074-1085.

Saatcioglu, M., Ghobarah, A., and Nistor, I. (2006). Performance of structures in Indonesia during the December 2004 great Sumatra earthquake and Indian Ocean tsunami. Earthquake Spectra, 22(S3), 295-319.

Santner, T. J., Williams, B. J., and Notz, W. I. (2013). The design and analysis of computer experiments: Springer Science & Business Media.

Schmit, L. A., and Farshi, B. (1974). Some approximation concepts for structural synthesis. AIAA journal, 12(5), 692-699.

Schmit, L. A., and Miura, H. (1976). Approximation concepts for efficient structural synthesis: US National Aeronautics and Space Administration. NASA Contractor Report, 2552

Schutte, J. F., and Groenwold, A. A. (2003). Sizing design of truss structures using particle swarms. Structural and Multidisciplinary Optimization, 25(4), 261-269.

Shi, Y. (2001). Particle swarm optimization: developments, applications and resources. IEEE Proceedings of the Congress on evolutionary computation, 81-86.

Shi, Y., and Eberhart, R. (1998). A modified particle swarm optimizer. Evolutionary Computation Proceedings, The 1998 IEEE World Congress on Computational Intelligence. 69-73.

Shokrieh, M., Lessard, L., & Poon, C. (1996). Three-dimensional progressive failure analysis of pin/bolt loaded composite laminates. The AGARD Conference Proceedings, Neuilly-Sur-Seine, France.

Siegel, R. A. (2000). America's Grand Strategy Choices: DTIC Document.

Tanweer, M. R., Suresh, S., and Sundararajan, N. (2015). Self regulating particle swarm optimization algorithm. Information Sciences, 294(0), 182-202.

Thomas, A. S., and Kopczak, L. R. (2005). From logistics to supply chain management: the path forward in the humanitarian sector. Fritz Institute, 15, 1-15.

Thomas, G. R., and Sia, B. J. (2013). A Rapidly Deployable Bridge System Structures Congress 2013: Bridging Your Passion with Your Profession, ASCE, 656-667.

Trilateral Design and Test Code For Military Bridging and Gap Crossing Equipment. (May 2005): Trilateral Design and Analysis Group of the United States, Federal Republic of Germany and the United Kingdom of Great Britain.

Tuwair, H., Volz, J., ElGawady, M., Mohamed, M., Chandrashekhara, K., and Birman, V. (2015). Testing and Evaluation of Polyurethane-Based GFRP Sandwich Bridge Deck Panels with Polyurethane Foam Core. Journal of Bridge Engineering, 0(0).

Venkayya, V. (1971). Design of optimum structures. Computers and structures, 1(1), 265-309.

Venkayya, V., Khot, N., and Reddy, V. (1968). Optimization of structures based on the study of energy distribution: DTIC Document.

Wight, R., Erki, M., Shyu, C., Tanovic, R., and Heffernan, P. (2006). Development of FRP short-span deployable bridge-Experimental results. Journal of Bridge Engineering, 11(4), 489-498.

Williams;, B., Shehata;, E., and Rizkalla, S. H. (2003). Filament-Wound Glass Fiber Reinforced Polymer Bridge Deck Modules. Journal of Composites for Construction, 7(3), 266-273.

Winney, M. (1994). On active service. New Civil Engineer (1077), Page. 1-20.

Xia, R., and Liu, P. (1987). Structural optimization based on second-order approximations of functions and dual theory. Computer Methods in Applied Mechanics and Engineering, 65(2), 101-114.

Xie, A. Y. (2007). Development of an FRP deployable bridge. M. Sc.Thesis, Royal Military College of Canada (Canada), Ann Arbor.

Yin, S., Lin, J., and Huang, P. (2013). Studies on new forms of portable bridges for disaster relief. Proceedings of the Thirteenth East Asia-Pacific Conference on Structural Engineering and Construction (EASEC-13), the Thirteenth East Asia-Pacific Conference on Structural Engineering and Construction (EASEC-13), G-3-2.

Yuhui, S., and Eberhart, R. (1998). A modified particle swarm optimizer. Procedings on the Evolutionary Computation, 1998.

Zetterberg, T., Åström, B. T., Bäcklund, J., and Burman, M. (2001). On design of joints between composite profiles for bridge deck applications. Composite structures, 51(1), 83-91.

Zhang, D., Zhao, Q., Huang, Y., Li, F., Chen, H., and Miao, D. (2014). Flexural properties of a lightweight hybrid FRP-aluminum modular space truss bridge system. Composite structures, 108, 600-615.

Zhou, A. (2002). Stiffness and Strength of Fiber Reinforced Polymer Composite Bridge Deck Systems. Ph.D. Thesis, Faculty of the Virginia Polytechnic Institute and State University, Blacksburg, Virginia, USA.

Zhou, A., Coleman, J. T., Temeles, A. B., Lesko, J. J., and Cousins, T. E. (2005). Laboratory and field performance of cellular fiber-reinforced polymer composite bridge deck systems. Journal of Composites for Construction, 9(5), 458-467.

Zhou, A., Qu, B.-Y., Li, H., Zhao, S.-Z., Suganthan, P. N., and Zhang, Q. (2011). Multiobjective evolutionary algorithms: A survey of the state of the art. Swarm and Evolutionary Computation, 1(1), 32-49.

Zhou, M., and Rozvany, G. (1993). DCOC: an optimality criteria method for large systems Part II: algorithm. Structural optimization, 6(4), 250-262.

Zhu, J., and Lopez, M. M. (2014). Performance of a lightweight GFRP composite bridge deck in positive and negative bending regions. Composite structures, 113(0), 108-117.

WEBSITES

Web-1:http://firstpeoples.org/wp/over-3-million-affected-by-massive-philippines-earthquake/, consulted 5 July 2015.

Web-2: http://newsinfo.inquirer.net/510343/11-bridges-in-bohol-reopened-to-traffic, consulted 5 Aug 2015

Web-3:http://home.hiroshima-u.ac.jp/bridge2/out-hiro/open/2009-sayo/sayo-shiso-flownbridges2.pdf, consulted 5 Aug. 2015

Web-4: https://www.wfel.com/downloads/wfel-mgb-brochure.pdf, consulted 5 Aug. 2015

Web-5: https://www.wfel.com/downloads/wfel-dsb-brochure.pdf, consulted 5 Aug. 2015